THERMAL ANALYSISOF SOLAR FLAT PLATE COLLECTOR COUPLED WITH HEAT STORAGE

A Thesis Submitted in Partial Fulfillment of the Requirements for the Degree of

DOCTOR OF PHILOSOPHY

by

Dawit Gudeta Gunjo

(Roll No. 136103030)

Department of Mechanical Engineering

Indian Institute of Technology Guwahati

Guwahati-781039

INDIA

February 2018

Department of Mechanical Engineering,
Indian Institute of Technology Guwahati,
Guwahati – 781039,
INDIA

CERTIFICATE

It is certified that the work contained in the thesis entitled **Thermal Analysis of Solar Flat Plate Collector Coupled with Heat Storage** submitted by **Mr. Dawit Gudeta**, a student in the Mechanical Engineering Department, Indian Institute of Technology Guwahati, India, for the award of the degree of **Doctor of Philosophy** has been carried out under our supervision and this work has not been submitted elsewhere for the degree.

Dr. Pinakeswar Mahanta
Professor
Department of Mechanical Engineering
Indian Institute of Technology Guwahati
Guwahati – 781039, India

Dr. P.S. Robi
Professor
Department of Mechanical Engineering
Indian Institute of Technology Guwahati
Guwahati – 781039, India

Declaration

I hereby declare that the information presented in this thesis is entirely original and my own research work which has not previously been submitted for a degree or diploma at this institute or any other educational institution. I have confirmed to the norms and guidelines given in the ethical code of the institute.

Dawit Gudeta Gunjo
Mechanical Engineering
Indian Institute of Technology Guwahati
Guwahati – 781039, India
February 2018.

Dedicated to

Gudeta Gunjo and Wudinesh Nigatu

Acknowledgements

I bow my head and record my sincere gratitude to the God almighty for giving me the strength, health and the sprit to complete my research work.

I wish to express my deep sense of gratitude to Professor Pinakeswar Mahanta and Professor P. S Robi for their invaluable guidance, encouragement and inspiration in bringing out this work to the existing shape.

I would like to thank my doctoral committee members, Prof. Niranjan Sahoo, Prof. U. K. Saha and Dr. V. V. Goud for their valuable suggestions and encouragement at different stages of research. I wish also like to express my sincere thanks to Dr. Amarash Dalal for providing computational facilities for simulation task and Prof. A. K. Dass for his help, suggestions and encouragement throughout my academic life.

I express my sincere thanks to Mr. D. Chetri, Mr. M. Sarma, Mr. L. Gogoi, Mr. N. Borah, Mr. B. Choudhury, Mr. J. Basumatary and other staff members of Central Workshop for helping me in various stages of fabrication of the experimental setups. Without their timely support this work could not be accomplished. I am thankful to Dr. Jai Manik and Mr. B. Negash for their encouragement and support during my stay in IIT Guwahati. I shall always be grateful to my IITG and childhood friends for their countless encouragement and wishes.

My deepest gratitude goes to my wife and families for their continuous love and support throughout my studies. I would especially like to thank my wife and sisters who endures all the difficulties alone during my stay at IIT Guwahati. Special thanks go to my sister in - law for their continual support and love.

Dawit Gudeta Gunjo

IIT Guwahati

Abstract

Energy is an essential requirement for the technological and industrial development of any nation. Among the various energy sources, solar energy and biogas have been identified as clean, safe, sustainable, abundantly available energy source with least environmental constraint. The production of biogas from organic waste is a temperature dependent process. There are three optimum temperature ranges for generating methanogens which is responsible for production of biogas. These are: psychrophilic (≤ 293 K), mesophilic (303 – 313K) and thermophilic (323 K – 333 K).This may be achieved by heating of feedstock in the biogas digester through a heat exchanger in which primary working fluid is water and same is heated with solar thermal collector. Since solar energy varies widely during the day and also dependent on weather as well as season of the year, utilizing the solar energy in continues manner is difficult. Further, geometry, shape and size of the water tubes (riser tube) play an important role in heat transfer. Thus there is a need to undertake detail experimental as well as numerical study on type of collectors (straight and bent tube) on performance of solar water heating system. The fluctuating nature of solar energy restricts its demand for various applications. Integrating the solar collector with the thermal energy storage system (TES) using paraffin wax as phase change material is favourable solution to smoothen the inconsistency.

The application of the integrated solar thermal system for biogas production process with controlling device is feasible to maintain the biogas digester at 308 ± 2 K. This was done with the help of controlling devices such as solenoid valves, Arduino microcontroller, motor driving modules, thermostat and DC voltage supply along with the solar water heating system and thermal storage. The C language program with necessary algorithms helped to develop the relationship between the temperature of the biogas digester and shell tank. This algorithm was essential for diverting the water flow away from the shell tank when the shell temperature exceeds the desired limit. Similarly when the shell temperature falls below desired

limit, the solenoidal valves are modulated to operate for the same. During this, the heat energy is stored/released in/from the LHS system.

The results from the controlled experiment revealed that the temperature of the fluid inside the shell varied from 308.9 K – 314 K and the biogas digester temperature varied in between 308.1 K – 309.2 K. Similar experiments were also performed for checking repeatability. It was noticed that the shell tank temperature varied from 309.2 K – 313.4 K whereas this variation in biogas digester was from 308.3 K – 309.1 K. The maximum temperature fluctuations in the biogas digester for all cases of controlled experiments were found to be 1.1 K which recommended for growing mesophilic methane-forming bacteria without affecting the stability of the process. This shows that the developed system is an alternate solution to increase the biogas production by supplying uniform temperature required for the same.

Additionally, the maximum error deviation in the prediction of outlet water and absorber plate temperature was observed to be less than 6% and 4%, respectively for both straight and bent tube collectors. Both the experiment and the numerical results showed the superiority of the bent tube arrangement in contrast to straight tube. Similarly, the numerical and experimental results of the paraffin filled LHS revealed a maximum deviation of ~ 5 K during charging and ~7 K during the discharging process. The low value of error establishes the confidence in the predictive capabilities of the developed numerical model.

Contents

Results and Discussion

List of Figures

List of Tables

Nomenclature

A	:	Area of the collector (m^2)
A_a	:	Area of the absorber plate (m^2)
A_{c1}	:	Area of collector - 1 (m^2)
A_{c2}	:	Area of collector - 2 (m^2)
A_{mushy}	:	Mushy zone constant
A_p	:	Aperture area (m^2)
B	:	Width of the collector (m)
Bi	:	Biogas
Bi_b	:	Biogas temperature at the bottom (K)
Bi_t	:	Biogas temperature at the top (K)
C_1	:	Model constant
C_2	:	Model constant
C_b	:	Bond conductance (W/m.K)
C_p	:	Specific heat (J/kg.K)
$C_{p.EFF}$	:	Effective heat capacity (J/kg)
$C_{p\ np}$	:	Specific heat of the nanoparticle (J/kg.K)
$C_{p\ npcm}$	:	Specific heat of nanoparticle enhanced phase change material (J/kg. K)
$C_{p\ pcm}$	:	Specific heat of the phase change material (J/kg.K)
$C_{p.L}$	:	Liquidous specific heat (J/kg)
$C_{p.S}$	:	Solidus specific heat (J/kg)
d	:	Diameter of the riser tube (m)
D	:	Outer diameter of the tube (m)
D_i	:	Inner diameter of the tube (m)
d_{np}	:	Diameter of nanoparticle (nm)

D_s	:	Shell diameter (m)
dT	:	Range of melting (K)
$\hat{E}$	:	Exergy efficiency (%)
$\dot{E}d$	:	Distracted exergy (W)
$\dot{E}d_{leak}$	:	Exergy loss due to leakage (W)
$\dot{E}d_{p-f}$	:	Distracted exergy between the plate and the working fluid (W)
$\dot{E}d_{s-p}$	:	Distracted exergy between the absorber plate and the sun (W)
$\dot{E}x_{abs}$	:	Absorbed exergy (W)
$\dot{E}x_{dest}$	:	Destructed exergy (W)
$\dot{E}x_{in}$	:	Inlet exergy (W)
$\dot{E}x_{\text{in.f}}$	:	Exergy of the inlet fluid (W)
$\dot{E}x_{\text{in.rad}}$	:	The exergy of absorbed heat from the sun (W)
$\dot{E}x_{out}$	:	Outlet exergy (W)
$\dot{E}x_{out.f}$	:	Exergy of the outlet fluid (W)
$\dot{E}x_{heat}$	:	The rate of exergy transferred in the form of heat (W)
$\dot{E}x_{p.f}$	:	Exergy transferred between the plate and the working fluid (W)
$\dot{E}x_{rad}$	:	The radiated solar exergy (W)
$E_{\text{L,C}}$	:	Latent heat stored during charging (MJ)
$E_{\text{L,D}}$	:	Latent heat stored during discharging (MJ)
$E_{\text{S,C}}$	:	Sensible heat stored during charging (MJ)
$E_{\text{S,D}}$	:	Sensible heat stored during discharging (MJ)
$E_{\text{T,C}}$	:	Total heat stored during charging (MJ)
$E_{\text{T,D}}$	:	Total heat stored during discharging (MJ)
f	:	Friction factor
$\vec{F}$	:	Body force (N/m^3)
F_R	:	Heat removal factor
F'	:	Collector efficiency factor
g	:	Acceleration gravity (m/s^2)

h_{fi}	:	Convective heat transfer coefficient of the fluid (W/m^2.K)
h_w	:	Convective heat transfer coefficient due to wind (W/m^2.K)
Hx $_e$	:	Heat exchanger temperature at the outlet side (K)
Hx $_i$	:	Heat exchanger temperature at the inlet side (K)
I	:	Solar insolation (W/m^2)
K	:	Loss coefficient due to entry effect, elbow, bend, fitting etc..
k_b	:	Thermal conductivity of the back insulation material (W/m.K)
K_f	:	Thermal conductivity of the working fluid (W/m.K)
k_i	:	Conductivity of the plate material (W/m.K)
K_{np}	:	Thermal conductivity of the nanoparticle (W/m.K)
K_{npcm}	:	Thermal conductivity of nanoparticle enhanced phase change material (W/m.K)
K_{pcm}	:	Thermal conductivity of the phase change material (W/m.K)
L	:	Length of the shell (m)
Δl	:	Length of the tube (m)
L_F	:	Latent heat of fusion (kJ/kg)
L_{np}	:	Latent heat of the nanoparticle (J/kg)
L_{npcm}	:	Latent heat of nanoparticle enhanced phase change material (J/kg)
L_{pcm}	:	Latent heat of the phase change material (J/kg)
M	:	Dimensionless number
m	:	Mass (kg)
m_{np}	:	Mass of the nanoparticle (kg)
$\dot{m}$	:	Mass flow rate (kg/s)
n	:	Number of tube
N_{ud}	:	Nusselt number
ΔP	:	Pressure drop (N/m^2)
P_{pump}	:	Pumping power (W)
Pr	:	Prandtl number
Q_i	:	Solar radiation received by the solar collector (W)

Q_{leak}	:	The rate of leakage heat from the absorber plate (W)
Q_o	:	The rate of heat loss (W)
Q_u	:	The rate of useful heat gain (W)
Re	:	Reynold number
S	:	Radiation heat flux (W/m^2)
$\vec{S}$	:	Darcy law's source term (N/m^3)
Ta	:	Shell tank
T_a	:	Ambient temperature (K)
Ta $_b$	:	Tank temperature at the top (K)
Ta $_t$	:	Tank temperature at the top (K)
T_g	:	Glass temperature (K)
T_i	:	Inlet temperature (K)
T_{ib}	:	Inlet temperature of the bent tube collector (K)
T_{ic1}	:	Inlet temperature of collector - 1 (K)
T_{ic2}	:	Inlet temperature of collector - 2 (K)
T_{int}	:	Initial temperature of the thermal energy storage (K)
T_{inlet}	:	Inlet temperature of the heat transfer fluid (K)
T_{is}	:	Inlet temperature of the straight tube collector (K)
T_L	:	Liquidous temperature (K)
T_m	:	Melting temperature (K)
T_o	:	Outlet temperature (K)
T_{ob}	:	Outlet temperature of the bent tube collector (K)
T_{oc1}	:	Outlet temperature of collector - 1 (K)
T_{oc2}	:	Outlet temperature of collector - 2 (K)
T_{os}	:	Outlet temperature of the straight tube collector (K)
T_p	:	Plate temperature (K)
T_{pb}	:	Plate temperature of the bent tube collector (K)
T_{ps}	:	Plate temperature of the straight tube collector (K)
T_{ref}	:	Reference temperature (K)
T_s	:	Sun temperature (K)

T_S	:	Solidus temperature (K)
T_{sky}	:	Sky temperature (K)
U	:	Overall loss coefficient (W/m^2.K)
U_b	:	Overall bottom loss coefficient (W/m^2.K)
U_t	:	Overall top loss coefficient (W/m^2.K)
u	:	Velocity along x direction (m/s)
V	:	Velocity of the fluid (m/s)
v	:	Velocity along y direction (m/s)
$\vec{v}$	:	Velocity of the phase change material (m/s)
V_{ol}	:	Volume (m^3)
V_w	:	Wind velocity (m/s)
W	:	Tube center to center distance (m)
w	:	Velocity along z direction (m/s)
X_{exp}	:	Experimental result
X_{sim}	:	Simulation result
x	:	Displacement along x direction (m)
y	:	Displacement along y direction (m)
z	:	Displacement along z direction (m)

Greek Symbols

δ	:	Thickness of the plate material (m)
σ	:	Boltzmann constant (J/K)
ε_g	:	Emissivity of the glass
ε_p	:	Emissivity of the plate
δ_b	:	Thickness of the back insulation (m)
β_a	:	Collector tilt angle
φ	:	Volume fraction (%)
θ	:	Melt fraction
β	:	Thermal expansion (1/K)

ε	:	Epsilon
ζ	:	Correlation factor
τ	:	Emissivity of the glass
α_{eff}	:	Absorptivity of the plate effective
η	:	Thermal efficiency (%)
η_o	:	Optical efficiency (%)
η_{ovl}	:	Overall efficiency (%)
η_s	:	Efficiency of straight tube collector (%)
η_b	:	Efficiency of bent tube collector (%)
η_{c1}	:	Efficiency of collector - 1 (%)
η_{c2}	:	Efficiency of collector - 2 (%)
ρ_{pcm}	:	Density of the phase change material (kg/m^3)
ρ	:	Density (kg/m^3)
ρ_{np}	:	Density of the phase change material (kg/m^3)
ρ_{npcm}	:	Density of nanoparticle enhanced phase change material (kg/m^3)
μ_{npcm}	:	Viscosity of nanoparticle enhanced phase change material ($N.s/m^2$)
μ_{pcm}	:	Viscosity of the phase change material ($N.s/m^2$)
μ	:	Viscosity ($N.s/m^2$)

Abbreviations

CFD	:	Computational Fluid Dynamics
C/N	:	Carbon to Nitrogen Ratio
CSP	:	Concentrated Solar Power
CST	:	Concentrated Solar Thermal
EHC	:	Equivalent Heat Capacity
FPC	:	Flat Plate Collect
GI	:	Galvanized Iron
HTF	:	Heat Transfer Fluid
KVIC	:	Khadi and Village Industries Commission
LHESS	:	Latent Heat Energy Storage System
LHS	:	Latent Heat Storage
PCM	:	Phase Change Material
SHC	:	Solar Heating and Cooling
SHS	:	Sensible Heat Storage
TES	:	Thermal Energy Storage
TESS	:	Thermal Energy Storage System
UPS	:	Uninterruptible Power Supply

Chapter - 1

Introduction

1.1Preface

Energy is an essential requirement for the technological and industrial development of any nation. The demands of energy for the last two centuries have been met mainly by utilizing fossil fuels. Due to the fossil fuel depletion and emission of pollutants deteriorating the environment, researchers are focusing their attention on exploiting renewable energy sources and technologies. Some of these are solar energy, wind energy, bioenergy and geothermal energy. Among the various renewable energy sources, solar energy and energy from biogas have been identified as energy sources, which are cheap, safe, sustainable and abundantly available with least environmental constraint.

1.2Harvesting Solar Energy

The solar energy appears to be the most promising alternative in terms of large-scale usage at a cheaper rate (Banos *et al.* 2011). It uses solar thermal collectors to convert the solar energy to thermal energy for various uses. Most of the solar thermal systems work at low or medium temperatures in the range from 40 to 120 ºC (Cruickshank 2009) which is sufficient for domestic hot water and space heating needs. Various types of solar thermal collectors exist and depend on the application temperature range, collector orientation and power output. Figure 1.1 illustrates various types of solar thermal collector. Presently, the demand for solar heating systems has increased attention due to simplicity, low running cost and reasonable investment cost. Among the various types of solar thermal collectors, flat plate collector (FPC) appears to be the best in terms of cost and simplicity for achieving moderate temperature (Janjai *et al.* 2000).

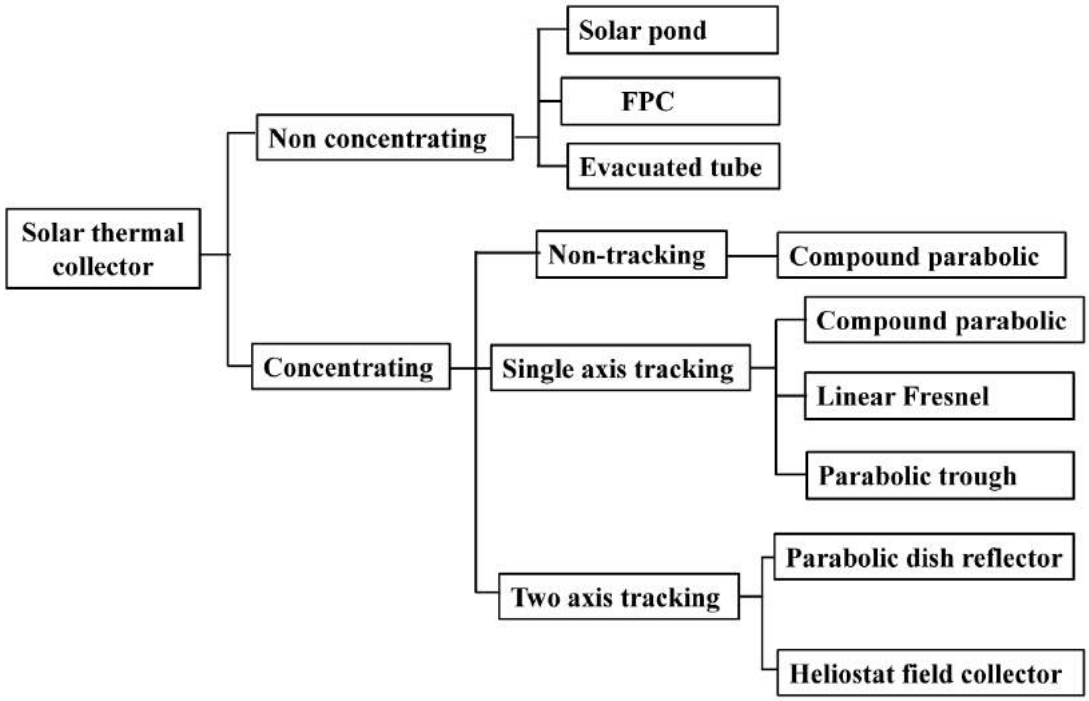

Fig.1.1 Classification of solar thermal collectors

1.2.1 Flat plate collector

Hottel and Whillier developed the first proper FPC with empirical correlations in 1950 (Vishal et al 2017). The FPC consist of: (i) transparent cover which helps to transmit the solar radiation to the plate, better transfer of solar radiation to the absorber plate and reduction in radiative and convective heat loss from the surface of absorber plate (ii) absorber plate to absorb the radiant solar energy (iii) tube(s) with working fluid to absorb heat from the absorber plate and (iv) insulated casing to eliminate losses from the collector (Karanth 2015). The transparent cover which is generally made of glass reduces the heat loss from the collector surface. The absorber plate material can be thermally stable polymers, steel, copper or aluminium which can be coated and painted black to increase the absorptivity. Figure 1.2 shows the typical components of an FPC.

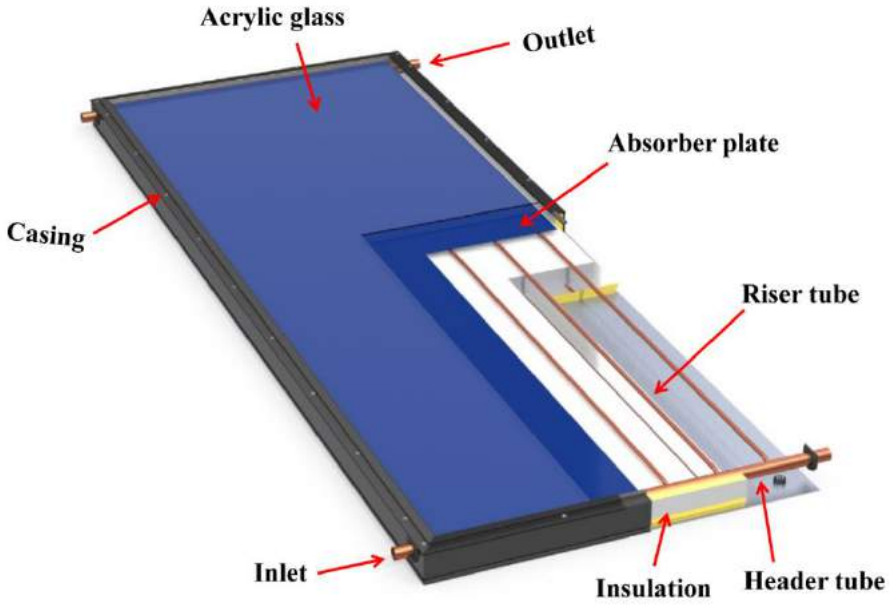

Fig.1.2 Cross section of basic components of FPC

Various types of absorbing tube arrangement exist for FPC, *viz*., serpentine, tube formed in metal sheet, parallel tube and trickle type corrugated sheet. These are depicted in Fig. 1.3. Due to simplicity in manufacturing, parallel tube arrangement is common for various applications.

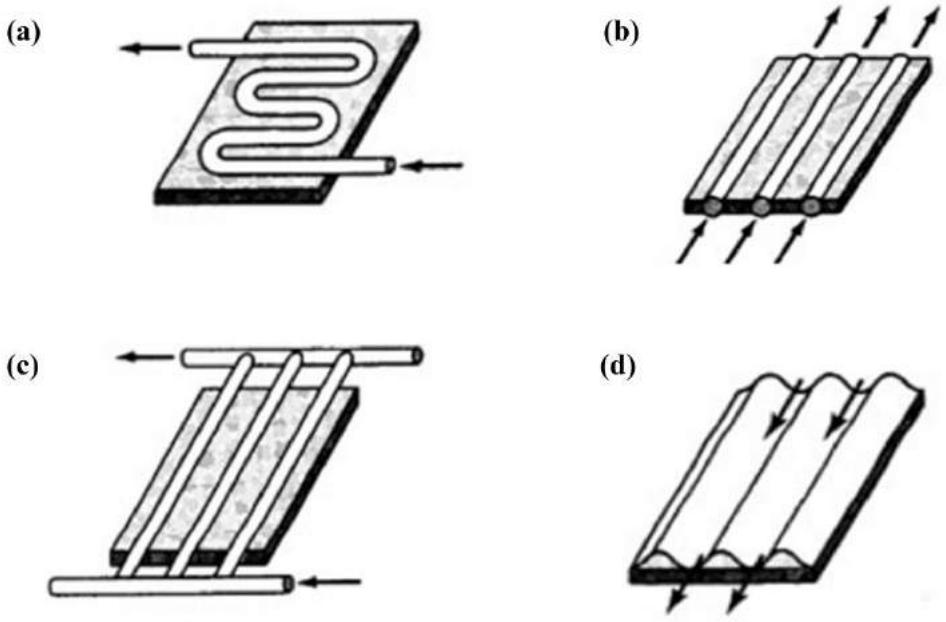

Fig.1.3Tube arrangement (a) serpentine (b) tube formed in metal sheet (c) parallel and (d) trickle corrugated sheet.(http://www.see.murdoch.edu.au/resources/info/Tech/lowtemp/hotwatersys.html)

1.2.2 Application of solar thermal technology

The various applications of solar thermal technology are illustrated in Fig.1.4. These are generally for heat applications and power applications. Depending upon the application temperature, solar thermal technology for heat applications is further categorized into low, medium and high-temperature systems.

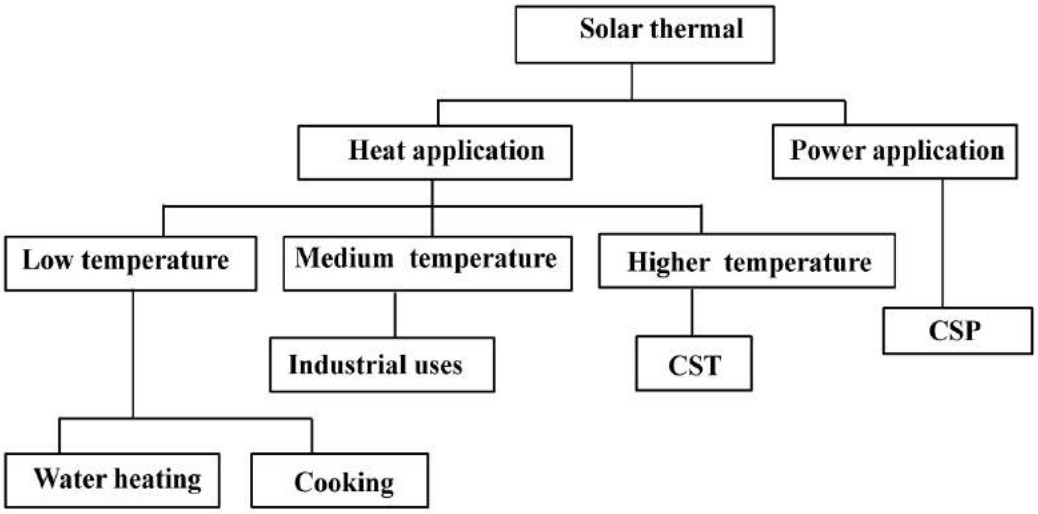

Fig.1.4 Applications of solar thermal technology

1.3Thermal Energy Storage Systems

Thermal Energy Storage System (TESS) is a technology which stores energy by heating, melting or vaporizing a storage medium and the stored energy is used at a later time for various applications by cooling or solidifying the storage medium. Due to the fluctuating nature of the solar radiation throughout the day, a TESS is required to be designed properly so as to achieve a continuous supply of heat. The system stores heat energy when available in sufficient quantity and discharges when there is shortage. Well-designed TESS for a specific application depends on the storage duration, costs, charging and discharging rate of temperature, storage capacity and space requirement. Sarbu and Sebarchievici (2018) and Ding and Riffat (2013) have identified four different types of thermal energy mechanisms namely latent heat, sensible heat, chemical reaction and thermochemical (sorption) thermal energy

storage systems. The different thermal energy storage mechanisms are illustrated in Fig.1.5.

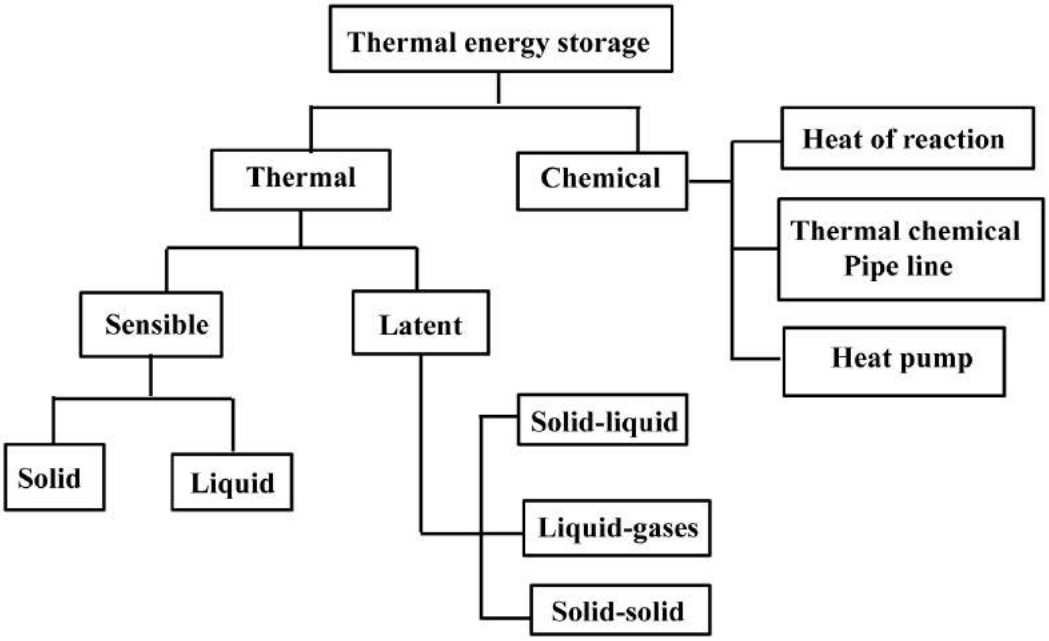

Fig. 1.5 Mechanisms of thermal energy storage

Among the four, sensible and latent heat storages are very common in thermal energy storage systems. In sensible heat storage (SHS), the energy is stored thereby raising the temperature of the solid or liquid medium. SHS system uses the heat capacity and the change in the temperature of the material during the process of charging and discharging. In latent heat storage (LHS) system, thermal energy is stored by melting a storage medium. The stored heat energy is released from storage material during solidification. In contrast to SHS, LHS is attractive due to (i) the ability to provide a high-energy storage density and (ii) store heat at a constant temperature corresponding to the phase change temperature of the storage substance (Farid *et al.* 2004).

One of the potential applications of solar thermal collector integrated with LHS is utilizing for biogas production process which requires uniform temperature for growing methane-forming bacteria for long period of time.

1.4Thermal Management of Biogas Digester

In a biogas digester, the rate of biogas production from organic matter depends on several factors such as pH, temperature, loading rate, feeding rate, C/N ratio, retention time, toxicity, etc. (Vindis *et al.* 2009 and Nijaguna 2006). Among these, temperature is one of the main parameter affecting the microbiological activity. The production rate of methane-forming bacteria increases with increase in digester temperature. Inside a biogas digester, the temperature changes due to the change in season and weather (climatic) condition. Higher temperature fluctuation leads to imbalance in the anaerobic digestion process resulting in failure of complete digestion process. The causes for temperature fluctuation inside the biogas digester are as follows:

- Supplying of new raw material (waste) in to the digester which has different temperature as compared to process temperature.
- Formation of temperature layer as a result of improper insulation.
- Ineffective and wrong placement of the heating system and insufficient mixing.
- Higher variation in temperature during summer and winter.

There are three optimum temperature ranges for generating methanogens (methane-forming bacteria). These are: psychrophilic (≤ 293 K), mesophilic (303 – 313 K) and thermophilic (323 – 333 K) (Nijaguna 2006 and De Mes *et al.* 2003). However, achieving the mesophilic and thermophilic temperature range for anaerobic digestion under normal condition is difficult.

Presently, several researchers are attempting to increase the temperature and reduce heat losses from the biogas digester in different ways. Some of these methods are: (i) building biogas digester underground, (ii) heating the digester directly or indirectly using solar collector and (iii) placement of the biogas digester at locations which receive direct solar radiation. Above techniques are being used since anaerobic fermentation needs stable temperature condition. The two most common methods of thermal management for heating biogas digester are as follows:

i. **Direct heating system** is injection of hot water into biogas digester. However, this injection of hot water increases the water content of the slurry and should only be used if such dilution is necessary. The drawback with this system is relatively higher cost for large-scale application.

ii. **Indirect heating system** is done with the help of heat exchangers placed either inside or outside of the biogas digester. This type of heating system depends on the shape of the digester, the nature of operating mode, and types of substrate (feed material) used. Indirect heating can be carried out in many ways such as heating the floor (bottom) of digester, heating internal and external part of the digester using heat exchanger.

1.5 Motivation

The energy crisis during the Second World War forced several countries that were highly dependent on fossil fuel to pay attention for producing competitive and environment friendly energy source. Courtney and Dorman (2003) reported the possibility of complete depletion of crude oil within 40 – 70 years and natural gas within 50 years. There is also a worldwide concern regarding future energy demand. In addition, the increase in greenhouse emission resulting from energy production using fossil fuel is of very high concern throughout the globe. Dow and Downing (2006) pointed out an increase of world average temperature from 1.4 °C to 5.8 °C by the year 2100 due to use of fossil fuel as energy source.The solution to the above-said challenge lies in the utilization of renewable energy. Solar energy and energy from biogas are widely accepted as clean, low initial cost, environmental friendly, cheap having higher potential and unlimited source of renewable energy.

Production of biogas from different waste materials is attained through anaerobic digestion of complex organic matter with the help of microorganisms which results in the formation of mixture of methane and carbon dioxide. However, the rate of methane production from organic matter mostly depends on the temperature of the feed material in the digester. Microbiological activity increases with an increase in digester temperature.

As mentioned in the previous section (section 1.4), there is a specific temperature range over which a biogas digester can operate with maximum production rate. However, achieving the optimum temperature ranges for anaerobic digestion under normal condition is difficult. In rural sector, if the biogas system can be integrated with a solar heating system, the biogas production can be increased. This was the main motivation behind the present study. The present work is aimed at developing a solar heating system integrated with heat storage along with controlling devices for maintaining a constant temperature of the feed material of a biogas digester.

Solar water heating devices are very common in countries which have solar radiation. Exploiting solar energy for heating requires the use of FPC which receives the incoming solar radiation and delivers a large fraction of the thermal energy to the working fluids. Solar FPC with metal absorber plate and covers are the most successful device that converts solar energy into heat at reasonable price without affecting environment. Since solar radiation is fluctuating throughout the day, the outlet temperature from the solar collector also varies and this causes non-uniform output.

Therefore, to smooth the inconsistency of the temperature which is coming from the solar collector, the LHS system with paraffin wax as phase change material (PCM) decided to be developed. The working principle and advantages of thermal energy storage system have been presented in section 1.3. The application of the integrated solar thermal system (solar collector, latent heat storage and controlling device) for biogas production process is tested experimentally and the results are reported.

1.6 Objectives of the Thesis

The following objectives have been addressed in the present investigation:

- To develop a bent tube solar collector, evaluate and compare its performance with a straight tube collector, both numerically as well as experimentally using exergy and energy analysis under different operating parameters.
- To investigate the thermal performance of the latent heat storage under various working parameter experimentally and numerically.

- To investigate the performance of Al_2O_3 nanoparticle dispersed latent heat storage and compare the results with pure paraffin based storage.
- To investigate the effectiveness of the integrated solar thermal system in biogas production process in terms of temperature variation with and without controlling conditions.

1.7Outline of the Thesis

The present thesis has been organized by focusing the concentration towards the fabrication of solar thermal system which comprises of straight and bent tube collectors, latent heat storage and heat exchanger. The thesis consists of eight chapters which are summarized as follows:

Chapter - 1: Introduces the importance of energy, harnessing solar energy, collector types, flat plate collector, application of solar thermal, thermal energy storage, thermal management for biogas digester, motivation and objectives of the present work.

Chapter - 2: The detailed survey of literature on the various aspects of solar collector, effect of various working parameters on the performance of the solar collector, thermal energy storage types, the effect of working parameters on thermal performance of the storage, numerical studies on flat plate collector, numerical studies on thermal energy storage have been presented. Additionally, the review on thermal management in biogas digester during anaerobic digestion process also reported.

Chapter - 3: Presents the theoretical formulation, the 3-dimensional numerical model, governing equations, boundary conditions, meshing, and grid independence test for the solar collector as well as for the thermal energy storage.

Chapter - 4: Presents the detailed experimental setup, procedures and the various measuring instruments used for the present work.

Chapter - 5: The experimental and numerical results of the solar collector along with results of parametric study have been presented. Energy and exergy analyses of the solar heating collector have also been presented and discussed.

Chapter - 6: Presents the result and discussions of the experimental and numerical investigation of the thermal storage system (latent heat storage).

Chapter - 7: The experimental setup and results of controlled and uncontrolled experiments for the integrated solar thermal system along with its application in biogas production have been presented and discussed.

Chapter - 8: The conclusions of the research work and scope for future work are presented. This chapter is followed by reference and appendices.

Chapter - 2

Literature Review

2.1 Introduction

This chapter presents the review of literature on solar thermal system and thermal energy storage along with the methods to improve the performances of the same. Sections 2.1 – 2.3 briefly describe the introduction of solar energy and review on solar water heating collectors. Effect of various operating parameters on the performance of solar heating systems is presented in section 2.4. The review on exergy analysis and numerical study on the flat plate solar collector are reported in sections 2.5 to 2.6. Literature related to the thermal energy storage and performances are presented in section 2.7. The enhancement technique for phase change material is reported under section 2.8. Section 2.9 presents the thermal management techniques for anaerobic digestion process. The various techniques used for controlling temperature inside biogas digester are reported in section 2.10. Finally, summary of the literature review is presented in section 2.11.

2.2 Solar Energy

Earth receives about 170×10^{12} kW of energy from sun out of this, 30% is reflected back to the outer atmosphere, 23% is utilized in photosynthesis process and 47% is received as low temperature energy at the surface (Duffie and Beckman 1991). The energy demands for the last two centuries are met mainly by utilizing carbon fuels. Due to the forecast of fossil fuel depletion, researchers are focusing their attention on other energy sources like nuclear energy and non-conventional energy (Cardinale *et al*. 2003). The increasing environmental concern due to global warming and the harmful effect of carbon emission have also created new demand for clean and sustainable energy, *viz*., solar, wind, biomass and geothermal sources of energy. Among the various sources, solar energy is widely accepted as a clean, environmental friendly, cheap and limitless energy source (Keyanpour *et al.* 2000).

2.3 Flat Plate Solar Collector

FPCs with metal absorber plate and covers are the most successful devices that convert solar energy in to heat at reasonable price without affecting the environment (Janjai *et al*. 2000 and Kalogirou 2009). These collectors can heat the working fluid to a maximum temperature of 80 °C –120 °C (Duffie and Beckman 1991 and Sukhatme and Nayak 2008). Even though temperature rise is small, it has the advantage of simplicity in design with lower maintenance cost (Tchinda 2009). Janjai *et al.* (2000) reported FPC as most efficient and simple means for collecting solar energy for water heating application. However, Madhusudan *et al*. (1981) had reported 22-30%, 5-7%, and 5-10% as the losses due to convection, radiation from the front surface of the absorber and radiation from the back surface of the collector, respectively.

2.4 Factors Affecting the Performance of Flat Plate Collector

The performance of a FPC is influenced by various factors. These factors are flow rate, transmittance of the glass, emissivity of the absorber plate, collector tilt angle, tube spacing, air gap between plate and glazing, absorber plate coating, inlet water and ambient temperature, solar insolation, wind speed, number of glazing covers, top heat loss coefficient, etc. (Sekhar *et al*. 2009 and Ho-Mingyeh *et al.* 1999). Study of these factors is necessary to enhance the thermal efficiency of the solar collector.

2.4.1 Effect of tube spacing and geometry

Ghamari and Worth (1992) performed experimental investigation on the effect of tube spacing on thermal efficiency and cost effectiveness. They reported higher thermal efficiency with tube spacing of 16 cm. Comparative study with tube spacing of 11 cm and 16 cm on thermal performance of FPC was carried by Fatigun *et al.* (2013). They found higher thermal performance with spacing of 16 cm followed by 11cm. Higher tube spacing results in an increase in the overall cost of the collector. Hobbi and Siddiqui (2009) performed experimental investigation on various tube

geometries, namely, regular tube with conical ridges, coil spring wire, circular tube, and twisted strip tabulators. The results indicate no significant change on the thermal performance of the solar collector with change in tube geometry. Ekramian *et al*. (2014) carried out numerical study with circular, triangular, hexagonal and square tubes on the thermal performance of FPC and observed higher thermal performance for circular tube geometry compared to others. The thermal efficiency with circular, triangular, square, and hexagonal tubes was reported to be 38.4%, 11.2%, and 6.6%, respectively.

Amrutkar*et al.* (2012) assessed the thermal performance of FPC with different absorber plate geometric configurations. It was found that changing the geometry of absorber plate and glazing material affects the thermal efficiency and outlet temperature of the fluid. Kundu (2001) carried out comparative study between various geometry of absorber plate such as rectangular, trapezoidal, and rectangular profile with a step change thickness profile on thermal performance. Higher thermal performance was observed for the trapezoidal profile compared to the others. However, this profile is hardly found in actual system due to difficulties in manufacturing.

2.4.2 Effect of air gap between plate and glass

The convective heat losses found in FPCs depends on the spacing between the glass and the absorber plate. Do Ango *et al.* (2013) investigated the effect of air gap on convective heat loss coefficient and thermal performance. The result revealed that an air gap of 1.0 cm resulted lower convection heat loss and higher thermal performance compared to higher air gap.

Ihaddadene *et al*. (2014) carried out investigation with air gap varying in the range from 0.5 – 6 cm to analyze the effect on the thermal efficiency and observed a decrease in efficiency with increase in the air gap. Sarmaand Hatibaruah (2014) investigated the effect of air gap on the top heat loss coefficient for single, double and triple glazed FPC. The air gap of 5 mm, 10 mm and 15 mm were considered for the investigation. The result indicated low top heat loss coefficient for the double

glazed with 10 mm air gap collector. Dovic and Andrassy (2012) reported that changing the air gap does not affect the performance of FPC significantly.

2.4.3 Effect of glazing material

Heat loss in FPCs is significant due to the convection and radiation from the front surface of the absorber and the back surface. Hence, glazing of the FPC is mandatory to reduce the mentioned losses. Smith (2011) reported the major advantages of glazing of collector. These advantages are: (i) reduction in radiative and convective heat loss from the surface of absorber plate, (ii) better transfer of solar radiation to the absorber plate and (iii) reduction in heat loss due to low temperature difference between the ambient and the glaze inside the FPC. Whiller (1963) and Wijeysundera *et al.* (1991) have also highlighted the advantages of cover and effect on thermal efficiency.

Glass and plastics are the two most common glazing material used for covering FPC systems. The main parameters for selection of glazing materials are reflection, absorption and transmission. Quaschning (2016) reported that the transmissivity of the cover material should be higher whereas reflection and absorption should be lower for maximum efficiency. Vejen *et al*. (2004) found 6% improvement of solar collector performance by using glass with good optical properties.

Study by Njomo and Michel (2006) on effects of number of cover on thermal efficiency reveal increase in thermal efficiency with increase in the number of cover. Agarwal *et al.* (1981) reported higher thermal performance using double glazed collector due to lower heat loss compared to single glazed FPC. Khan *et al.* (2010) carried out comparative study between glazed and unglazed collector on thermal efficiency and outlet water temperature. The thermal efficiency and outlet water temperature were found to be 57.3%, 82.4 ^{o}C for glazed collector and 33.3%, 65.5 ^{o}C for unglazed collector, respectively.

Murugavel*et al.* (2008) conducted comparative study on glass with 3 mm and 6 mm thickness on thermal efficiency. The result indicated higher performance for 3mm thick glass. Bakari *et al*. (2014) studied the effect of various thicknesses of low iron

glass (3mm, 4mm, 5mm and 6mm) on thermal performance of FPC. The result showed higher thermal performance with 4mm thick glass. Maatouk (2006) reported the effect of glazing cover thickness on the radiative and conductive heat transfer. The result indicated that increasing the thickness of the glass cover decreases the heat losses. Comparison study between single, double and triple glazed collectors with a 5 mm thickness cover on thermal efficiency were carried out by Mustafa and Ismail (2013). The study reveals higher thermal efficiency for triple glazed glass whereas single glazed glass exhibited lowest thermal efficiency.

2.4.4 Effect of absorber plate coating

Absorber plate materials are commonly developed from metal such as aluminium, steel and copper due to the high heat conductivity. The surface of the absorber plate is usually coated with special coating and painted with black ink to maximize the absorptance of the radiant energy. Investigations by Madhukeshwara and Prakash (2012) revealed that use of special surface coatings increased the incident solar radiation and heat resistivity of the material.

Prakash *et al.* (2013) carried out both theoretical and experimental investigation on the effect of nanocoating of absorber plate material on absorptance and emittance. The result indicated higher absorptance and lower emittance due to the presence of nanocoating. Study by Katumba *et al.* (2008) revealed higher aborptance and thermal emissivity for the absorber plate when coated with NiO.

Nidal (2012) investigated the influence of coating with mixture of nanochromium with black ink on thermal and optical efficiencies. The result indicated 15% and 4.5% increment of thermal performance and optical efficiency, respectively, compared to conventional coated solar collector. AlShamaileh (2010) recommended a special coating consisting of nickel aluminum (NiAl) alloy along with black paint. The result indicated higher absorption efficiency with 6% NiAl alloy compared to conventional black paint coating.

2.4.5 Effect of collector tilt angle

The thermal performance of a solar collector depends on the orientation and tilt angle of the collector. The solar energy reaching the surface of the solar collector changes with tilt angle and orientation of the collector. Collector installed at an optimum tilt angle and with proper orientation resulted in maximum radiation on the surface of collector. Several researchers reported collectors installed in the northern hemisphere oriented to south and tilted at a certain angle (Wang and Hong 2015).
The effect of tilt angle on the collector performance carried by Ahmad and Tiwari (2009) revealed that the collector energy loss is almost 1% when the collector tilt angle was adjusted seasonally instead of adjusting each month.

Chiou and El-Naggar (1986) and Kern and Harris (1975) developed an empirical relationship to determine optimum tilt angle for south facing solar collector based on beam radiation. Elsayed (1989) developed a relationship to determine the optimum tilt angle based on effect of latitude, number of glazing, solar reflectivity and clearing index. Garg and Rani (1980) estimated the overall heat loss coefficient and collector thermal efficiency under different collector tilt angle. Iqbal (1979) and Kern and Harris (1975) reviewed the various methods for determining the optimum tilt angle based on latitude.

Investigation by Eke (2011) revealed higher thermal performance for the collector where the tilt angle was adjusted monthly compared to the collector with fixed tilt angle. Markvart (2000) developed a solar tracking collector which follows the sun motion to increase the direct solar radiation over the surface of the collector and observed 40% more solar energy using the developed model. The same study revealed that 95% of solar energy could be collected using fully automated solar tracking system.

2.4.6 Effect of fluid flow rate

Experimental investigation to optimize the fluid flow rate inside the solar water heating collector carried out by Bolaji (2006), revealed that the maximum thermal efficiency was achieved at an optimum flow rate of 0.1 kg/s. Study by Facão (2015)

conducted to optimize the flow rates in riser and header arrangement collector revealed homogenous temperature distribution for flow rates less than 0.025 kg/s. Weitbrecht *et al*. (2002) carried out experimental investigation with low flow rate to analyze flow distribution through the collector and obtained uniform temperature distribution in each riser tube. Kalogirou (2004) suggested an optimum fluid flow rate of 0.02 kg/s during testing of solar FPC.

Experimental investigations on the effect of varying flow rate on outlet water temperature by Ismail (2005) and Ismail (2007) indicates high outlet water temperature at low flow rate. Analytical study on the thermal efficiency of solar collector by Duffie and Beckman (1991) revealed higher collector efficiency factor at higher flow rate.

Parametric study by He *et al.* (2016) indicates a decrease in outlet water temperature resulting in an increase in thermal efficiency of the collector from 60.8% to 70.0% as the water inlet velocity was increased from 0.016 to 0.04 m/s. Investigation by Badach *et al*. (2012) revealed that the fluid mass flow rate had higher impact on the thermal efficiency of FPC compared to solar radiation and / or inlet tube diameter.

2.4.7 Effect of inlet water temperature

The inlet water temperature also influences the thermal efficiency of solar collector. As the inlet water temperature increases, the thermal efficiency of the solar collector decreases. In order to achieve maximum thermal efficiency from the solar collector, the water inlet temperature should be low. Result of the study by Teyeb *et al.* (2008) revealed high thermal efficiency of FPC at low water temperature. Parametric study by He *et al.*, 2016 indicated a decrease in thermal efficiency from 72.5% to 51.1% as the inlet water temperature increased from 20 ºC to 45 ºC. The effect of inlet water temperature on exergy and energy efficiencies carried out by Farahat *et al.* (2009) revealed maximum exergy and energy efficiencies at lower inlet water temperature.

2.4.8 Effect of ambient temperature

Among the various climatic factors, it has been found that ambient temperature also has an effect on the thermal efficiency of the solar collector. Heat loss by conduction, convection and radiation decreases with increase in the ambient temperature (Kalogirou 2013). Result of the parametric study by He *et al*. (2016) indicates that the thermal efficiency of an FPC increased from 48% to 74% when the ambient temperature was increased from 5 ºC to 40 ºC. The effect of ambient temperature on exergy and energy efficiencies carried out by Farahat *et al.* (2009) revealed maximum exergy and energy efficiencies at higher ambient temperature.

2.4.9 Effect of solar insolation

The heat gain and heat transfer rate of the solar collector depends on the amount of solar radiation falling on the surface of the solar collector. He *et al.* (2016) investigated the effect of solar radiation on thermal efficiency of an FPC. As the solar radiation increased from 200 – 1000 W/m^2, the outlet water temperature increased from 32.2 ºC to 42.1ºC resulting in an increase in the thermal efficiency from 38.1% to 64.8%. The influence of solar insolation on energy and exergy efficiencies conducted by Farahat *et al.* (2009) revealed maximum exergy and energy efficiencies at higher ambient temperature.

2.4.10 Effect of wind speed

The convective heat loss from the surface of the solar collector is influenced by wind speed. With increase in wind speed over the surface of the collector results in an increase in heat loss thereby decrease in the thermal efficiency of the FPC Farahat *et al.* (2009). Study by Madhusudan *et al.* (1981) indicates that with increase in wind speed, the convective heat loss over the collector surface of an FPC could reach even up to 22-30 %.

Teyeb *et al.* (2008) and Farahat *et al.* (2009) reported the convective heat loss between ambient media and front side of the collector. The result showed a decrease in thermal efficiency by 6%. Experimental investigation by Bhatt *et al.* (2013) reveals an increase in thermal efficiency at lower wind speed and radiative heat loss.

2.4.11 Effect of insulation

In most commercial FPCs, since the heat losses (33-50%) happen due to convection (22-30%) and radiation (5-7%) from the front surface of the absorber, and also radiation losses (5-10%) from the back surface, insulation of the solar collector is mandatory ensure reduction in heat losses (Madhusudan *et al.* 1981).

Matuska *et al.* (2009) predicted the thermal efficiency of a solar collector for various insulation thicknesses. The result indicates drastic increase in thermal efficiency when the insulation thickness increased from 20 to 50 mm. Beyond 50 mm, the thermal efficiency almost remained constant. Similar study by Jafarkazemi*et al.* (2013) revealed that the increase in insulation thickness beyond 50 mm do not have any significantly influence on the thermal efficiency or exergy efficiency of an FPC.

2.5 Reviews on Exergy Analysis of Flat Plate Collectors

Most of the theoretical and experimental studies (Zhao *et al*. 2010, He *et al.* 2016, Taherian *et al.* 2011, Tanha *et al*. 2015, Khalifa 1999, Kalogirouand Christos 2000, Shariah and Bassam 1997, Kalogirou 2009 and Dagdougui *et al.* 2011)have been carried out based on the first law of thermodynamics. However, the first law alone does not include all the internal losses from the solar collector (Farahat *et al.* 2009). Analysis by second law of thermodynamics is useful to quantify the efficiency of the system and in identifying the optimal operating conditions (Luminosu and Fara 2005). Hence, second law analysis is an effective means to obtain precise and valuable information about energy efficiency and losses due to irreversibility in actual situation. The present trend in the design of actual processes is the minimization of entropy generation apart from economical and technological feasibility (Bejan 1996)]. It is therefore essential to consider both exergy and energy analysis for estimating the thermal performance and optimizing the working parameters like mass flow rate and collector area (Suzuki*et al.* 1987 and Tyagi *et al.* 2007).

The thermodynamic analysis based on output exergy, entropy generation and exergy efficiency for a solar collector is reviewed in depth byLiu *et al.* (1995). They also

developed a general correlation for exergy generation and destruction for FPC.Kurtbas and Durmus (2004) conducted study on exergy analysis for solar air heater and obtained higher exergy efficiency at higher flow rate and decrease in exergy with increase in heat transfer area.

Bejan (1996), Bejan (1988) and Bejan (1982) have developed a solar collector system by employing the entropy generation minimization technique at optimum mass flow rate, geometry and collector temperature. Dutta *et al*. (1990) carried out exergy and energy analysis at constant overall heat loss coefficient and found optimal range of inlet fluid temperature which maximizes the exergy and energy efficiencies. Altfeld *et al*. (1988) carried out investigation on solar air heater at constant overall loss coefficient and found optimal fluid inlet temperature, flow rate, duct geometry and exergy efficiency. Luminosu and Fara (2005) studied the effects of fluid flow rate, fluid inlet temperature and collector area on the exergy and overall heat loss coefficient.

Suzuki (1988) compared the performance of an FPC and evacuated tube collector based on exergy analysis. Wing Han *et al*. (1991) used exergy analysis techniques to compare four different collectors by keeping the overall heat loss coefficient constant. Torres*et al*. (2004) employed dimensionless correlation for various exergy components and obtained optimal inlet fluid velocity, fluid inlet temperature, duct length and exergy efficiency for a solar air heater. Experimental study on a closed loop solar water heater by Gunerham and Hepbasli (2007) revealed a maximum exergy efficiency of 4% and identified the location where maximum exergy loss occurred. Gupta and Kaushik (2008) investigated the influence of length to width ratio of the absorber plate on the exergy of a solar air heater.

Benli (2013) conducted experimental study on five different types of solar air heater and compared their exergy and energy efficiencies. The result revealed that changing the shape of the absorber plate leads to an increase in the pressure drop and overall heat loss coefficient. Alta *et al*. (2010) carried out comparison study between three flat plate solar air heaters with different tilt angles, mass flow rates and fluid inlet temperatures based on energy and exergy efficiencies. Akpinar *et al*.

(2010) studied the effects of solar radiation, flow rate, fluid inlet temperature and fins on exergy and energy efficiencies of the solar air heater experimentally. Farahat *et al.* (2009) conducted investigation on the optimization of FPC based on exergy analysis and found maximum efficiency and optimal design parameters at fixed fluid inlet and ambient temperature.

Hazemi *et al.* (2010) carried out experimental studies on the exergy and energy efficiencies of a thin layer concrete absorber plate collector. Xiaowu and Ben (2005) analyzed the design parameters and exergy efficiency for a domestic solar water heater. The results showed that the exergy efficiency of the system could increase with careful selection of plate width and number of cover. Ucar and Inalli (2006) investigated the economic analysis and optimization of solar assisted heating system based on exergy analysis.

2.6 Numerical Study of Flat Plate Collectors

Hottel and Woertz (1942) analyzed the heat transfer in a flat plate solar collector by means of lumped system analysis. Duffie and Beckman (1991) used lumped analysis by incorporating the resistance between the tube and the fluid and obtained expressions for fluid temperature as well as the plate temperature. Lecoeuche and Lalot (2005) applied neural network technique to predict the thermal performance of a solar FPC. Amer *et al.* (1998), using a transient testing technique, studied the effects of tilt angle and inlet water temperature on the performance of a solar collector. Shariah and Shalab (1997) attempted to optimize the design parameters for maximizing the solar water heater efficiency using transient simulation program (TRNSYS). Gorla (1997) predicted the performance of solar collectors based on a two-dimensional finite element method.

Akhtar and Mullick (2007) carried out numerical investigation on the thermal performance of double and single-glazed solar collectors. The developed numerical equation was used for calculating the glass temperature at inner and outer surface for different solar insolation values. A numerical study for investigating the performance of a single glazed FPC was reported by Selmi *et al.* (2008). Numerical

analysis on a wavy absorber plate collector carried out by Varol and Oztop (2007) indicated higher heat transfer rate at higher Rayleigh number and aspect ratio. Budihardjo *et al*. (2009) carried out both numerical and experimental study for developing correlation in terms of solar radiation, inclination angle, aspect ratio and tank temperature for evacuated tubes collector.

Kumar and Saini (2009) developed solar air heater and validated the experimental results with computational fluid dynamics (CFD) values under turbulent and laminar flow conditions. Gertzos *et al.* (2008) and Gadi (2000) used CFD to predict the system performance of an FPC with minimal error. Sultana *et al.* (2012) used CFD software to study the thermal performance of a solar collector by predicting heat loss, radiation, and convection heat transfer inside the collector and maximized the overall thermal efficiency. The study revealed good agreement between the CFD results and experimental data.

Zhu *et al*. (2010) experimentally estimated the heat on the surface of an absorber plate and validated the result with the CFD values. Al-Ansary and Zeitoun (2011) investigated a parabolic trough collector using CFD simulation. Numerical modeling was used for calculation of conduction and convection heat losses from the surface of the collector. Effect of insulation on the heat loss was also studied and reported. The numerical results showed that the insulation can significantly reduce the overall heat loss. Martinopoulos *et al*. (2010) investigated a polymer solar collector using CFD analysis. In the above study, the effect of operating parameters such as flow rate, temperature, solar insolation, etc. on the thermal efficiency were determined. Good agreement between the experimental and simulation results was achieved. Facão (2015) conducted both the experimental and CFD study to optimize the flow rates in riser and header arrangement for an FPC and found uniform flow and homogenous temperature distribution at low flow rate.

2.7 Thermal Energy Storage System

Up to now, the world energy demands are achieved mainly using fossil fuels. Due to the number of problems while using fossil fuels, *viz*., varying prices, emission of

harmful gases and depleting resources, researchers have focused their attention in developing technologies to take advantages of renewable energy sources. Due to the unpredictable and fluctuating nature of renewable energy sources, thermal energy storage system provides a sustainable option (Niyas *et al*. 2017). Ding and Riffat (2013) and Sarbu and Sebarchievici **(**2018) have identified four different types of thermal energy mechanisms such as sensible heat, latent heat, chemical reaction and thermo-chemical (sorption) energy storages. Among these, sensible heat storage (SHS) and latent heat storage (LHS) systems are the most common in thermal energy storage devices. The detail review of the LHS is presented in subsection 2.7.1.

2.7.1 Latent heat energy storage system

Latent heat energy storage system (LHESS) is used to store the existing thermal energy for later usage and increases its utilization. Further, it provides a favourable solution for smoothing the inconsistency between energy demand and supply. LHESS uses phase change materials (PCMs) as energy storage mediums. Energy is stored during melting and released during solidification. Several researches have used LHESSs for various applications such as solar domestic hot water systems (Mazman *et al.* 2009), space heating and cooling (Halawa and Saman 2011, Fang *et al.* 2010), integrating PCMs into building element (Soares*et al.* 2013, Baetens *et al.* 2010,Liu and Awbi 2009) and application in automobile designed to reduce emission at start-up (Gumus 2009).

PCM used in the LHS has an interesting characteristic of storing capacity of up to 14 times more energy than SHS over relatively a small temperature interval (Sharma, *et al.* 2009).The stored energy in the storage tank is directly proportional to the latent heat of fusion of the PCM (MehlingandCabeza 2002).This makes LHS technology feasible for storing thermal energy during solar thermal process especially when the time of energy capturing and utilization does not match. The main advantage of a PCM system is the higher energy storage density and almost constant temperature (isothermal) process (Agyenim *et al.* 2010). The main drawback of LHS system is the low thermal conductivity of PCMs which impede the use in different

applications (Mills *et al.* 2006). Presently researchers design LHS which promotes natural convection to speed up the overall melting process by increasing the heat transfer rate in the liquid PCM (Liu and Awbi 2009). Hence, there is a need for experimental and numerical investigation that accounts for natural convection to tackle the above mentioned issues.

Niyas*et al.* (2017) investigated a lab scale LHS, experimentally and numerically, using a mixture of potassium nitrate, sodium nitrate and sodium nitrite as PCM and found good agreement with experimental results. Kibria *et al.* (2014) performed both numerical and experimental investigation in shell and tube LHS using paraffin wax as PCM. The result revealed that the mass flow rate had small effect on the performance of LHS compared to the inlet temperature of the HTF. Lacroix (1993) performed theoretical study on 2D shell and tube LHS system. It was suggested that for a typical PCM, selecting proper parameters would increase the performance of the storage system. Ng *et al.* (1988) developed a 2D theoretical model to investigate the melting behaviour of PCM in a horizontal cylinder and found higher melting rate at higher natural convection.

Tiari *et al.* (2016) developed 2D transient numerical model of finned heat pipe LHS to predict the discharging rate. The result indicate higher discharging rate with increased number of HTF tubes. The effect of cylinder orientations (vertical and horizontal orientation) of shell and tube LHS on the thermal performance was carried out by Seddegh *et al.* (2016). The result revealed better performance with horizontal oriented storage compared to the vertical orientation. The effect of storage material properties on the thermal behaviour of LHS was studied numerically by Aly and El-Sharkawy (1990). The result indicates higher rate of storing capacity with storage medium having higher density or specific heat. Wang *et al*. (2013) carried out numerical study on the effect of inlet temperature and mass flow rate of HTF on the thermal performance of shell and tube LHS. The result revealed that the inlet temperature of HTF had more impact on melting rate and thermal energy storing capacity than mass flow rate.

Khodadadi and Zhang (2001) numerically studied the melting process of PCM in spherical container. They observed faster melting of the PCM at the top portion compared to bottom portion of the sphere. In addition, the effect of convection on melting rate was also investigated. Seddegh *et al.*(2015) developed two numerical models of shell-and-tube LHS to investigate the performance using combined conduction-convection model and conduction model. The result indicates that the combined conduction-convection model result was close to the experimental value than the pure conduction model. Moreover, they concluded charging as a natural convection dominant process whereas discharging is a conduction dominant process.

Li and Kong (2014) carried out numerical investigation for evaluating the performance of a shell and tube LHS system using paraffin as PCM. Water and air was used as HTF. The effect of inlet velocity of HTF on the outlet temperature, melt fraction and Nu was determined by parametric study. The result revealed that the inlet water velocity had low impact on the outlet water temperature whereas the inlet air velocity had more impact on the outlet air temperature and heat transfer rate. Comparison of the thermal performance between smooth and finned heat pipe based LHS by Khalifa *et al.* (2014) revealed better performance in finned heat pipe LHS system. The effect of fins on the performance of LHS system was investigated by Darzi *et al.* (2016). They reported that increasing the number of fins on the HTF tube increases melting rate and solidification rate of PCM. Ren and Chan (2016) investigated the effects of longitudinal fins on melting rate of PCM and observed better performance and faster melting rate with increase in the number of fins.

Investigation by Rathod and Banerjee (2015) indicated that both melting and solidification rates increased by 24.5 % and 43.6 %, respectively, by providing fins for the LHS system. Effect of number of fins on heat transfer and melting rate in rectangular container was investigated experimentally by Kamkari and Shokouhmand (2014). By providing single and triple fins to the rectangular container, the melting rate and heat transfer rate increased by 18 % and 37 %, respectively. Investigation by Vyshak and Jilani (2007) reveals faster melting rate using shell and tube compared to a rectangular LHS for the same heat transfer area

and volume. The impact of number of longitudinal fins and length on thermal storage performance was investigated numerically by Kalbasi and Salimpour (2015) indicates higher natural convection in system with more number of longitudinal fins with shorter length compared to few fins with longer length.

The flow direction of HTF during charging and discharging had an impact on the performance of LHS. Numerical study on the effect of flow direction on LHS performance by Gong and Mujumdar (1997) revealed better performance by charging and discharging of cold and hot fluids from the same end compared to that from the opposite end of the storage unit. Esapour *et al.* (2016) studied the effect of number of HTF tube on the melting time and storage performance of LHS. They observed that increasing the number of tubes from 1 – 4 reduced the melting time by 29% thereby improved the storage performance.

Experimental investigation of the thermal behaviour of paraffin wax having melting temperature of 60 ºC by Rathod and Banerjee (2014) indicates higher effect of inlet temperature on the melt fraction of the PCM compared to the mass flow rate. Study by Jesumathy *et al.* (2012) and Jesumathy *et al.* (2014) revealed inlet temperature had greater impact on the melting rate compared to the mass flow rate. Investigation of He and Setterwall (2002) reveals RT-5 paraffin as a viable PCM material for cold storage application due to its stability and higher melting rate.

Trp (2005) studied the thermal behaviour of RT-30 paraffin for use in shell-and tube heat exchanger at constant mass flow rate of water (HTF) and observed non-isothermal phase change within the melting zone. Avci and Yazici (2013) discussed the melting and solidification behaviour of paraffin in a horizontal tube-in-shell LHS. Akgun *et al.* (2007) carried out experimental study on the melting and solidification behaviours of PCM in a vertical shell and tube heat exchanger. The result revealed a significant decrease in melting time by increasing the HTF temperature. Further, they reported that low HTF mass flow rate leads to lower energy consumption. Experimental investigation by Medrano *et al.* (2009) on the heat transfer characteristics of five small heat exchangers during charging and

discharging processes revealed higher heat storage capacity for double pipe heat exchanger.

2.8 Melting Enhancement of Phase Change Material

Some methods have been used to enhance the heat transfer properties of PCMs by (i) dispersion of high thermal conductivity powder particles in the PCM (Zeng*et al*. 2006, Ai*et al*. 2010 and Wu *et al*. 2010), (ii) placing metal structure in PCM (Khodadadi and Hosseinizadeh 2007), and (iii) impregnations of porous materials (Zhong *et al*. 2010 and Sari 2004). Improvements of thermal conductivity of paraffin with nanoparticles have been attempted by many researchers (Ramezanzadeh *et al*. 2011). Addition of high thermal conductivity particles, *viz*, ceramic particle (Wu *et al*. 2009), nanomagnetic particle (Sahan *et al*. 2015), and carbon material (Zeng *et al*. 2009) improved the conductivity of paraffin. Though carbon nanotube is a good choice for enhancing the thermal conductivity of paraffin (Babu and Kumar 2011), difficulty to disperse and high cost restrict it use for further application. Velraj *et al.* (1999) reviewed the heat-transfer enhancement methods for LHS and carried out three different experiments to support these techniques.

Li (2013) studied the effect of nanographite on phase change temperature, latent heat of fusion and thermal conductivity. The study revealed considerable decrease in melting temperature and 7.41% improvement in thermal conductivity. Zeng *et al.* (2012) reported that the addition of Cu nanowires in PCM resulted in decrease in phase change enthalpy and thermal stability. Simultaneously the thermal conductivity and melting speed of the PCM increased. Teng and Yu (2012) experimentally studied the thermal performance of LHS filled with paraffin containing Al2O3, TiO_2, $SiO_2$and ZnO nanoparticles. The study revealed that among the additives, TiO_2 incorporated paraffin exhibited higher thermal conductivity. Wang *et al.* (2009) used multi-walled carbon nanotube paraffin wax with mass fraction of 2.0 % and found 35–40% improved thermal conductivity.

Mills *et al.* (2006) compared the thermal conductivity of pure paraffin and paraffin/graphite composites. The result indicated that paraffin/graphite composite

exhibited 83 times higher thermal conductivity. Xia *et al.* (2010) compared the thermal conductivity of paraffin /10% graphite composite and pure paraffin. The result revealed 12 times higher thermal conductivity for the paraffin/graphite composite compared to pure paraffin. Wang *et al.* (2014) studied the thermal property enhancement of paraffin wax by addition of TiO_2 nanoparticles. Ho and Gao (2009) carried out experimental investigation on the thermal properties of paraffin wax by dispersing 5 wt. % of non-ionic surfactant and 10 wt. %, of alumina (Al_2O_3) nanoparticles. The result indicated improvements of dynamic viscosity of 20% and 28% for 5 wt. % non-ionic surfactant and 10 wt. % of alumina nanoparticles, respectively.

Valan *et al.* (2013) carried out investigation on the addition of 10 wt. % Al_2O_3 and 4 wt. % CuO nanoparticles on the rate of melting and solidification of paraffin wax and found higher thermal performance for Al_2O_3 compared to CuO nanoparticles. Cai *et al*. (2011) and Wang *et al*. (2009) reported the 0.2 vol. % to 4 vol. % as the optimum range of Cu nanoparticle addition for enhancing the thermal property of paraffin wax. They opined to use lowest percentage due to the high cost of Cu nanomaterials. Though higher percentage of nanoparticle enhances thermal conductivity of the PCM, care has to be taken since it (i) increases the dynamic viscosity, (ii) reduces the available latent heat of PCM and (iii) may reduce the stability of nanoPCM due to agglomeration and sedimentation. Hence, selecting a proper nanoparticle material and identifying optimum percentage is essential to improve heat transfer performance of the PCM during melting and solidification processes.

2.9 Thermal Management for Anaerobic Digestion

Conversion of woody biomass, animal waste such as cattle dung, chicken litters, pig manure, municipal solid and agricultural wastes, etc.to biogas (methane gas) under oxygen free environment and favorable temperature range is called anaerobic digestion. The process involves four stages, namely, hydrolysis, acidogenesis, acetogenesis and methanogenesis. There are various factors which affect the

production of biogas production such as temperature, hydraulic retention time, total solid percentage, loading rate, types of feed material, pH of the solution, carbon to nitrogen ratio, effects of toxicity, effects of mechanical stirring and agitation, effects of additive, etc. However, effect of temperature on methane forming bacteria is reported to be significant for biogas production (Luostarinen 2005, Madigan *et al*. 1997, Prasad and Sathyanarayan 1979 and Tiwari 1988).

Though higher temperature accelerates the chemical and enzymatic reactions this is applicable only for certain optimum temperature limits. Exceeding the temperature above the limit may damage the protein and cellular components of the microbes and lowering of the temperature below the lower limit result in very slow microbial growth rate and chemical / enzymatic reactions. In both cases, biogas production rate will be ineffective. To achieve stable chemical reactions and higher biogas yield, maintaining the temperature within range is very important (Luostarinen 2005 and Madigan *et al.* 1997).

The digestion of organic wastes inside anaerobic digester occurs over a wide range of microbes temperature. Psychrophilic microbes grow at a temperature in the range from 0 – 20 °C (Coelho *et al.* 2011, Kashyap *et al.* 2003 and Madigan *et al.* 1997). Usually these biogas plants operate at lower temperatures and are used for treating waste water with high amount of soluble compounds. Psychrophilic digestion is considered to be a difficult process due to slower degradation rate and longer hydraulic retention time (Lettinga et al. 2001). The optimum temperature needed for mesophilic and thermophilic microbes is in the range from 30 °C to 40 °C, and 50 °C to 60 °C, respectively. Mesophilic and thermophilic process are common for digesting variety of heterogeneous raw material such as manure and various biodegradable wastes (Chen *et al*. 2008 and Madigan *et al*. 1997).

Duran and Speece (1997), Van Lier (1995),Lo *et al.* (1985) and Buhr and Andrews (1977) have reported the benefits and drawbacks of thermophilic digestion over mesophilic digestion. The benefits are: (i) higher reaction rates for destruction of organic matter; (ii) higher efficiency while destroying huge quantity of organic matter and (iii) complete destruction of viral and pathogens. The drawbacks are: (i)

higher heat input consumption to maintain digester temperature and to pre-heat slurry, (ii) poor process stability and (iii) bad quality of effluent due to dissolved solids. Vindis *et al.* (2009) investigated the impact of mesophilic and thermophilic digestion on biogas production for different maize types. Better quality and higher biogas yield was achieved for thermophilic digestion compared to mesophilic digestion.

Garba (1996) and Sambo *et al*. (1995) carried out experimental investigation on the effect of temperature on biogas production for lignocellulosic biomass. They observed higher biogas yield at thermophilic conditions compared to mesophilic conditions. Mackie and Bryant (1995) reported that the anaerobic digestion under thermophilic condition of cattle waste was more stable than mesophilic at different hydraulic retention time of 10, 15 and 20 days. Varel *et al.* (1977) carried out experimental investigation on thermophilic methane production from cattle dung and revealed that higher biogas yield at a temperature of 60 °C. They also observed rapid digestion with shorter retention time at higher loading rate.

Kroeker *et al.* (1979) reported that temperature fluctuation up to 8 ºC in anaerobic digestion of swine manure did not affect the stability of the process under mesophilic digestion. The hydraulic retention time in this case ranged from 6 to 30 days. Chen *et al.* (1980) carried out study on the kinetics of digestion of livestock manure at thermophilic and mesophilic temperature ranges. They observed accelerated digestion under thermophilic temperature range. Heukelekian (1930) and Fisher and Greene (1945) reported an increased in the digestion rate by increasing the temperature to the thermophilic range. Further, most of the sludge could be treated under thermophilic conditions rather than under mesophilic conditions.

Wiegant *et al.* (1986) and Hill *et al.* (1985) obtained higher biogas yield and higher methanogenic activities under thermophilic condition. Bonmati *et al.* (2001) carried out experimental studies on the effect of temperature on biogas production for digestion of pig slurry and found higher biogas yield for thermophilic followed by mesophilic digestion. Zinder *et al*. (1984) optimized the temperature required for growing methanogens under mesophilic and thermophilic digestion conditions. The

result revealed that the growth rate and biogas production rate were higher in thermophilic compared to mesophilic condition. Van Lier *et al*. (1995) investigated the effect of temperature on growth rate of methanogenic bacteria for phychrophic, mesophilic and thermophilic conditions and revealed higher growth rate for thermophilic followed by mesophilic and phychrophilic conditions, respectively. Figure 2.1 presents the growth rate of bacteria versus temperature.

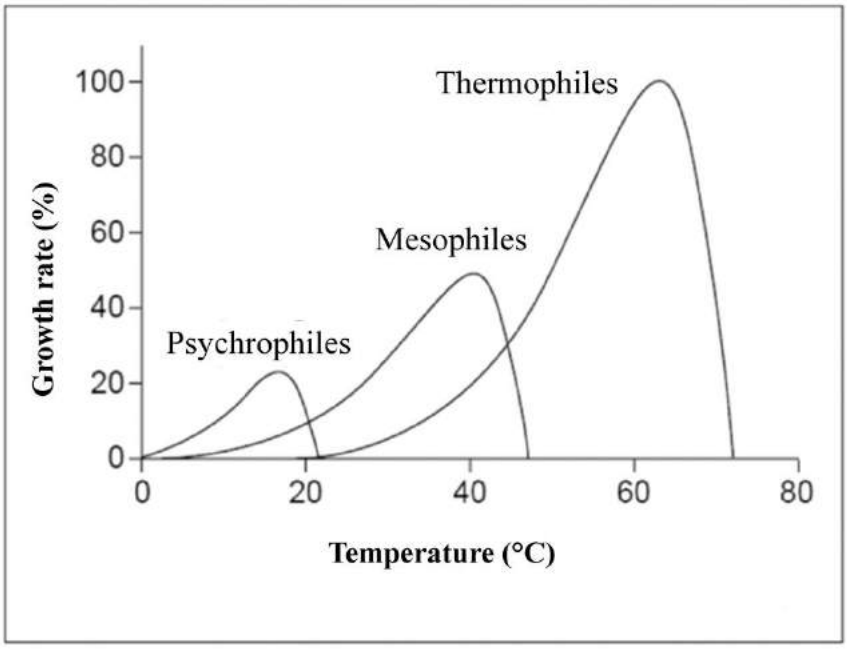

Fig.2.1 Growth rate of psychrophilic, mesophilic and thermophilic methanogens (Van Lier *et al*. 1995)

2.10 Temperature Controlling Methods inside Biogas Digester

Achieving optimum temperature for mesophilic digestion is very difficult especially during winter seasons. Usmani *et al.* (1996) and Meynell (1976) reported that the rate of biogas production through anaerobic digestion is become negligible at a slurry temperature below 15 ºC. These situations are regular during winter season where the ambient temperature and slurry temperature drop below 13 ºC (Mahanta *et al.* 2005 and Meynell 1976). At lower temperature, the biogas production decreases drastically and may stop. Therefore, in order to reduce the heat loss from the biogas plant, insulating the plant is very important.

Comparison study between conventional biogas plants without glazing, with glazing and glazing with movable insulation were carried by Tiwari *et al.* (1988). The result revealed that during winter seasons (i) a constant slurry temperature of 29 ºC could be maintained for the conventional biogas plant with glazing and movable insulation, (ii) a constant slurry temperature of 26 ºC could be achieved in the conventional plant with glazing and (iii) a slurry temperature of 21 ºC could be maintained in the conventional biogas plant without glazing and insulation. Figure 2.2 illustrates the variation of slurry temperature with time (Tiwari *et al.* (1988).

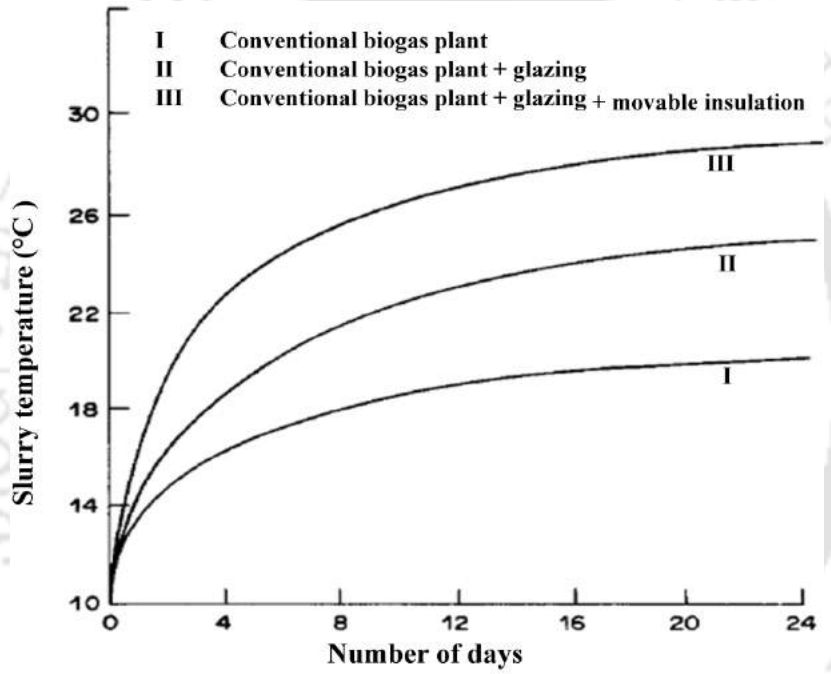

Fig.2.2 Variation of slurry temperature with number of days (Tiwari *et al.* 1988)

Heating of feed material is another method to maintain the required slurry temperature in the biogas digester. It can be implemented using solar energy directly (Gupta *et al.* 1988) or through heat exchanger (Beba 1988). However, sufficient care should be taken to ensure a controlled heating to avoid destruction of the methane forming bacteria (Subramanyam 1989). Gupta *et al.* (1988) carried out transient analytical investigation on a fixed dome type biogas plant integrated with solar collector. The result showed that increasing number of solar collector and length of

the heat exchanger which was immersed in the digester increased the slurry temperature. Figure 2.3 depicts the reported result of (Gupta *et al.* 1988).

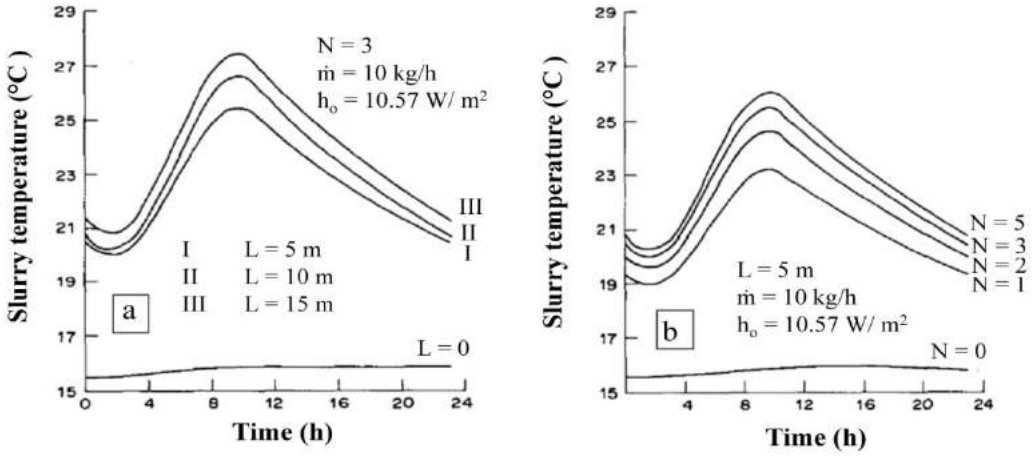

Fig.2.3 Hourly variation of slurry temperature by changing (a) length of pipe, (b) number of panels

Prasad and Sathyanarayan (1979) developed an analytical solar thermal model for a conventional biogas plant for estimating the heat transfer from the surrounding to the gas holder and slurry. The result revealed the necessity of maintaining higher slurry temperature for biogas production. The amount of heat required to compensate the net heat losses from the biogas plant was estimated analytically. Reddy *et al.* (1979) were the first to modify KVIC design by integrating with a solar water heater above the gasholder (dome) to prevent heat losses from the gasholder. They obtained higher biogas production even under worst condition for the modified plant compared to conventional biogas plant.

Singh *et al.* (1985) integrated biogas plant with solar pond. Bansal *et al.* (1985) integrated biogas plant with greenhouse effect to heat the slurry with trapped solar energy. Tiwari and Chandra (1986) integrated biogas plant with solar water heater during off sunshine hours to improve the performance especially during winter season. Tiwari *et al.* (1988) developed effective transient analysis for biogas plant integrated with movable insulation during off sunshine hours for better gas yield. Yadav *et al.* (1986) conducted analytical investigation on KVIC biogas plant model

which was integrated with greenhouse, solar water heater, movable insulation and solar canopy.

Figure 2.4 depicts the variation of time dependent slurry temperature for a (i) conventional biogas plant (ii) water heater, (iii) water heater with solar canopy and (iv) water heater with solar canopy and movable insulation. The figure indicated higher slurry temperature for movable insulation and lowest slurry temperature for conventional biogas plant.

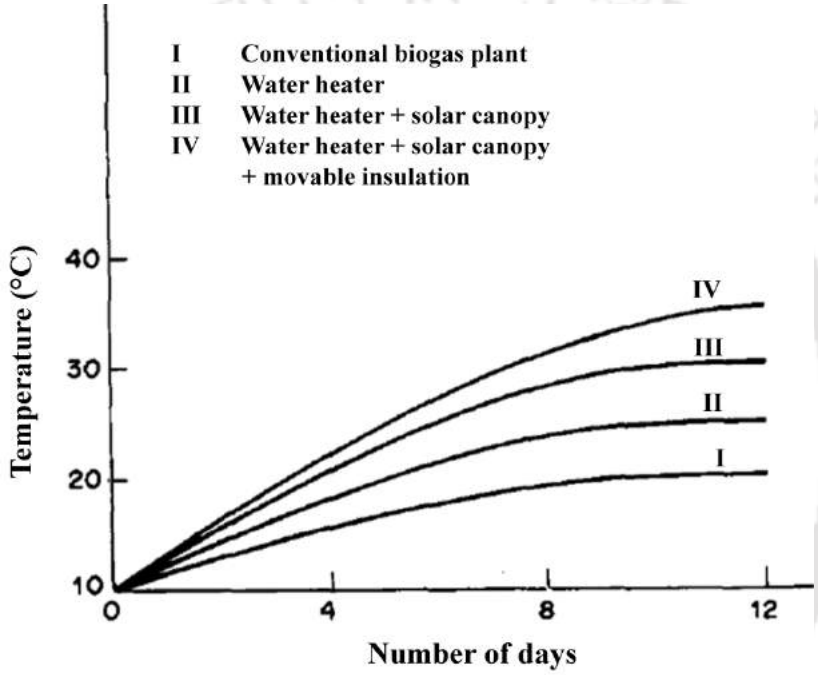

Fig.2.4 Transient variation of slurry temperature versus number of days (Yadav *et al.* 1986)

2.11 Summary

Literature reveals that harnessing of solar thermal energy has been proved to be useful, reliable, environmental friendly and cost-effective. Hence, several countries that were heavily dependent on the imported oil focused their attention to development of solar thermal devices for domestic as well as industrial applications (Potter 2008). It is evident that the designing of a solar thermal plant component depends on the various working parameters. The numerical techniques may give viable and suitable options and can save a number of experimental trials. It is observed from the literature review that there is a scope for improvement of solar

flat plate collector in terms of efficiency considering diurnal and seasonal variation of solar irradiation. Further, application of the same towards heating of feedstock of biogas digester is a challenging task.

Considering these facts, the present work aims at development of an improved solar flat plate collector integrated with thermal energy storage for biogas production and analyze the thermal performance. The thermal system heats the fluid kept inside the shell through heating coil, which heats up the biogas digester. The experimental investigation is carried out in two ways, namely controlled and uncontrolled conditions. The uncontrolled conditions help to develop relationship between the shell and biogas digester in terms of temperature. Using the developed relationships, automatic controlling mechanismis developed to maintain the temperature inside biogas digester. The next chapter reports the theoretical and numerical formulation of the FPC and TESSs.

Chapter - 3

Flat Plate Collector and Thermal Energy Storage Systems: Theoretical and Numerical Formulation

3.1 Introduction

This chapter presents the theoretical and numerical formulation of FPC along with latent heat storage system. The design step for FPC with straight and bent tubes as well as the LHS system is presented in detail. Theoretical formulations for exergy and energy efficiencies of the collector and performance parameters of the storage are discussed and reported. The governing equations used for simulation of FPC and LHS systems are also assessed. Finally, modelling and meshing procedure for the solar collector and the thermal energy storage are discussed.

3.2 Theoretical Analysis of Flat Plate Collector

3.2.1 Designing of flat plate collector

There are three important area terms used for designing of FPC. These are:

(i) Gross area (A):– the outer dimensions of the collector including frame and glazing material.

(ii) Absorber area (A_a):– the dimensions of the absorber plate. For unglazed FPC (A=A_a= A_p).

(iii) Aperture area (A_p):– the area over which the solar radiation enters the collector. The aperture area is the most relevant area from the energy conversion point of view.

The gross area (A) and width (B) for the glazed FPC are obtained based on the correlation given in the **Appendix–A**. Table 3.1 presents the materials and properties considered for designing the FPCs.

Table - 3.1 Materials and properties used for the designing of flat plate collector

Part name	Material
Absorber plate	Copper
Casing	Wood and aluminum sheet
Flow cross section	Circular
Insulation	Glass wool
Fins	Copper
Riser tube and header tube	Copper
Thermal conductivity of the plate	385 W/m.K
Density of the plate material	8960 kg/m^3
Specific heat of water	4200 J/ kg.K
Absorptivity of the absorber plate	0.95
Glass cover emissivity	0.85
Bond conductance	30 W/m.K
Insulation thermal conductivity	0.044 W/m.K
Location of the collector	Guwahati, 26. 7^0 N, 91.7° E

The riser and header tube arrangement consist of 10 straight and bent tubes which were arranged in parallel. The diameters of the riser and header tubes were 12.5 mm and 25 mm, respectively. The risers were connected to the headers by drilling and brazing. The top of the collector was covered by 4.0 mm thick acrylic glass having good optical properties and attached to side of the collector with aluminum frame. In order to decrease the overall heat loss coefficient, an optimum air gap of 30 mm was maintained between the glass and the absorber plate. To achieve better heat transfer rate, a 0.7 mm thin copper absorber plate was attached over the riser tubes by soldering. The surface of the absorber plate was cleaned to remove dust and painted with black ink to increase the absorptivity. The side and back of the collector was insulated by 50 mm thick glass wool to reduce heat losses from the collector. Figures 3.1 (a) and (b) show the diagrams for straight and bent tube collectors. The design detail of this are presented in **Appendix–A**. The detailed specifications of the two solar collectors are presented in Table 3.2.

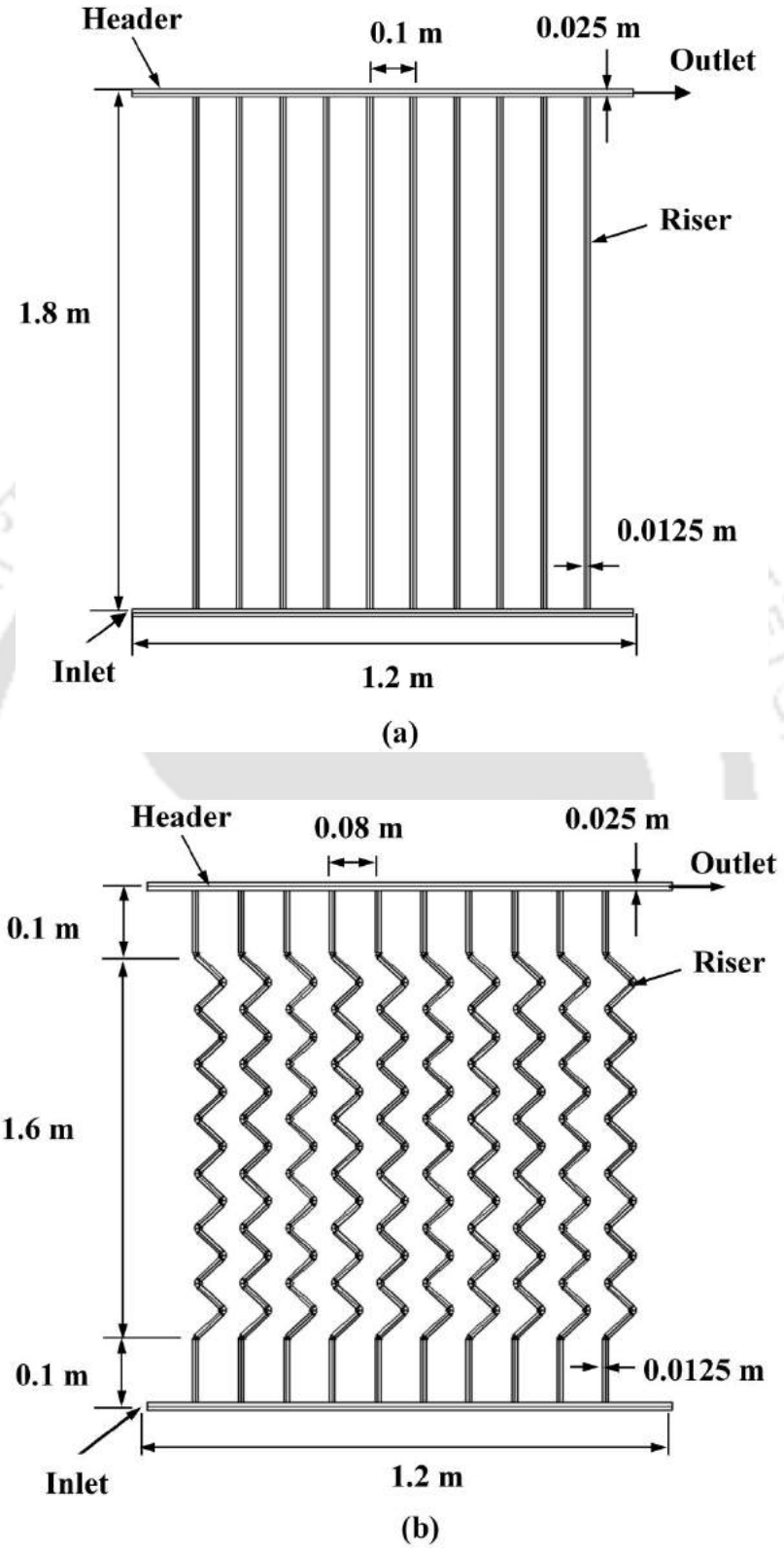

Fig.3.1 Schematic of (a) straight tube and (b) bent tube collector

Table - 3.2 Detail specifications of the FPC

Specification	Value
Gross area	1.8 m^2
Aperture area	1.6 m^2
Aperture width	1000 mm
Length of the absorber plate	1650 mm
Width of the absorber plate	1200 mm
Plate thickness	0.7 mm
Air gap between the plate and glass	30 mm
Tube centre to centre distance for straight tube	100 mm
Tube centre to centre distance for bent tube	80 mm
Number of tubes	10
Thickness of the glass	4.0 mm
Diameter of the riser tube	12.5 mm
Diameter of the header tube	25 mm
Thickness of the insulation material	2.5 mm
Thickness of the riser tube	1.5 mm
Thickness of the header tube	1.5 mm
Bottom insulation thickness	50 mm

3.2.2 Analysis of optical property of glass

The optical efficiency (η_o) of the collector was determined from the value of the transmissivity of the glass (τ) and effective absorptivity of the absorber plate (α_{eff}) using the expression

$$\eta_0 = \tau\alpha_{eff} \tag{3.1}$$

The radiation heat flux (S) on the surface of the collector was determined by the relationship (Sukhatme 2008)

$$S = \eta_0 I \tag{3.2}$$

where I is solar insolation.

3.2.3 Energy analysis

Figure 3.2 presents a schematic drawing of the heat flow through FPCs. The plot is essential to describe step-by-step heat flow equations of the FPCs.

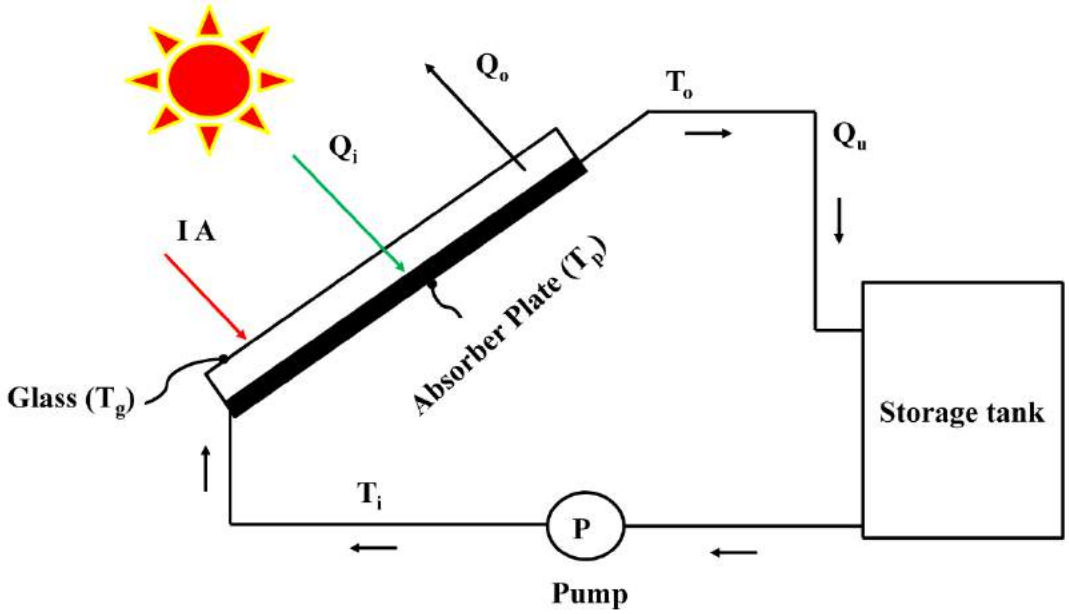

Fig.3.2Typical flat plate solar collector system

The amount of solar radiation received by the solar collector (Q_i) was determined by the relationship (Park *et al.* 2014)

$$Q_i = I(\tau\alpha_{eff}).A \tag{3.3}$$

where A is collector area.

The rate of heat loss (Q_o) in the form of overall heat loss (U), plate temperature (T_p) and ambient temperature (T_a) was determined from (Duffie and Beckman 2013)

$$Q_o = UA(T_p - T_a) \tag{3.4}$$

The heat gained (Q_u) as a function of plate temperature was determined using the expression (Duffie and Beckman 2013)

$$Q_u = A\left[S - U\left(T_p - T_a\right)\right] \tag{3.5}$$

The heat gained (Q_u) in the form of inlet temperature (T_i) was estimated using the relationship (Jafarkazemi and Ahmadifard 2013)

$$Q_u = AF_R\left[S - U\left(T_i - T_a\right)\right] \tag{3.6}$$

where F_R is the heat removal factor.

The useful energy gain with respect to inlet (T_i) and outlet (T_o) temperature of the fluid was determined using the expression

$$Q_u = \dot{m}C_p(T_o - T_i) \tag{3.7}$$

where $\dot{m}$ *and* C_p are mass flow rate and specific heat of the fluid, respectively.

The thermal efficiency (η) of the solar collector is defined as the ratio of the output useful energy to the absorbed solar energy and is expressed as (Rabha *et al.* 2017)

$$\eta = \frac{Q_u}{AI(\tau\alpha_{eff})} \tag{3.8}$$

Substituting Eq.3.7 in Eq.3.8 leads to the following expression for the thermal efficiency

$$\eta = \frac{\dot{m}C_p(T_o - T_i)}{AI(\tau\alpha_{eff})} \tag{3.9}$$

The temperature distribution on the surface of the solar collector along the direction of the fluid flow was determined by the expression (Duffie and Beckman 2013)

$$\frac{T_o - T_a - S/U}{T_i - T_a - S/U} = \exp\left(\frac{-F'UA}{\dot{m}C_p}\right) \tag{3.10}$$

where F' is the collector efficiency factor.

Using Eq. 3.9 to Eq. 3.10, the expression for the thermal efficiency attains the form

$$\eta = \frac{\dot{m}C_p\left[\left(T_i - T_a - \frac{S}{U}\right)\left(\exp\left(\frac{-F'UA}{\dot{m}C_p}\right) - 1\right)\right]}{AI} \tag{3.11}$$

The overall heat loss coefficient (U), heat removal factor (F_R) and other term used for finding the thermal efficiency is highlighted in **Appendix–B**.

3.2.4 Energy analysis for cascaded flat plate collector

The term cascaded means joining of two or more collector together. This is schematically represented in Fig.3.3. The energy analyses for the two collectors include determination of individual collector efficiency and overall efficiency.

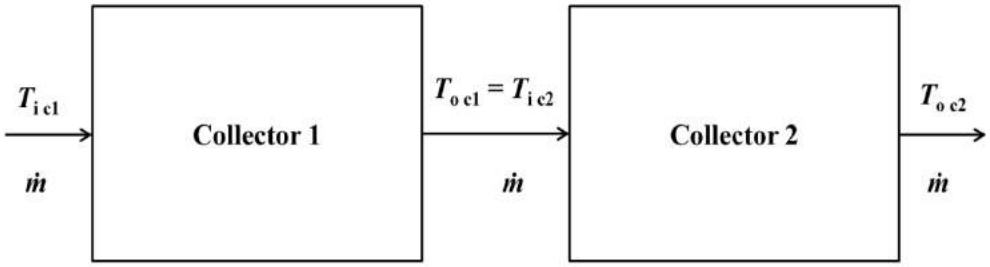

Fig.3.3Schematic diagram for heat flow in cascaded collector

The instantaneous efficiency of the cascade collector in terms of inlet temperature (T_i) and outlet temperature (T_o) of the fluid for the first collector (η_{c1}) and second collector (η_{c2}) were obtained using the expression (Rabha *et al.* 2017)

$$\eta_{c1} = \frac{\dot{m}C_p(T_{oc1} - T_{ic1})}{I(\tau\alpha_{eff})A_{c1}} \tag{3.12}$$

$$\eta_{c2} = \frac{\dot{m}C_p(T_{oc2} - T_{ic2})}{I(\tau\alpha_{eff})A_{c2}} \tag{3.13}$$

where T_{oc1} is outlet water temperature from collector-1, T_{oc2} is outlet water temperature from collector-2, T_{ic1} is inlet water temperature to collector-1, T_{ic2} is inlet water temperature to collector-2, A_{c1} is area of collector-1 and Ac_2 is area of collector-2. Since $T_{oc1} = T_{ic2}$ and $A_{c1} = A_{c2} = A$, Eq. 3.13 can be express as

$$\eta_{c2} = \frac{\dot{m}C_p(T_{oc2} - T_{oc1})}{I(\tau\alpha_{eff})A} \tag{3.14}$$

The overall efficiency (η_{ovl}) was determined by the relationship (Rbha *et al.* 2017)

$$\eta_{ovl} = \frac{\dot{m}C_p(T_{oc2} - T_{ic1})}{I(\tau\alpha_{eff})(A_{c2} + A_{c1})} \tag{3.15}$$

3.2.5 Exergy analysis

Exergy is defined as the maximum amount of work which can be produced by the system when it is in equilibrium with the surrounding (Kotas 1995). The analysis was performed based on the general form of exergy equation. The assumptions for the analysis were: (i) the flow assumed to be steady and (ii) the kinetic and potential energies effect were neglected. Figure 3.4 presents the exergy flow diagram of FPCs.

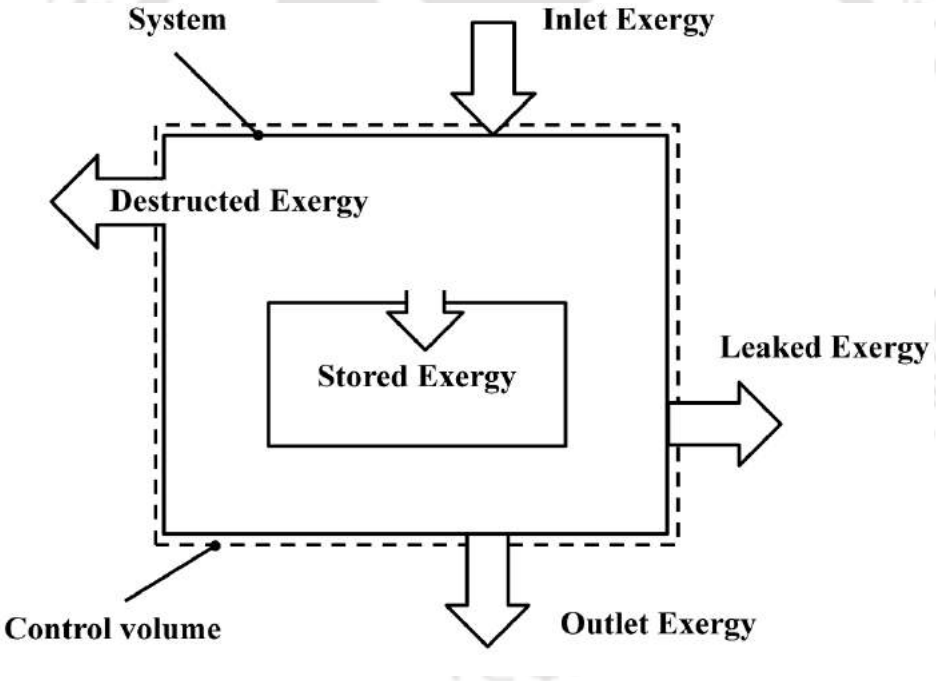

Fig.3.4 Exergy flow diagram of the flat plate collector

Under steady state condition, the exergy balance equation can be expressed as (Suzuki 1988)

$$\sum \dot{E}x_{in} - \sum \dot{E}x_{out} = \sum \dot{E}x_{dest} \tag{3.16}$$

where $\dot{E}x_{in}$, $\dot{E}x_{out}$ and $\dot{E}x_{dest}$ are total inlet exergy, total outlet exergy and destructed exergy, respectively.

The total inlet exergy ($\sum \dot{E}x_{\text{in}}$) comprises of the exergy of the inlet fluid ($\dot{E}x_{\text{in.f}}$) and the exergy of absorbed heat from the sun ($\dot{E}x_{\text{in.rad}}$). The radiated solar exergy ($\dot{E}x_{rad}$) was obtained using the expression (Jafarkazemi and Ahmadifard 2013)

$$\dot{E}x_{rad} = IA\left(1-\frac{T_a}{T_s}\right) \tag{3.17}$$

where T_s is the sun temperature of the exergy source which is 75% of the black body temperature of the sun. In the present study, T_s = 4350 K (Petela 1964).

The exergy of the inlet fluid ($\dot{E}x_{in.f}$) is expressed as

$$\dot{E}x_{in.f} = \dot{m}C_p\left(T_i - T_a - T_a \ln\left(\frac{T_i}{T_a}\right)\right) \tag{3.18}$$

The absorbed exergy by the FPC absorber plate ($\dot{E}x_{abs}$) was determined using the relationship (Jafarkazemi and Ahmadifard 2013)

$$\dot{E}x_{abs} = \eta_0 IA\left(1-\frac{T_a}{T_p}\right) \tag{3.19}$$

The exergy of the outlet fluid ($\dot{E}x_{out.f}$) is expressed by

$$\dot{E}x_{out.f} = -\dot{m}C_p\left(T_o - T_a - T_a \ln\left(\frac{T_o}{T_a}\right)\right) \tag{3.20}$$

The exergy loss was determined using Eq. 3.18 and Eq. 3.20 and is expressed as

$$\dot{E}x_{out.f} - \dot{E}x_{in.f} = -\dot{m}C_p\left(T_o - T_i - T_a \ln\left(\frac{T_o}{T_a}\right)\right) \tag{3.21}$$

The exergy transferred in the form of heat ($\dot{E}x_{heat}$) due to the difference between the temperature of the sun and ambient temperature. $\dot{E}x_{heat}$ can be expressed as (Liu *et al.* 1995)

$$\dot{E}x_{heat} = Q_{leak}\left(1-\frac{T_a}{T_s}\right) \tag{3.22}$$

The destructed exergy comprises of three terms. The first term is caused by the temperature difference between the absorber plate and the solar radiation. This was determined by subtracting Eq. (3.19) from Eq. (3.17) and can be obtained by

$$\sum \dot{E}d_{s-p} = IA\left(1-\eta_0+\eta_0\frac{T_a}{T_p}-\frac{T_a}{T_s}\right) \tag{3.23}$$

The second part of distracted exergy is due to leakage (Q_{leak}) from the absorber plate to atmosphere. Q_{leak} can be obtained using the expression

$$Q_{leak} = UA\left(T_p - T_a\right) \tag{3.24}$$

The exergy loss due to leakage from the absorber plate ($\dot{E}d_{leak}$) was determined using the relationship (Dutta Gupta and Saha, 1990)

$$\dot{E}d_{leak} = UA\left(T_p - T_a\right)\left(1-\frac{T_a}{T_p}\right) \tag{3.25}$$

The third part of distracted exergy is caused by the heat transfer between the plate and the working fluid ($\dot{E}x_{\text{p}.f}$). It was determined using (Jafarkazemi and Ahmadifard 2013)

$$\dot{E}x_{\text{p}.f} = \dot{m}C_p\left(T_o - T_i\right)\left(1-\frac{T_a}{T_p}\right) \tag{3.26}$$

The exergy destructed ($\dot{E}d$) during the heat transfer between the plate and the working fluid was obtained using the expression (Suzuki 1988)

$$\dot{E}d_{\text{p}-f} = \dot{m}C_pT_a\left[\left(\ln\frac{T_o}{T_i}\right)-\frac{T_o-T_i}{T_p}\right] \tag{3.27}$$

Using Eq. (3.17) and Eq. (3.27), the exergy efficiency ($\hat{E}$) can be obtained by the expression

$$\hat{E} = \frac{\dot{m}C_p\left[\left(T_o - T_i\right) - T_a\left(\ln\frac{T_o}{T_i}\right)\right]}{AI\left[1 - \frac{T_a}{T_s}\right]} \tag{3.28}$$

3.3 Pumping Power

The pressure drop throughout the collector is specified by ΔP, which was determined by the relationship (White 2003)

$$\Delta P = f\frac{\rho V^2 \Delta l}{2d} + K\frac{\rho V^2}{2} \tag{3.29}$$

where K is the loss coefficient, V is the mean flow velocity of fluid, d is tube diameter, ρ is density, f is friction factor and Δl is length of the tube. The velocity of the fluid was given by

$$V = \frac{4\dot{m}}{\rho\pi d^2} \tag{3.30}$$

The frictional factor, f for laminar flow condition was determined by the relationship (Kahani *et al.* 2013)

$$f = \frac{64}{\mathrm{Re}} \tag{3.31}$$

where Re is the Reynolds number and is expressed as

$$\mathrm{Re} = \frac{\rho V d}{\mu} \tag{3.32}$$

The pumping power (P_{pump}) was determined using the relationship (Garg and Agarwal 1995 and Balaji *et al.* 2017)

$$P_{pump} = \frac{\dot{m}\,\Delta P}{\rho} \tag{3.33}$$

3.4 Theoretical Analysis of Thermal Energy Storage System

3.4.1 Design of latent heat storage system

The size of the LHS bed was determined considering 5 MJ energy storing capacity. The volume of the LHS was estimated using the expression

$$V_{ol} = \frac{m}{\rho} = \left(\frac{\pi D_s^{\,2}}{4} \right) L \tag{3.34}$$

where L *and* D_s is the length and diameter of the storage, respectively.

The amount of PCM required was determined from the relationship

$$Q = mC_p(T_o - T_i) + mL_F \tag{3.35}$$

where L_F is latent heat for paraffin wax and m is the mass of paraffin wax.

3.5 Performance Parameters of Latent Heat Storage System

Performance parameters of LHS include determination of (i) melt fraction, (ii) charging and discharging time (iii) energy stored and (iv) energy recovered. These are presented below.

3.5.1 Charging time

Charging time for LHS is defined with respect to temperature rise of the PCM. The LHS is said to be fully charged when the entire PCM is completely melted, i.e. when the melt fraction reaches a value of one.

3.5.2 Discharging time

Discharging time for LHS is defined with respect to the temperature decrease of the PCM. The LHS is said to be fully discharged when the entire PCM is solidified, i.e. the melt fraction becomes zero.

3.5.3 Melt fraction

Melt fraction is generally referred as the liquid fraction of the PCM when it exists in a 2-phase form. The highest temperature below which the material is completely in

the solid state is called solidus temperature (T_S) and the lowest temperature above which the material is in the liquid state is called liquidus temperature (T_L).

Melt fraction (θ) of the PCM was obtained from the relationship (Niyas and Muthukumar 2013)

$$\theta = \frac{T - T_S}{T_L - T_S} = \frac{T - T_m + \Delta T_m}{2\Delta T_m} = \begin{cases} 0 & for\ T < T_S \\ 0-1 & for\ T_S \le T \le T_L \\ 1 & for\ T > T_L \end{cases} \quad (3.36)$$

where T_m is melting temperature of paraffin wax.

3.5.4 Energy stored

The total heat stored in the LHS system ($E_{T,C}$) consists of the sensible heat ($E_{S,C}$) and the latent heat ($E_{L,C}$). These can be obtained from the relationship (Niyas *et al.* 2017)

$$E_{S,C} = mC_p(T - T_{int}) \quad (3.37)$$

$$E_{L,C} = mL_F\theta \quad (3.38)$$

$$E_{T,C} = m\left[C_p(T - T_{int}) + \mathrm{L_F}\,\theta\right] \quad (3.39)$$

3.5.5 Energy recovered

The total heat discharged from the LHS system ($E_{T,D}$) consists of the sensible heat ($E_{S,D}$) and the latent heat ($E_{L,D}$). These are expressed as (Niyas *et al.* 2017)

$$E_{S,D} = mC_p(T_{int} - T) \quad (3.40)$$

$$E_{L,D} = mL_F(1-\theta) \quad (3.41)$$

$$E_{T,D} = m\left[C_p(T_{int} - T) + L_F(1-\theta)\right] \quad (3.42)$$

3.6 Modified Thermo-Physical Properties of nano-PCM

Due to the poor thermo-physical property of pure paraffin wax, dispersion of Al_2O_3 nanoparticle in the paraffin wax (nanofluid) was considered to enhance the thermal conductivity. In the present investigation, the volume fraction of Al_2O_3 was 10%. This was decided based on the report of Ho and Gao (2009) and Valan *et al.* (2013). Energy storing and discharging expressions(Eq.3.37 –Eq.3.42) were used for the evaluation of the storage performance. The correlations used for determining the modified thermo-physical properties are highlighted in **Appendix–C**. The thermo-physical property of the paraffin wax and Al_2O_3 is given in Table 3.3.

Table - 3.3 Thermo-physical properties of nanofluid (Sasmito *et al.* 2011)

Parameters	**Value**	**Unit**
C_{pnp} (Al_2O_3)	765	J/kg.K
d_{np}(Al_2O_3)	59×10^{-9}	m
K_{np} (Al_2O_3)	36	W/m.K
ρ_{np} (Al_2O_3)	3600	Kg/m^3
T_{ref}	273.15	K
T_{inlet}	343.15	K
T_{int}	298.15	K
T_m	321.15	K
dT	3	K
T_S	$T_m - dT$	K
T_L	$T_m + dT$	K
C_1 (Al_2O_3)	0.9830	-
C_2 (Al_2O_3)	12.959	-

3.7 Numerical Modelling for the Flat Plate Collector

For numerical modelling, the dimensions used were same as that of the actual collector fabricated for carrying out experiments. These are (i) absorber plate length of 1.65 m, (ii) absorber plate width of 1.1 m, (iii) tube diameter of 0.0125 m and (iv) tube thickness of 0.007 m. A single straight and bent tube attached to an absorber plate for estimating the outlet water and absorber plate temperature was considered for the CFD model. Since the numerical model considered a single riser tube, the inlet flow rate of the fluid through the riser tube is assumed to be$1/10^{th}$ of the total flow rate of the header tube.

3.7.1 Model geometry and meshing of the straight tube collector

Computational domain was modelled using solid work and meshing was carried out using ANSYS CFD software. The developed CFD model of the straight riser tube solar collector is shown in Fig. 3.5.

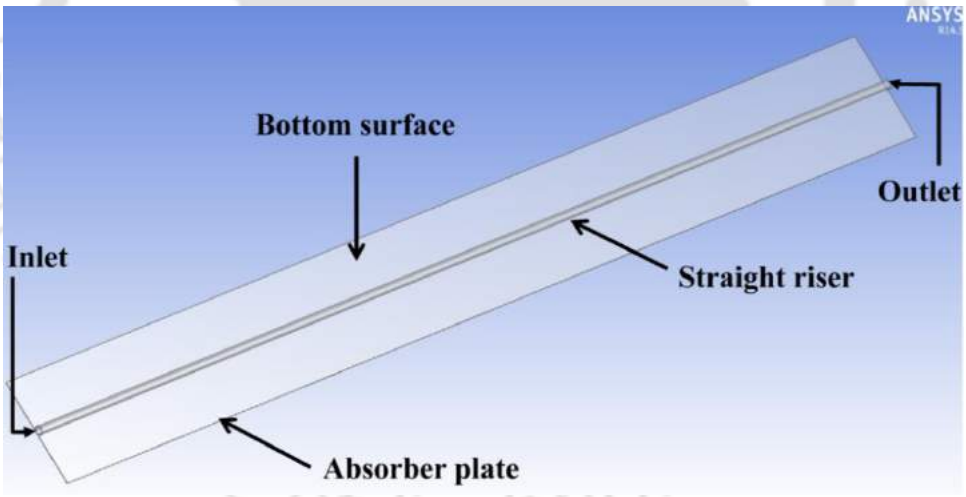

Fig.3.5 Model geometry of the straight riser tube with plate

To check the numerical results dependency on the size of mesh element, simulations with mesh element number of 221,546, 400,000 and 675,000 were carried out. The variation of absorber plate and outlet water temperature between larger mesh elements with middle mesh elements was less than ±0.6%. The number of elements selected for the computational domain consisting of water, water tube and absorber plate was 400,000. The solutions converged for the values of residuals below

1.0×10^{-6} in the computational domain. The magnified mesh of the straight tube attached plates is shown in Fig. 3.6.

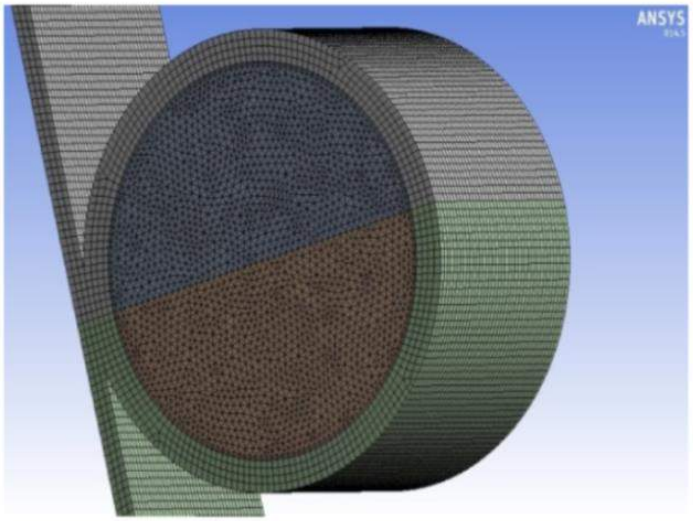

Fig.3.6 Magnified mesh part of the straight tube with plate

3.7.2. Model geometry and meshing of the bent tube collector

Similar to straight riser tube collector, the developed CFD model consist of a single bent riser tube and absorber plate attached with the absorber plate was considered for the investigation. The developed CFD model of the bent riser tube collector is depicted in Fig.3.7.

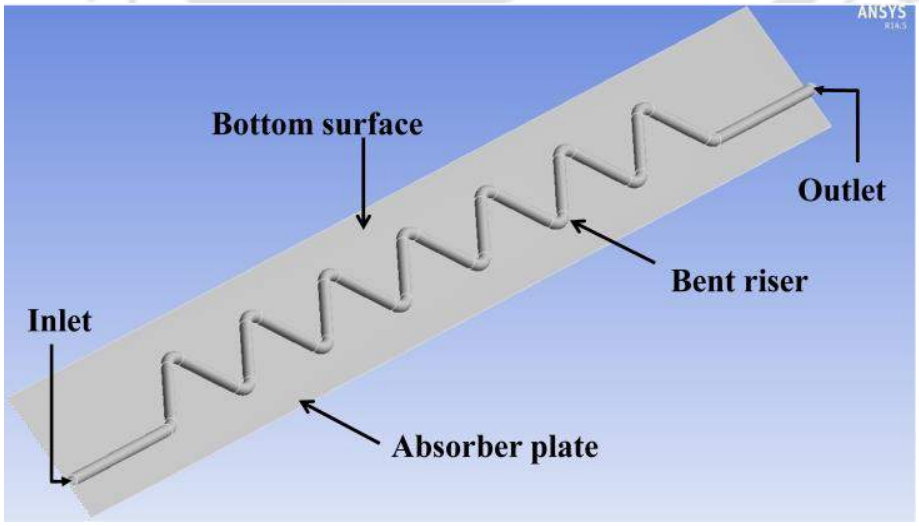

Fig.3.7 Model geometry of the bent riser tube with plate

Since 10 riser tubes were used, the flow rate in each riser tube considered was $1/10^{th}$ of the total flow rate of the header tube. To check the numerical results dependency on the size of mesh element, simulations with mesh element number of 0.9 million, 1.3 million and 2.2 million were carried out. The variation of absorber plate and outlet water temperature between larger mesh elements with middle mesh elements was less than ±0.8%. The number of elements selected for the computational domain consisting of water, water tube and absorber plate was 1.3 million. When the entire residuals fell below 1.0×10^{-6}, the convergence was found to be effective. The magnified mesh of the bent tube attached plates is shown in Fig.3.8.

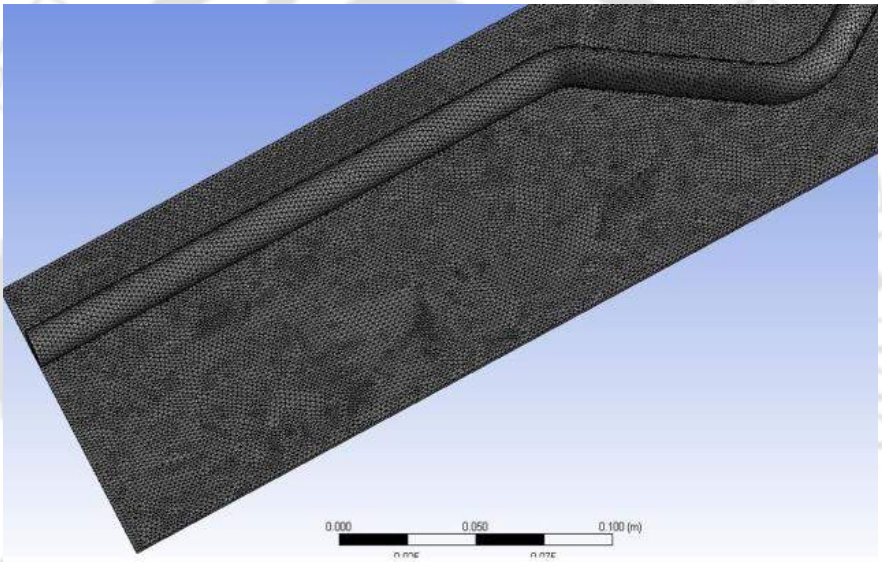

Fig.3.8 Magnified mesh part of the bent tube with plate

3.8 Governing Equations for Flat Plate Collector Analysis

The governing equations used for the simulation of the FPC system are carried out based on assumptions. These assumptions are: (i) the thermal and physical property of the absorber plate, tube and the working fluid remain constant during the flow, (ii) the fluid is incompressible and continuous, (iii) heat loss from the bottom side of the absorber tube and plate occurs by convection and is dependent on the wind speed and (iv) effects of gravity and buoyancy are negligible. Based on the assumptions,

The continuity equation was determined by the expression

$$\frac{\partial u}{\partial x}+\frac{\partial v}{\partial y}+\frac{\partial w}{\partial z}=0 \tag{3.43}$$

The momentum equation was given by the relationship

$$\frac{\partial \vec{v}}{\partial t}+(\vec{v}.\nabla)\vec{v}=\frac{1}{\rho}\left(-\nabla P+\mu\nabla^2\vec{v}+\vec{F}+\vec{S}\right) \tag{3.44}$$

The energy equations of the fluid and collector part were expressed by

$$\rho C_p u\frac{\partial T}{\partial x}+\rho C_p v\frac{\partial T}{\partial y}+\rho C_p w\frac{\partial T}{\partial z}=K\left[\frac{\partial^2 T}{\partial x^2}+\frac{\partial^2 T}{\partial y^2}+\frac{\partial^2 T}{\partial z^2}\right] \tag{3.45}$$

$$\frac{\partial^2 T}{\partial x^2}+\frac{\partial^2 T}{\partial y^2}+\frac{\partial^2 T}{\partial z^2}=0 \tag{3.46}$$

Finite volume method was used to solve the momentum and energy equations. SIMPLE algorithm available with FLUENT software was used for coupling the pressure with velocity. The boundary conditions used for the present model were velocity flow boundary condition and pressure outlet boundary condition for the inlet and outlet flow, respectively. First order upwind was used for discretizing pressure and second order upwind for the momentum and energy equations. The input parameter for the computational model was solar insolation (I), ambient temperature (T_a), inlet water temperature (T_i), and mass flow rate. The solar insolation at the top surface of the absorber plate used for the simulation was the average solar insolation measured from the experiment. Convective wall boundary condition was assumed for the bottom surface.

The convective heat loss coefficient at the bottom surface due to wind (h_w) (as a function of wind speed (V_w)) was obtained using the expression (Watmuff *et al.*1977)

$$h_w=2.8+3V_w \tag{3.47}$$

3.9 Numerical Modelling for Thermal Energy Storage System

3.9.1 Model geometry for the latent heat storage system

Figure 3.9 illustrates the sectional view of the 3D shell and tube type storage system filled with heat transfer medium in the shell and water in the HTF tube. Since the developed model is symmetric about the X-axis, only 1/4th of the model was taken for the investigation. The diameter of the LHS shell and the HTF tube, length of the LHS shell and thickness of the HTF tube were 200 mm, 12 mm, 1000 mm and 1.5 mm, respectively which are similar to the fabricated storage system. Paraffin wax was used as a PCM for the LHS model. The thermo-physical properties of the PCM are provided in Table 3.4.

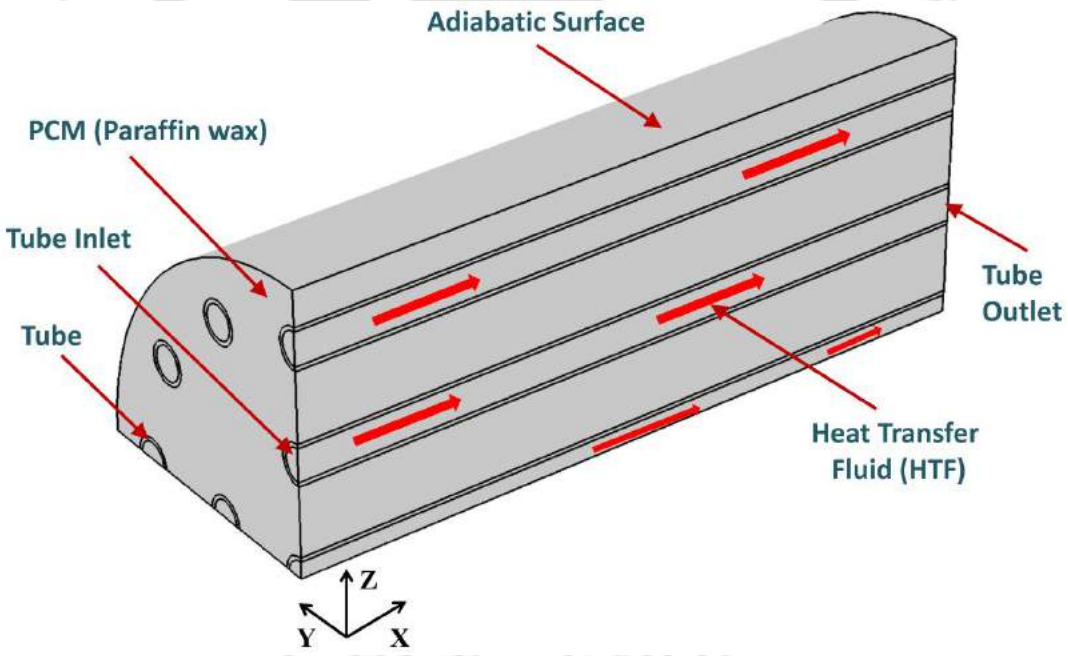

Fig.3.9 Numerical model of the LHS system

Table-3.4 thermo-physical properties of paraffin wax (Niyas and Muthukumar 2013)

Properties	Values
Latent heat of fusion (kJ/kg)	168
Thermal conductivity (W/m.K)	0.2
Density (kg/m^3)	780
Specific heat (J /kg.K)	2000
Dynamic viscosity (Pa.s)	0.0039
Thermal expansion coefficient (1/K)	0.0006
Melting temperature range (K)	321
Solidus temperature	318
Liquidus temperature	324

3.9.2 Meshing for latent heat storage system

The numerical solution of paraffin and nanofluid based LHS depends on the number of mesh elements. Grid generation was performed using tetrahedral cells for both the domain and boundaries which is presented in Fig.3.10.

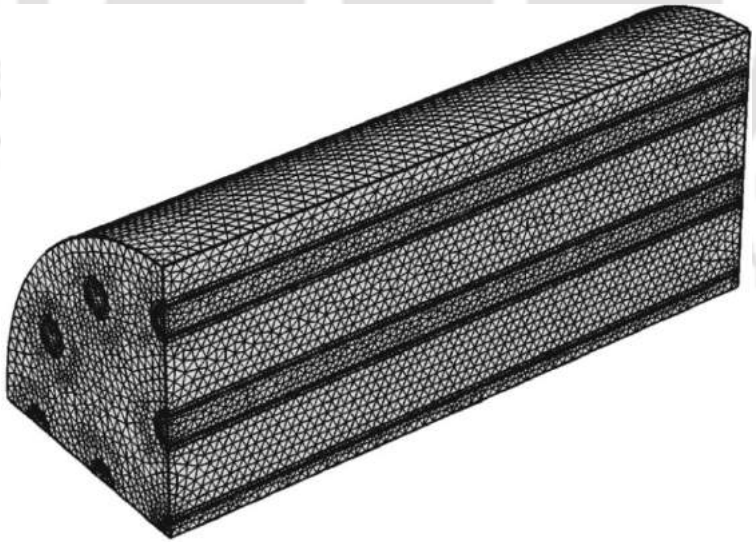

Fig.3.10 Meshed part of the LHS model

The smaller section such as HTF tube thickness was highly refined with sufficient volume elements. In order to capture the boundary layer in the near wall regime,

special meshing features of COMSOL Multiphysics, *viz*., boundary layers was used for the developed model. This feature helped for predicting the near wall velocity and thermal gradient with utmost accuracy and precision.

3.10 Governing Equations for Thermal Energy Storage System

This section presents the governing equations used for simulating the latent heat energy storage system. The mass conservation, momentum conservation and energy conservations used are briefly described below.

3.10.1 Governing equations for latent heat storage system

Simulating the numerical model of LHS comprises the HTF flow, conduction, convection and phase change. The following assumptions were made while simulating the physical model of the LHS: (i) HTF is incompressible and Newtonian, (ii) HTF flow is laminar and negligible viscous dissipation, (iii) the initial temperature of the PCM is uniform, (iv) phase change during melting and solidification occur only within melting range, (v) the heat losses through the outer wall are negligible and (vi) PCM is homogenous and isotropic.

The developed LHS physical model was solved by the coupled conjugate heat transfer problems which simultaneously solve both the flow behaviour of the HTF and the phase change behaviour of the PCM. This was solved by implementing the equivalent heat capacity (EHC) method, which comprises both the specific heat and latent heat of the PCM in a single term called EHC.

Bonacina *et al.* (1973) used EHC method for the first time for solving the problem. The modified heat capacity of the PCM and the effective heat capacity are obtained from the expression (Niyas and Muthukumar 2013)

$$C_p = \begin{cases} C_{p.s} \ \ for\ T < T_s \\ C_{p.EFF} \ \ for\ T_s \le T \le T_L \\ C_{p.L} \ \ for\ T > T_L \end{cases} \tag{3.48}$$

$$C_{p.EFF} = \frac{C_{p.S} + C_{p.L}}{2} + \frac{L_F}{T_L - T_S} \tag{3.49}$$

where subscript *S* and *L* stands for solid and liquid, respectively.

The melting range is also known as mushy zone. The discontinuous modified heat capacity method is implemented in the COMSOL Multiphysics software using a smoothed Heaviside function with a continuous second derivative.

The continuity equation (Eq.3.43) and energy equation (Eq.3.45) were used for simulating the LHS model but the momentum equation (Eq.3.44) was modified to include the effect of buoyancy ($\vec{F}$) and Darcy law's source term ($\vec{S}$). However, these terms are zero for the solar collector. The effect of buoyancy is included to simplify the complexity in solving Navier-stokes equations using Boussinesq approximation which was obtained using the expression (Niyas *et al.* 2017)

$$\vec{F} = \rho \vec{g} \beta (T - T_m) \tag{3.50}$$

where β is thermal expansion of the PCM.

In order to nullify the velocity in the solid region of the PCM, Darcy law's source term was incorporated in the momentum equation. ($\vec{S}$) was determined using the expression (Niyas *et al.* 2017)

$$\vec{S} = \frac{(1-\theta)^2}{\theta^3 + \varepsilon} A_{mushy} \vec{v} \tag{3.51}$$

where A_{mushy}, ε and $\vec{v}$ are mushy zone constant, a constant value of 0.001 and velocity of PCM, respectively.

The mushy zone constant is defined as the transition of velocity in the mushy region. The mostly recommends value for the mushy zone constant is in the range 10^3 – 10^7. In the present study, a value of 10^4 for mushy zone constant was decided based on the reported work (Niyas *et al.* 2017). The higher values of mushy zone constant lead to steeper damping curve thereby reducing the velocity drop to zero during solidification of PCM.

3.10.2 Governing equations for nanofluid based latent heat storage system

Along with the assumption used for pure paraffin wax filled LHS, the following assumptions were also included for the simulation of the nanofluid based LHS (i) there is no agglomeration or sedimentation in the shell, (ii) the initial temperature of nanofluid is uniform and (iii) the nanofluid is homogeneous and isotropic. The continuity, momentum and energy equations used were similar to the pure paraffin wax filled LHS presented under subsection 3.9.1. The modified thermal properties of nanofluids are given in **Appendix–C**.

3.11 Boundary Conditions Used for the Thermal Energy Storage System

The boundary conditions used for the TES are: (i) there is no agglomeration or sedimentation in the shell,(ii) the flow of HTF is laminar with negligible viscous dissipation, (iii) the HTF is incompressible and Newtonian, (iv)the properties of nanofluid is homogeneous and isotropic, (v)the heat loss through the outer wall of the shell is assumed to be negligible, (vi)the initial temperature of nanofluid is taken to be uniform and the phase change during melting/solidification occurs within a temperature interval, (vii) fluid initialization of charging/discharging is done by assuming a constant temperature of 343 K/298 K followed by constant velocity of the HTF and (viii) initially, there is no flow of HTF through the tubes and all the domains are at constant temperature of 298 K/343 K during charging/discharging process, respectively.

3.12 Summary

In this Chapter, the theoretical formulations of FPC (straight, bent and cascaded) and thermal energy storage (latent heat storage) were presented in detail. Subsequently, methods for simulation and constitutive equations for the same were also elaborated. The next chapter reports the detail experimental descriptions of the FPC with straight, bent and cascaded collectors along with the latent heat storage system.

Chapter - 4

Experimental Setup and Procedure

4.1 Introduction

This chapter presents the description of experimental setup consisting straight tube solar collector, bent tube solar collectors, cascaded solar collector and latent heat storage system. The experiments were performed to study the heat transfer characteristics and performance by varying the operating parameters. Further, various measuring devices used for the investigation is discussed and experimental procedure is elaborated in subsequent sections.

4.2 Details Experiment Representation

Experimental procedure followed for the present work is illustrated in the flow chart of Fig.4.1.

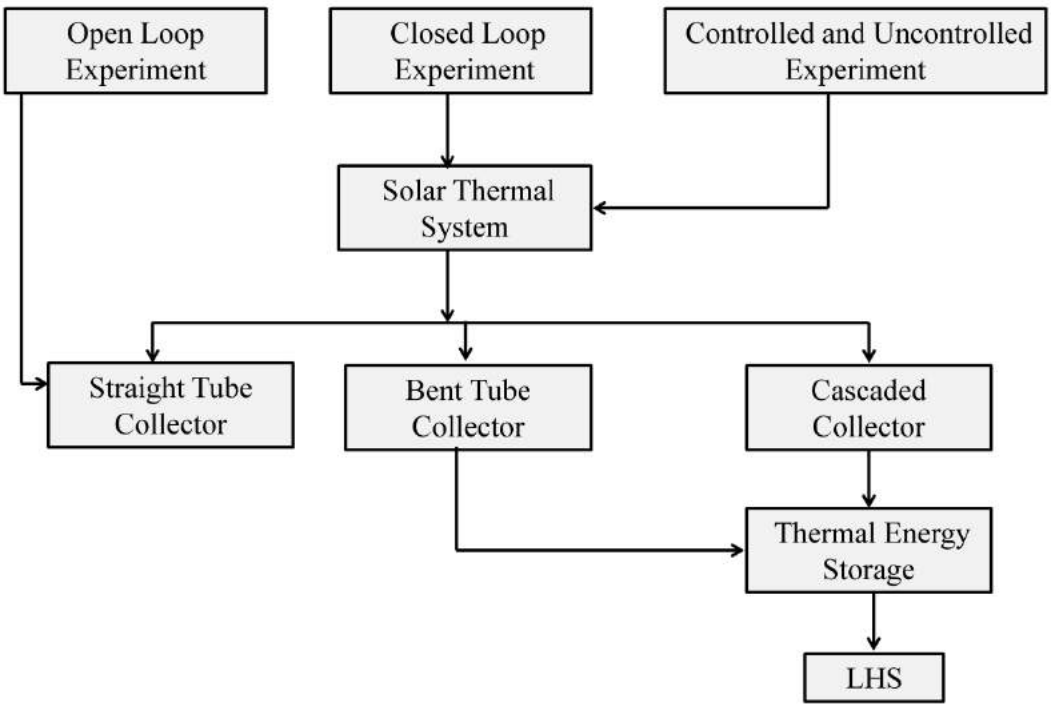

Fig.4.1 Detail representation of the experimental study

The experimental study using solar thermal system is carried out for (i) open loop experiment, (ii) closed-loop experiment and (iii) controlled/uncontrolled experiments. The open loop experiment is performed only for straight tube collector. As the same was demanding for the large quantity of water, subsequent experiments were conducted with the closed-loop system for a particular mass flow rate. Similar experiments were conducted for different mass flow rates of water and same procedures were followed. Investigation of latent heat storage (LHS) system was carried out experimentally as well as numerically. The detailed explanation and experimental method of each test are presented in the next sections.

4.3 Experimental Setup

Photograph of the complete experimental setup of the integrated solar thermal system used for the present investigation is shown in Fig.4.2.

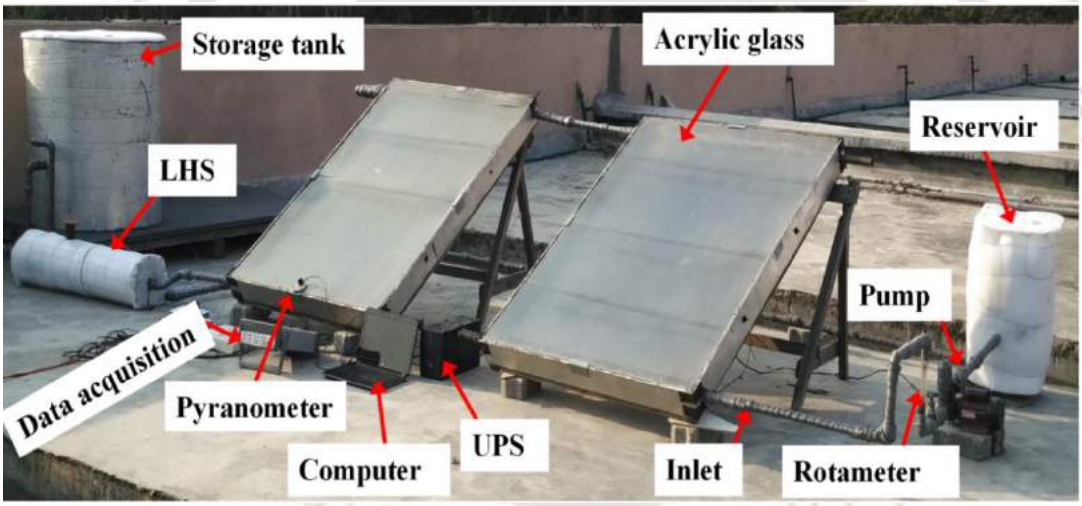

Fig.4.2 Photograph of the complete setup

The experimental setup consists of two flat plate solar collectors (straight and bent tube collectors), latent heat storage (LHS), storage tank, heat exchanger and reservoir tank. The outlet of the pump is connected to the inlet of the first FPC. The outlet of this FPC is connected to the second FPC through GI pipe and copper socket. The FPCs were connected to the LHS and heat exchanger using GI pipes.

Each of the solar collectors comprises of 10 straight and bent tubes as shown in Figs. 3.1 (a) and (b), respectively. The diameters of the riser and header tubes were 12.5 mm and 25 mm, respectively. The risers are connected to the headers by drilling and brazing. The top of the collector was covered by 4 mm thick acrylic glass having good optical properties and attached to the side of the collector with aluminium frame. The optimum air gap of 30 mm was maintained between the glass and the plate to decrease overall heat loss coefficients. For ensuring better heat transfer characteristics, a 0.5 mm thin copper absorber plate was attached over the riser tubes by soldering. The surface of the absorber plate was cleaned to remove dust and painted with black to increase the absorptivity. Side and back of the collector were insulated by 50 mm thick glass wool to reduce heat losses from the side of the collector.

The LHS consists of 17 steel tubes fixed to the shell. The shell diameter of 300 mm, 1000 mm length and 12.5 mm tube diameter was considered in the present study. The tubes were placed inside the stainless steel shell. The shell was fully filled with 20 kg paraffin wax in order to store/release heat when the hot/cold fluid circulates through the tube. The outer surface of the shell was insulated by thermo foam to reduce heat losses. The storage tank carried two tanks, namely biogas digester and shell tank. The shell tank was filled with water whereas the biogas digester was filled with feed materials. To eliminate heat loss from the shell, the inverted tank placed over the biogas digester and is shown in Fig.7.2. The helical coiled heat exchanger comprises of six turns of copper tube with 12.5 mm tube diameter, 540 mm coil diameter and 70 mm pitch as shown in Fig. 7.3. The helical coil is mainly to transfer the heat to the fluid kept in the storage tank.

4.3.1. Details of the open loop system

Figure 4.3and 4.4shows the schematic diagram and photograph, respectively for the open loop experimental setup using straight tube collector. Cold water from the storage tank is pumped into the FPC through the bottom part of the collector and exits through the top of the collector pipe. Inlet water while circulating through the riser tube gets heated up and the hot water was stored in the hot water storage tank.

The surface of the collector was cleaned to remove dust and to increase the absorptivity before the beginning the experiments. This test was conducted only for straight tube collector due to the need of large quantity of water. During the test, the flow rate of the fluid was measured by a rotameter and adjusted using gate valve in order to raise the working fluid temperature.

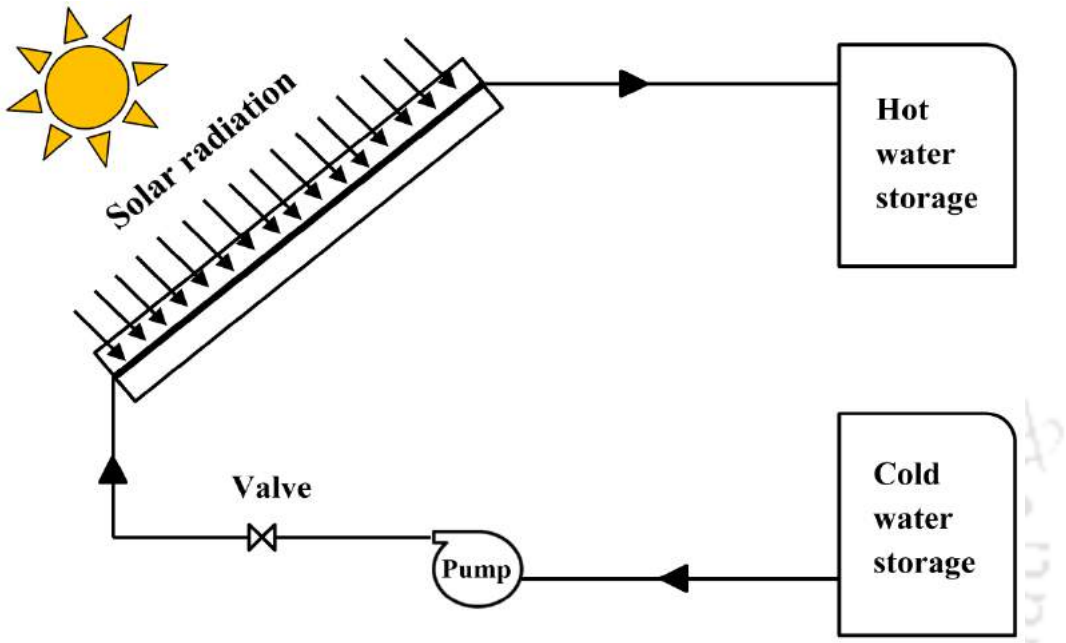

Fig.4.3 Schematic diagrams of the open loop water heating collector

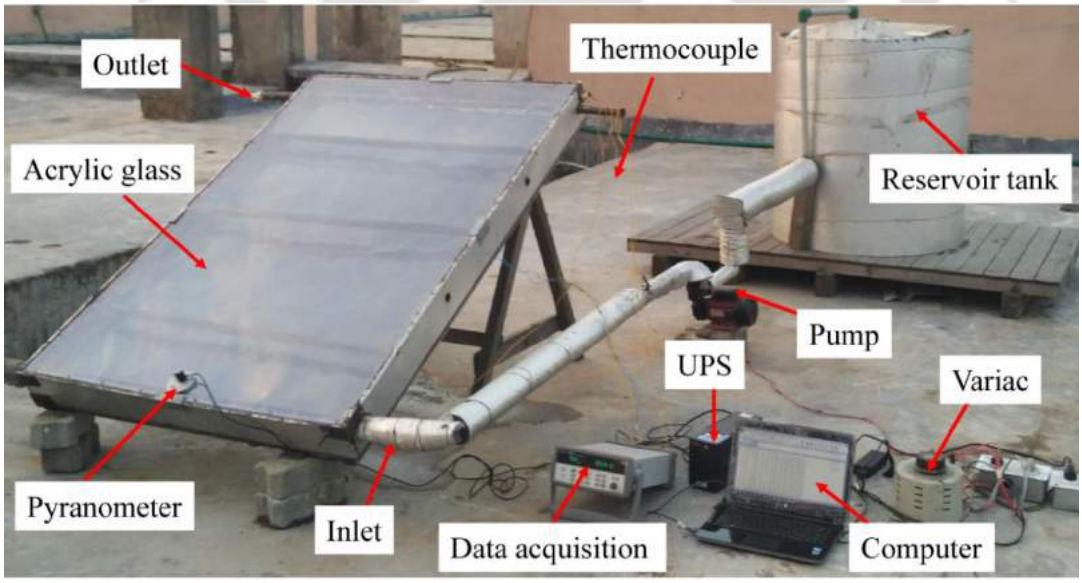

Fig.4.4 Photograph of the open loop water heating collector

4.3.2 Details of the closed loop system

The photograph and schematic diagram of the closed loop heating system are presented in Figs. 4.5 and Fig. 4.6, respectively.

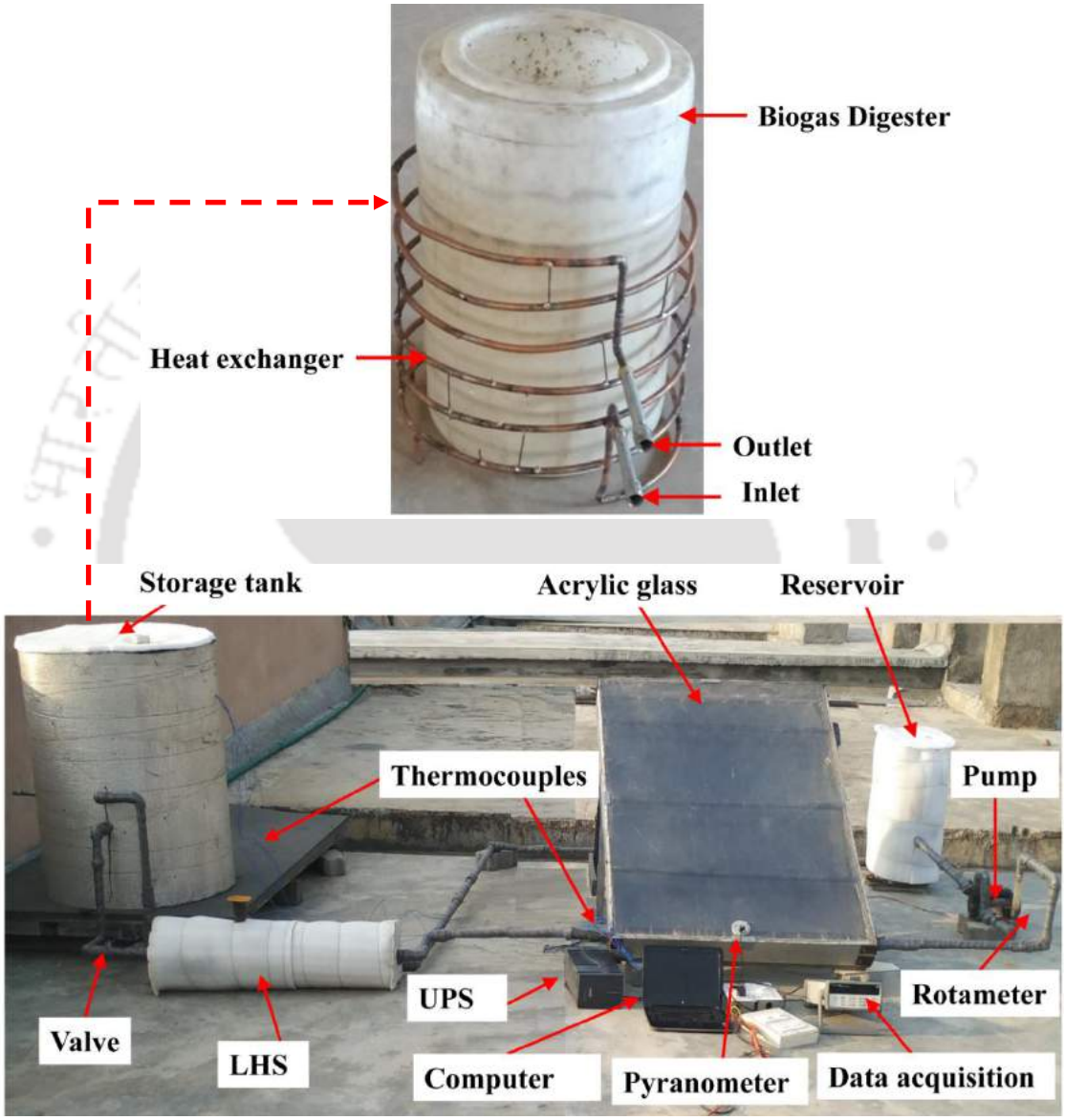

Fig.4.5 Photograph of the closed loop water heating collector

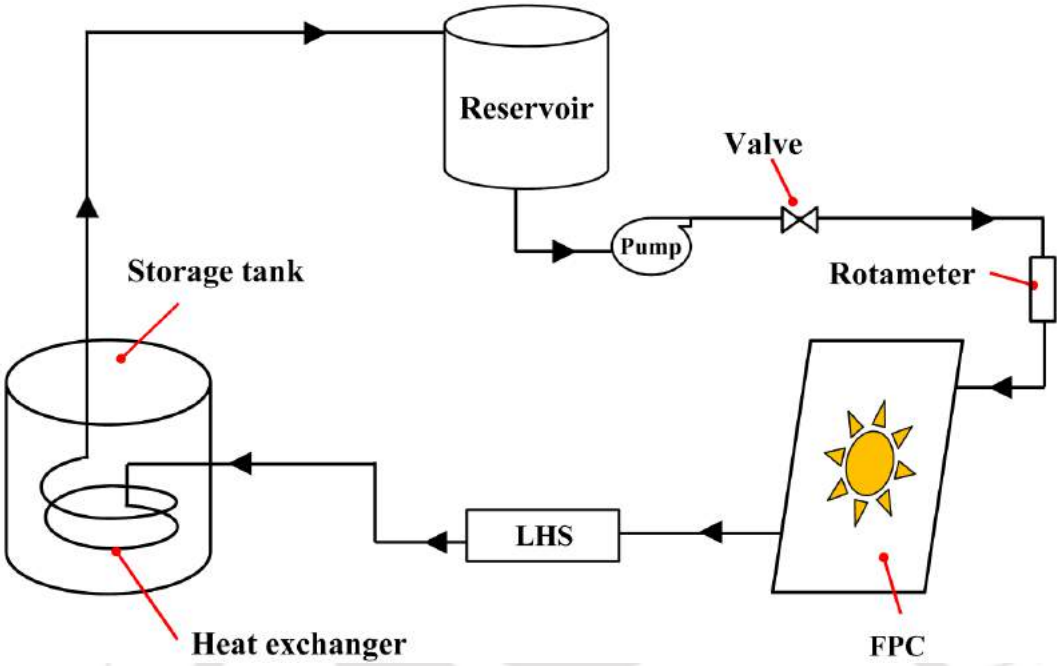

Fig.4.6 Schematic diagrams of the closed loop water heating collector

In the closed-loop test, water is pumped from the reservoir to the collectors allowing heat absorption by FPC. Water from the FPC is circulated through heat exchanger located inside the storage tank and back to the reservoir. The heat exchanger transfers heat from the collector loop fluid to the fluid kept in the storage tank. The surface of the collector was cleaned to remove dust and to increase the absorptivity before the beginning of the experiments. These experiments are carried out for the straight tube collector, bent tube collector, cascaded collector and LHS system.

4.3.3 Details of the cascaded collector system

The experimental setup for the cascaded solar collectors is depicted in Fig.4.7. In this experiment, water from the cold water reservoir tank is pumped through the inlet of the bent tube collector. As the cold water circulates through the bent tube collector, it absorbs heat energy resulting in an increase in water temperature. The outlet from the first collector is circulated through the inlet of the second collector. As the heated water circulates through the second collector, the warm water further absorbs heat. The heated water from the second collector transfer heat to the fluid kept in the storage tank through the heat exchanger and then repeats the cycle.

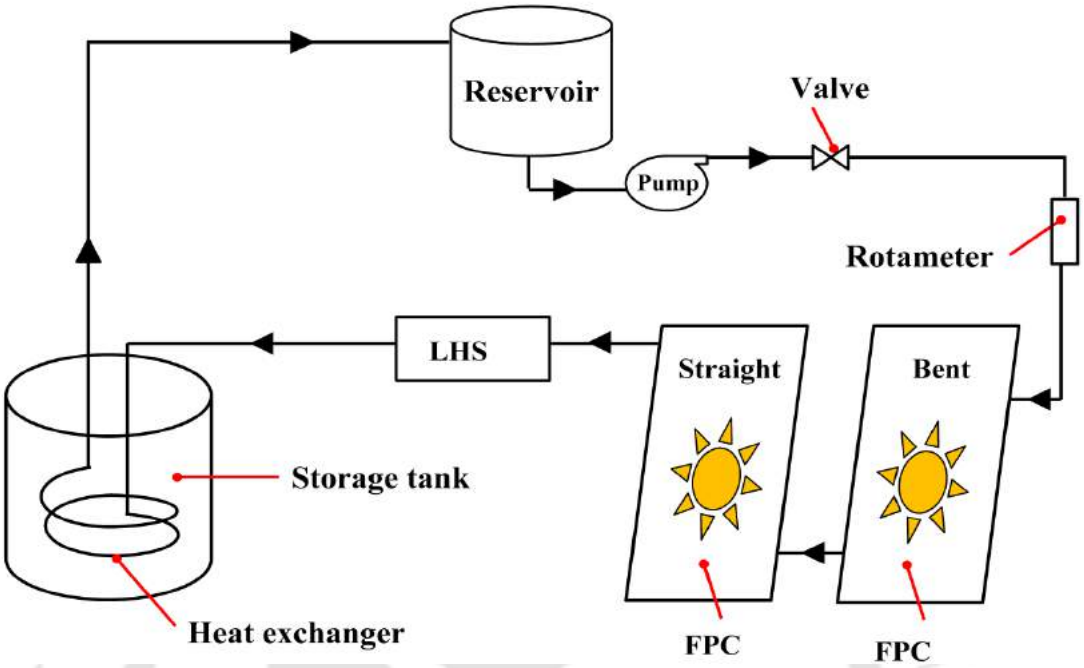

Fig.4.7 Schematic diagram of the cascaded solar collector

4.4 Experimental Procedure of the Flat Plate Collector System

The mass flow rate of water is measured by rotameter which was kept between the pump and the collector. Solar insolation (I) was measured with an accuracy of ±5 W/m^{2}using the pyranometer placed over the surface of the solar collector. Since the solar collector was tilted at an angle of 26.3º to the horizontal, the pyranometer was also tilted at the same angle. The outlet water temperature, inlet water temperature, glass temperature, absorber plate temperature, paraffin wax temperature and ambient temperature were measured using T-type thermocouples with an accuracy of ±0.5 ºC. The pyranometer and thermocouples were connected to a 20-channel multiplexer and a data acquisition system (Agilent-34972 A) to record the solar intensity and temperature at an interval of 10 s. The reading from the data acquisition system was stored in the computer. The entire sets of the experiment were conducted for two winter and summer seasons of two consecutive years (2015 – 2017). Hence, result and discussions cover both the temporal and average variation of the parameters.

At the beginning, the straight tube and bent tube collectors were isolated from the system and experimental study carried out under different operating parameters. The

experiments were carried out for open loop, closed loop and controlled/uncontrolled conditions subsequently. The open loop test was conducted only for straight tube collector whereas the closed-loop test was carried out for straight, bent as well as for the cascaded collectors. Similar methodologies were followed for the experiments with the latent heat storage system in closed-loop for the cascaded collectors. Finally, the integrated thermal system with and without control conditions in the closed-loop arrangement were tested. The next section presents a step-by-step experimental procedure followed for the individual experiments.

4.5 Experimental Descriptions and Procedure of the Latent Heat Storage System

Photograph of the LHS system is shown in Fig.4.8. The location of the thermocouple and other components can be seen in the photograph. The positions of the thermocouples inside the LHS system are depicted in Fig. 4.9.

When there is sufficient solar radiation, the hot water from the solar collector is supplied to the LHS system in order to heat the paraffin wax kept in the shell. Likewise, during unavailability of solar radiation or at the cloudy time, cold water/ low-temperature water from the reservoir tank through the solar collector is circulating in the LHS system to absorb heat from the paraffin wax.

During the charging/discharging process, the hot/cold water at 343 K/ 298 K is supplied from the reservoir tank through the HTF tubes kept in LHS system. Since solar radiation is fluctuating throughout the day, it is difficult to obtain constant temperature at the inlet of the thermal storage tubes for validation purpose. Hence, electric heater with the thermostat was used for heating the water in the reservoir to attain constant temperature.

The inlet and outlet water temperatures from the LHS and the top surface temperature of the paraffin wax [T1, T2, T3 and T4] were determined using T-type thermocouples with an accuracy of ± 0.5 ºC. The mass flow rate of water and solar insolation on the surface of the solar collector was measured by rotameter and pyranometer. The data acquisition system was used to record the temperature at an

interval of 10 s. The validation was carried out by taking the average temperature of the four thermocouples T1 to T4.The experimental procedures for both controlled and uncontrolled experiments along with the heat exchanger are presented briefly in Chapter 7.

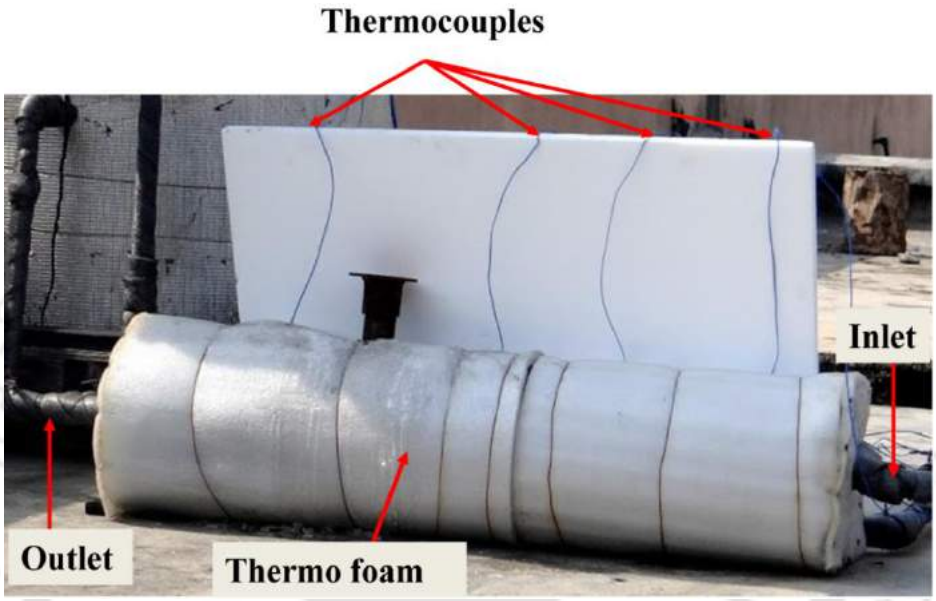

Fig.4.8 The photograph of paraffin wax filled LHS system

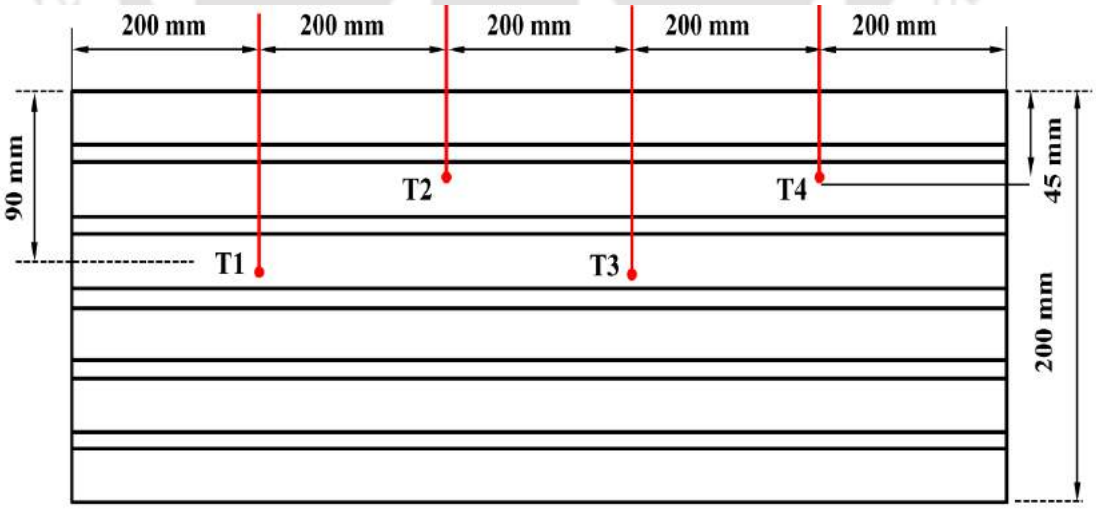

Fig.4.9 The sectional view of the LHS system

4.6 Summary

The experimental setup and procedure of straight and bent tube solar collectors, cascade solar collector and latent heat storage system has been presented in this Chapter. Further, the detail instrumentation used for measuring operating parameters was also elaborated. Chapter 5 presents the results and discussion of flat plate collectors along with the parametric study.

Chapter - 5

Results and Discussion: Investigation on Flat Plate Collectors

5.1 Introduction

Experimental and numerical investigations were carried out to ascertain the thermal performance of straight tube FPC, bent tube FPC, cascaded FPC and thermal energy storage systems. The results are presented and discussed in this Chapter. The results of parametric study and uncertainty analysis is also presented and discussed.

5.2 Experiments

Experimental values of inlet water temperature, mass flow rate, ambient temperature, wind speed and solar insolation were used as input parameters for the computational model for predicting the outlet water and absorber plate temperature. The input parameters obtained at one-hour interval was used to predict the time averaged outlet water and absorber plate temperature. Validation of the model was carried out comparing the simulation results with the experimental data. Based on the reported result of Facão (2015), the present study considered flow rates of 0.0083 $kg.s^{-1}$, 0.125 $kg.s^{-1}$, 0.0167 $kg.s^{-1}$, 0.021 $kg.s^{-1}$ and 0.025$kg.s^{-1}$ for the entire investigations. Experimental results of outlet water and absorber plate temperature agree well with the results obtained from simulation.

5.3 Measured Input Parameters Using Straight Tube Collector

Based on the experimental procedures presented in Chapter 4, the input parameters for the computational model, *viz*., solar insolation (I), ambient temperature (T_a), inlet water temperature (T_i), and mass flow rate ($\dot{m}$) were measured from experiment. Figures 5.1 (a) and (b) illustrate the results of the experiments carried out using straight tube FPC at water flow rates of 0.0125 $kg.s^{-1}$ and 0.025 $kg.s^{-1}$, respectively from 8:00 h to 16:00 h.

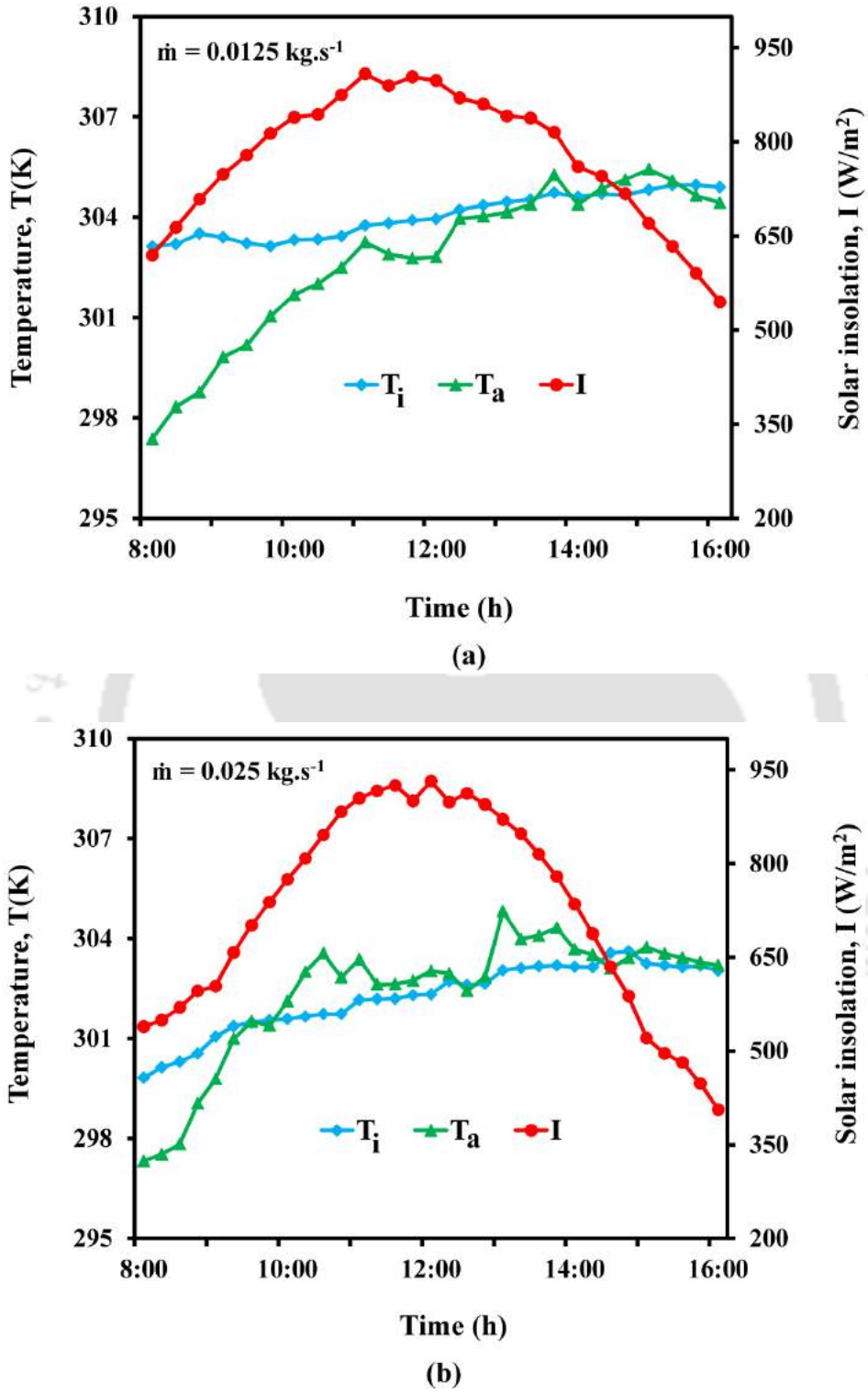

Fig.5.1 Variation of inlet water temperature, ambient temperature and solar insolation versus time at flow rate of (a) $\dot{m}$ = 0.0125 kg.s^{-1} and (b) $\dot{m}$ = 0.025 kg.s^{-1}

The figure indicated that for the above two cases the solar insolation showed a parabolic path with the peak value attaining during the mid-day which subsequently decreasing. The solar insolation was minimum in the morning and increased with time. It attained a maximum of 908 $W.m^{-2}$ at 11:00 h for the above-mentioned cases. Similarly, the ambient temperature and inlet water temperature increased from the morning and attained the peak value at 14:00 h and 16:00 h, respectively.

5.4 Model Validation Using Straight Tube Collector

5.4.1 Temperature distribution of the straight tube collector

Results of CFD analysis for the variation of outlet water temperature along the riser tube, at the outlet pipe and absorber plate at 11:00 h for the flow rate of 0.025 $kg.s^{-1}$ are presented in Figs.5.2 - 5.4.

The variation of water temperature along the riser pipe length at 11:00 h shown in Fig.5.2 indicates higher outlet water temperature at the upper portion of the collector compared to the lower portion. This is expected since the inlet water absorbs heat as it moves upward through the riser tube.

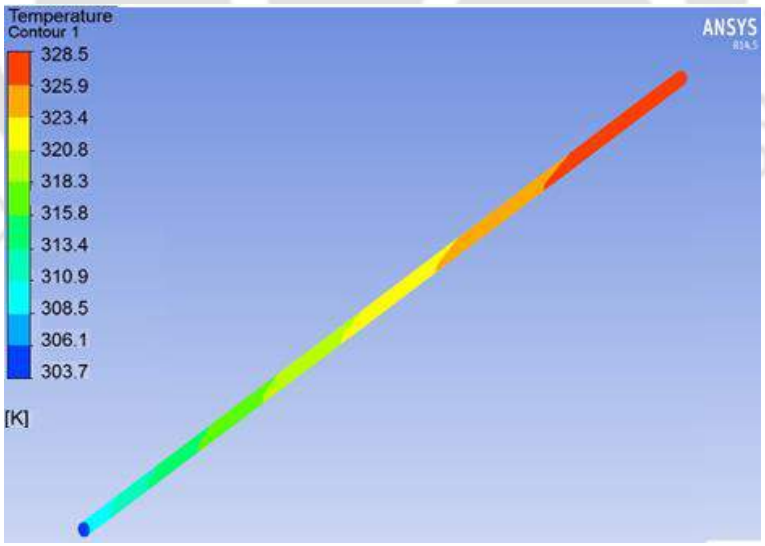

Fig.5.2 Variation of water temperature along the riser pipe at 11:00 h

Figure 5.3 depicts the variation of temperature across the outlet tube diameter. The temperature at the tube surface is 18 K higher compared to the centre. As one side of the tube is brazed with the hot absorber plate, the temperature distribution at one

side of the tube is higher compared to the other side. The heat transfer-taking place is by a sequence of radiation, conduction through the tube thickness followed by convection inside the tube. Since it takes more time for the heat flow to reach the centre of the tube by convection, the water temperature at the centre of the tube is lower than at the surface.

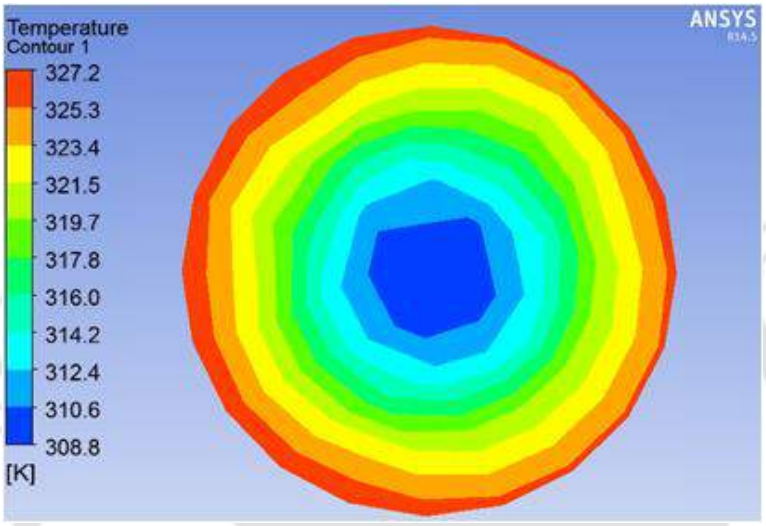

Fig.5.3 Simulated water temperature at the outlet pipe at 11:00 h

Figure 5.4 illustrates the variation of absorber plate temperature at the top surface. The temperature variation across the absorber plate length indicates a difference of 25 K between the inlet and outlet side of the plate.

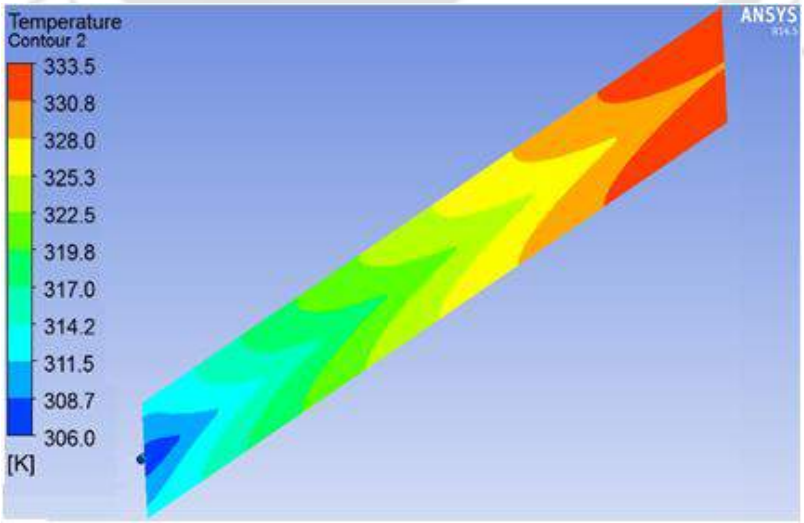

Fig. 5.4 Simulated absorber plate temperature at the top surface at 11:00 h

Since heat is absorbed by the cold fluid flowing through the riser tube which is in contact with the absorber at the mid-width section, there was a variation of around 5 K across the plate width.

5.4.2 Comparison between experimental and predicted outlet water temperature

Figures 5.5 (a) and 5.5 (b) illustrate the comparison of the experimental and simulation values of outlet water temperatures for mass flow rates of 0.0125 $kg.s^{-1}$ and 0.025 $kg.s^{-1}$, respectively. The percentage deviations in error between the experimental (X_{exp}) and simulation (X_{sim}) values were determined using the relationship (He *et al*. 2016)

$$Error\ (\%) = \frac{\left| X_{sim.} - X_{\exp.} \right|}{X_{sim.}} \times 100 \qquad (5.1)$$

The maximum deviation error between the experiment and simulation using Eq. 5.1 indicates good agreement. The error values are of 5.2% and 4.4%, respectively for the above-mentioned flow rates. The error deviation obtained in the present study was small compared to the result of Attar and Farhat (2015) and Taherian *et al.* (2011) using two meter square size collector.

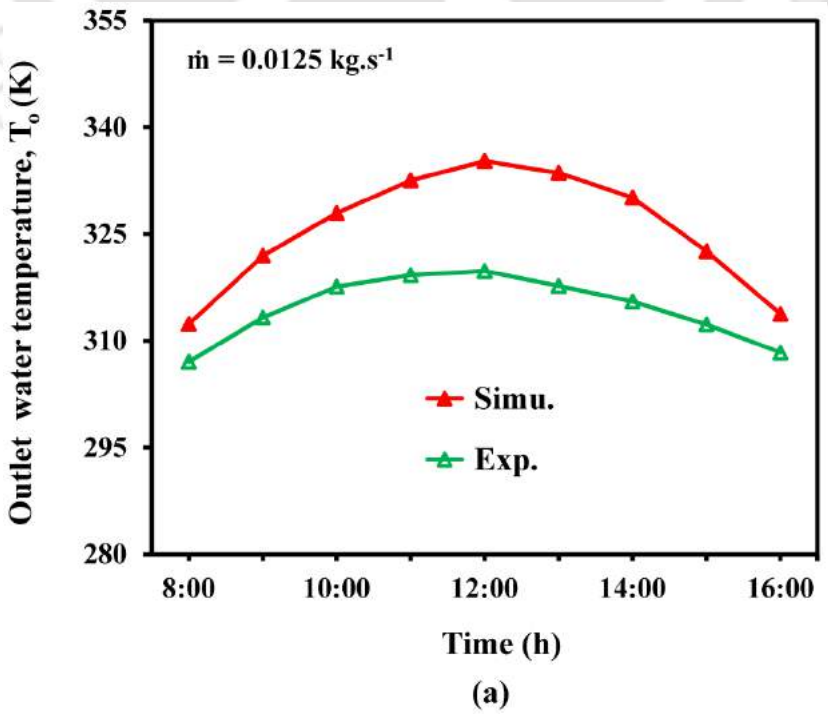

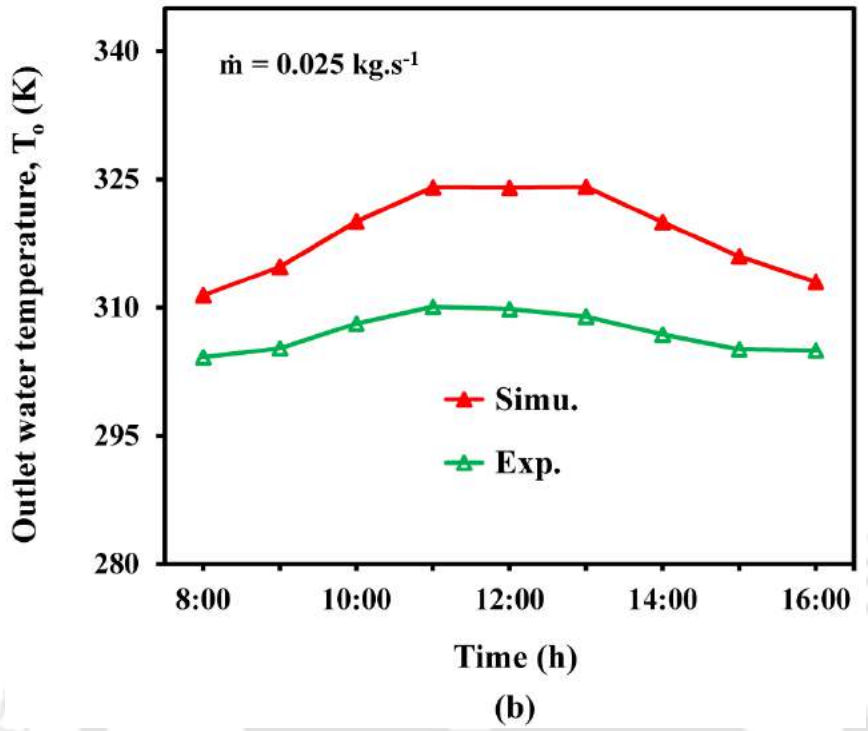

Fig.5.5 Variation of predicted and experimental outlet temperature versus time at flow rate of (a) $\dot{m}$ = 0.0125 kg.s^{-1} and (b) $\dot{m}$ = 0.025 kg.s^{-1}

5.4.3 Comparison between experimental and predicted absorber plate temperature

Plots of experimental and simulation values of absorber plate temperatures versus time for the two flow rates are shown in Figs. 5.6 (a) and (b).

The figure indicates that the experimental values of plate temperature are higher than the computational values for both flow rates. Since the simulation was based on the assumption of a perfect contact between the absorber plate and the tube, better heat transfer occurs between the plate and the tube compared to the actual case. Hence, the simulated absorber plate temperature values are lower than that of the experimental values. The error deviation obtained between experiment and simulation on the surface of the absorber plate did not exceed ± 2%.

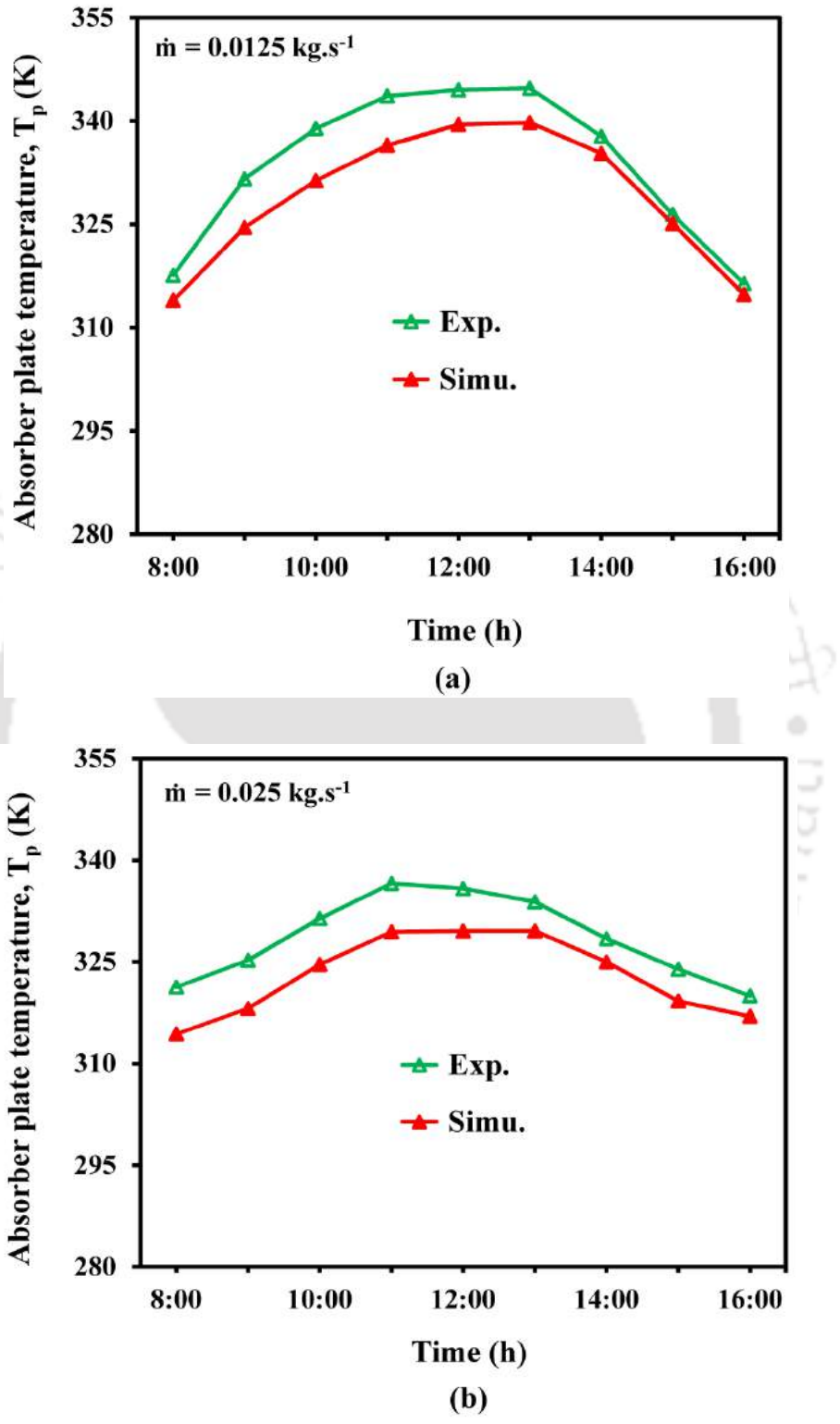

Fig.5.6 Variation of predicted and experimental absorber temperature versus time at flow rate of (a) $\dot{m}$ = 0.0125 kg.s^{-1} and (b) $\dot{m}$ = 0.025 kg.s^{-1}

5.4.4 Thermal efficiency of the straight tube collector in open loop system

Thermal efficiency, inlet water temperature, outlet water temperature, ambient temperature and solar insolation for open loop heating system at flow rate of 0.0125 $kg.s^{-1}$ and 0.025 $kg.s^{-1}$ are depicted in Figs. 5.7 (a) and (b), respectively. Figures indicate that for the period of experiment, the inlet water temperature increased to a maximum of 3 K (301 K to 304 K) and 8 K (299 K to 307 K), respectively at flow rate of 0.0125 $kg.s^{-1}$ and 0.025 $kg.s^{-1}$. The solar insolation was found to be increasing in the morning, reaching its maximum value of 916 $W.m^{-2}$ at 12:00 h. The outlet water temperature increased slowly from 8:00 h to 10:00 h because of the lower solar insolation and ambient temperature at the morning. The maximum outlet water temperature of 318.1 K and 308.1 K was observed at flow rate of 0.0125 $kg.s^{-1}$ and 0.025 $kg.s^{-1}$, respectively. Similarly, the maximum ambient temperature was found to be 307 K at 0.0125 $kg.s^{-1}$ flow rate whereas it was 303.7 K at 0.025 $kg.s^{-1}$ flow rate. Further, the average thermal efficiencies were found to be 44.3% and 40.6% for the above mentioned flow rates. Since at lower flow rate, the fluid was retained in the riser tubes for more time, higher outlet water temperature was obtained.

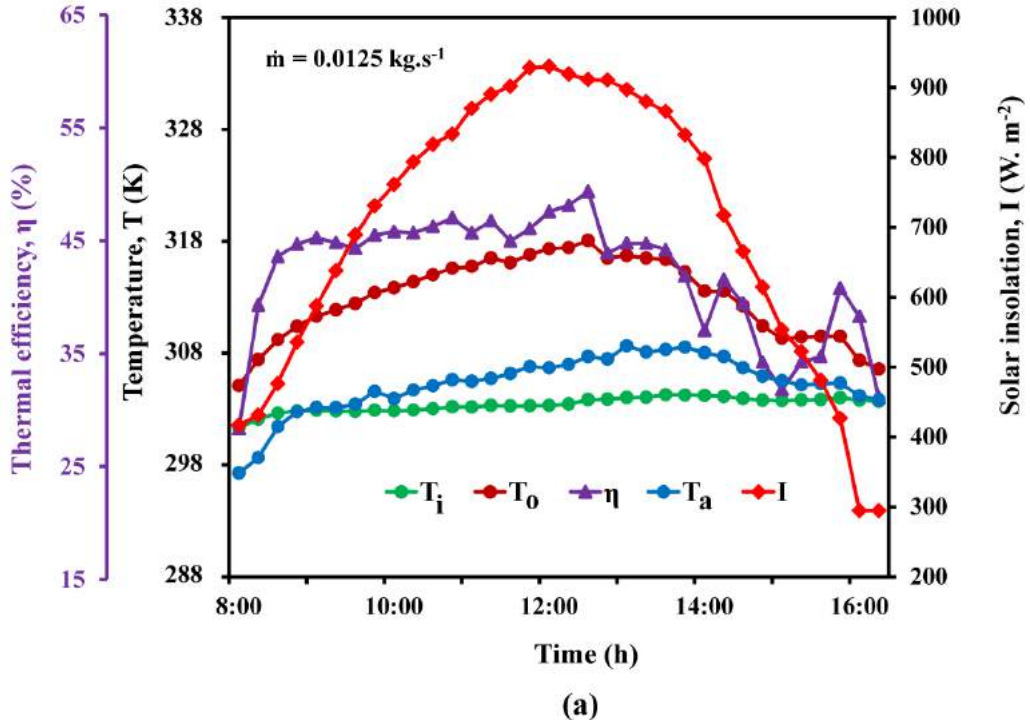

(a)

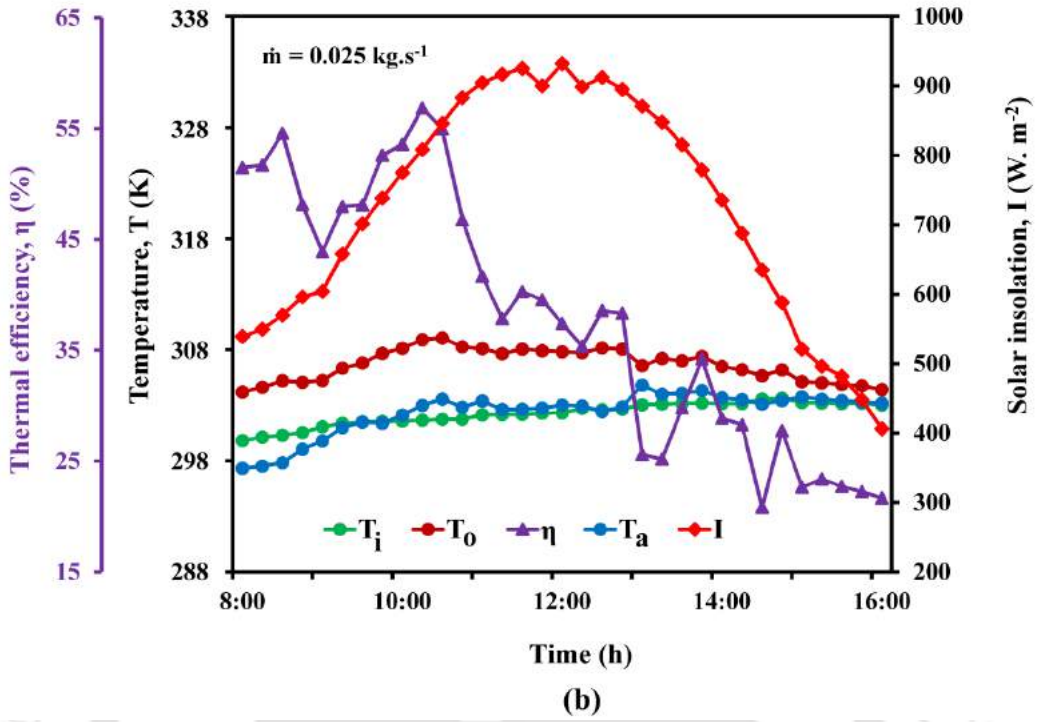

Fig.5.7 The results of straight tube solar water heating system in open loop at flow rate of (a) $\dot{m}$ = 0.0125 kg.s^{-1} and (b)$\dot{m}$ = 0.025 kg.s^{-1}

5.4.5 Thermal efficiency of the straight tube collector in closed loop system

Following the closed-loop experimental procedure presented in Chapter 4, the measured value of ambient temperature, inlet water temperature, outlet water temperature, thermal efficiency and solar insolation at flow rate of 0.0125 kg.s^{-1} are depicted in Fig. 5.8.

The solar insolation received on the collector surface showed a parabolic path with its peak value attained during the mid-day and later it decreases as the time increases. The solar insolation was found to be increasing in the morning, reaching its maximum value of 928 W.m^{-2} at 12:30 h. The ambient temperature increases from 8:00 h and reaches a maximum value at 14:00 h. Likewise, inlet water temperature increased from 297 K morning and reaches a peak value of 320.8 K at 16:00 h. The outlet water temperatures increased slowly from 8:00 h to 10:00 h because of the lower solar insolation and ambient temperature. Both the inlet and outlet water temperature increased almost linearly from 10:00 h to 15:00 h and followed the same trend. After 15:00 h, the outlet water temperature decreased due

to the decreasing solar insolation, ambient temperature and increasing of inlet water temperature. This is mainly by the increasing of energy loss from the solar heating system at higher inlet water temperature. Peak outlet water temperature of 323.8 K and inlet water temperature of 320.8 K were also observed.

Similarly, the peak thermal efficiency observed at 11:40 h was 59% and decreased after 14:00 h. This was expected since the change in water temperature decreased due to the decrease in solar insolation. After 16:00 h, change in water temperature was close to zero because of lower solar insolation thereby reducing the thermal efficiency.

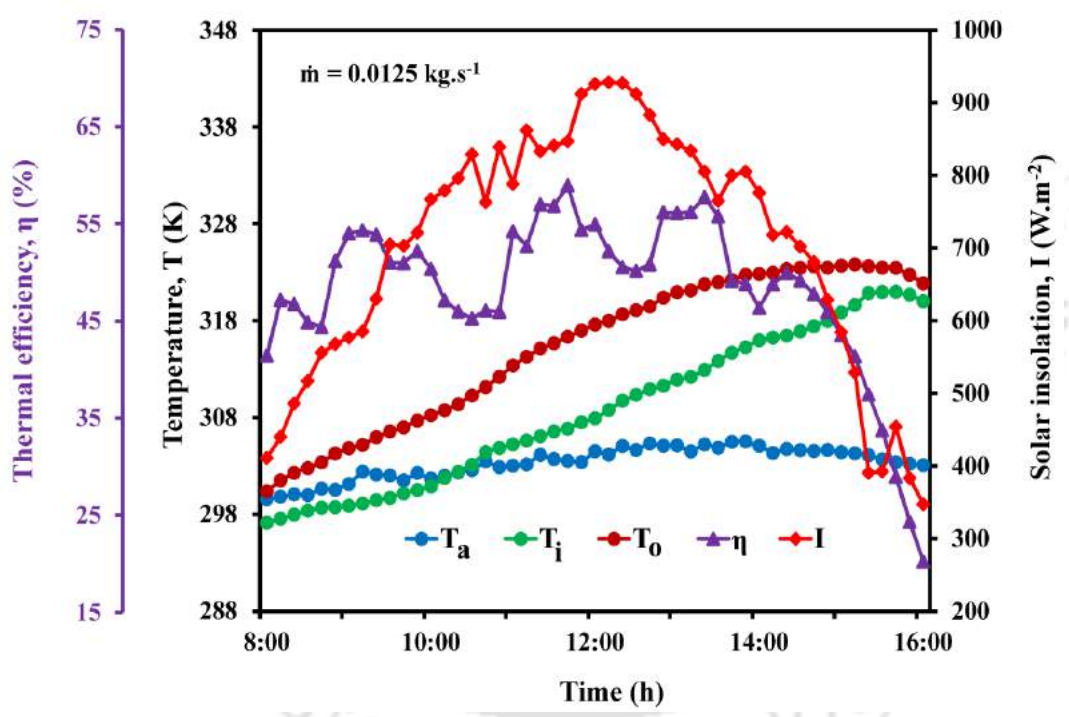

Fig.5.8 The results of straight tube solar water heating system in close loop

5.4.6 Exergy efficiency for straight tube collector in closed loop system

The formulation described in subsection 3.2.5 was used to plot the exergy efficiency variation considering inflow exergy, outflow exergy and destructed exergy. The variation in the exergy efficiency of the straight tube solar water heater at flow rate of 0.0125 $kg.s^{-1}$ depicted in Fig.5.9. The measured input parameters, *viz.*, ambient temperature, inlet water temperature, solar insolation and outlet water temperature

used for plotting the exergy efficiency was taken from Fig.5.8. The figure indicates an average exergy efficiency of 3.6% for the above-mentioned flow rate. Gunerhan and Hepbasli (2007) reported almost similar value using two meter square solar collector.

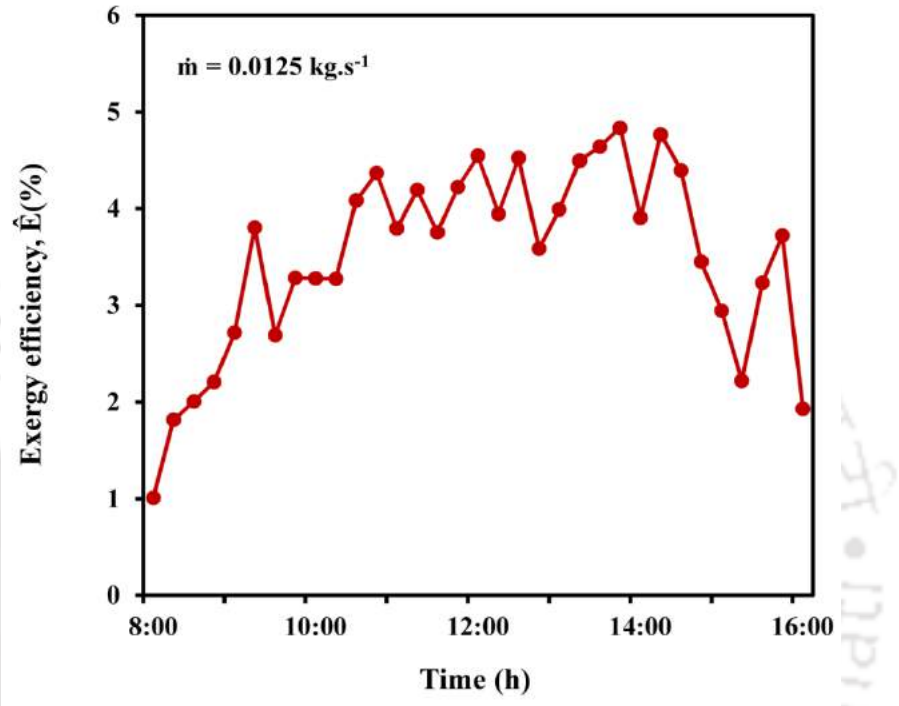

Fig.5.9 Variation of exergy efficiency versus time using straight tube collector

5.5 Measured Input Parameters Using Bent Tube Collector

Similar to straight tube collector, the measured experimental data obtained from bent tube collector used as the input parameters for computational model. Figures 5.10 (a), (b), and (c) illustrate the hourly variation of the measured solar insolation, inlet water temperature and ambient temperature at flow rates of 0.0083 $kg.s^{-1}$, 0.016 $kg.s^{-1}$, and 0.021 $kg.s^{-1}$, respectively. The figure shows that the average solar insolation increases from 8:00 h and reaches a maximum value in between 11:00 h and 12:00 h. The ambient and inlet water temperatures increases from 8:00 h and reaches the maximum value during mid-day. Further, the maximum inlet water temperature was noticed at lower flow rate as compared to higher flow rate. Experiments carried out beyond 16:00 h resulted in a decrease in solar insolation, ambient and inlet water temperatures.

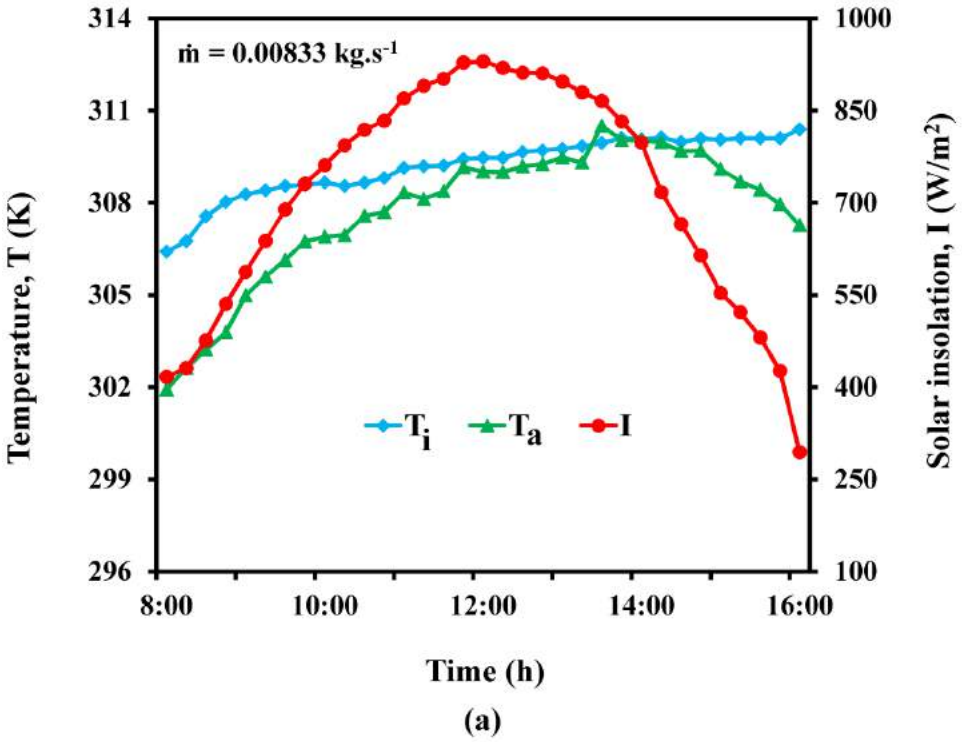

(a)

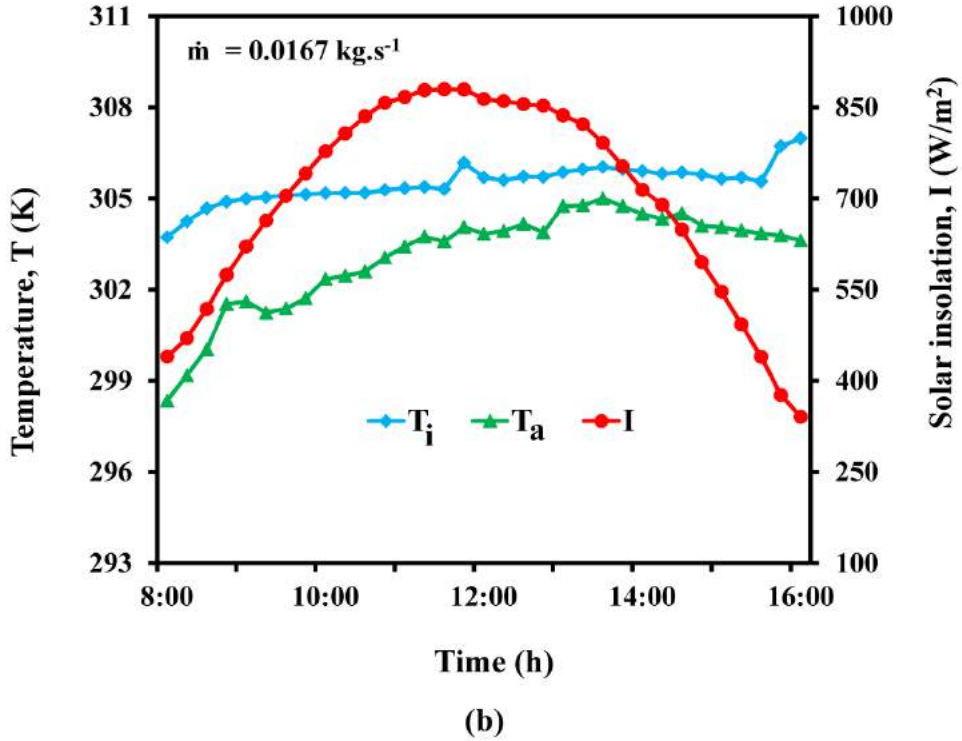

(b)

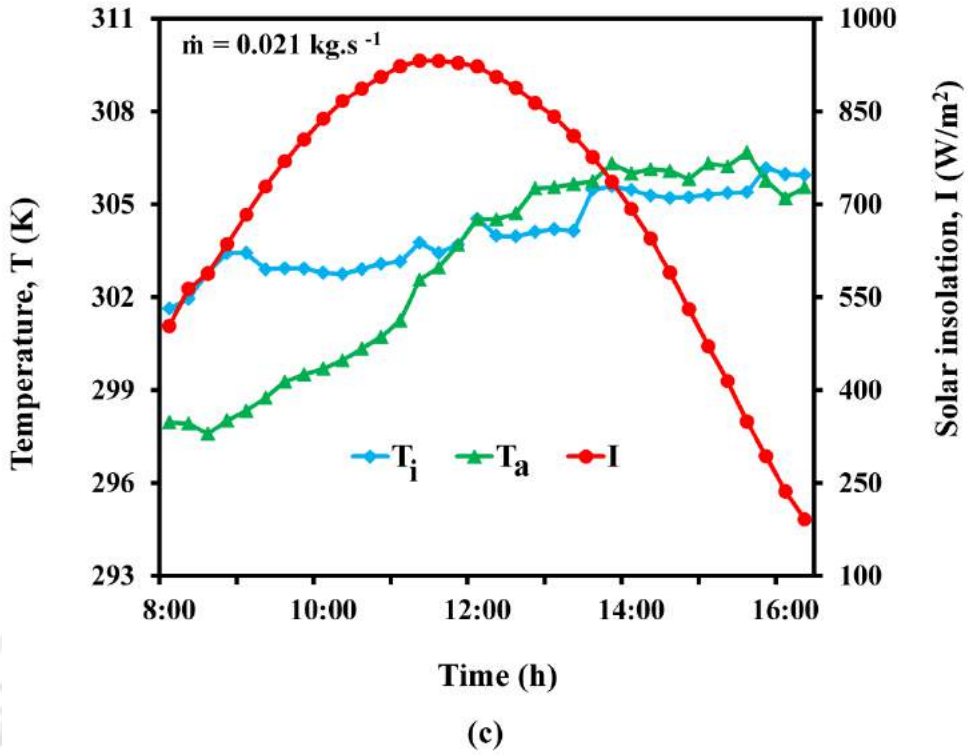

(c)

Fig.5.10 Variation of inlet water temperature, ambient temperature and solar insolation versus time at flow rate of (a) $\dot{m}$ = 0.0083 kg.s^{-1} (b) $\dot{m}$ = 0.0167 kg.s^{-1} and (c) $\dot{m}$ = 0.021 kg.s^{-1}

5.6 Model Validation Using Bent Tube Collector

5.6.1 Temperature distribution of the bent tube collector

Variation of simulated CFD results of the outlet water temperatures along the bent tube at flow rate of 0.0083 kg.s^{-1} is depicted in Fig.5.11. The variations of water temperature along the length of the bent tube at 12:00 h shown in Fig.5.11 indicate higher water outlet temperatures at the upper portion of the tube compared to the lower portion. Since the entry of the fluid is at the lower portion of the collector, the temperature at the upper portion was higher compared to the lower portion of the collector.

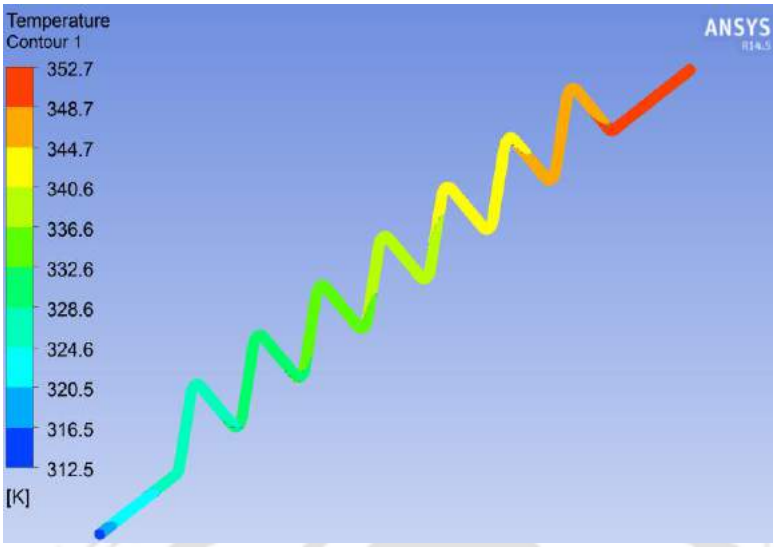

Fig.5.11 Variation of water temperature along the tube interface at 12.00 h

Figure 5.12 presents the variation of temperature across the outlet tube diameter at 12:00 h. Since almost half of the tube side was brazed with the hot absorber plate, the water temperature at the centre of the tube was 6 K lower than at the surface. The heat transfer was taking place by a sequence of radiation, conduction through the tube thickness followed by convection inside the tube. Due to this, it takes more time for the heat to reach the centre of the tube by convection.

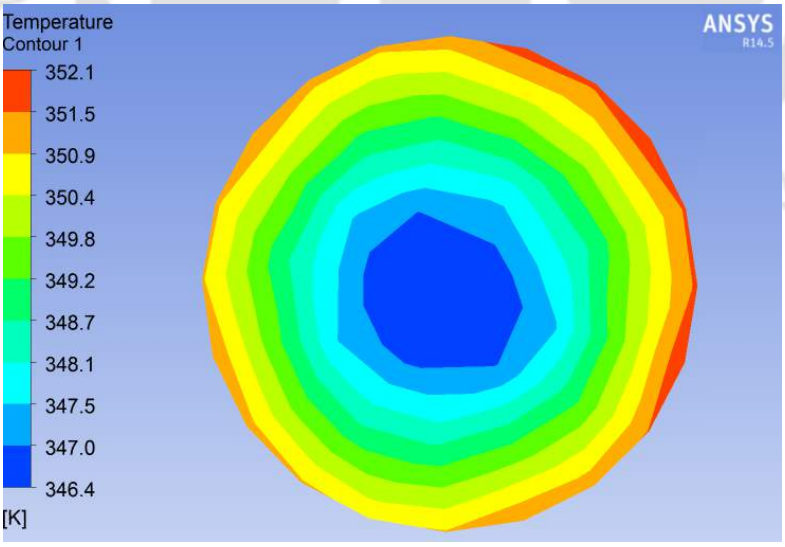

Fig.5.12 Variation of water temperature at the outlet pipe at 12.00 h

Figure 5.13 depicts the variation of absorber plate temperature at 12:00 h. Variation of temperature across the absorber plate length indicates a difference of 38 K between the inlet side and outlet side of the plate. Heat is absorbed by the cold fluid flowing through the riser tube. Since the riser tube is in contact with the absorber at the mid-width section, there is a variation of around 6 K across the plate width.

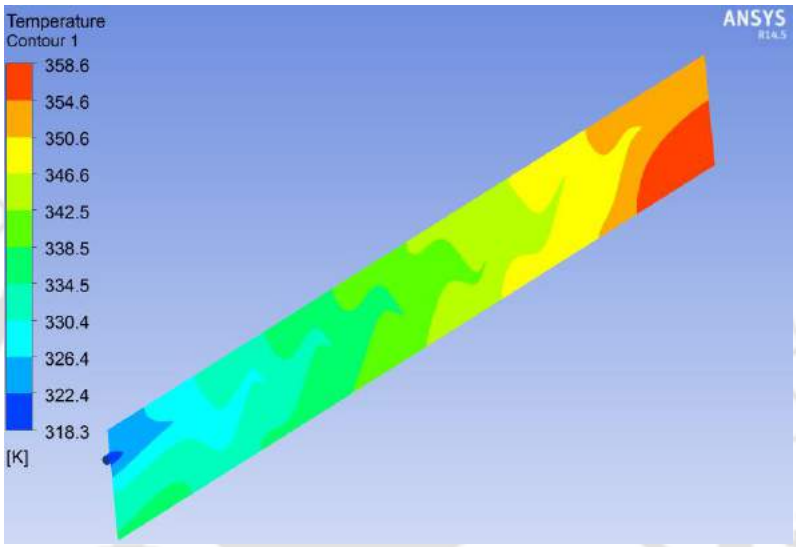

Fig.5.13 Variation of absorber plate temperature at 12.00 h

5.6.2 Comparison between experimental and predicted outlet water temperature

The comparison of predicted and experimental outlet water temperature versus time at flow rates of 0.0083 $kg.s^{-1}$, 0.0167 $kg.s^{-1}$, and 0.021 $kg.s^{-1}$ shown in Figs. 5.14 (a), (b) and (c), respectively. The experimental and simulated results reveal that the outlet water temperature is higher at lower flow rate compared to at higher flow rates. Though the simulation outlet water temperature is always higher than the experimental values, the trend in the variation with time is similar. The comparison of the result shows that both experimental and simulated result followed the same pattern with a maximum error deviation of 3.5%, 3.1% and 4.8% at flow rates of 0.0083 $kg.s^{-1}$, 0.0167 $kg.s^{-1}$, and 0.021 $kg.s^{-1}$, respectively. The maximum experimental outlet water temperature of 332 K at flow rate of 0.0083 $kg.s^{-1}$ and the minimum temperature of 319 K at 0.021 $kg.s^{-1}$ were observed.

Further, the figure also illustrates that the outlet water temperature increment obtained from the experiments is lower compared to the simulated result at higher solar insolation.

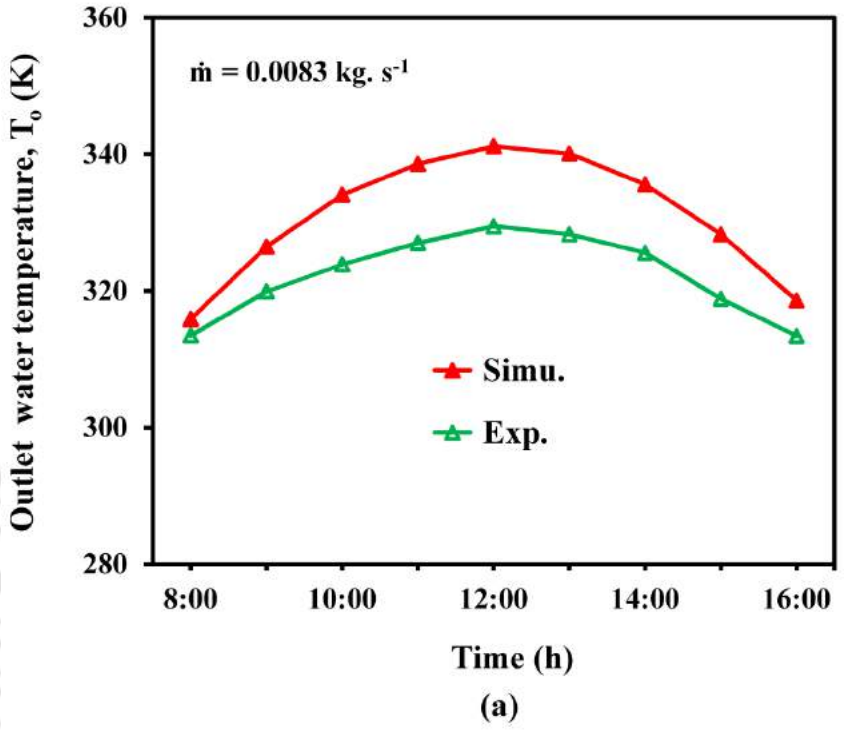

(a)

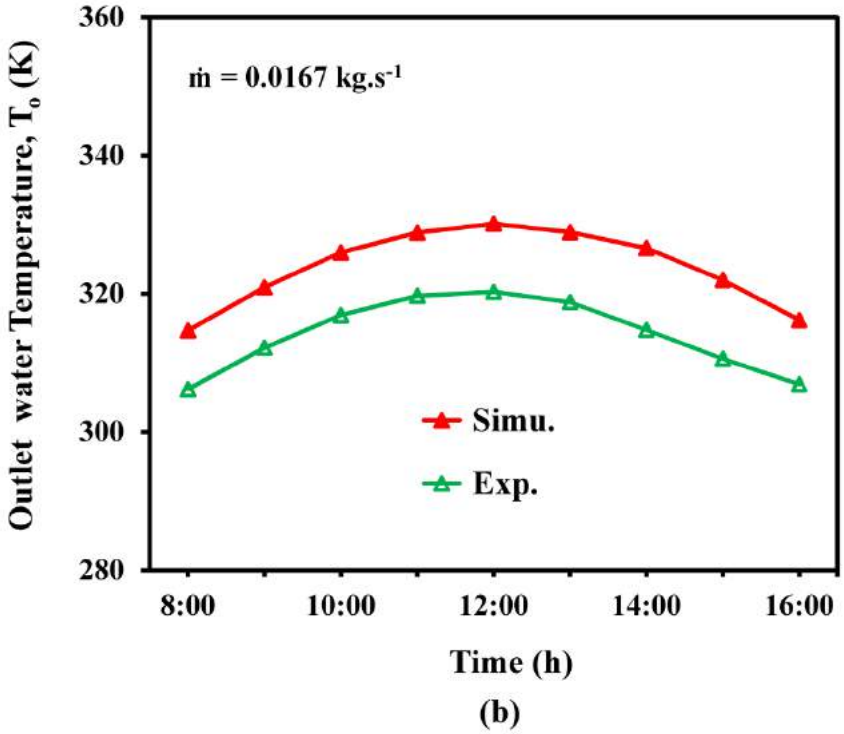

(b)

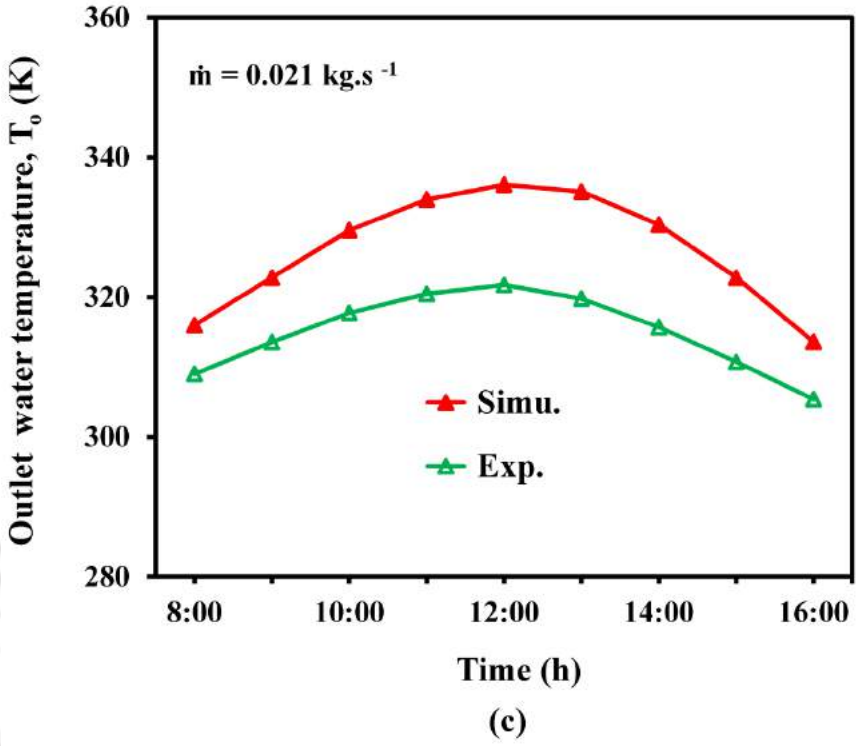

Fig.5.14 Variation of predicted and experimental outlet water temperature versus time at flow rates of (a) $\dot{m}$= 0.0083 kg.s^{-1}, (b)$\dot{m}$= 0.0167 kg.s^{-1} and (c) $\dot{m}$ = 0.021 kg.s^{-1}

Accordingly, the error values at peak solar insolation were maximum. During the experiments, since the result was influenced by the weather conditions, accurate estimation of convective heat loss coefficient along the day was not possible. Hence, for the simulation purpose, the average value of the convective heat transfer coefficient was considered for the entire day. Therefore, the error value during the peak solar insolation was found to be highest for all the cases.

5.6.3 Comparison between experimental and predicted absorber plate temperature

The variation of experimental and simulation results of plate temperature versus time for the bent tube collector at flow rates of 0.0083 kg.s^{-1}, 0.0167 kg.s^{-1}, and 0.021kg.s^{-1} are depicted in Figs. 5.15 (a), (b) and (c), respectively.

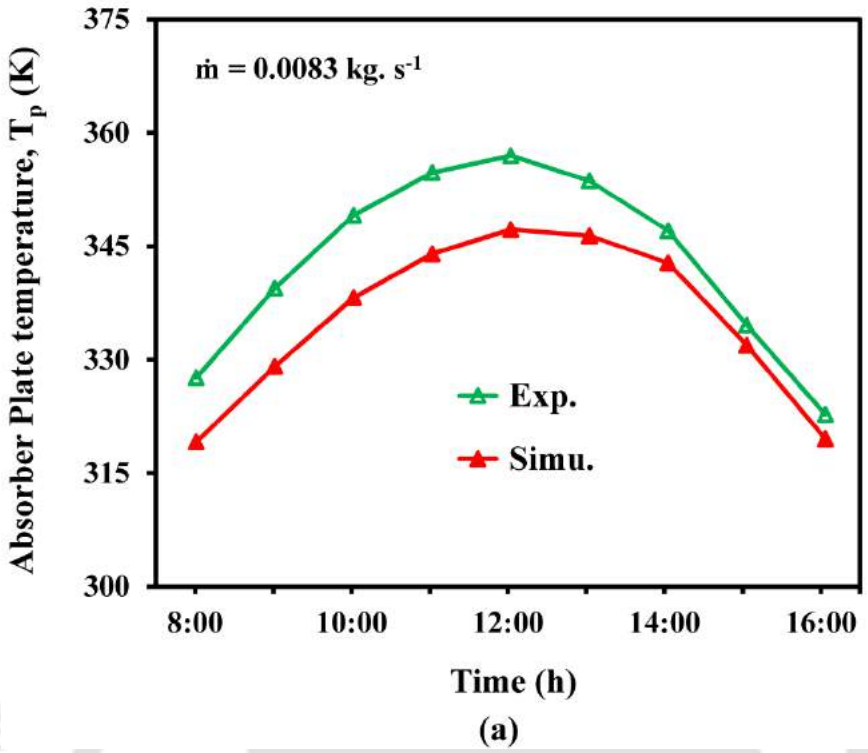

(a)

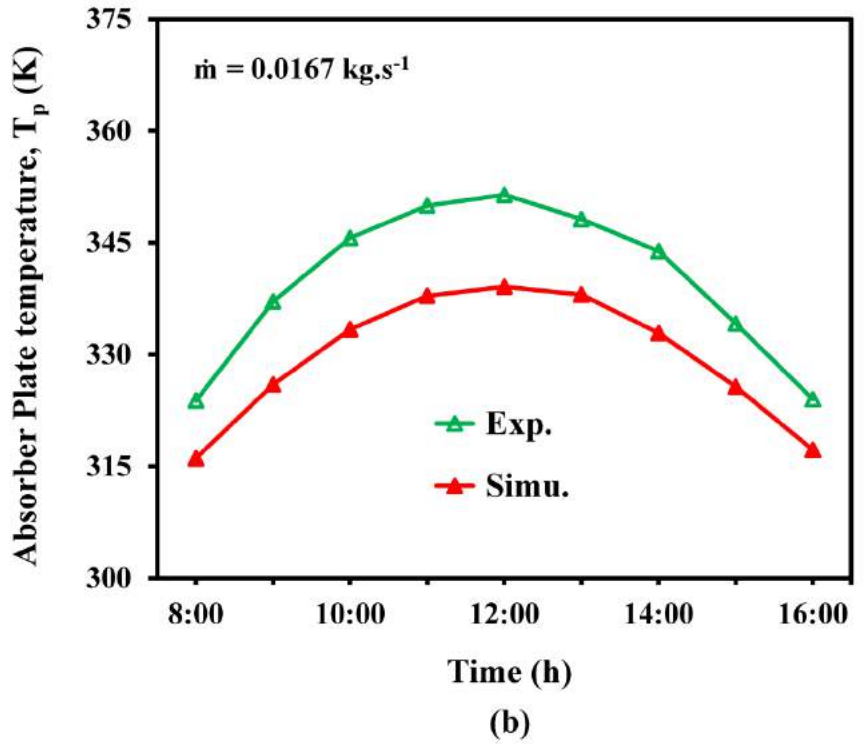

(b)

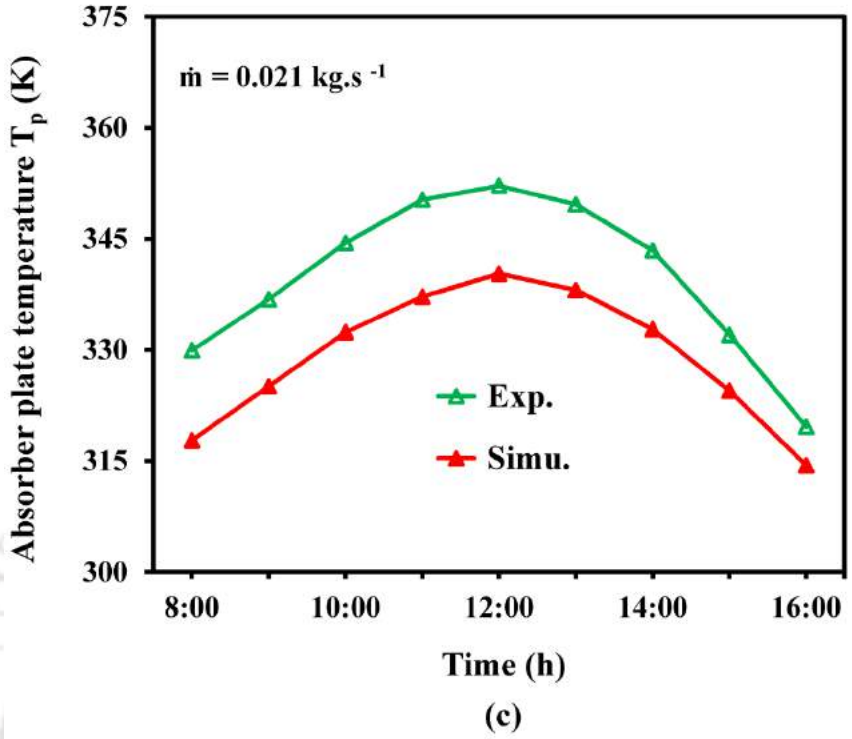

Fig.5.15 Variation of predicted and experimental absorber plate temperature versus time at flow rate of (a) $\dot{m}$ = 0.0083kg.s^{-1}, (b)$\dot{m}$ = 0.0167 kg.s^{-1} and (c) $\dot{m}$= 0.021 kg.s^{-1}

The experimental result indicates a continuous increase in the plate temperature from 8:00 h. The temperature reaches maximum value at 12:00 h beyond which it starts decreasing for all investigated flow rates. The maximum experimental absorber plate temperature of 356 K at a flow rate of 0.0083 kg.s^{-1} and the minimum temperature of 347 K at flow rate of 0.021 kg.s^{-1} were observed. For all investigated flow conditions, the experimental values of the plate temperature were higher than simulated values with maximum deviation error ≤ 4%. This is mainly due to the assumption that perfect contact was maintained between the plate and the tube leading to the higher heat transfer rate from plate to the fluid compared to the experimental conditions.

5.6.4 Thermal efficiency of the bent tube collector in closed loop system

The measured experimental results of inlet water temperature, outlet water temperature, thermal efficiency and solar insolation of the bent tube solar collector are depicted in Fig.5.16.

The solar insolation received on the collector surface varied parabolically with a maximum value of 864 W.m^{-2}at 12:00 h. The solar insolation decreased with further elapse of time. The inlet and outlet water temperatures increased from 8:00 h to 16:00 h. The inlet water temperature increased continuously from 301.8 K in the morning to 326.2 K. Likewise, the outlet water temperature increased from 308.1 K to 334.8 K. Moreover, both the inlet and outlet water temperatures increased almost linearly and followed the same trend. The peak solar thermal efficiency of 71% was achieved at around 10:30 h.

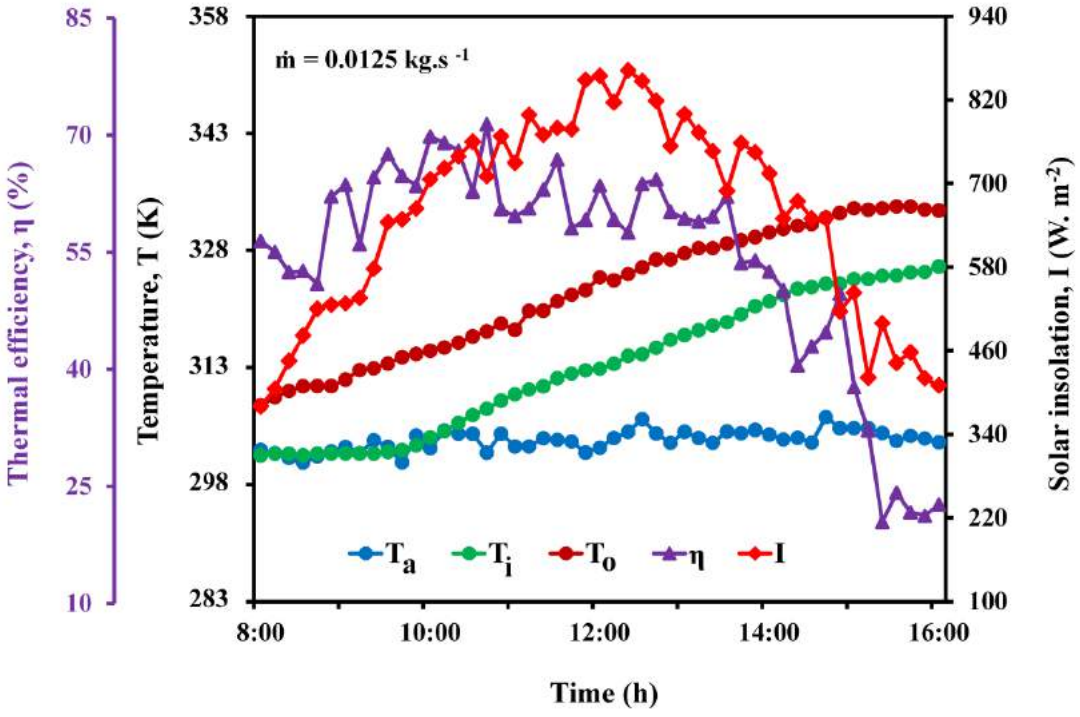

Fig.5.16 The results of bent tube solar water heating system in close loop

5.6.5 Exergy efficiency of the bent tube collector in closed loop system

Figure 5.17 elaborates the variation of exergy efficiency versus time at a flow rate of 0.0125 kg.s^{-1}. The input data used for the exergy efficiency of the bent tube collector is plotted in Fig 5.16. The result indicates that the exergy efficiency increases from 2% at 8:00 h and reaches maximum value of 5.6% at 13:15 h and then decreases as the solar insolation decreases. The exergy efficiency obtained from the bent tube

collector was 1.2 times higher than that of straight tube collector reported by Gunerhan and Hepbasli (2007).

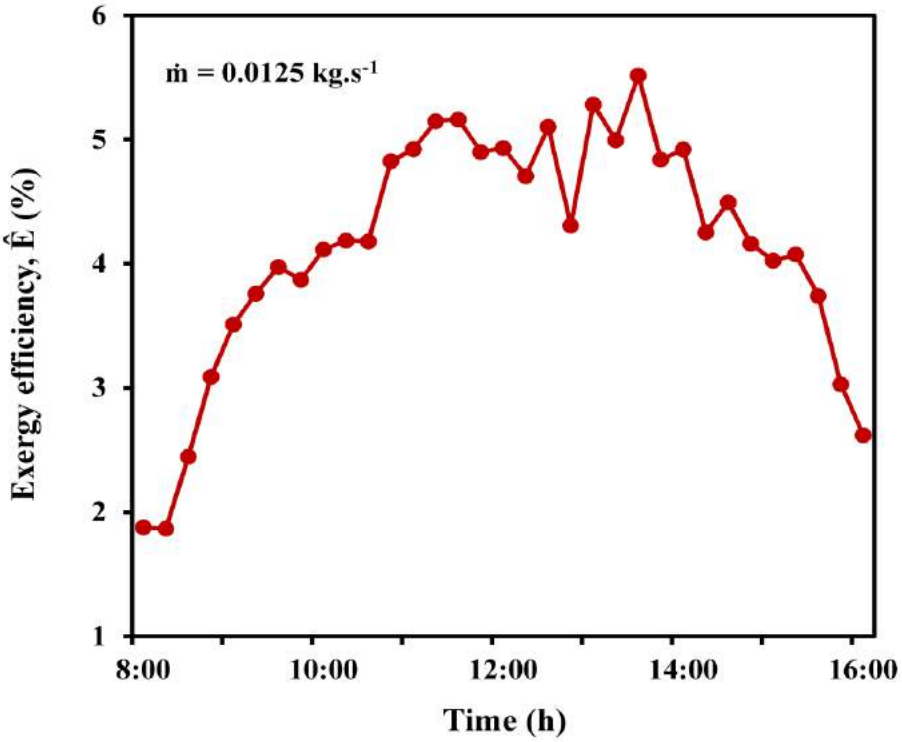

Fig.5.17 Variation of exergy efficiency versus time

5.7 Comparison of Straight and Bent Tube Solar Collectors

5.7.1 Measured input parameters

The outlet water and absorber plate temperature was predicted using the data of solar insolation, ambient temperature and inlet water temperature given in Table 5.1 and 5.2 as input parameter. The validations between simulation and experimental results of outlet water and absorber plate temperature for the two solar collectors are presented briefly in subsection 5.7.2 and 5.7.3.It is observed from the table that the average solar insolation increases from 8:00 h and reaches maximum value in between 11:00 h and 12:00 h. The inlet water temperature variation was high at low flow rates compared to that at high flow rates. Beyond 16:00 h, the solar insolation, ambient temperature, and inlet water temperature observed to below.

Table - 5.1 Result of experimental values used for simulation

Time (h)	Mass flow rate of 0.0083 kg.s^{-1}			Mass flow rate of 0.016 kg.s^{-1}		
	Solar insolation I (W.m^{-2})	Ambient temperature T_a (K)	Inlet water temperature T_i (K)	Solar insolation I (W.m^{-2})	Ambient temperature T_a (K)	Inlet water temperature T_i (K)
8:00	417.1	301.9	303.4	440.2	298.4	303.7
9:00	580.2	304.9	306.2	621.5	301.6	305.1
10:00	757.1	306.8	308.6	778.3	302.3	305.2
11:00	864.1	308.2	310.9	867.4	303.4	305.3
12:00	930.8	309.1	313.5	863.9	303.8	305.7
13:00	899.8	309.4	310.7	837.3	304.7	305.8
14:00	805.7	309.9	310.1	714.5	304.5	305.9
15:00	562.4	309.1	310.1	547.2	304.1	305.6
16:00	316.4	307.3	310.3	326.7	303.6	306.7

Table- 5.2 Result of experimental values used for simulation

Time (h)	Mass flow rate of 0.021 kg.s^{-1}			Mass flow rate of 0.025 kg.s^{-1}		
	Solar insolation I (W.m^{-2})	Ambient temperature T_a (K)	Inlet water temperature T_i (K)	Solar insolation I (W.m^{-2})	Ambient temperature T_a (K)	Inlet water temperature T_i (K)
8:00	503.8	297.9	301.6	480.3	296.2	299.9
9:00	684.9	298.3	303.4	658.1	297.9	301.9
10:00	838.1	299.7	302.8	808.5	300.6	302.9
11:00	923.2	301.2	303.2	916.7	303.9	302.5
12:00	922.7	304.5	304.5	928.7	305.7	302.9
13:00	841.9	305.5	304.2	848.1	306.9	304.1
14:00	692.3	306.1	305.5	687.9	307.1	304.3
15:00	470.9	306.3	305.3	474.9	306.7	305.2
16:00	238.2	305.2	306.1	435.2	306.4	305.7

5.7.2 Comparison study using outlet water temperature

Figure 5.18 presents the experimental and numerical results of the variations of outlet water temperature (T_o) versus time for bent and straight tube solar collectors at mass flow rates of 0.0083 kg.s^{-1}, 0.0167 kg.s^{-1}, 0.021 kg.s^{-1} and 0.025 kg.s^{-1}, respectively.

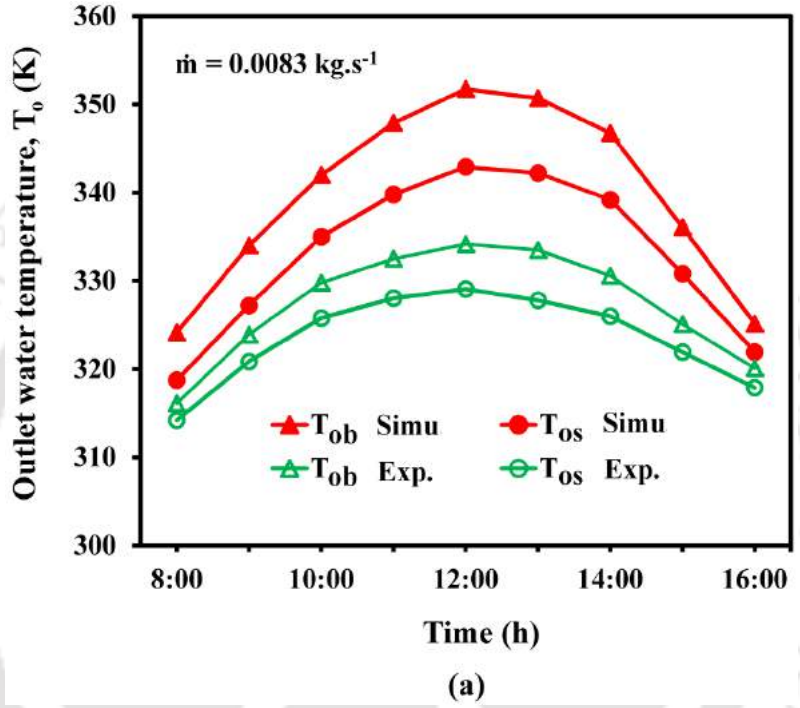

(a)

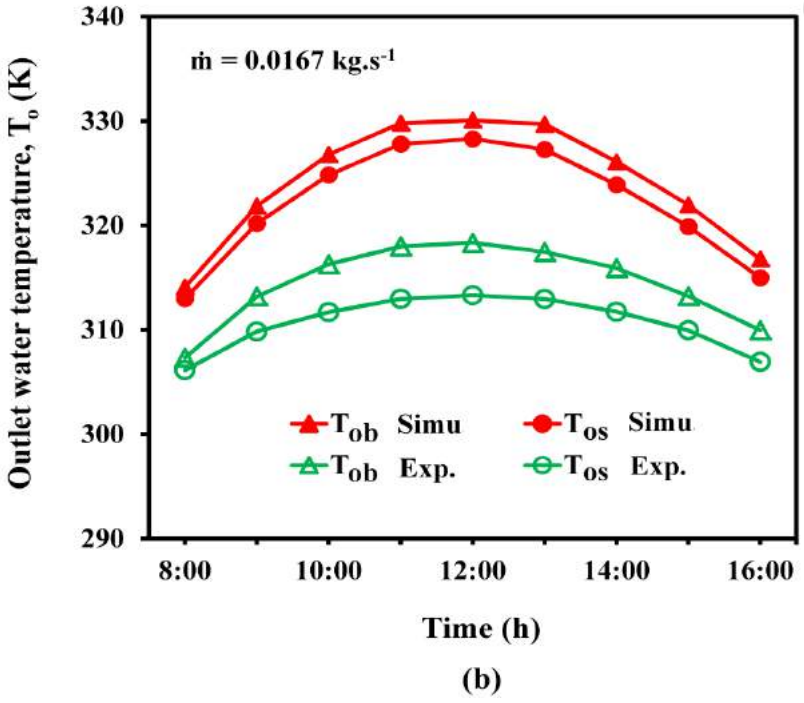

(b)

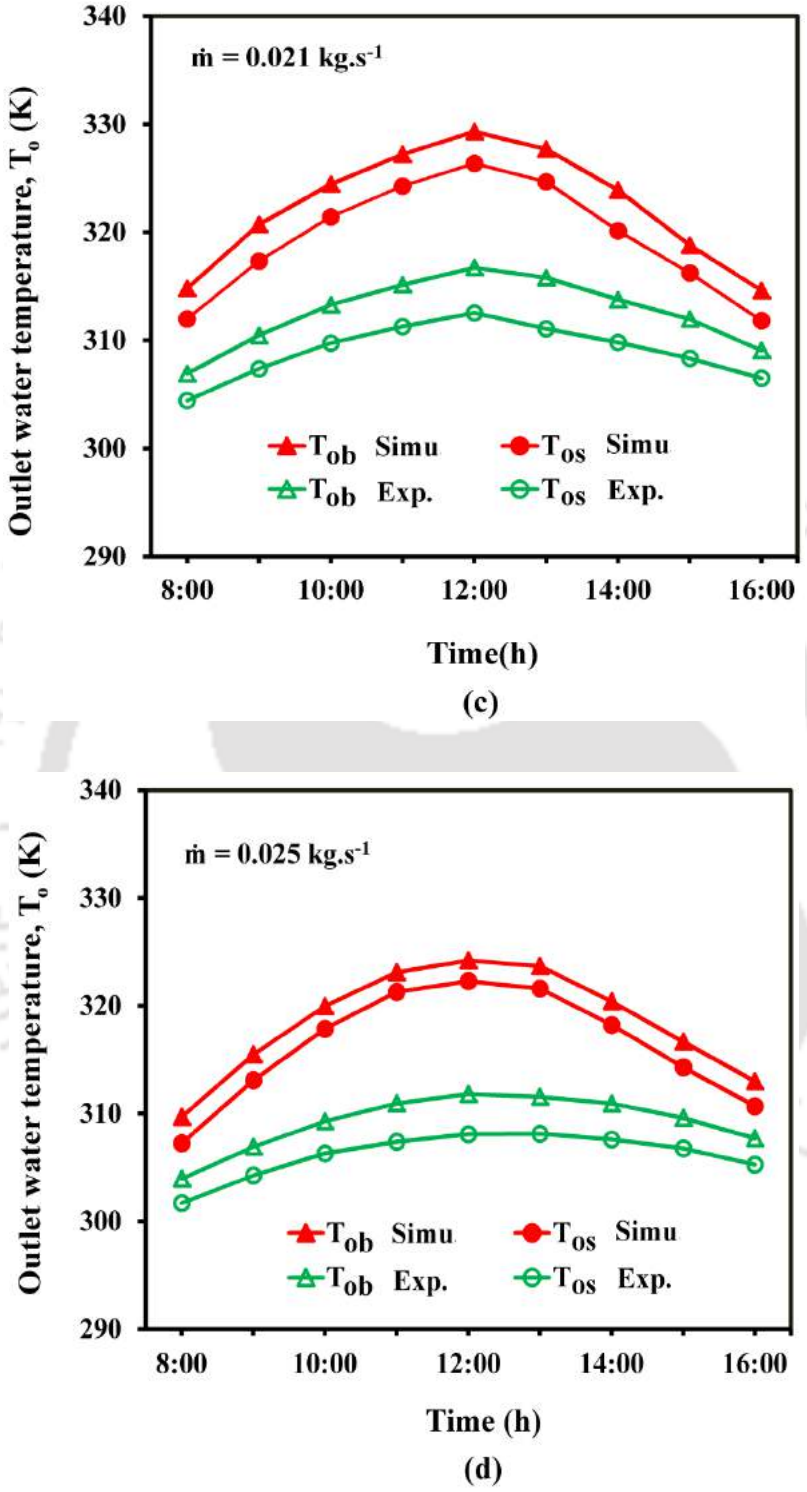

Fig.5.18 Variation of predicted and experimental outlet temperature versus time at flow rate of (a) $\dot{m}$ = 0.0083 kg.s^{-1}, (b) $\dot{m}$ = 0.0167 kg.s^{-1} (c) $\dot{m}$ = 0.021 kg.s^{-1} and (d) $\dot{m}$ = 0.025 kg.s^{-1}

The suffix (s) and (b) shown in the figure indicate the straight tube and bent tube collector, respectively. The experimental and simulation results reveal that the outlet water temperature was higher for both bent and straight tube water heating system at lower flow rate compared to that of higher flow rates. It is also seen from the figure that the simulated outlet water temperature was always higher than the experimental values. The maximum error deviation for straight tube collector was 4.0%, 3.9%, 4.24% and 4.3% at flow rate of 0.0083 $kg.s^{-1}$, 0.0167 $kg.s^{-1}$, 0.021 $kg.s^{-1}$ and 0.025 $kg.s^{-1}$, respectively. The respective values for the bent tube collector were 4.8%, 4.5%, 4.27% and 4.7% for the above-mentioned flow rate. The developed model predicted the outlet water temperature within a maximum error of 5% deviation. The maximum experimental outlet water temperature for bent tube collector of 334 K at a flow rate of 0.0083 $kg.s^{-1}$ and the minimum temperature of 311 K at 0.025 $kg.s^{-1}$ were observed. Similarly, for the above-mentioned flow rates, the maximum and minimum outlet water temperature from the straight tube collector was found to be 326 K and 306 K, respectively.

Further, the outlet water temperature increments obtained from the experiments are lower compared to the simulation results at higher solar insolation. Thus, the error values at peak solar insolation were maximum. Generally, from the experimental as well as numerical study it can be concluded that the outlet water temperature of the bent tube collector is always higher than straight tube collector for all flow rates.

5.7.3 Comparison study using absorber plate temperature

Figure 5.19 shows the variation of experimental and numerical values of plate temperature versus time for the bent tube and straight tube solar collectors at different flow rates. The figure indicates a continuous increase in plate temperature from 8:00 h and reaches the maximum at 12:00 h beyond which it starts decreasing for all investigated flow rates. The experimental value of the plate temperature was higher than the simulation value at lower flow rate compared to that at higher flow rates. At lower flow rate, the flow is laminar and uniform temperature distribution across the plate exists. Due to this, the heat transfer rate from the plate to the fluid is lower resulting in higher plate temperature compared to the simulation values.

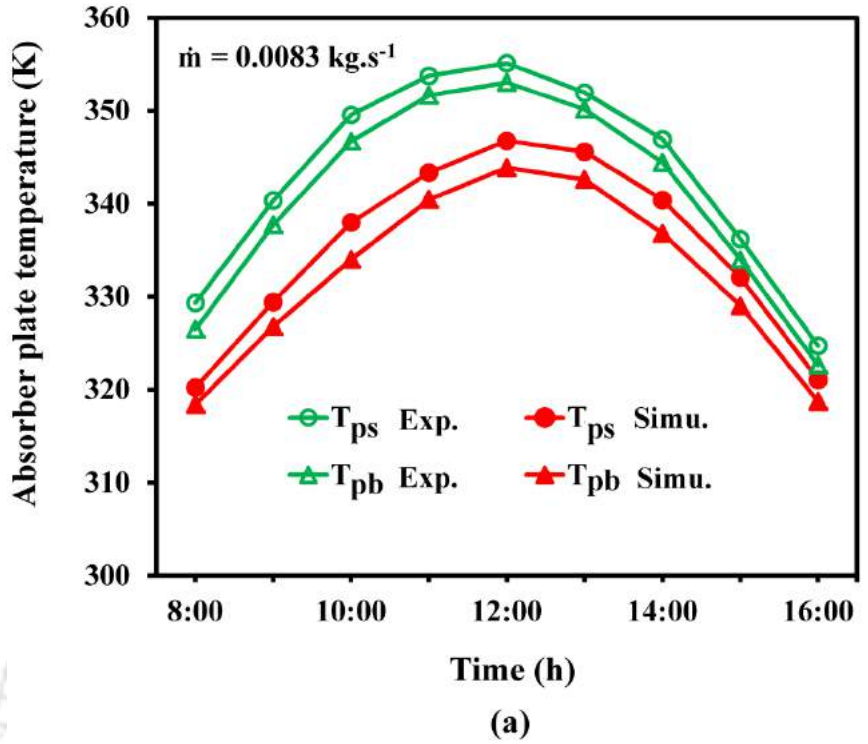

(a)

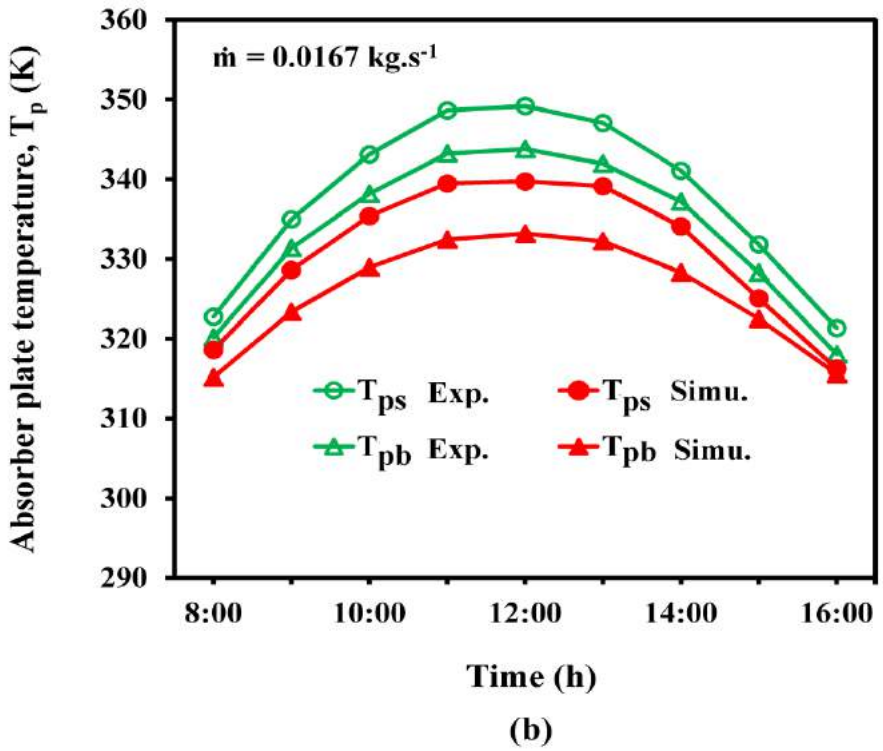

(b)

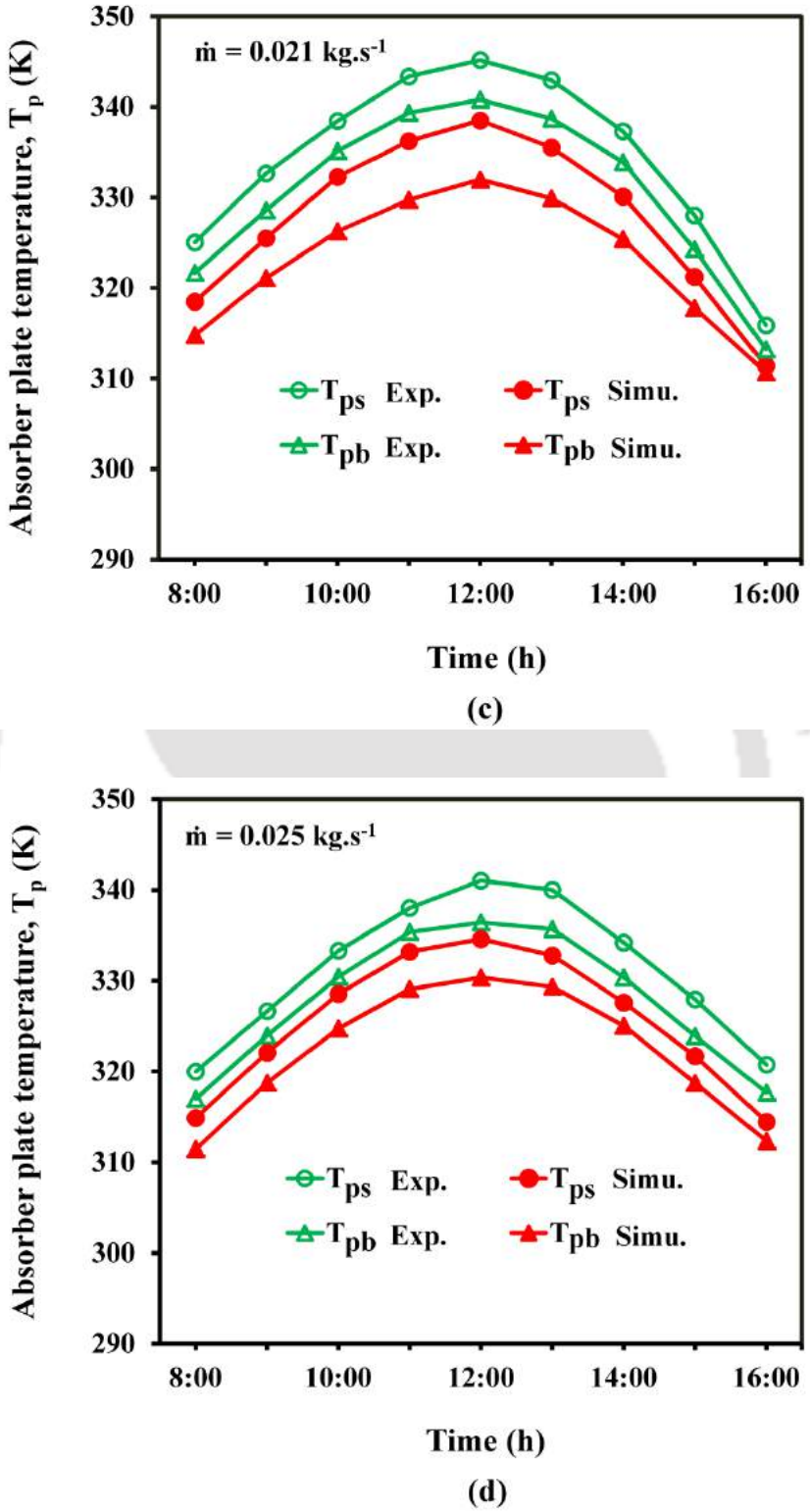

Fig.5.19 Variation of predicted and experimental plate temperature versus time at flow rates of (a) $\dot{m}$ = 0.0083 kg.s^{-1}, (b) $\dot{m}$ = 0.0167 kg.s^{-1} (c) $\dot{m}$ = 0.021 kg.s^{-1} and (d) $\dot{m}$ = 0.025 kg.s^{-1}

The contact area between the absorber plate and the tube is lower for the straight tube collector resulting in lower heat transfer rate between the plate and the fluid compared to the bent tube collector. Hence, the absorber plate temperatures of the straight tube collector were found to be higher than the bent tube collector. The maximum experimental absorber plate temperature of 346 K for the straight tube collector and 342 K for the bent tube collector was observed. For all investigated flow conditions, the experimental values of plate temperature were higher than the simulation values with maximum deviation error of less than 3.4% for the two solar collectors.

5.7.4 Comparison study using thermal efficiency in closed loop system

The measured experimental results of inlet water temperature, outlet water temperature, thermal efficiency, and solar insolation of the straight and bent tube solar collectors are depicted in Fig.5.20.

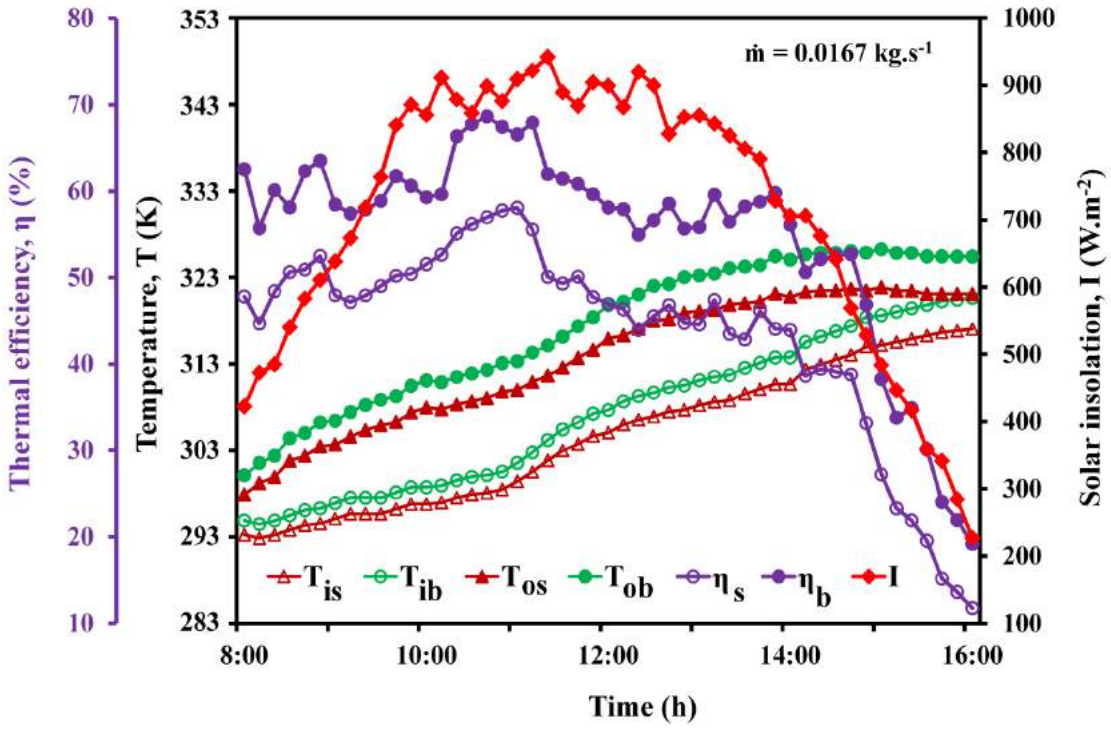

Fig.5.20 The result of bent and straight tube solar heating systems in close loop

The solar insolation received on the collector surface showed a parabolic trend with the maximum value of 942 W.m^{-2}attained at 11:20 h which decreased with further elapse of time. The inlet water temperature of the bent tube and straight tube solar collectors increased continuously from 295.4 K and 293.3 K in the morning to 320.2 K and 317.1 K at 16:00 h, respectively. The outlet water temperature of bent and straight tube collectors increased continuously from 300 K to 326 K and 301 K to 320.8 K, respectively. Further, it was observed that both the inlet and outlet water temperatures increased almost linearly and followed the same trend. The peak solar thermal efficiencies of 69.1% and 57% were achieved at around at 11:30 h for the bent and straight tube solar collectors, respectively.

5.7.5 Comparison of thermal efficiency using ASHRE standard

Figure 5.21 shows the thermal efficiency (η) versus collector loss parameter ((T_m – T_a)/I) plots for the bent and straight tube collectors determined from experimental data.

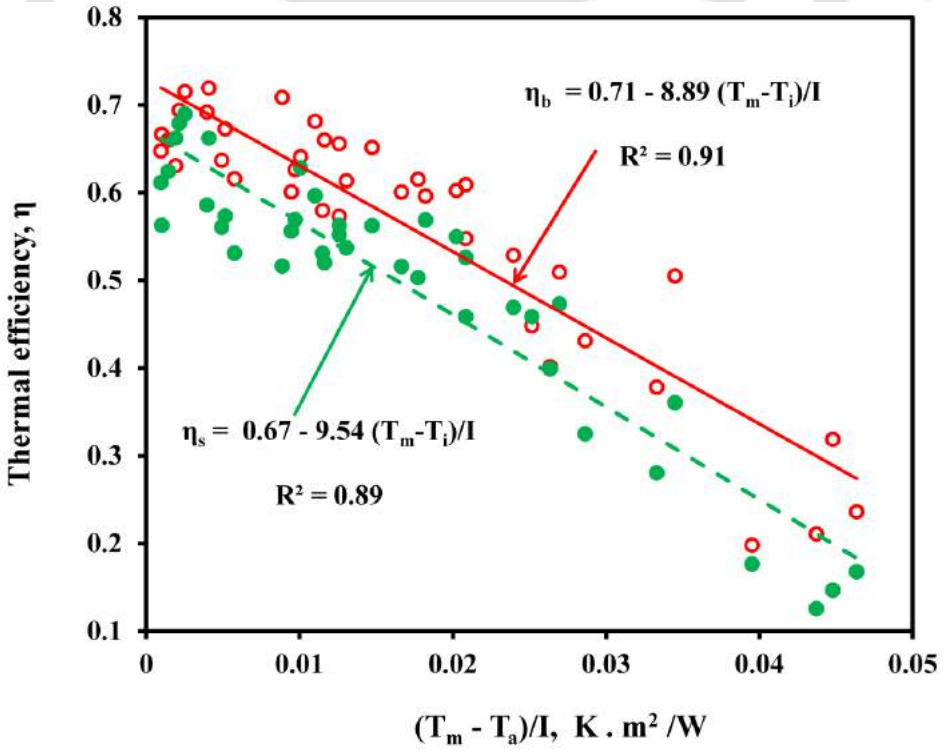

Fig.5.21 Thermal efficiency versus collector loss parameter ((T_m-T_a)/I) for bent (*b*) and straight (*s*) tube solar water heating collector

The thermal efficiency of the solar heating collector depends on mean temperature (T_m) of the water across the collector, ambient temperature and solar insolation. The collector thermal efficiency η was determined using the straight-line relationship (Zhao *et al*. 2010)

$$\eta = \eta_0 - \alpha_0 \frac{(T_m - T_a)}{I} \tag{5.2}$$

where η_0 and α_0 stand for thermal efficiency of collector and slope of loss parameter, respectively. From the intercept and slope of the fitted line, it is evident that higher thermal efficiency is observed by the bent tube collector compared to the straight tube collector.

5.7.6 Comparison study using exergy efficiency

The comparison study between straight and bent tube collectors using exergy efficiency at flow rate of 0.0167 $kg.s^{-1}$ is shown in Fig. 5.22. The input parameters used for plotting the exergy efficiency of both collectors were taken from Fig.5.20.

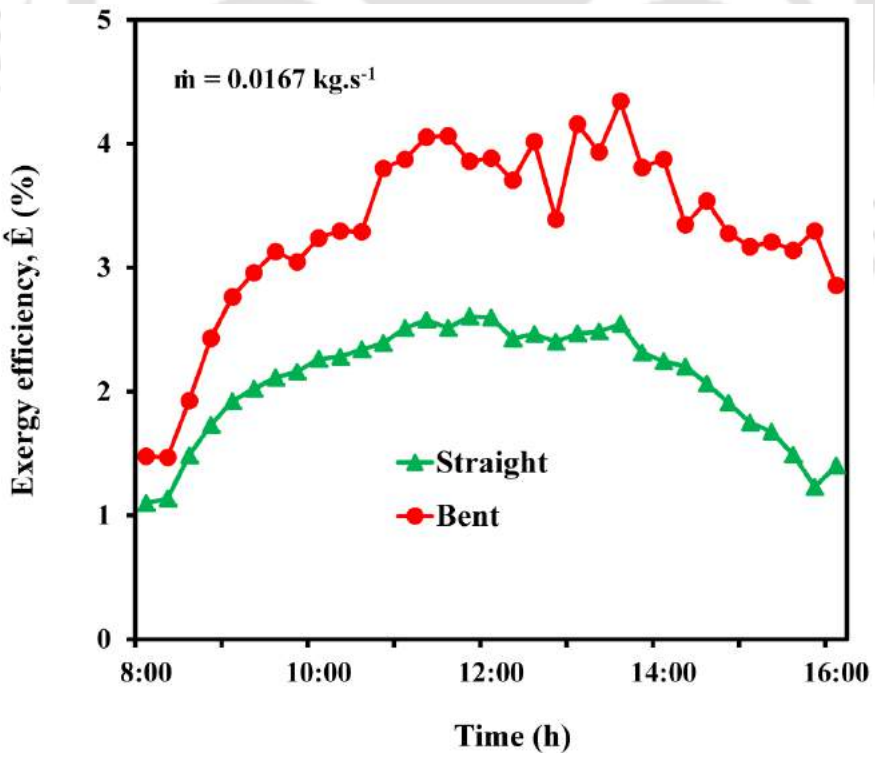

Fig.5.22 Variation of exergy efficiency versus time for straight and bent tube collectors

The exergy efficiencies for both collectors increased from the morning and reached a peak value at the mid-day followed by continues decrease due to decrease in solar insolation. The maximum average exergy efficiency was 3.4% for the bent tube collector whereas it was 2.08% for the straight tube collector.

5.8 Pressure Drop and Pumping Power in Straight and Bent Tube Collector

5.8.1 Variation of pressure drop

Pressure drop inside the solar collector occur due to frictional resistance, joints and buoyancy force. In the present study, the pressure drop is determined considering only frictional resistance and fitting joints. Head loss due to fitting joint was determined during the water flow from lower header to the absorber tube. Head loss due to friction of fluid was determined using Eq. (3.31).The variation of pressure drop versus mass flow rate is depicted in Fig.5.23. It is evident from the figure that increasing the mass flow rate decreased the pressure drop and increased the friction factor. For the investigated flow rates, the pressure drop in bent tube collector was 1.8 times higher than straight tube collector.

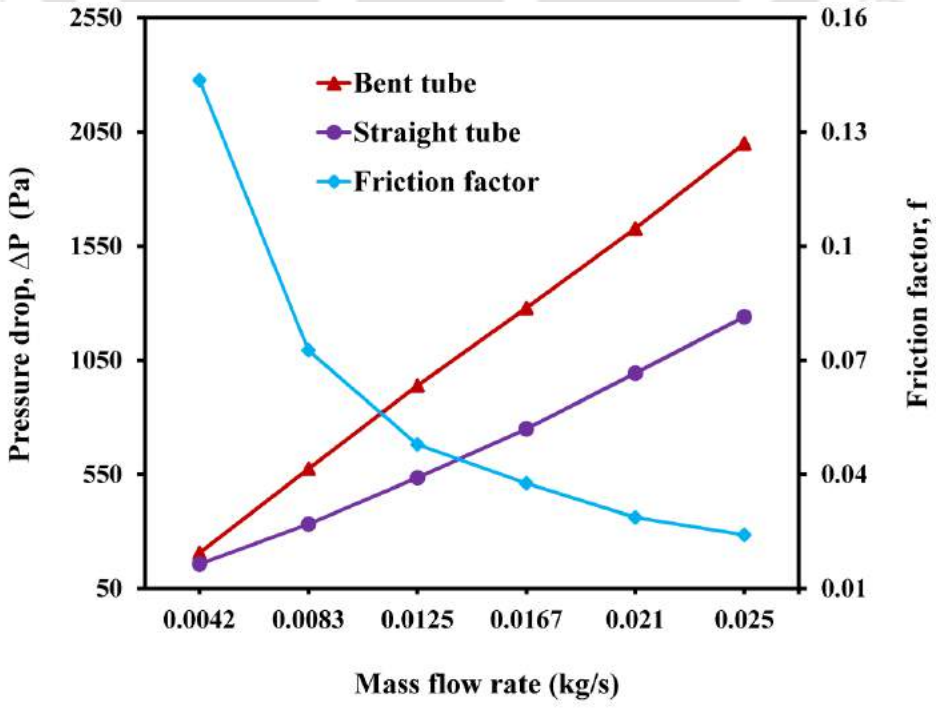

Fig.5.23 Variation of pressure drop and friction factor versus mass flow rate

5.8.2 Variation of pumping power

The pressure drop due to buoyancy force, friction and fitting plays a vital role in determining pumping power. The pumping power was determined using Eq. (3.33). The variation of pumping power versus mass flow rate is depicted in Fig. 5.24.

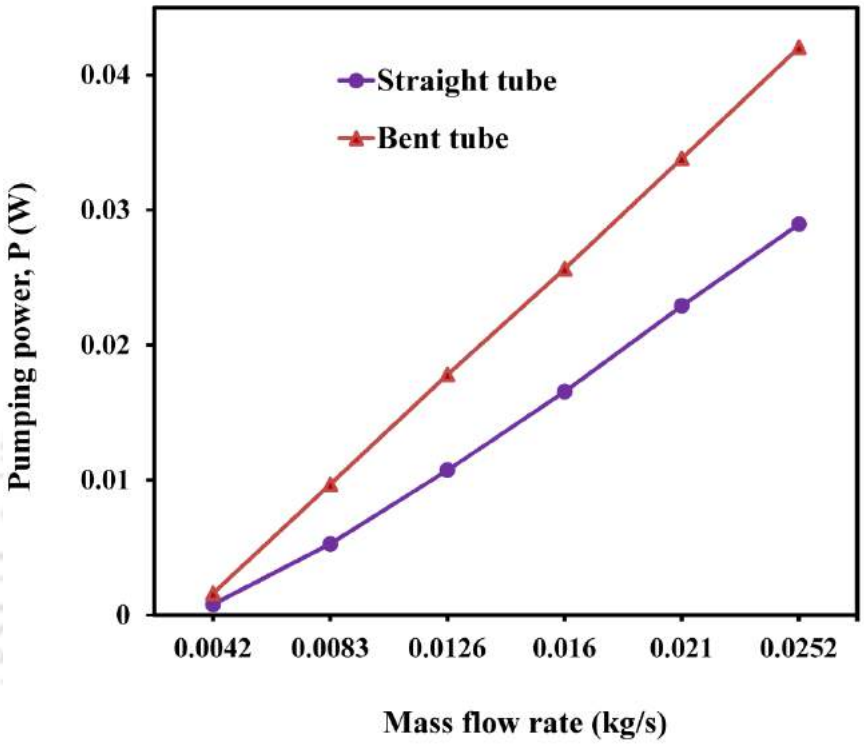

Fig.5.24 Variation of pumping power versus mass flow rate

It can be observed from the figure that for both collectors the pumping power increased with the increase of mass flow rate. The bent tube collector required higher pumping power to circulate the working fluid compared to the straight tube collector. At lowest mass flow rate, the pumping power needed for straight and bent tube collectors were almost similar. Cost required for operating the bent tube solar collector at a mass flow rate of 0.025kg/s was INR ₹1.96 for 8 h operation whereas this cost was INR ₹ 0.96 for straight tube collector. This indicates the bent tube collector required two times higher operating cost than the straight tube collector.

5.9 Cascaded Collector System

5.9.1 Variation in solar insolation and water temperature using cascaded collector

Figure 5.25 (a) and (b) shows the plot for variations in solar insolation, inlet water temperature and outlet water temperature versus time for the cascaded collector at flow rates of 0.0083 kg.s^{-1}and 0.0167 kg.s^{-1}, respectively. The figures indicate a continues increase in the average solar insolation from 8:00 h and attains maximum value around the mid-day. Figure 5.25 (a) indicate a maximum solar insolation of 825 W.m^{-2} whereas for Fig. 5.25 (b) it was 880 W.m^{-2}. The outlet water temperature was minimum in the morning which increased further with the elapse of time. The maximum outlet water temperature of collector-1 (T_{oc1}) was 333 K at flow rate 0.0083 kg.s^{-1} whereas it was 317 K at flow rate of 0.0167 kg.s^{-1}. Similarly, at flow rate of 0.0083 kg.s^{-1}, the outlet water temperature of collector-2 (T_{oc2}) was 340 K and it was 323 K at flow rate of 0.0167 kg.s^{-1}. The outlet water from collector-1 was the inlet of the collector-2.

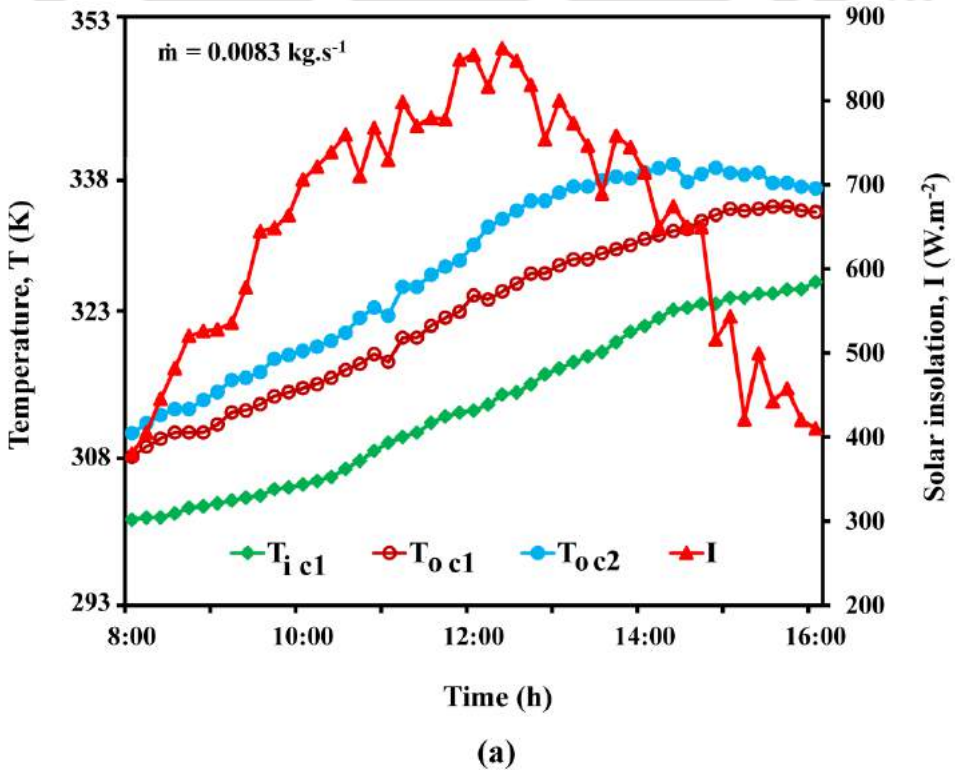

(a)

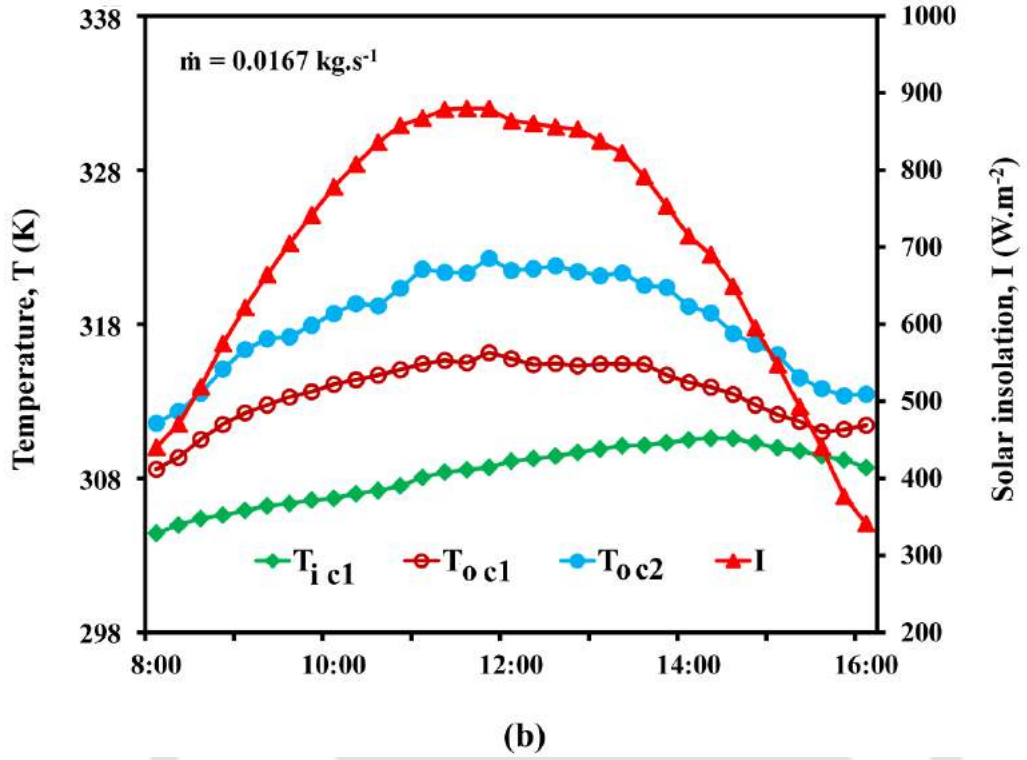

Fig.5.25 Variation of solar insolation and water temperature versus time at flow rate of (a) $\dot{m}$ = 0.0083 kg.s^{-1} and (b) $\dot{m}$ = 0.0167 kg.s^{-1}

The higher inlet water temperature of collector-2 resulted in a higher temperature of the absorber plate of the solar collector. Due to this, the heat losses from the absorber plate of the collector increased as result of re-radiation and convection (Sukhatme and Nayak 2008). Hence, the temperature difference (ΔT) across collector-1 was higher compared to that across collector-2.

5.9.2 Thermal efficiency of cascaded collector

The variation in the thermal efficiency of the cascaded collector from 8:00 h to 16:00 h at flow rates of 0.0083 kg.s^{-1}and 0.0167 kg.s^{-1}, respectively are illustrated in Fig.5.26. The thermal efficiency was determined using Eqs. (3.12 – 3.15). Figure 5.26 (a) indicates the daily average thermal efficiency of 37% for collector-1, 18% for collector-2 and 28% overall efficiency at flow rate of 0.0083 kg.s^{-1}. The respective value of Figure 5.26 (b) was 60 % for collector-1, 37% for collector-2 and 46% overall efficiency at flow rate of 0.0167 kg.s^{-1}.

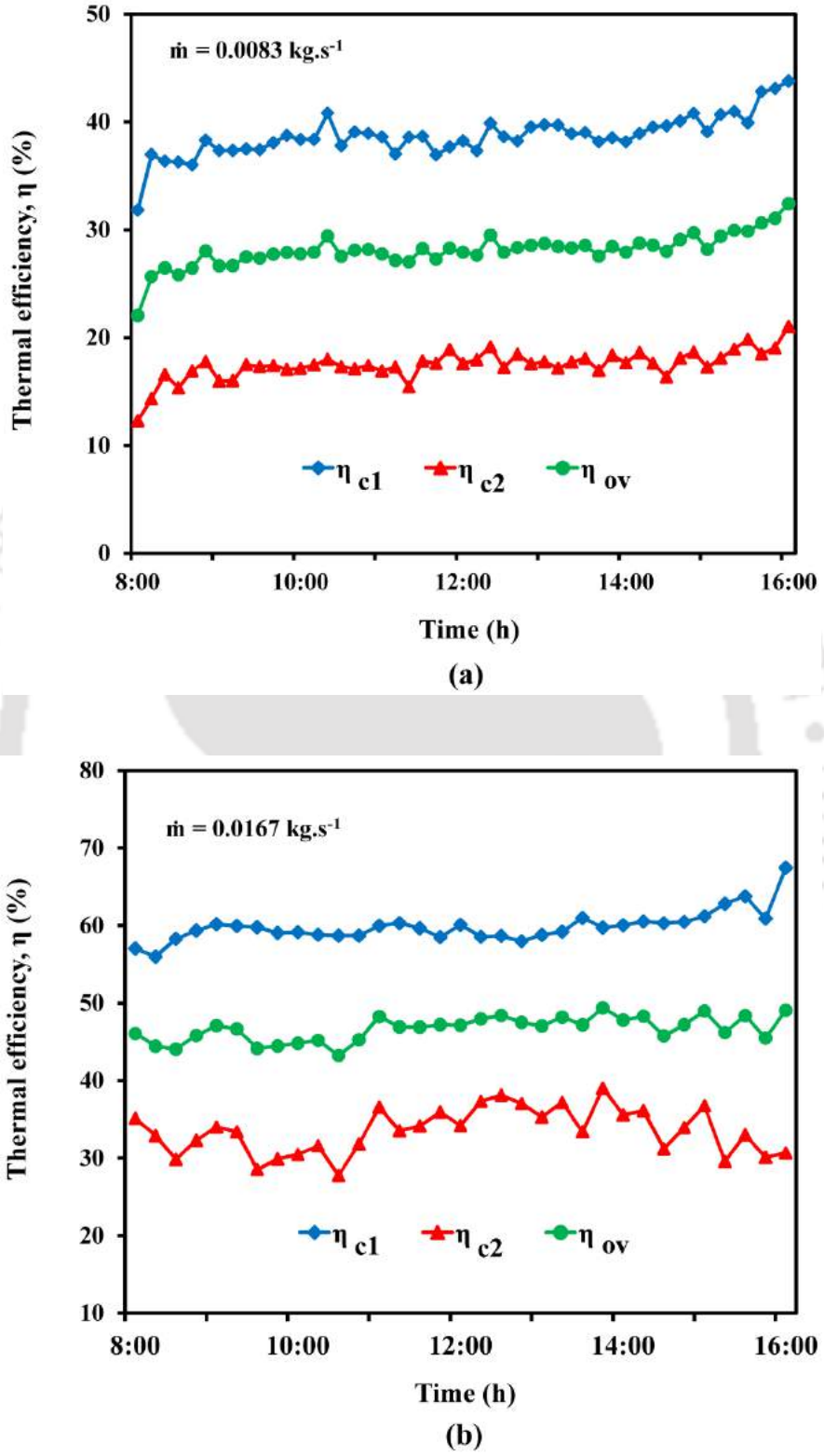

Fig.5.26 Variation of thermal efficiency versus time using cascaded collector system at flow rate of (a) $\dot{m}$ = 0.0083 kg.s^{-1} and (b) $\dot{m}$ = 0.0167 kg.s^{-1}

Since the outlet water temperature from collector-1 at lower flow rate was higher, heat-absorbing rate by collector-2 is lower. Further, it is also evident that the thermal efficiency of the cascaded collector was higher for higher flow rate compared to lower flow rate. This trend is similar to the result reported by Rabha *et al.* (2017) and Karsli (2007) using solar air heater.

5.10 Effect of Operating Parameters on Thermal Efficiency

Parametric study was carried out for straight tuber collector using various input parameters like inlet water temperature, ambient temperature, flow rate, solar insolation, optical efficiency and heat loss coefficient. For the straight riser tube model a flow velocity of 0.03 m/s, solar insolation 700 $W.m^{-2}$, absorber plate temperature 343 K, inlet water temperature 303 K, ambient temperature 298 K, wind speed 3 m/s, collector tilt angle 22.5º and collector area of 1.8 m^2 were considered. The material properties such as conductivity of the insulation material 0.004 W/m.K, emissivity of the plate (ε_p = 0.1) and emissivity of the glass (ε_g = 0.85) were taken from standard design books (Duffie and Beckman 2013). Since the flow is turbulent for higher water flow rates, flow was modelled with the standard k-ε model. The parametric study was conducted based on the formulation presented in section 3.2.

5.10.1 Effect of ambient temperature on thermal efficiency

Figure 5.27 shows the results of thermal efficiency and outlet water temperatures versus ambient temperature at inlet water temperature of 303 K, inlet water velocity of 0.03 m/sand 700 $W.m^{-2}$solar insolation.

As the ambient temperature increases from 278 K to 313 K, the thermal efficiency and outlet water temperature increases from 32% to 66% and 311.7 K to 320.7 K, respectively. As the ambient temperature increases, the collector heat loss decreases thereby increases the thermal efficiency of the solar collector. With higher ambient temperature, the collector receives heat from the sun as well as from the surrounding atmosphere thereby increases the outlet water temperature.

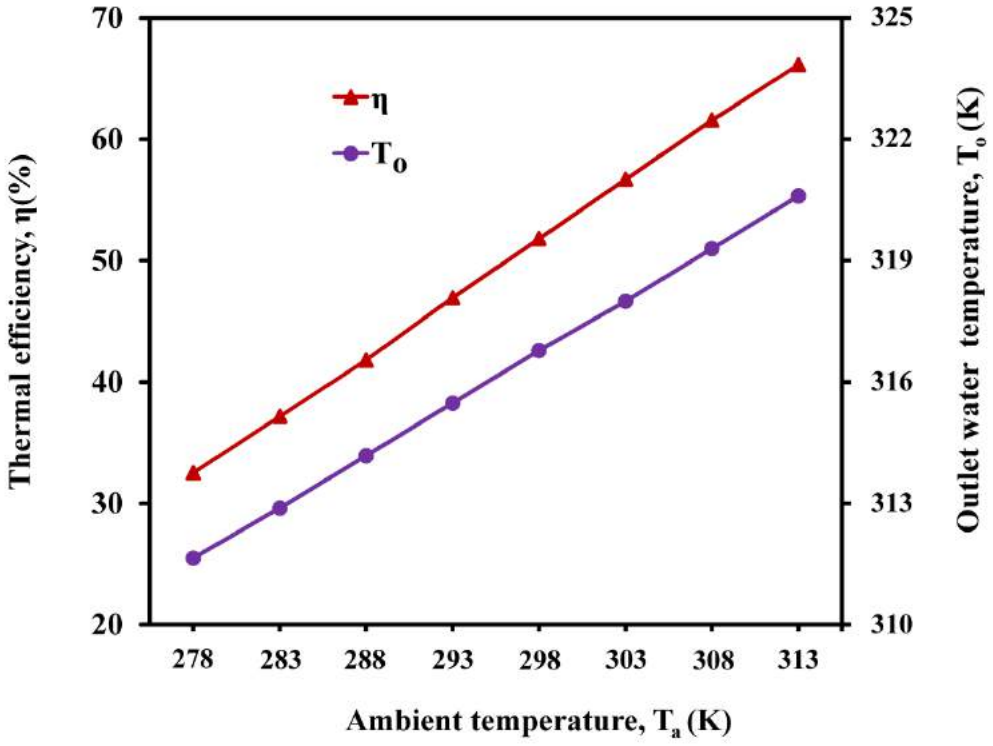

Fig.5.27 Thermal efficiency and outlet water temperature versus ambient temperature

5.10.2 Effect of inlet water temperature on thermal efficiency

Variation of collector efficiency and outlet water temperature versus inlet water temperature for a water velocity of 0.03 m/s, ambient temperature of 298 K and solar insolation of 700 $W.m^{-2}$ is shown in Fig.5.28.

As the inlet water temperature increases from 293 K to 318 K, the thermal efficiency of the collector decreases from 62.5% to 37.3% whereas the outlet water temperature increases from 309.3 K to 328.1 K. Since at higher inlet water temperature, ΔT decreases thereby decreases the thermal efficiency.

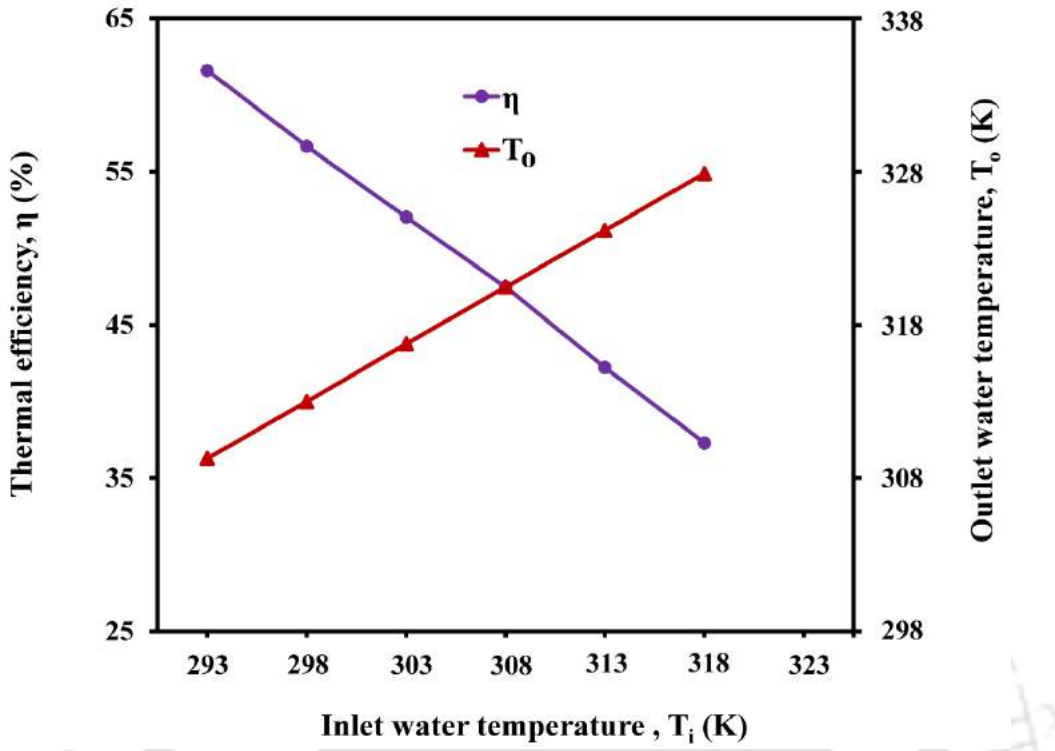

Fig.5.28 Thermal efficiency and outlet water temperature versus inlet water temperature

5.10.3 Effect of solar insolation on thermal efficiency

Plots of thermal efficiency and outlet water temperature versus solar insolation at water flow rate of 0.03 m/s, 298 K ambient temperature and inlet water temperature of 330 K is shown in Fig. 5.29.

Increasing the solar insolation from 150 $W.m^{-2}$to 1050 $W.m^{-2}$increases the thermal efficiency from 33% to 53% and outlet water temperature from 304.9 K to 325.3 K, respectively. The increase in solar insolation leads to increase in heat gain and collector heat transfer rate resulting in increase in the thermal efficiency and outlet water temperature.

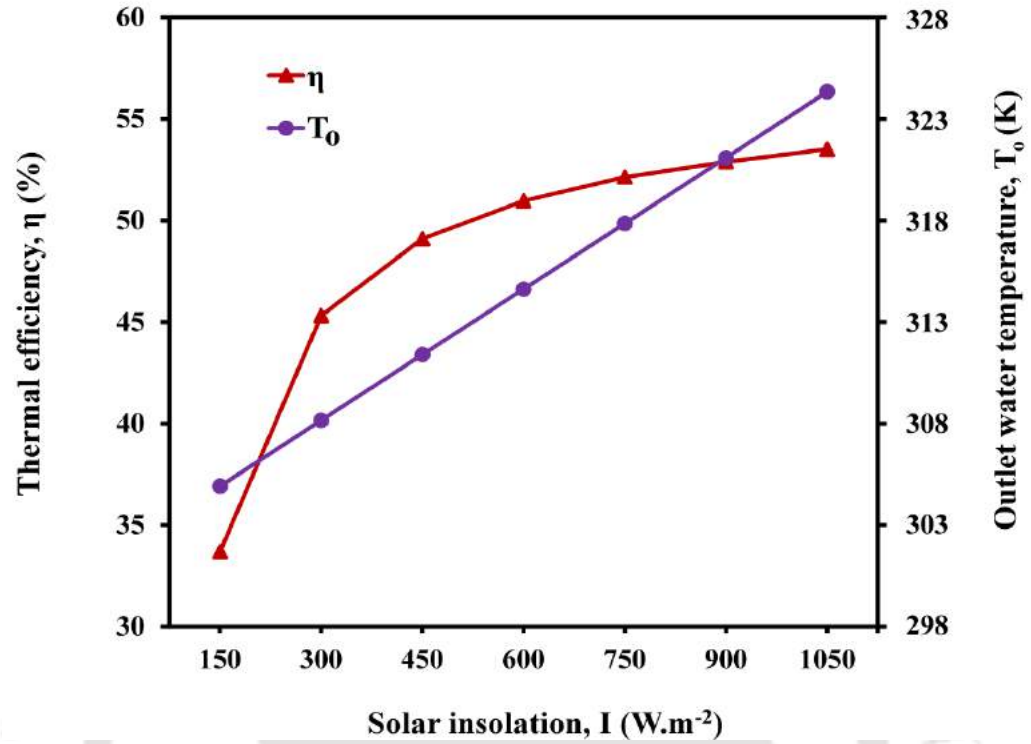

Fig.5.29 Thermal efficiency and outlet water temperature versus solar insolation

5.10.4 Effect of flow rate on thermal efficiency

Figure 5.30 shows the plot of collector efficiency and outlet water temperature versus inlet water velocity at 303 K inlet water temperature, 298 K ambient temperature and 700 W.m^{-2}solar insolation.

As the water flow velocity increases from 0.03 m/s to 0.16 m/s, the outlet water temperature decreases from 318 K to 307 K whereas the collector thermal efficiency increases from 50.7% to 80.1%, respectively. As the water flow rate increases, the heat transfer rate increases leading to the decrease in plate temperature. This results in a decrease in heat losses from the system with a concomitant increase in thermal efficiency.

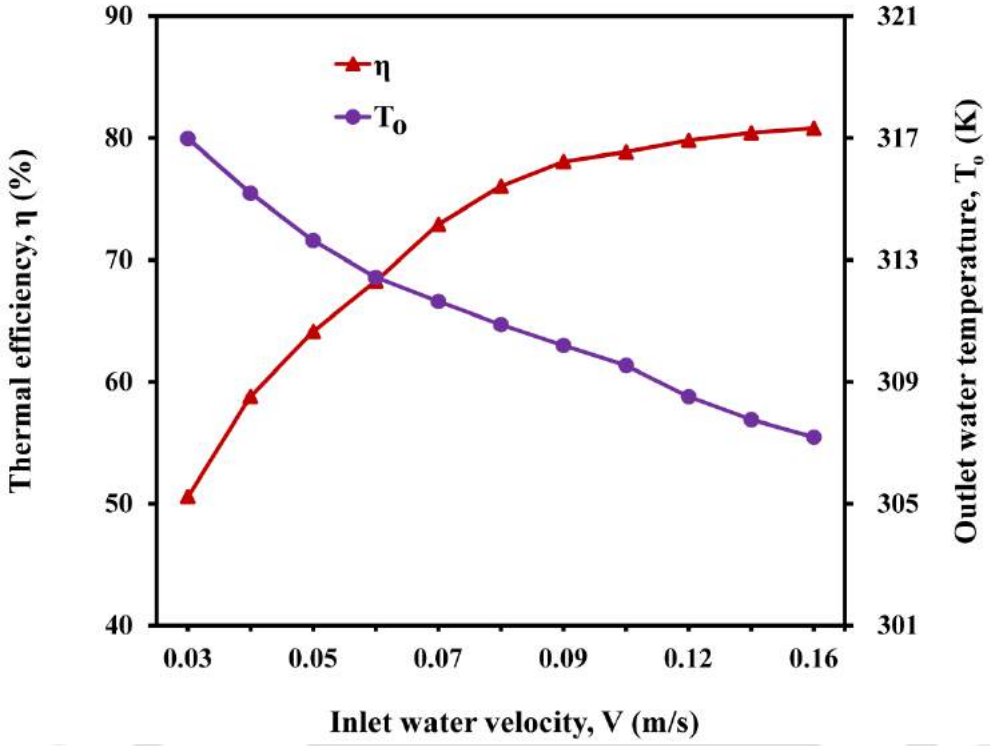

Fig.5.30 Thermal efficiency and outlet water temperature versus inlet water

5.10.5 Effect of plate material on thermal efficiency

The most important section in FPC is absorber plate, which absorbs the solar radiation and transfers heat to the risers and fluid medium. The material properties of absorber plate play an important role in heat transfer from the absorber to the riser tubes. The effect of collector energy loss parameter ((T_i - T_a)/I) on the thermal efficiency at a water velocity of 0.03 m/s, ambient temperature 298 K and solar insolation 700 $W.m^{-2}$ were studied using copper, aluminium, and steel as the absorber plate materials. The results of the study are illustrated in Fig. 5.31. The figure indicates that the thermal efficiency of the collector decreases with increase in heat loss parameter for all materials. Higher thermal efficiency is obtained when copper is used as the plate material whereas the least thermal efficiency was obtained with steel as the plate material. This is due to the higher thermal conductivity of copper compared to aluminium and steel. The thermal efficiency of the collector was only 2% less with aluminium as the plate material compared to copper.

Use of aluminium as the plate material may be a better option compared to copper in terms of weight and cost of the collector.

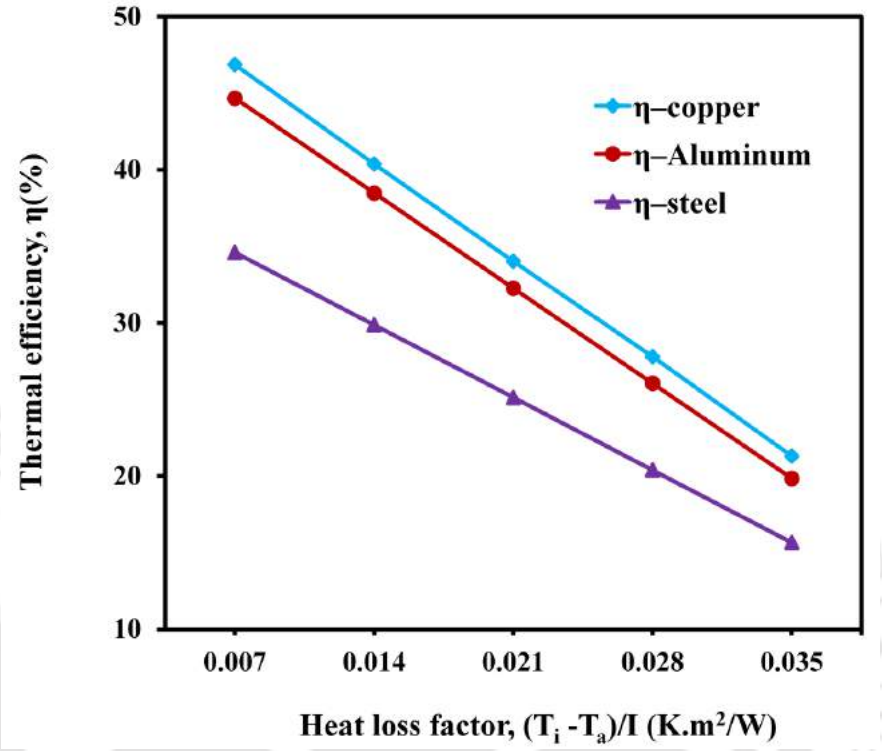

Fig.5.31 Variation of thermal efficiency versus time for different absorber plate materials

5.10.6 Effect of transmissivity coefficient on thermal efficiency

The optical characteristic of the glass cover is an important parameter for FPC efficiency. Figure 5.32 presents variation of thermal efficiency versus transmissivity coefficient by varying emissivity of the glass (τ_g) and keepings all other parameters constant. The figure reveals that the thermal efficiency is linearly increasing with the transmissivity coefficient of the glass cover. Higher transmissivity ratio of glass cover results higher thermal efficiency.

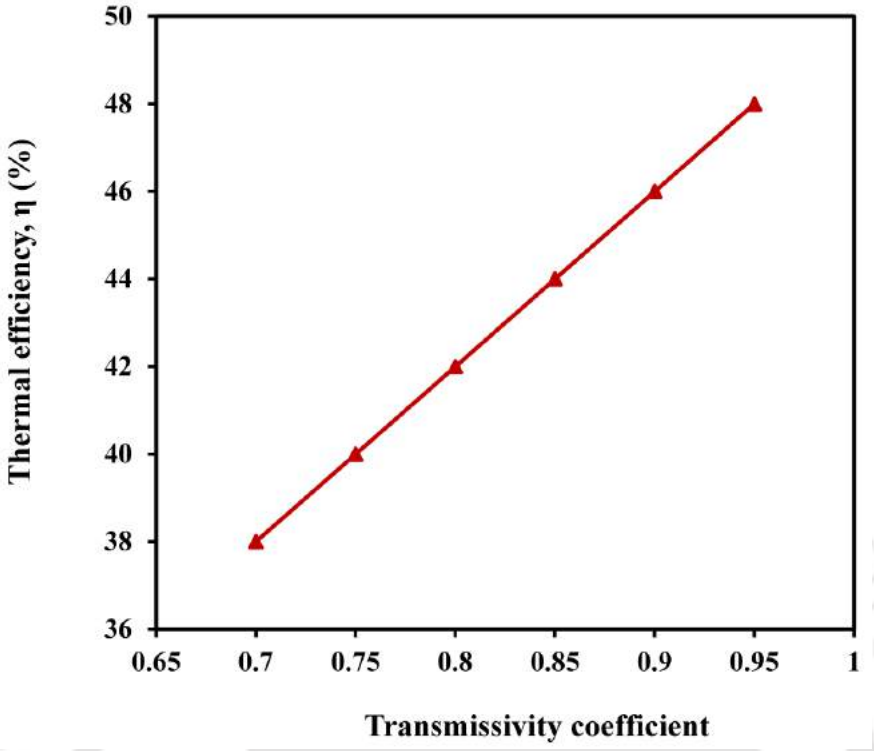

Fig.5.32Variation of thermal efficiency versus transmissivity coefficient

5.10.7 Effect of wind speed on thermal efficiency

The variation of thermal efficiency versus wind speed is depicted in Fig. 5.33. The relationship between overall heat loss and wind speed was determined by Eq. (B10) and Eq. (3.11) was used for linking heat loss with thermal efficiency. Figure 5.33 shows that as the wind speed increases from 2 m/s to14 m/s, the convective heat losses increases thereby reducing the thermal efficiency from 49% to 46.5%. Hence covering with glazing material is mandatory to reduce the overall heat loss from the solar collector.

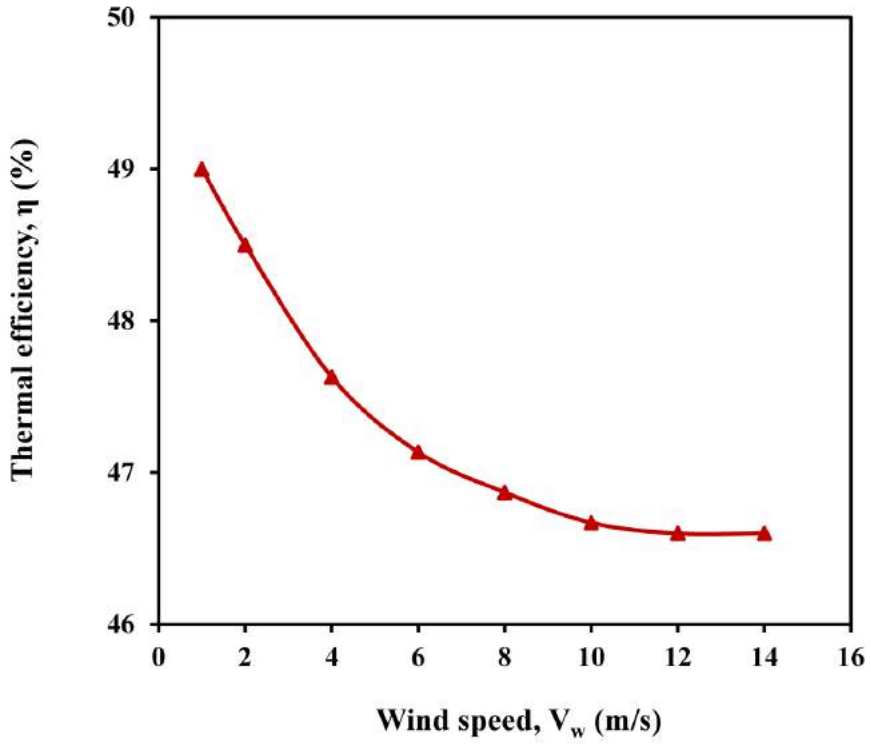

Fig.5.33 Variation of thermal efficiency versus wind speed

5.10.8 Effect of flow rate and collector loss factor on thermal efficiency

The plot of thermal efficiency versus mass flow rate and collector loss parameter $(T_i - T_a)/I$ are illustrated in Fig.5.34. Increasing collector loss factor leads to decrease in the thermal efficiency of the solar collector. The increase in water flow rate leads to a decrease in plate temperature thereby decreases the overall heat loss coefficient from the collector. This leads to the increase in thermal efficiency of the collector. For a fixed mass flow rate, increasing collector heat loss factor from 0.001 to 0.1 $m^2.K.W^{-1}$ leads to decrease in thermal efficiency from 82% to 40%.

Similarly, for fixed collector loss factor of 0.001 $m^2.K.W^{-1}$, increasing the mass flow rate from 0.001 $kg.s^{-1}$to 0.1 $kg.s^{-1}$ increases the thermal efficiency from 65% to 80%.

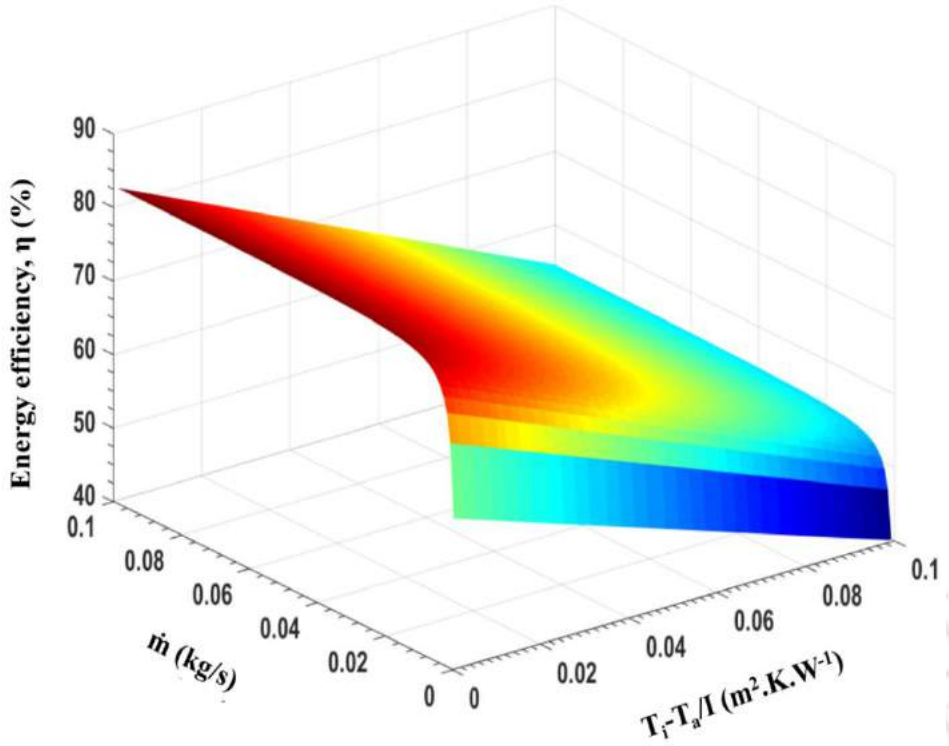

Fig.5.34 Variation of thermal efficiency versus mass flow rate and collector loss parameter

5.11 Effect of Operating Parameters on Exergy Efficiency

The effect of solar insolation, ambient temperature, inlet water temperature, collector heat loss factor, optical efficiency, working fluid type and insulation thickness on exergy efficiency is presented based on the formulation given in subsection 3.2.5. The data used for the parametric study is similar to the data given in section 5.10.

5.11.1 Effect of solar insolation on exergy efficiency

Plot of exergy efficiency versus solar insolation based on Eq. (3.28) at mass flow rate 0.0167 kg/s, ambient temperature 300 K, and inlet water temperature 303 K is shown in Fig. 5.35. The plot indicates that increasing the solar insolation from 110 $W.m^{-2}$ to 1060 $W.m^{-2}$ increases the exergy efficiency from 4.0% to 6.5%. Increase in solar insolation leads to the increase in heat gain and collector heat transfer rate which subsequently increases the exergy efficiency.

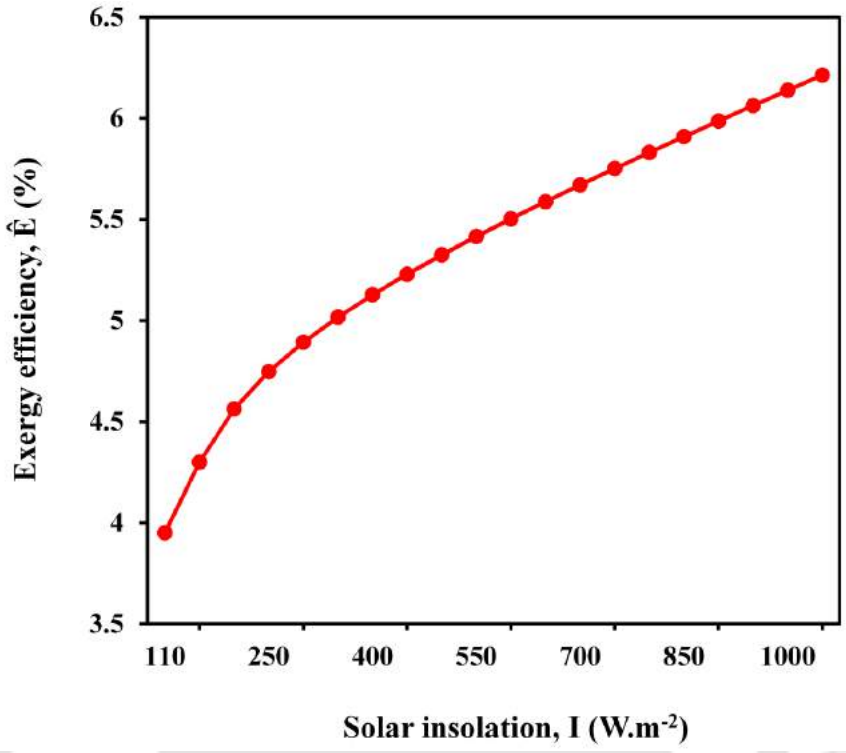

Fig.5.35 Variation of exergy efficiency versus solar insolation

5.11.2 Effect of ambient temperature on exergy efficiency

Figure 5.36 shows the plots of exergy efficiency versus ambient temperature at 303 K inlet water temperature, 700 $W.m^{-2}$solar insolation and 0.0167 $kg.s^{-1}$ mass flow rates.

As the ambient temperature increases from 300 K to 320 K, the exergy efficiency decreases from 5.8% to 1%. It is evident from Eq. (3.5) and Eq. (3.6) that with the increase in ambient temperature, the collector heat loss decreases which leads to the increase in energy efficiency of the solar collector. Also at higher ambient temperature, the collector receives more heat from the solar radiation as well as from the surrounding atmosphere which leads to the increase in exergy destruction component between the plates to the working fluid. This results in a decrease in exergy efficiency.

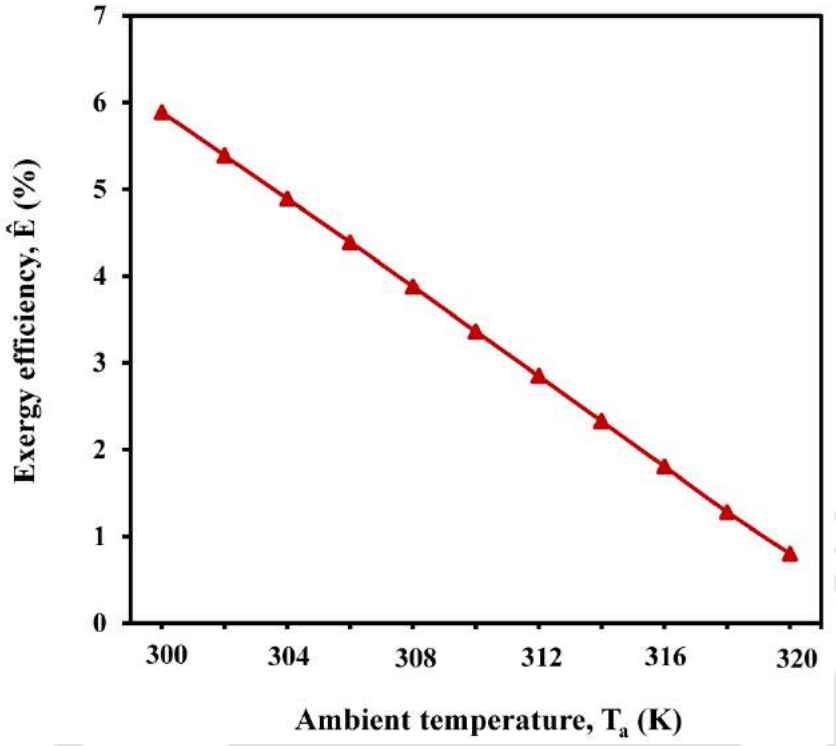

Fig.5.36 Variation of exergy efficiency versus ambient temperature

5.11.3 Effect of optical efficiency on exergy efficiency

The plot of exergy efficiency versus optical efficiency at 0.0167 $kg.s^{-1}$ water flow rate, 300 K ambient temperature, 303 K inlet water temperature and solar insolation of 700 $W.m^{-2}$ is depicted in Fig. 5.37. Equation (3.5) indicates that with an increase of the optical efficiency, there is an increase in the useful heat by the solar collector. The result reveals that increasing the optical efficiency from 0.1 to 1.0 increases the exergy efficiency from 0.5% to 7%.

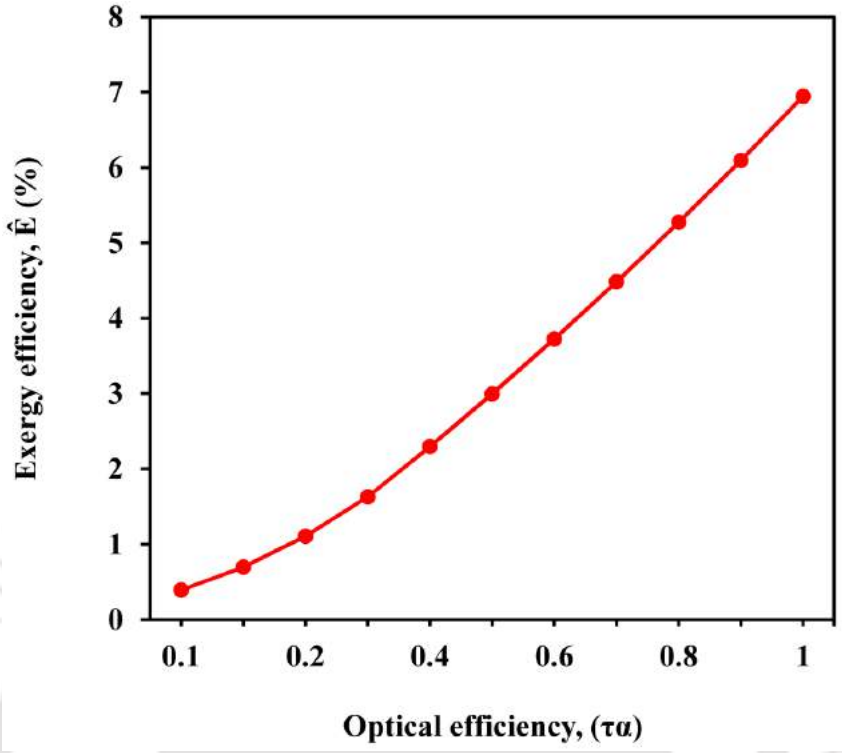

Fig.5.37 Variation of exergy efficiency versus optical efficiency

5.11.4 Effect of mass flow rate and collector loss factor on exergy efficiency

Figure 5.38 illustrates the 3D surface plot of the variation of exergy efficiency versus mass flow rate and collector loss parameter $(T_i - T_a)/I$. As the difference between inlet water and ambient temperature increases, the exergy efficiency of the collector increases. This is due to the increase in absorber plate temperature and corresponding inlet water temperature. It can also be seen that the exergy efficiency of the collector decreases sharply with increase in the mass flow rate, especially in the range from 0.001 to 0.005 $kg.s^{-1}$.

For a fixed mass flow rate, increasing the collector loss factor from 0.001 to 0.1 $m^2.K.W^{-1}$ results in an increase in exergy efficiency from 1.0% to 14%. At lower water flow rate, the plate temperature increases and results in an increase in heat transfer between the absorber plates and working fluid. Further, increasing the mass flow rate increases the exergy destruction due to the decrease in the absorber plate temperature. Apart from the heat loss factor, the main reason for exergy loss in FPC is the change in temperature between the plate (T_p) and the sun (T_s). As the absorber

plate temperature increases, the temperature difference increase which ultimately decreases the collector exergy loss.

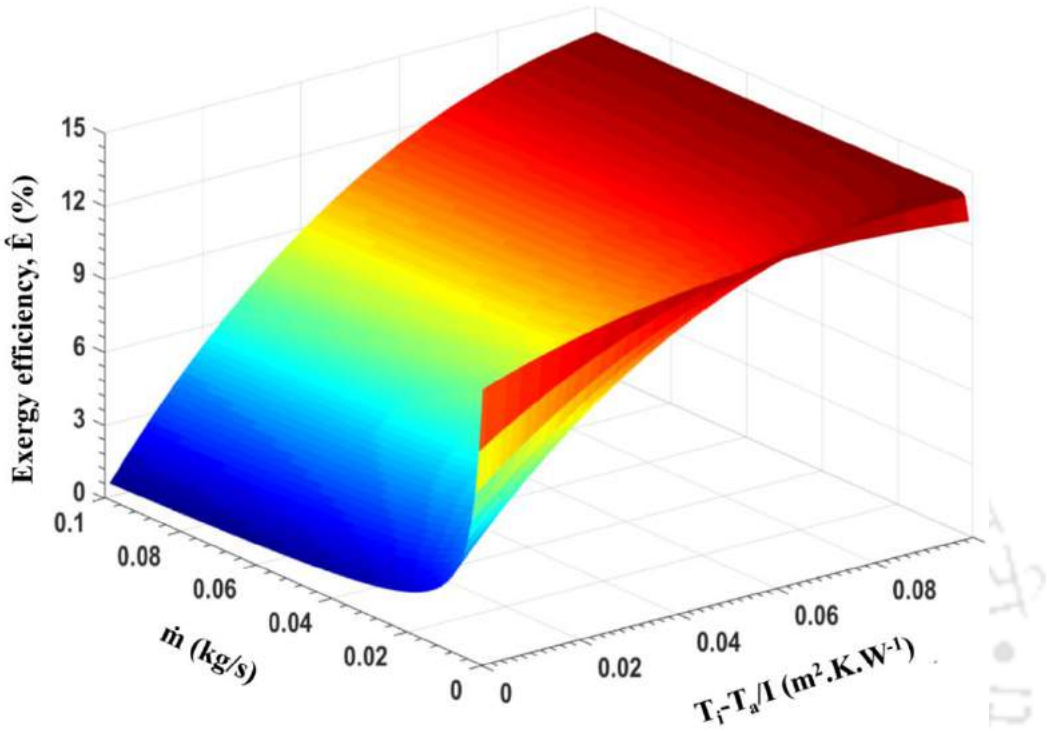

Fig.5.38 Variation of exergy efficiency versus mass flow rate and collector loss parameter $(T_i - T_a)/I$

5.11.5 Effect of back insulation thickness on exergy and energy efficiencies

Figure 5.39 illustrates the exergy and energy efficiencies versus back insulation thickness at 0.0167 $kg.s^{-1}$ mass flow rates, inlet water temperature of 303 K, ambient temperature of 300 K and 700 $W.m^{-2}$ solar insolation. The figure indicates that increasing the insulation thickness from 0.01 m to 0.05 m results in an increase in the exergy efficiency by 52% and energy efficiency by 45.9 %. Increase in the insulation thickness from 0.05 m to 0.2 m results in further increase in exergy efficiency by 4.7% and energy efficiency by 1.85%.

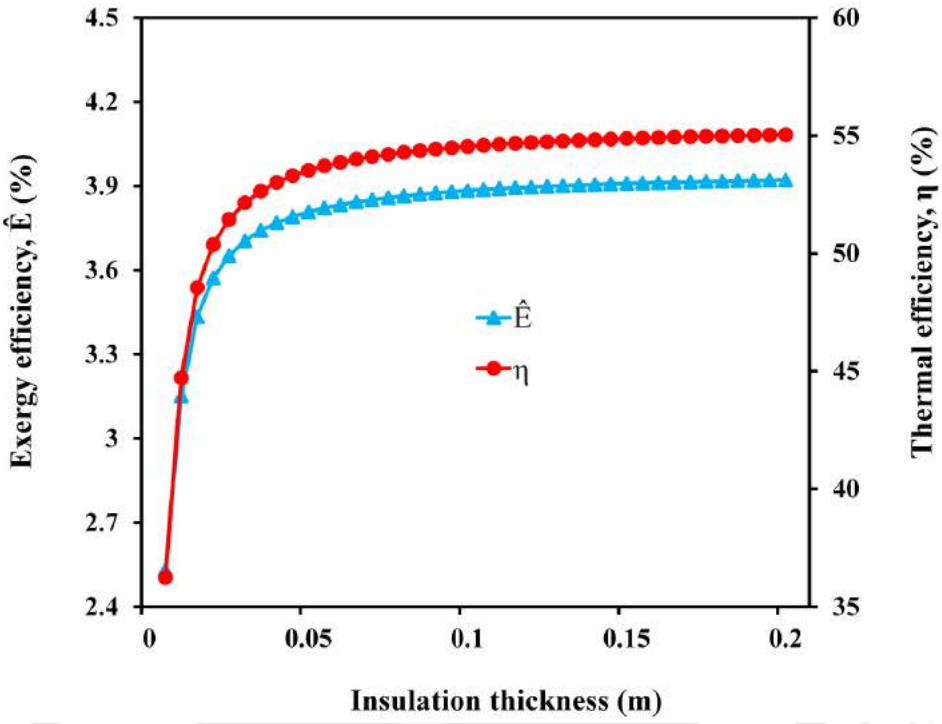

Fig.5.39 Variation of exergy and thermal efficiency versus back insulation thickness

5.11.6 Effect of working fluid on exergy and thermal efficiencies

An important parameter in FPC is the working fluid. The effect of collector loss parameter $(T_i - T_a)/ I$ on the exergy and energy efficiencies was studied by varying the inlet temperature from 300 K to 350 K, using water and ethylene glycol as working fluids. Figure 5.40 shows the results obtained based on Eq. (3.11) and Eq. (3.28) at 0.0167 kg.s^{-1} mass flow rate, 300 K ambient temperature and 700 W.m^{-2} solar insolation. It is evident from the figure that the energy efficiency of the collector decreases with increase in heat loss parameter for the two working fluids. Similarly, exergy efficiency increases with collector loss parameter of the working fluid. Higher exergy and energy efficiencies were obtained when ethylene glycol was used as a working fluid whereas the least exergy and energy efficiencies were obtained with water.

It was also observed that the exergy efficiency of the collector with water as the working fluid was 3% lower compared to ethylene glycol. It is common knowledge that water is cheap and abundantly available working fluid as compared to ethylene glycol. Water can be used as a substitute for ethylene glycol as working fluid in

terms of a small difference in exergy efficiency, cost, and availability. However, in cold climate, problem may encounter due to freezing if water is used as the working fluid.

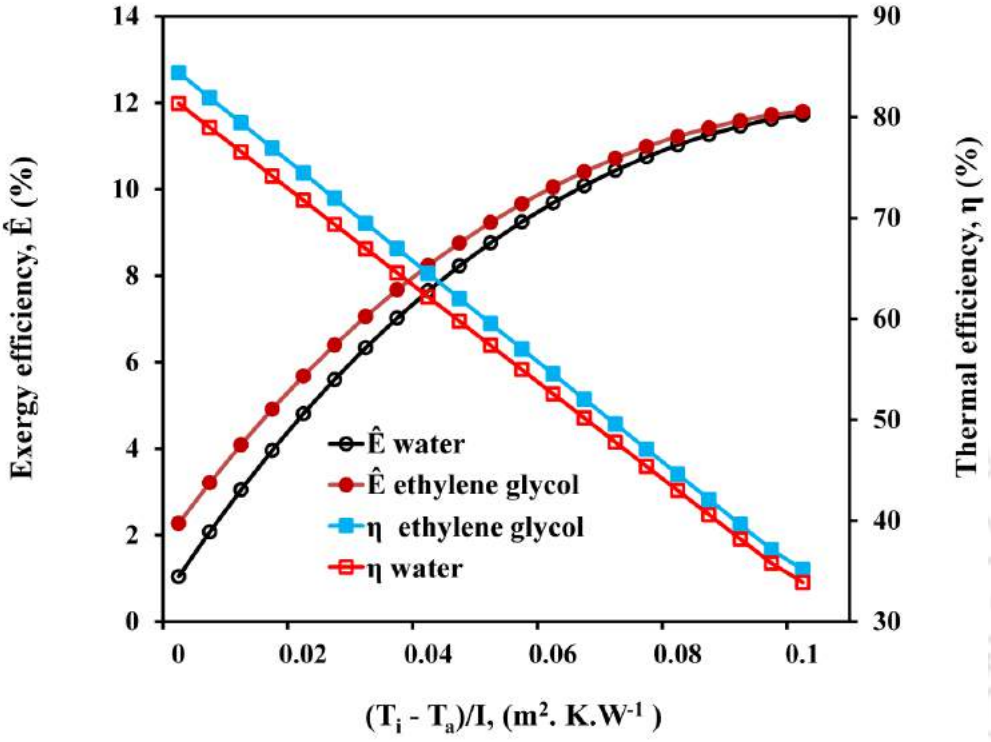

Fig.5.40 Variation of exergy and thermal efficiency versus collector loss parameter $(T_i - T_a)/I$ using water and ethylene glycol

5.12 Uncertainty Analysis

Uncertainty in the measurement of various parameters occurs due to many reasons, *viz*., reading, calibration, observation, sensitivity, drift, etc. The various independent parameters measured during the experiment were the temperature of water at the inlet and outlet side of the collector, the temperature of absorber plate, ambient air, the mass flow rate of water and solar insolation. Uncertainty in the independent variable such as Reynold number, thermal efficiency and exergy efficiency is presented in Table 5.3.The formula used for determining the uncertainty results are given in **Appendix–D**.

Table- 5.3 Uncertainty in the dependent and independent variables

Parameters	Uncertainty
Uncertainty in the measurement of tube diameter (mm)	±0.006
Uncertainty in the temperature measurement (°C)	±0.2
Uncertainly in the solar insolation measurement (W/m^2)	±5.0
Uncertainty in the measurement of mass flow rate of water (kg/s)	±0.001
Uncertainty in the measurement of Reynolds number (%)	±2.5
Uncertainty in the thermal efficiency of the solar water heater (%)	±3.7
Uncertainty in the exergy efficiency of the solar water heater (%)	±3.9

5.13 Summary

Series of experiments were carried out in order to investigate the effects of operating parameters on the performance of FPC using exergy and energy analysis and validated with numerical results. The validation of numerical result with experimental values indicated good agreement. The maximum error in deviation using straight tube collector was 5% while predicting outlet water temperature and the corresponding value was less than 2% for the absorber plate temperature. Similarly, this value was 4.8% for the outlet water temperature and it was less than 4% in the prediction of absorber plate temperature using bent tube collector. The average exergy efficiency and thermal efficiency obtained using both straight and bent tube collector was comparable with the published result. The thermal efficiency was 71% for the bent tube collector and 59% for the straight tube collector. Further, the effect of various operating parameters on exergy and thermal efficiencies were also studied. Chapter 6 presents the results of the experiment and numerical study carried out for the latent heat energy storage system using paraffin wax as phase change material.

Chapter - 6

Results and Discussion: Investigation on Thermal Energy Storage System

6.1 Introduction

Results of the experimental and numerical investigation on the thermal performance of paraffin wax filled LHS system have been presented and discussed in this Chapter. The optimization of the number of charging/discharging tube, the effect of the tube arrangement and cylinder orientation on charging/discharging time and parametric study are also investigated. Finally, the result obtained by melting enhancement and performance evaluation of LHS system using paraffin wax dispersed with Al_2O_3 nanoparticles presented and discussed.

6.2 Experiments

The outlet temperature reading obtained from the solar collector was used for the numerical model of the thermal energy storage system. Temperature at four different location of the storage was measured by T-type thermocouples. The average value of the experimental results was compared with the developed numerical model. Initially, to ensure the authenticity of the computer code, the result obtained from the developed 3D model was compared with the earlier published work. The comparison of this indicated good agreement. Subsequently, predicted average temperature of the PCM was compared with the experimentally obtained results.

6.3 Preliminary Numerical Model using Paraffin Wax Filled Latent Heat Storage

Optimization of number HTF tube and tube arrangement is mandatory to have cost-effective and efficient LHS system. This section presents the optimization of number

of charging/discharging tubes, effect of tube arrangement and cylinder orientation on average temperature and melt fraction of the phase change material (PCM).

6.3.1 Optimization of number of charging/discharging tubes

The main setback of PCMs is its poor thermal conductivity which impairs its use for different applications. Hence, implementing heat transfer enhancement technique is mandatory to increase the melting rate. Increasing the number of charging/discharging tubes of the HTF, using fins, inserting metallic material in PCM and mixing of nanoparticle with PCM were among the different techniques used by several researchers to increase the heat transfer rate. The present study was done by increasing the number of charging tubes. A 2D numerical model was developed to optimize the number of charging/discharging tubes. The diameter of the storage and HTF tube considered for the numerical model study was similar to the experimental setup shown in Figs.4.8 and 4.9. Figure 6.1 indicates the various charging/discharging tubes used for the optimization process.

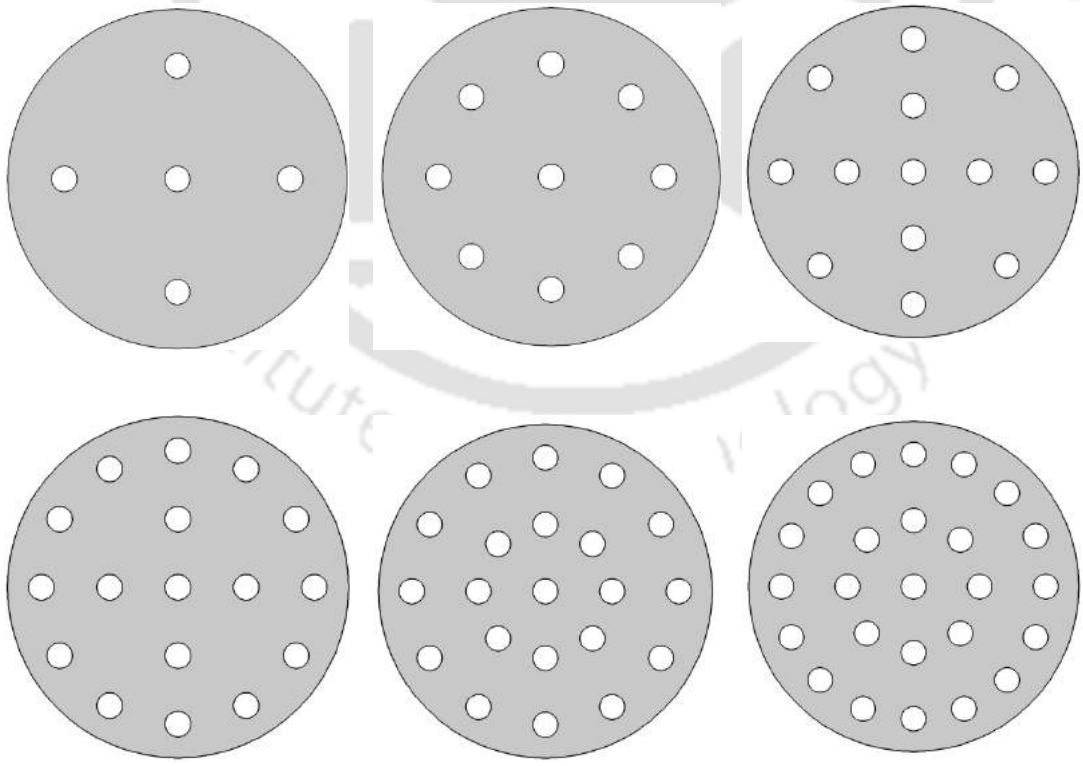

Fig.6.1Number of charging/ discharging tubes considered for optimization

The number of HTF tubes considered for the investigation was 5, 9, 13, 17, 21 and 25. The optimization was carried out based on the charging time. Optimization of the number of tubes based on discharging time was reported by Niyas *et al*. (2017), but this method took almost four times computational time than optimization using charging time. This is due to the slower discharging process of the PCM compared to the working fluids. Hence, the present study considered charging time as main criteria for the optimization of HTF tubes.

The charging time versus the number of charging tubes is presented in Fig. 6.2 considering the inlet temperature of water (T_{inlet}) as 343 K and initial temperature (T_{int}) of the PCM as 298 K. The melting temperature of the paraffin wax considered for the numerical model was 321 K as per the reported result of Niyas and Muthukumar (2013). The parameters used for the numerical model is given in Table 3.3.

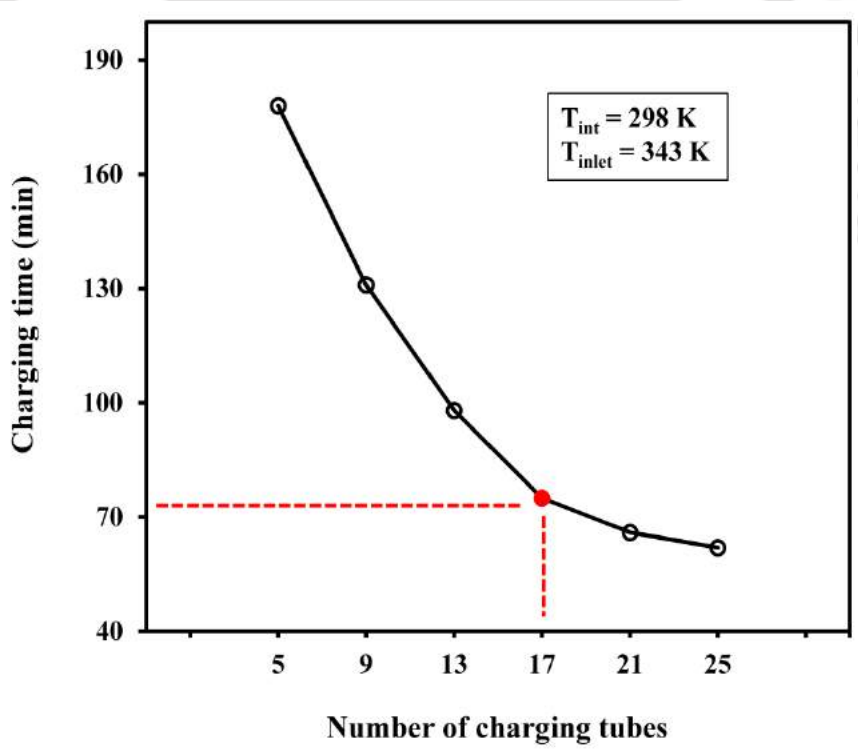

Fig.6.2 Variation of charging time versus number of charging tubes

Figure 6.2 indicates that the rate of change of charging time with respect to number of charging tubes are high for number of tubes up to 17. Further increase in the number of charging tube resulted in only a marginal reduction in charging time of the LHS system. The variation in charging time for 21 tubes compared to 25 tubes was 6.5 minute. The benefits of using 25 and 21 tubes are that the time saved is less than 9 minutes at the expense of 4 to 8 tubes compared to 17 tubes. Hence, latent heat storage with 17 tubes is found to be the optimized configuration for the present investigation.

6.3.2 Effect of tube arrangement

The effect of tube arrangement on discharging time for the optimized LHS model at a discharge time of 120 minutes is presented in Fig.6.3.

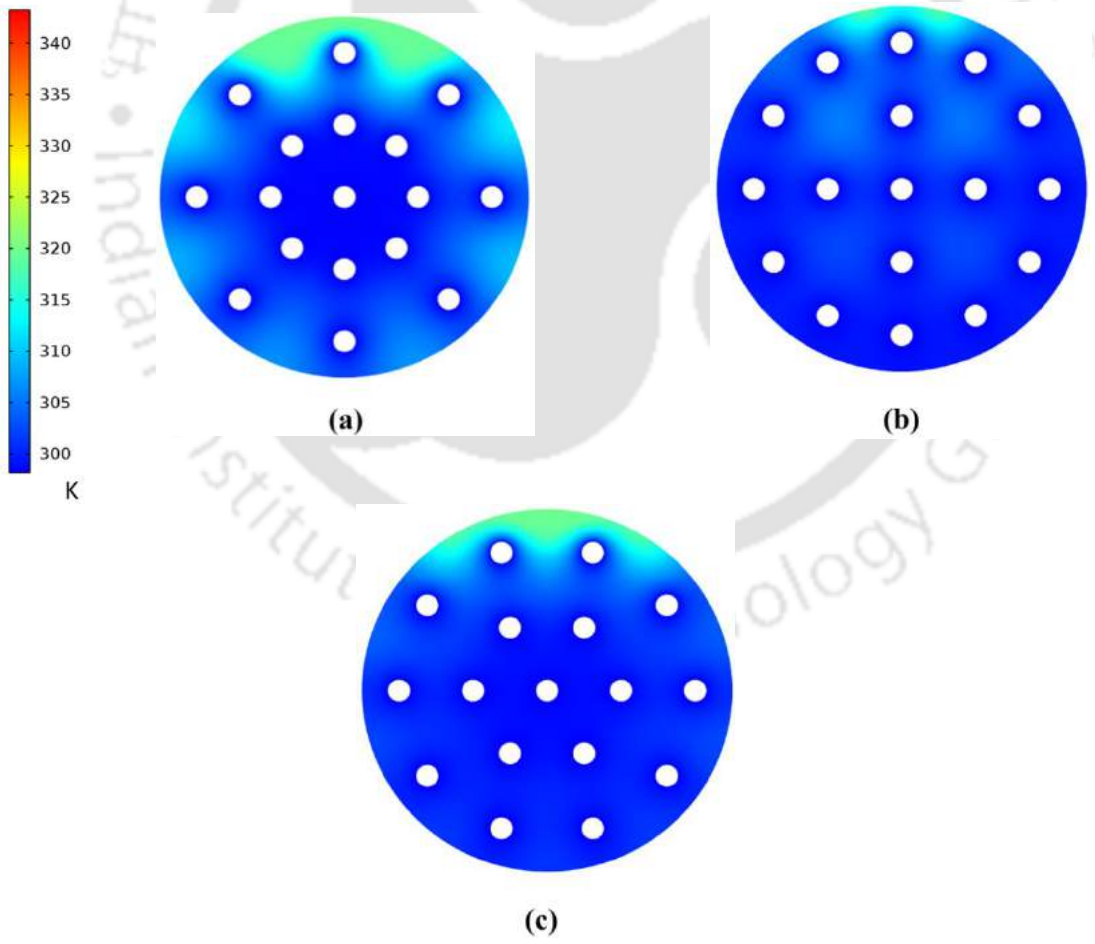

Fig.6.3 Variation of average temperature during discharging process

The arrangement of 8 tubes at the centre with 8 tubes at the outer [Fig.6.3 (a)], 4 tubes at the centre with 12 tubes at the outer [Fig.6.3 (b)] and 6 tubes at the centre with 10 tubes at the outer [Fig.6.3 (c)] were considered for the present investigation to select the best arrangement. Initially, the temperature of the PCM in the shell was 343 K and water at 298 K was circulated through the HTF tube. Complete discharge is termed as the case when the entire temperature of PCM in the shell reaches the temperature of the HTF tube. It is exhibited from the figure that the discharging rate of 4 tubes at the centre and 12 tubes at the outer [Fig.6.3 (b)] was faster than 8 tubes at the centre and 8 tubes at the outer or with 6 tubes at the centre and 10 tubes at the outer. Since the requirement of latent heat storage is to have faster-discharging rate, 4 tubes at the centre with 12 tubes at the outer [Fig.6.3 (b)] was found to be the best arrangement for the present investigation.

6.3.3 Effect of cylinder orientations

Figure 6.4 illustrates the comparison of the average temperature and melt fraction of PCM during charging process for Horizontal (H) and Vertical (V) LHSs unit. The study considered a 3D single tube and shell to investigate the effect of cylinder orientation on melting time and average temperature of the PCM. It is clearly seen from Fig.6.4 (a) that the temperature variation in both horizontal and vertical orientation is nearly similar for the first 8 minute. Once the PCM reaches the melting temperature (321 K), PCM temperature for both horizontal and vertical systems increases sharply and reaches fully charged zone. The maximum variation in temperature between horizontal and vertical system after reaching the melting temperature (321 K) was 2.9 K whereas it was 2.3 K before melting temperature. Further, the horizontally oriented system reaches the full charged temperature (343 K) at 52 minute which is 18 minutes less compared to the vertical system.

It can also be observed from Fig. 6.4 (b) that the variation in average melt fraction for both systems is almost similar for the first 10 minute. In case of the horizontal cylinder, when PCM starts melting, the liquid PCM makes a recirculation region that creates a strong convective heat transfer due to buoyancy effect.

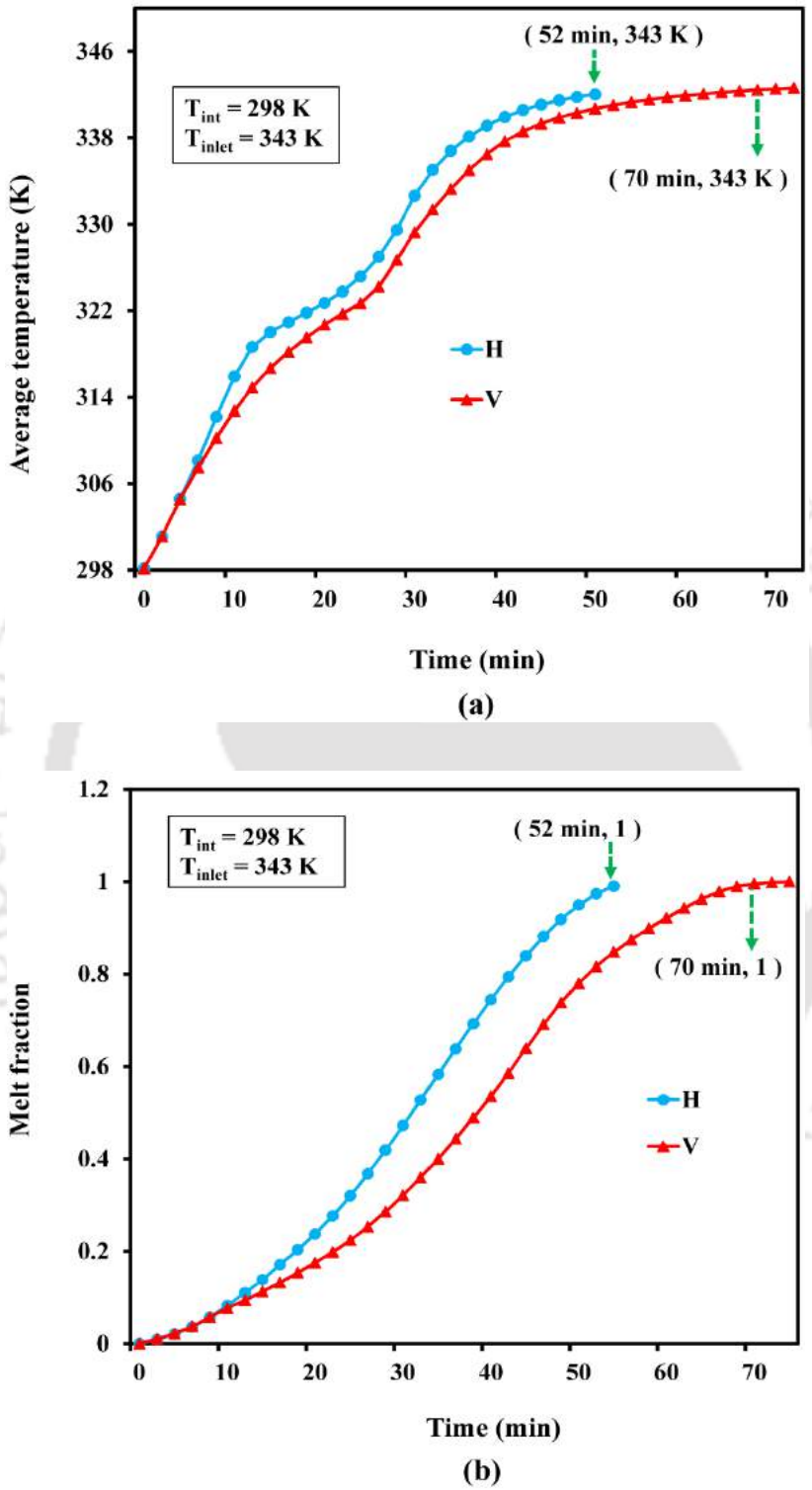

Fig.6.4 Average temperature and melt fraction versus time in horizontal and vertical cylinder

The recirculation region in the horizontal system along the axial direction is much higher than the recirculation region along the radial direction in the vertical unit. Therefore, the rate of melting in the horizontal system is much higher than the vertical unit. Further, it is also noticed that the time needed to get a complete melt was nearly 52 minute for the horizontal whereas it was 70 minutes for the vertical orientation. Similar result was reported by He and Setterwall (2002). Due to faster melting rate, horizontal orientation has been selected for the present investigation.

6.4 Grid Independent Test

The numerical results of a mathematical model depend on the mesh size. To check the dependency of numerical results on the mesh size, simulations with different mesh sizes were performed for the charging process. The variation of the average temperature of the LHS versus charging time for different mesh element numbers, i.e. 237,458, 306,464 and 392,382 for charging process is depicted in Fig.6.5.

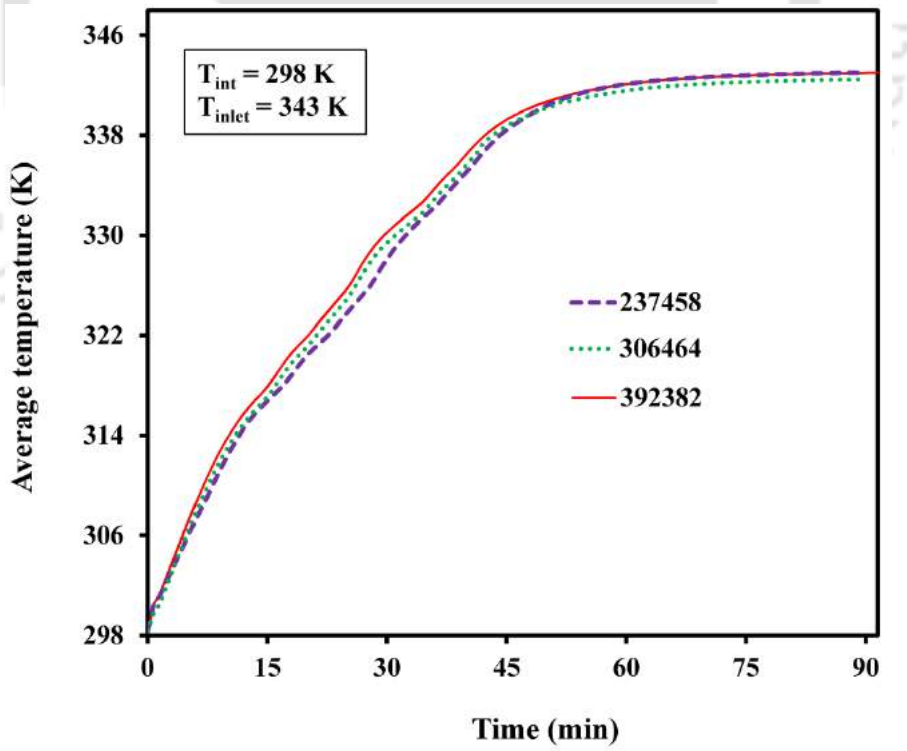

Fig. 6.5 Grid independent test during charging process

There was difficulty on the convergence for achieving the result for the developed model with mesh elements less than 237,458 during charging process.The variation of average temperature between 392,382 elements with the 306,464 elements was less than ± 0.5%. Hence, the model with 306,464 elements is found to be grid independent for charging process. The HTF inlet flow rate of 0.0083 kg/s and 343 K inlet temperature were taken during charging process for the grid independent test.

6.5 Model Validation and Performance Study

The numerical model was validated for the charging/discharging process by comparing the results of the predicted values with the average experimental values of the paraffin filled LHS. The location of thermocouples [T1, T2, T3, T4] are shown in Fig.4.9. Initially, the latent heat storage was at 298 K/ 343 K during charging/discharging process at (t = 0). When the heat transfer fluid passed through the tubes at a temperature of 343 K / 298 K and flow rate of 0.0083 kg/s, heat transfer occurs across the HTF and PCM. This section presents the results of the comparison study between predicted and experimental values of the LHS system during charging/discharging process.

6.5.1 Plot of average melt fraction

Figure 6.6 presents the contour plots of average melt fraction of the paraffin wax versus time during charging/discharging process. It can be observed from Fig. 6.6 (a) and (b) that the average melt fraction of the latent heat storage is varied from 0 to 1 at the start of the charging/discharging processes at (t = 0 min). It is evident from Fig.6.6 (a) that the LHS is fully charged at (t = 90 min). However, it can be seen from Fig.6.6 (b) that the LHS is not fully discharged in 90 minutes time, i.e., discharging process is slower than charging process. The main cause is the presence of natural convection heat transfer during the charging process. This effect is shown in Fig. 6.6 (a) at (t =10 min to 80 min). However, the variation in natural convection heat transfer was not seen during the discharging process since it is a conduction dominated process. The complete solidification of the paraffin wax was achieved at t = 120 min.

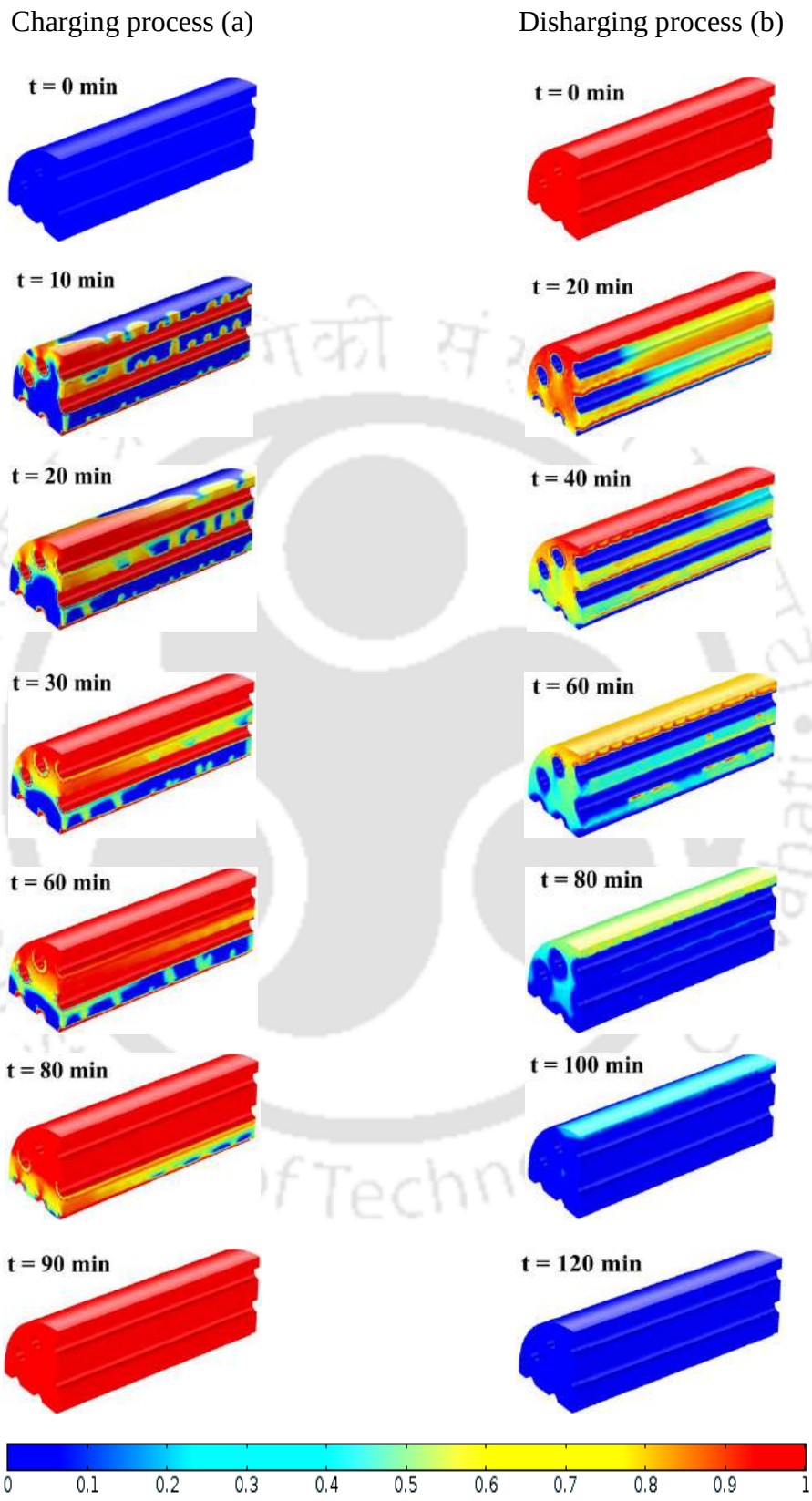

Fig.6.6. Plot of melt fraction of the paraffin during (a) charging and (b) discharging process

6.5.2 Validation of top surface temperature during charging/discharging process

The validation of average temperature at the top surface of the storage was carried out as per the description presented in section 4.5. The comparison between experimental and numerical averaged temperature of the paraffin wax at the top surface of the storage during charging/discharging process is depicted in Fig. 6.7.

From the result, it was evident that the maximum deviation between simulation and experimental values of average temperature of paraffin wax was ~ 5 K during the charging process and ~ 7 K during the discharging process. This indicates that the developed model predicted the average temperature with reasonable accuracy. In all cases, the numerical values were found to be higher than experimental results. Further, it was noticed that the trend of the numerical result resembles the same as that of the experimental value. Similar trend was reported by Gumus (2009) and Niyas and Muthukumar (2013).

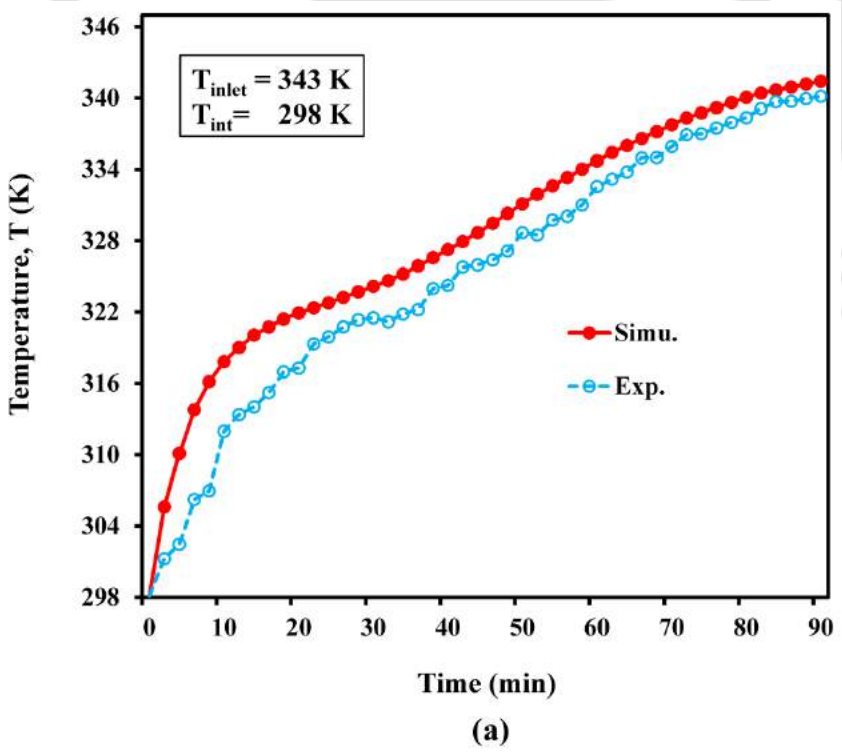

(a)

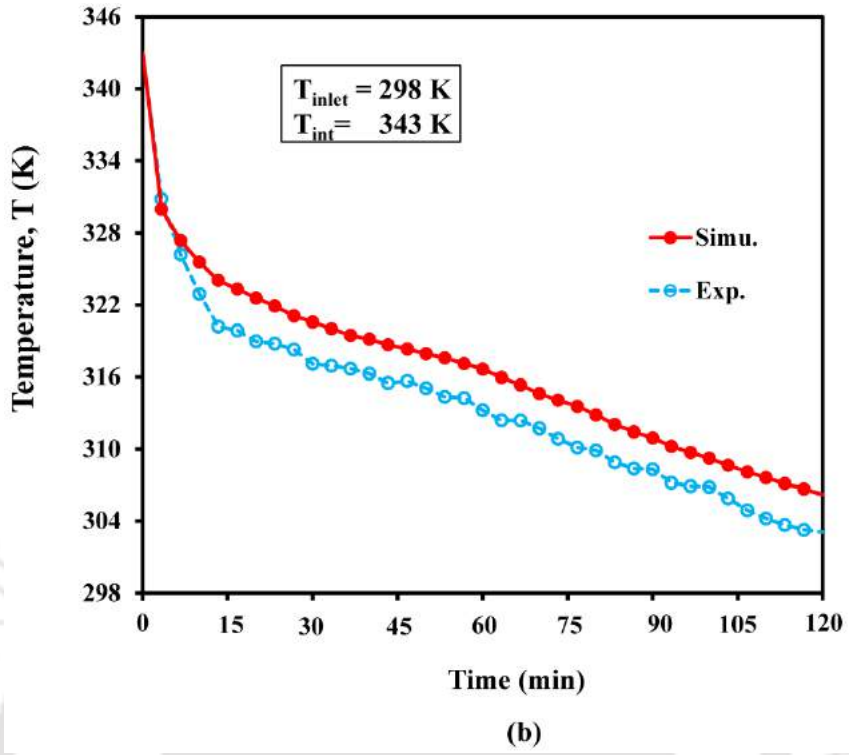

(b)

Fig.6.7 Variation of average temperature at top surface versus time during (a) charging and (b) discharging process

6.5.3 Average melt fraction of paraffin wax

The main parameter which affects the performance of any latent heat storage during melting/solidification process is melt fraction. The average melt fraction in the present case is the volumetric average melt fraction of all the meshed element of the numerical model that varied between 0 to 1. The variation of average melt fraction during charging/discharging process is depicted in Fig.6.8.

It is evident from Fig. 6.8 (a) and (b) that the rise/fall of the average melt fraction of LHS during charging/discharging process is faster at the beginning due to the presence of higher heat transfer rate between the HTF and PCM. After certain period of time, this becomes slower due to the low heat transfer rate between the HTF and PCM. The time needed for complete charging/discharging of the paraffin wax filled LHS system was 90 min / 120 min.

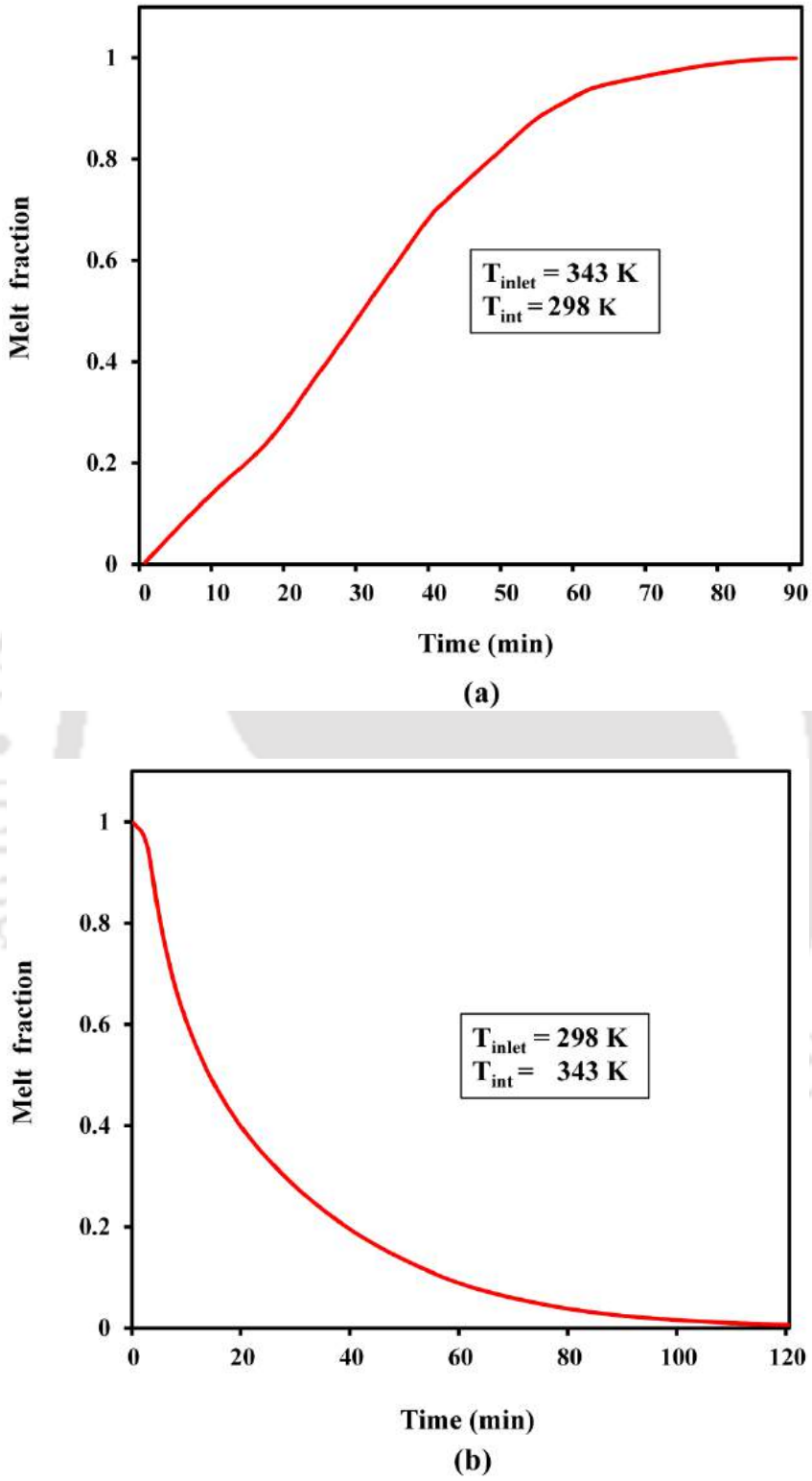

Fig.6.8 Variation of average melt fraction of paraffin wax during (a) charging and (b) discharging process

6.5.4 Average temperature of paraffin wax

Similar to the melt fraction, the average temperature is the volumetric average temperature of all the mesh elements of the numerical model. Initially, the paraffin wax filled LHS is at 343 K / 298 K during charging/discharging process. When the HTF fluid circulates through the tube at a temperature of 343 K/ 298 K, heat transfer is take place between HTF and PCM. The average temperature variation of the paraffin wax during charging/discharging process is illustrated in Fig.6.9. It is observed from Fig.6.9 (a) and (b) that the variation of average temperature curve at the beginning of the process indicates a sharp increase/decrease of temperature during charging/discharging process. This is mainly due to the presence of higher potential for heat transfer during the initial period of the process. After 10 minute, the slope of the temperature versus time plot starts decreasing. The temperature of the paraffin wax reaches approximately 343 K / 304 K in 90 min / 120 min during charging and discharging process. This indicates charging is faster process compared to discharging process. The reason behind this is the addition of convective heat transfer that increases the heat transfer rate of the storage during the charging process.

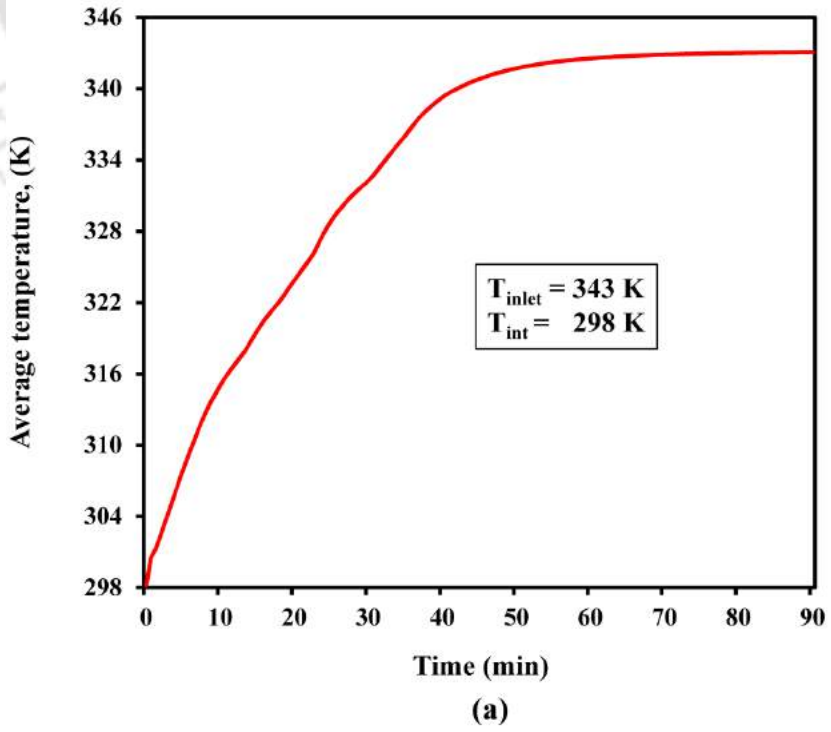

(a)

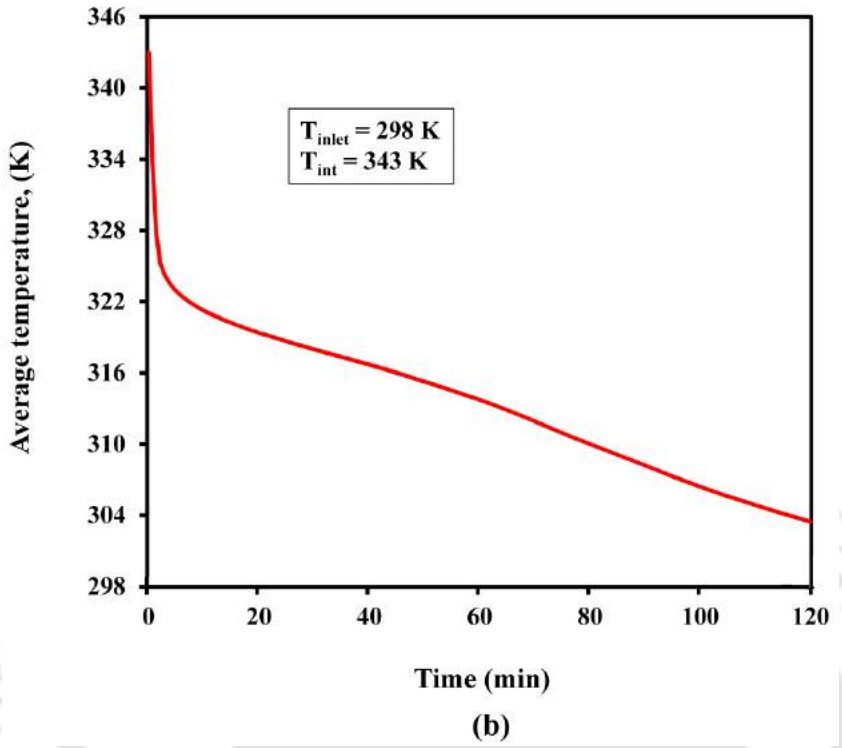

Fig.6.9 Average temperature of the paraffin versus time during (a) charging and (b) discharging process

6.5.5 Energy stored/discharged

The variation of rate of energy stored/discharged, i.e., sensible, latent and total energy during charging/discharging process is illustrated in Fig.6.10. During charging/discharging process, the heat transfer fluid is circulated through the tube at a temperature of 343 K/298 K. Due to this, heat transfer take place between the HTF and the PCM. At the beginning of charging/discharging process, the heat gets stored/discharged in the form of sensible heat only. Once the paraffin temperature reaches nearly the phase change temperature (321 K), heat gets stored/ discharged in the form of latent heat. The heat stored/discharged after complete phase change is also sensible energy. When the average temperature of the paraffin reaches 343 K within 90 min during the charging process, the amount of sensible, latent and total energy stored in the LHS are 1.7 MJ, 3.4 MJ and 5.1 MJ, respectively. The range of temperature in which the paraffin stores the sensible heat is around 45 K, i.e., (343 K – 298 K).

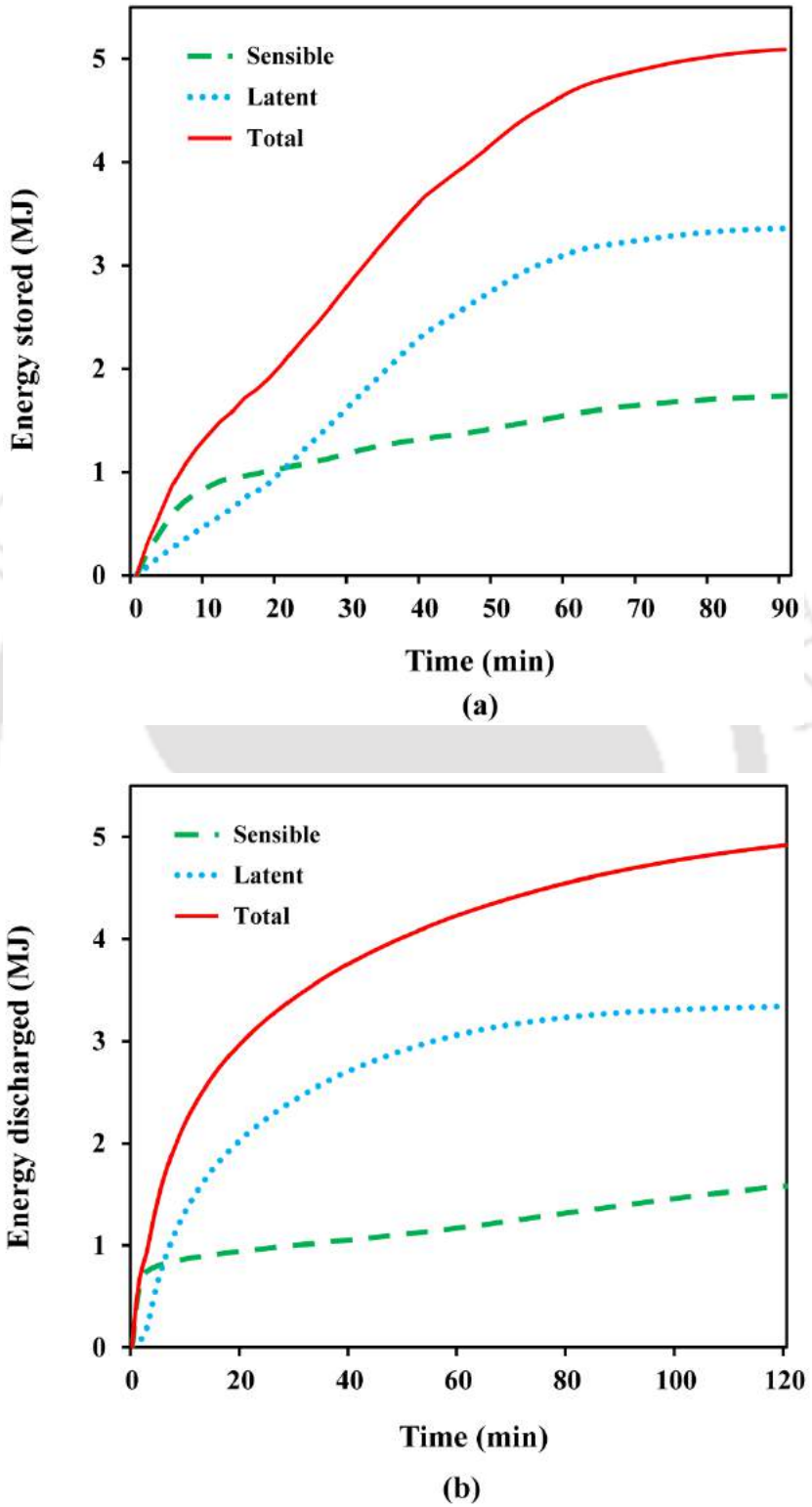

Fig.6.10 Energy stored/ discharged rate of paraffin during (a) charging and (b) discharging process

Similarly, when the temperature of the PCM reaches to 304 K within 120 min during the discharging process, the amount of sensible, latent and total energy discharged from the paraffin filled LHS is 1.3 MJ, 3.2 MJ and 4.5 MJ, respectively. The range of temperature in which the paraffin discharges the sensible heat is around 39 K, i.e., (343 K – 304 K).

6.5.6 HTF outlet temperature variation

The variation of HTF outlet temperature and the temperature difference between outlet and inlet of paraffin filled LHS during charging/discharging process is plotted in Fig.6.11. The outlet temperature of the HTF depends on the thermo-physical properties of the paraffin and the heat transfer between the paraffin and heat transfer fluid. It is clearly observed from the figure that there is a sharp rise/fall of the HTF outlet temperature during charging/discharging process. This is due to the presence of higher potential for heat transfer at the starting of the process. Later, the rate of outlet temperature with time of the HTF reduced due to the reduction of thermal gradient across the HTF and paraffin wax. The temperature difference between the HTF and paraffin temperature reaches nearly 2 K at 90 min whereas it was nearly 5 K at 120 min during the discharging process.

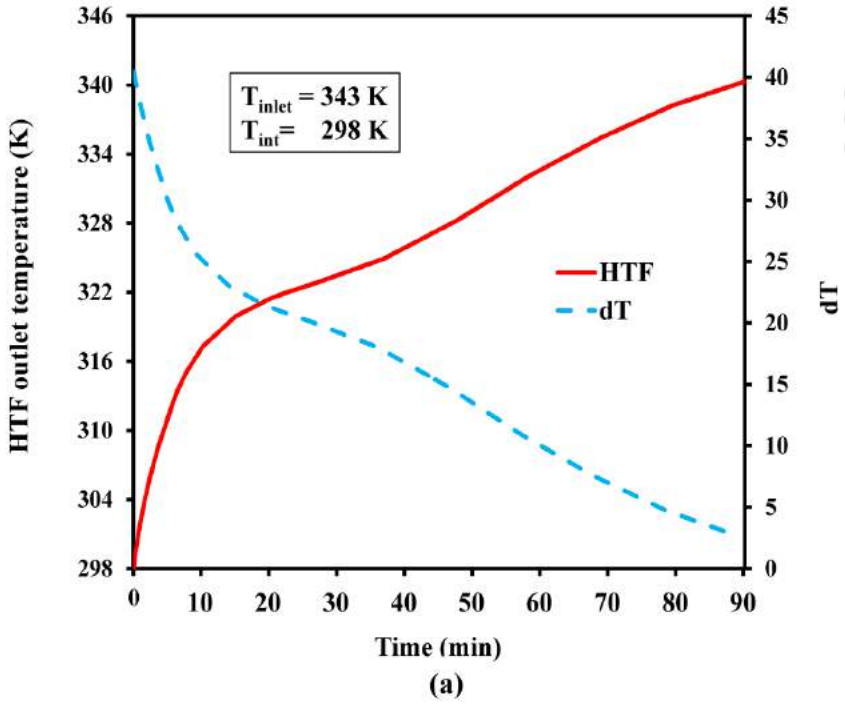

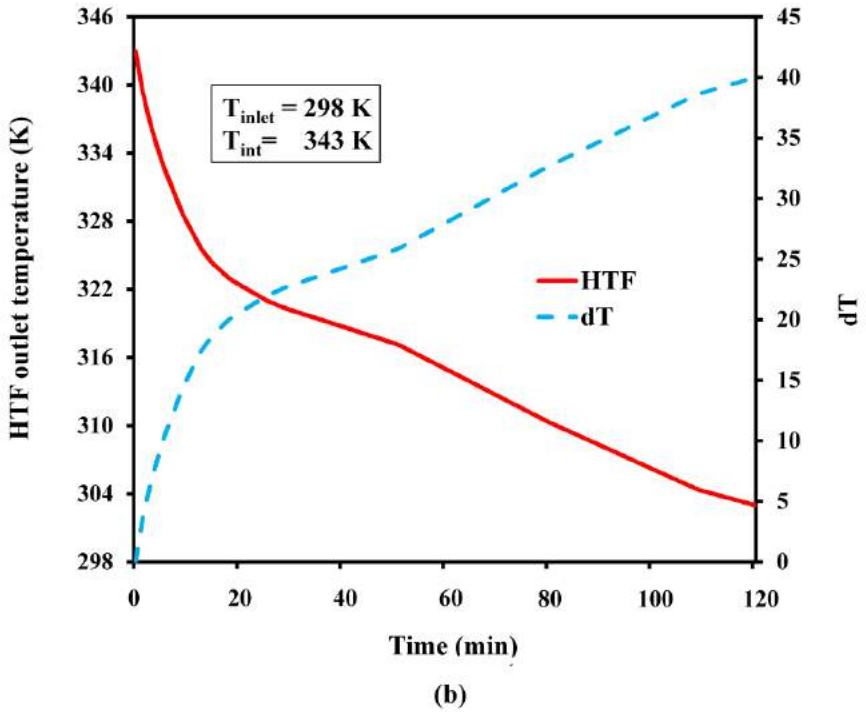

Fig.6.11 Variation of HTF outlet temperature and dT versus time during (a) charging and (b) discharging process

6.6 Temperature Variation of Paraffin Wax during Charging Process

The aim of this section is to study the variation of temperature of paraffin wax using the experimental description presented in section 4.5. The variation of solar insolation, inlet water temperature, outlet water temperature and ambient temperature versus time at flow rate of 0.0083 kg/s is depicted in Fig. 6.12. The measured experimental results of solar insolation, inlet water temperature and outlet water temperature increases from 8:00 h and reach the maximum value at 12:30 h. The maximum solar insolation recorded was 908 $W.m^{-2}$. The outlet water temperature from the solar collector increased from 307 K and reached a peak value of 343 K. Similarly, the inlet water temperature increased continuously from 303 K to 332 K and then decreased with time. Since the inlet of the LHS is the outlet from the solar collector (Fig.4.5 and 4.6), the temperature of the latent heat storage at the entry was taken as 343 K, which was the maximum temperature of the solar collector.

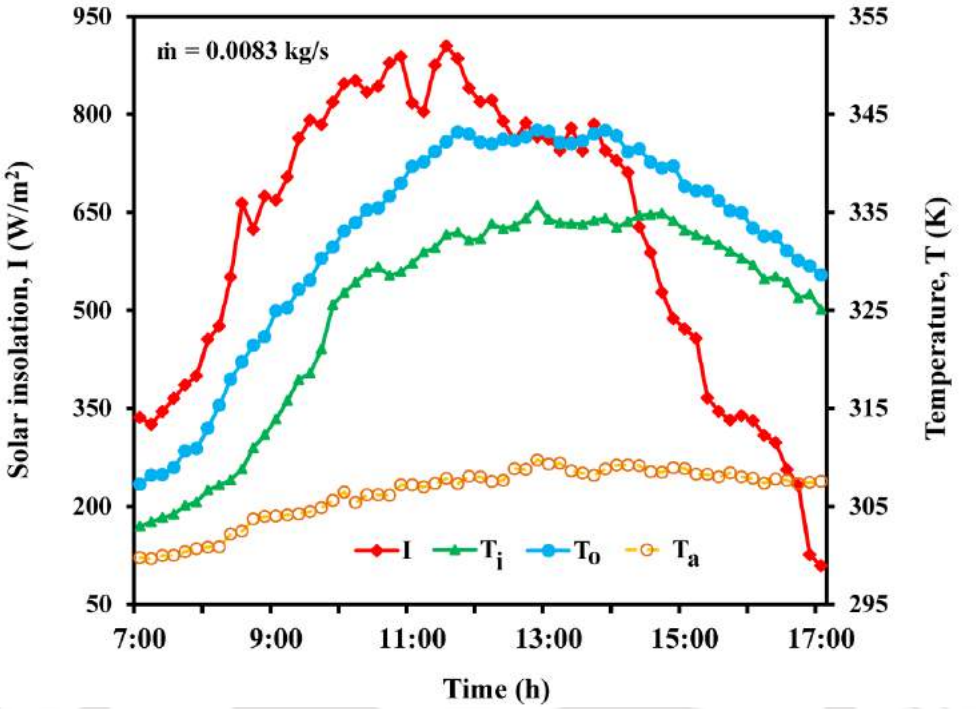

Fig.6.12 Variation of measured experimental result versus time

Figure 6.13 shows a plot of temperature versus time for the paraffin wax during the charging process.

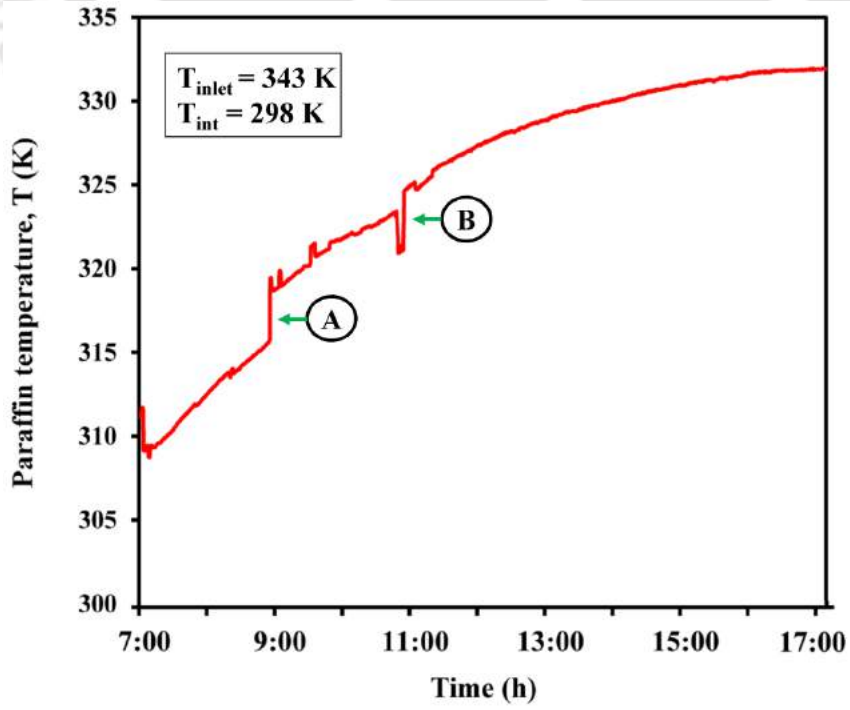

Fig.6.13 Variation of paraffin wax temperature versus time

The result was plotted by taking the average temperature of the four thermocouples T1 to T4 shown in Fig.4.9. From the figure two sudden rise in temperature was observed; (i) 315 K- 318.5 K labelled A and (ii) 320 K- 323.5 K labelled B. This observed phenomenon may be due to the presence of impurities in the paraffin wax. Taking the average value between the two labels gives the paraffin temperature of 321 K which is in the range of 318.5 K to 323.5 K. The average temperature of paraffin wax obtained in the present study is similar that of the melting temperature of pure paraffin wax reported by Niyas and Muthukumar (2013). Hence, the melting temperature taken for the numerical model in the present study was acceptable.

6.7Melting Enhancement and Performance Evaluation of Paraffin Wax Dispersed with Al_2O_3 Nanoparticles

This section presents the comparison study between pure paraffin and paraffin wax dispersed with alumina oxide (Al_2O_3) nanoparticle filled storage in terms of performance parameter. The comparison was carried out using the numerical model. The volume fraction of the nanoparticles considered for the present investigation was 10%. This was decided based on the experimental results of Ho and Gao (2009) and Valan *et al.* (2013). Henceforth, paraffin wax dispersed with Al_2O_3 nanoparticles will be referred as "nanofluid".

6.7.1 Variation in thermo-physical properties

The change in thermodynamic properties namely, density, dynamic viscosity, thermal conductivity, latent heat of fusion and specific heat with respect to temperature and volume fraction of nanoparticle were determined based on the correlations given in **Appendix–C**. The results are plotted in Fig.6.14. The main observations from Fig.6.14 are: (i) Addition of 10% Al_2O_3 nanoparticles resulted in an increase in density of paraffin from 760 kg/m^3 to 1031 kg/m^3 (Fig.6.14 (a)), (ii) Addition of 10% Al_2O_3 nanoparticles resulted in an increase in dynamic viscosity of paraffin from 0.003 Pa.s to 0.013 Pa.s ((Fig.6.14 (a)), (iii) Addition of 10% Al_2O_3 nanoparticles resulted in an increase in thermal conductivity of paraffin from 0.2 W/m.K to 0.37 W/m.K (Fig.6.14 (c)), (iv) Addition of 10% Al_2O_3 nanoparticles

resulted in reduction in specific heat of paraffin from 2000 J/kg.K to 1575 J/kg.K (Fig.6.14 (d)) and (v) Addition of 10% Al_2O_3 nanoparticles resulted in reduction in latent heat of fusion of paraffin from 168 kJ/kg to 1575 J/kg (Fig.6.14 (e)).

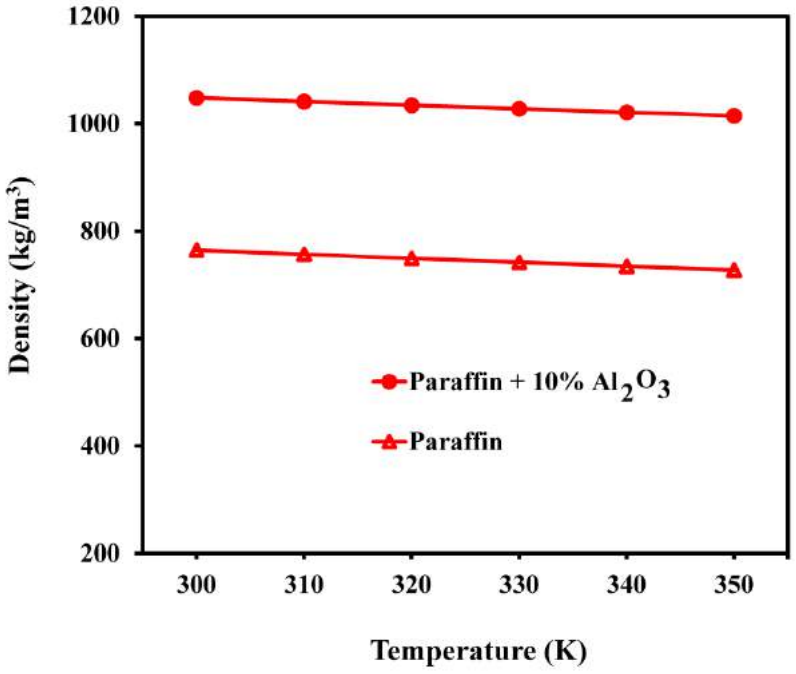

(a)

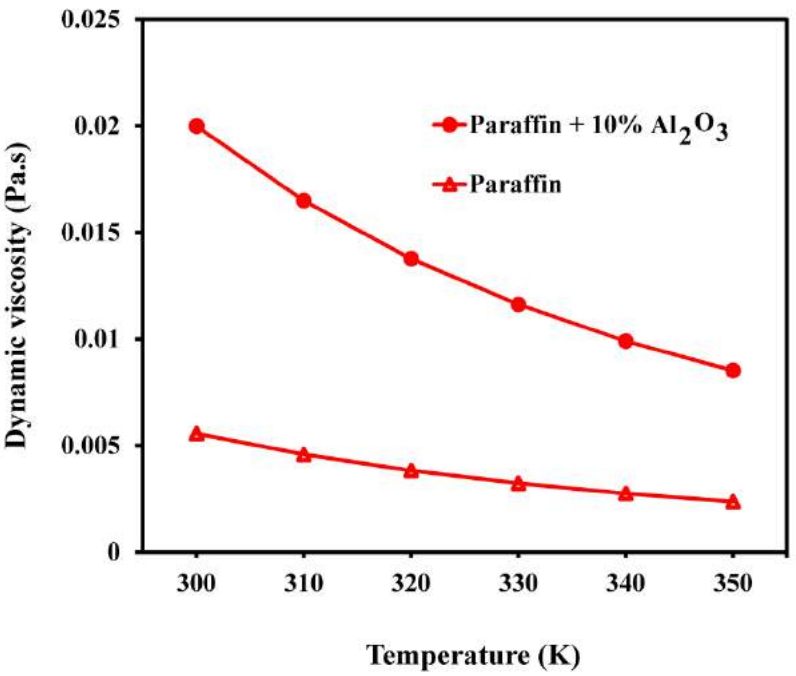

(b)

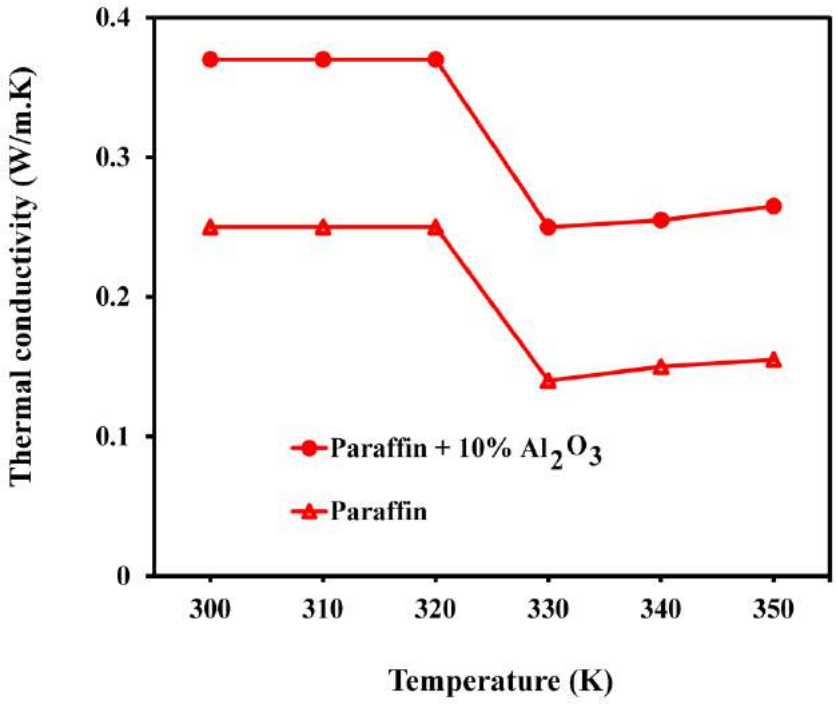

(c)

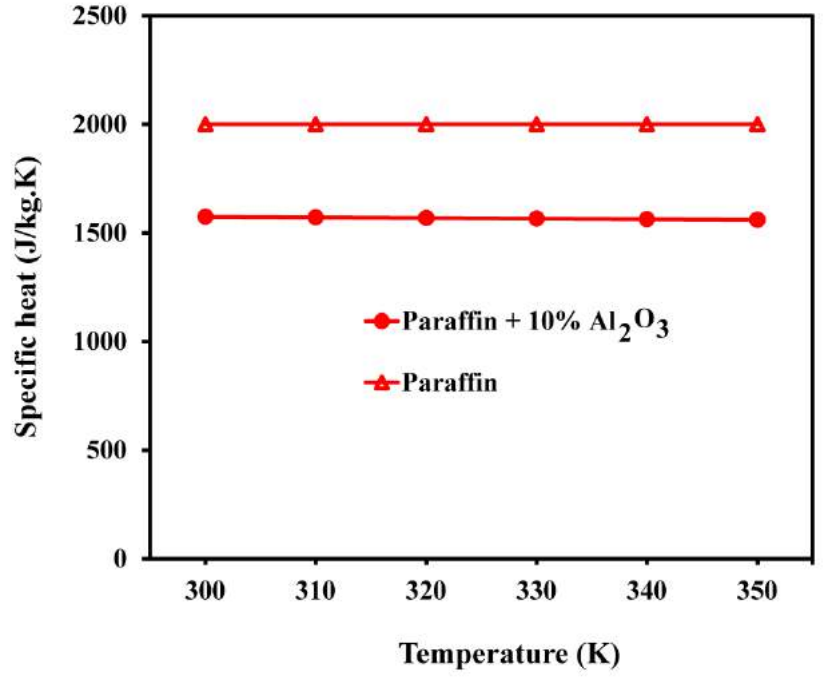

(d)

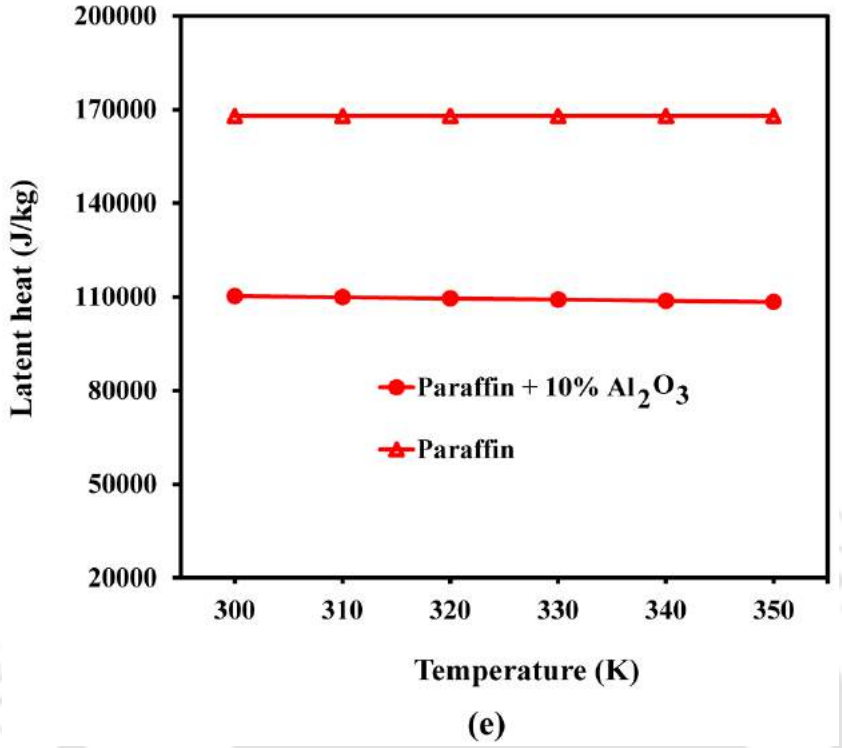

Fig.6.14.Variation in (a) density (b) dynamic viscosity (c) thermal conductivity (d) specific heat and (e) latent heat versus temperature

It can be concluded from the observation that addition of nanoparticles enhances the natural convection heat transfer due to increase in dynamic viscosity and reduces the storage capacity of the LHS due to the reduction in specific heat and latent heat of fusion.

6.7.2 Plot of average melt fraction

Figure 6.15 presents the plots of melt fraction for Al_2O_3 nanoparticle dispersed paraffin at different time during charging and discharging process. It is seen from the figure that the time taken to reach complete charging is very less compared to the time take to reach a complete discharged state. The total time taken for the nanofluid to melt completely is 40 min. However, at that particular time, the solidification process was only partial. This is due to the presence of natural convection heat transfer during the charging process whereas the discharging process is conduction dominated.

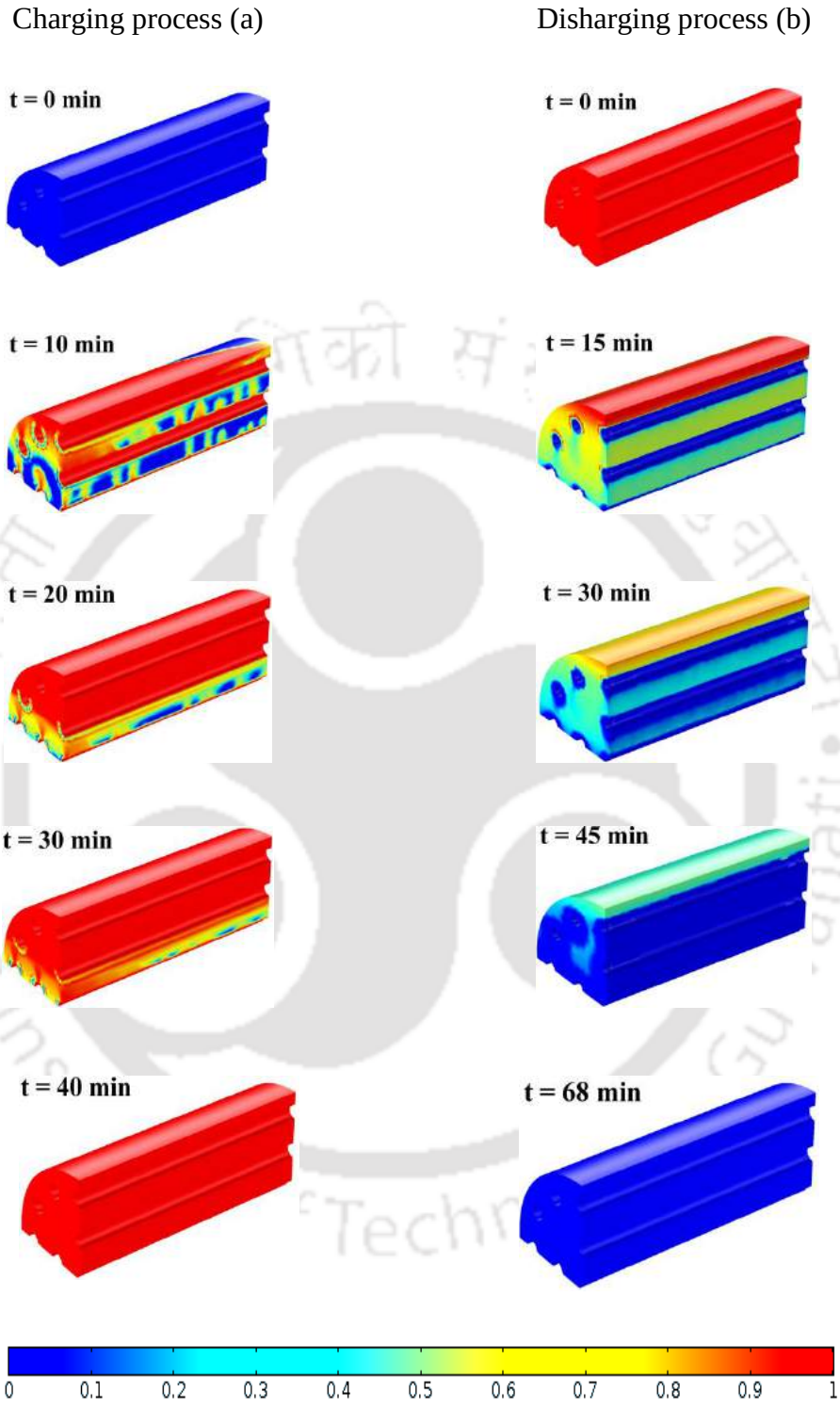

Fig.6.15 Plot of melt fraction versus time (a) charging and (b) discharging process

6.7.3 Effect of nanoparticle addition on average melt fraction

Figure 6.16 plots the variation in average melt fraction with time during charging and discharging process.

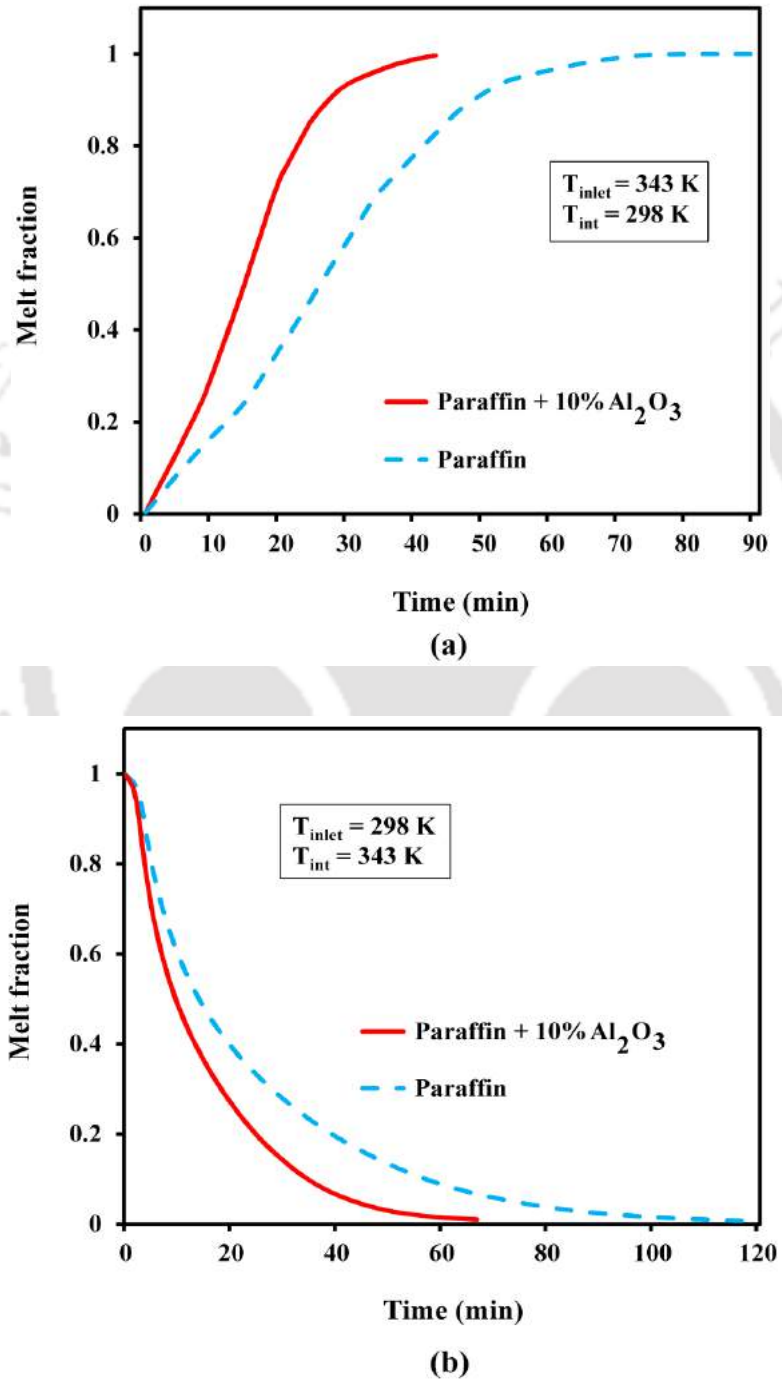

Fig.6.16 Variation of average melt fraction versus time during (a) charging and (b) discharging process

The HTF fluid is maintained at 343 K/ 298 K during the charging/discharging process. As shown in Fig.6.16 (a), the melt fraction varies slowly with time during the initial phase. During charging, as the nanofluid is initially in a solid state, the primary heat transfer occurs by molecular diffusion. However, with an increase in time, phase change occurs facilitating natural convection which gradually favours faster melting.

It can be observed from Fig. 6.16 (a) that the slope of variation in melt fraction with time in the initial phase is relatively steeper for nanofluid. The possible mechanism is the enhancement in conductivity upon dispersing highly conductive nanoparticles. It is further noticed that pure paraffin wax based PCM takes 90 min to reach a completely melt stage whereas nanofluid attains this stage in 40 min, which is 45% faster.

Figure 6.16 (b) shows that the time taken to reach a fully discharged state is nearly 1.8 times faster with nanofluid compared to with pure paraffin wax. As the PCM remains initially in liquid stage, buoyancy effect dominates the discharging process and the primary mode of heat transfer occurs by natural convection. In due course of time, as the PCM gets solidified, conduction heat transfer takes place. For both pure paraffin and nanofluid, the discharging time is significantly more than the charging time.

6.7.4 Effect of nanoparticle addition on average temperature

The effect of variation in volumetric averaged temperature during charging/ discharging is shown in Fig.6.17 (a) and (b). It is evident from the simulation data (Fig.6.17 (a)) that the time taken to reach completely charged state for pure paraffin and nanofluid is 90 min and 40 min respectively, i.e., 1.8 times faster for the nanofluid. Figure 6.17 (b) indicate that the pure paraffin wax based PCM requires 120 min for complete discharging whereas the nanofluid takes 68 min which is comparatively 1.8 times lesser. Moreover, the average temperature variation followed the same trend with reported results of Thapa *et al.* (2014) for nanofluid and Niyas and Muthukumar (2013) for paraffin-based LHS.

Generally, the dispersion of Al_2O_3 nanoparticle in paraffin wax is more effective for charging/discharging process compared to pure paraffin.

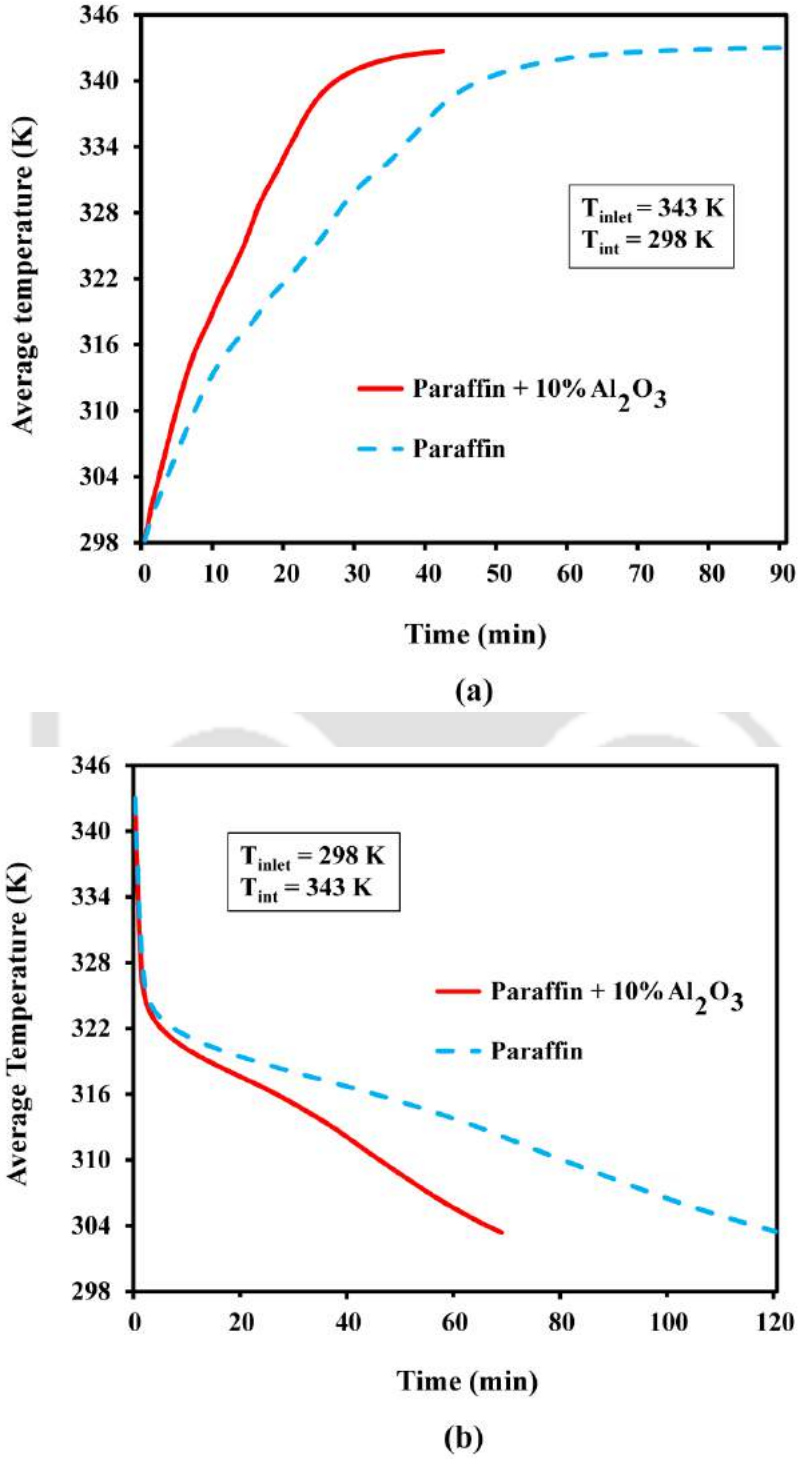

Fig.6.17 Variation of average melt fraction versus time during (a) charging and (b) discharging process

6.8 Energy Stored /Released

This section presents the energy stored/discharged for pure paraffin and nanofluid during charging and discharging process. The energy stored/discharged includes sensible energy, latent heat energy and total energy.

6.8.1 Sensible heat stored/discharged

The variation of sensible heat stored/discharged for nanofluid and pure paraffin wax filled LHS is depicted in Fig.6.18.

It is evident from equations (Eq. (3.37) and (3.40)) that the sensible heat is directly affected by the specific heat of the phase change material. As the volumetric percentage of nanoparticle increases, the specific heat of the phase change material decreases. This is clearly observed from Fig. 6.14 (d) that the specific heat of pure paraffin initially was 2000 J/kg.K and addition of 10% of nanoparticle in paraffin wax reduced the specific heat to 1582 J/kg.K.

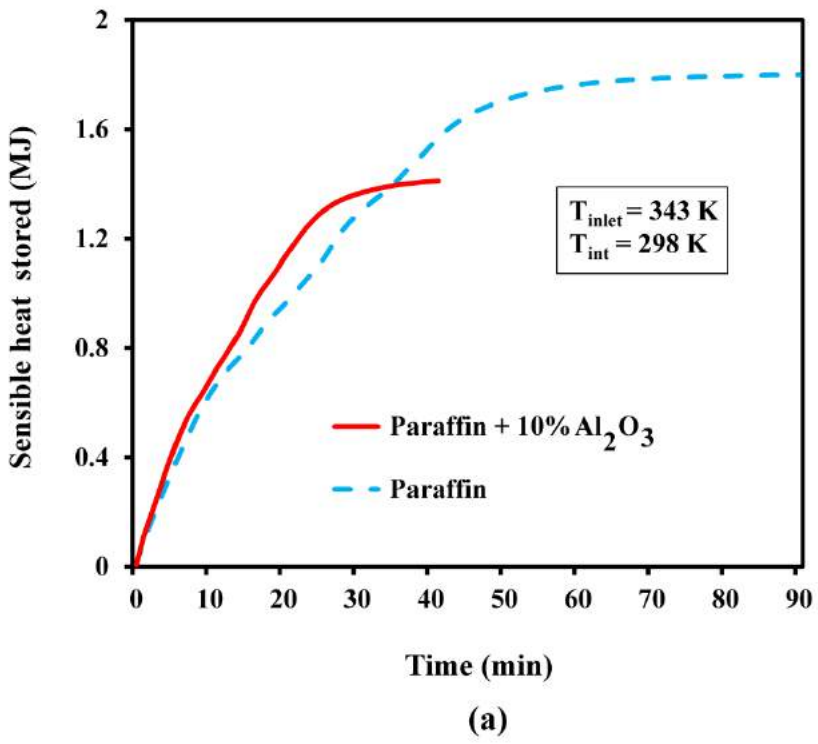

(a)

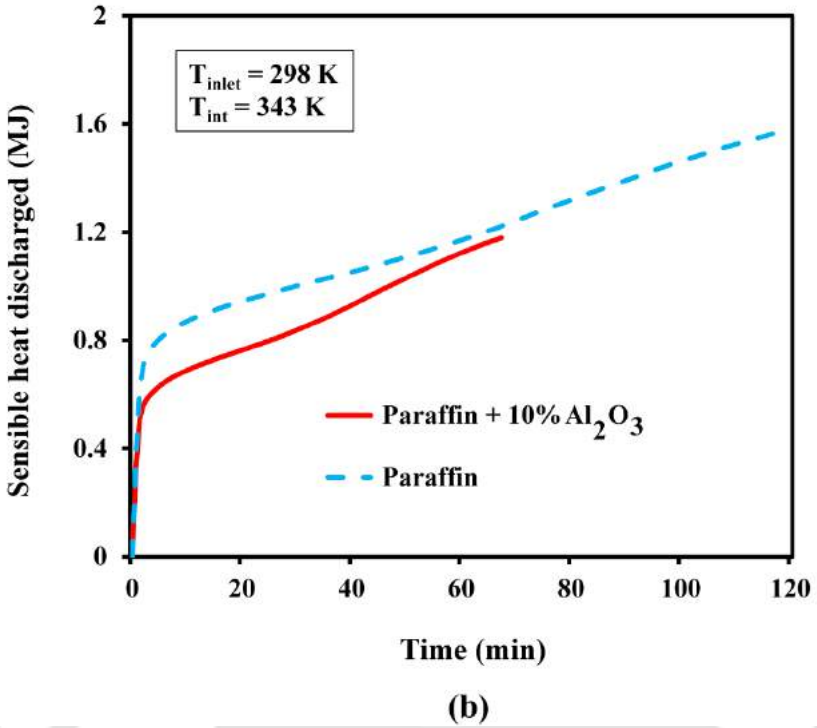

Fig. 6.18 Variation of sensible heat stored/released during (a) charging and (b) discharging process

During the charging process, it is noticed (Fig. 6.18 (a)) that the maximum sensible heat stored was 1.37 MJ for the nanofluid at 40 minutes whereas it was 1.8 MJ for pure paraffin wax filled LHS at 90 minutes. The result also reveals that the addition of 10% Al_2O_3 reduces the sensible heat stored by 1.3 times compared to the pure paraffin. Similarly, during the discharging process (Fig. 6.18 (b)), the amount of sensible heat released from the nanofluid in the storage was 1.1MJ at 68 minutes whereas this value was 1.6 MJ for pure paraffin filled storage at 120 minutes. This indicates that the sensible heat discharged using pure paraffin based storage was 1.45 times higher compared to nanofluid storage.

6.8.2 Latent heat stored/discharged

The variation of latent heat stored/discharged for nanofluid and pure paraffin wax filled LHS was plotted based on Eq. (3.38) and (3.41). The plot is illustrated in Fig. 6.19.

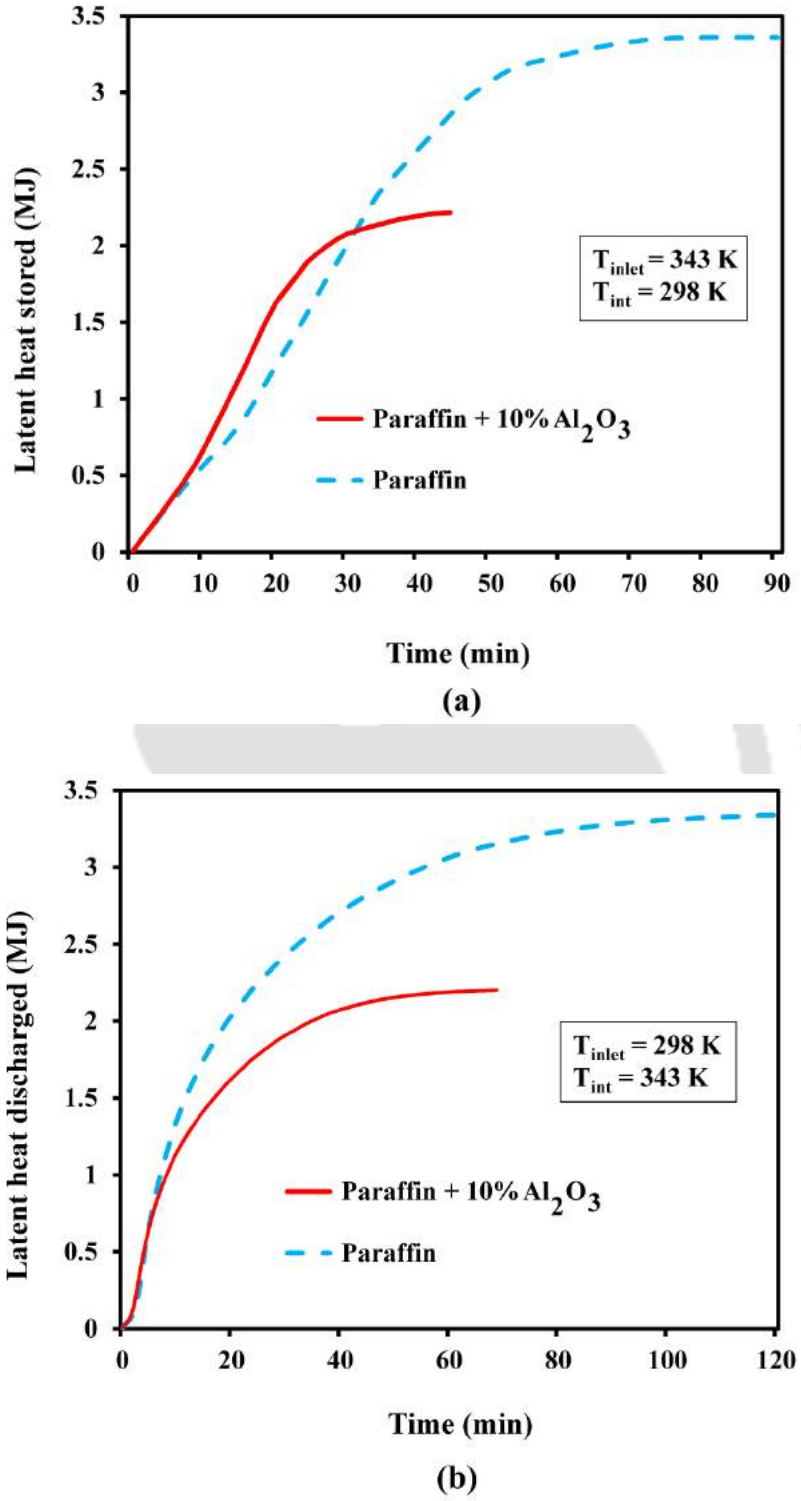

Fig. 6.19 Variation of latent heat stored/released during (a) charging and (b) discharging process

It is seen from the equations that the PCM latent heat of fusion affects the latent heat storing capacity. Increasing the volumetric percentage of nanoparticle decreases the PCM latent heat of fusion. It is evident from Fig. 6.14 (e) that the latent heat of fusion for pure paraffin was 168 kJ/kg and dispersion of 10% of Al_2O_3 nanoparticle reduced the latent heat of fusion to 111 kJ/kg.

Figure 6.19 (a) indicate that the maximum latent heat stored was 2.2 MJ with the nanofluid at 40 minutes whereas this value was 3.44 MJ with pure paraffin wax filled LHS at 90 minutes during the charging process. Similarly, the amount of latent heat discharged from the nanofluid (Fig 6.19 (b)) was 2.2 MJ at 68 minutes and 3.2 MJ for pure paraffin filled storage at 120 minutes during the discharging process.

6.8.3 Total heat stored/discharged

The variation of total energy stored/discharged for nanofluid and pure paraffin wax filled LHS was plotted based on Eq. (3.39) and (3.42). This variation in total heat stored/discharged versus time is plotted in Fig.6.20.

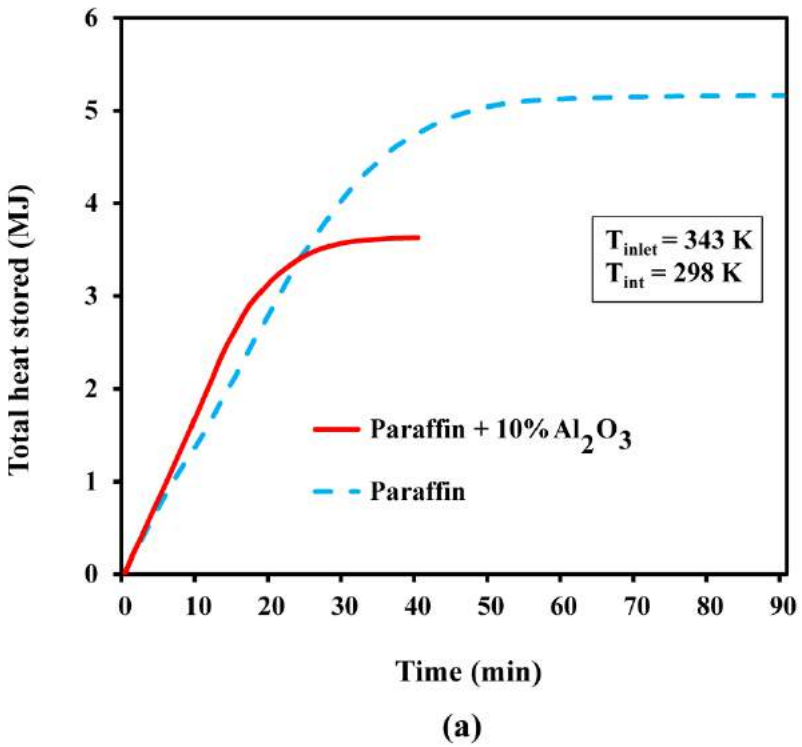

(a)

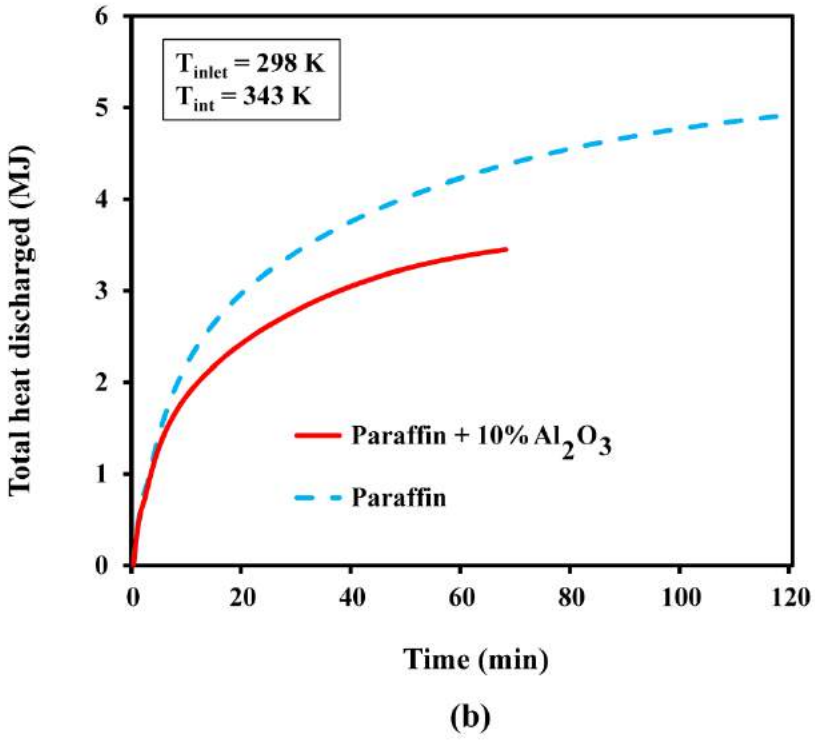

(b)

Fig. 6.20 Variation of total heat stored/released during (a) charging and (b) discharging process

The total heat stored depends on the latent heat of fusion and specific heat of the PCM. Since dispersion of nanoparticle decreases the latent heat and specific heat of PCM, the total energy stored in the LHS is expected to be lower than pure paraffin based LHS. It is clear from Fig.6.20 (a) that during the charging process, the total heat stored was 3.57 MJ for the nanofluid at 40 minutes whereas it was 5.24 MJ for pure paraffin wax based LHS at 90 minutes. Similarly, during the discharging process, the total heat released from the nanofluid based storage was 3.3 MJ at 68 minutes and 4.8 MJ for pure paraffin based LHS at 120 minutes (Fig.6.20 (b)).

6.9 Summary

A 3D numerical model of shell-and-tube LHS is developed for investigating the storage characteristics during charging and discharging processes using paraffin wax as PCM. The study also covered optimization of the number of charging/discharging tube, cylinder orientation and tube configuration. To validate the numerical model

with experimental results, the developed model was compared with experimental results and was found to be good agreement. Further, performance parameters like melt fraction, charging/discharging time, energy stored/ discharged was also estimated. Since the conductivity of paraffin wax is low, enhancement in thermal conductivity was found to be necessary. The dispersion of Al_2O_3 nanoparticle (nanofluid) in paraffin wax and comparison study with pure paraffin based storage was also carried out. Further, validation of the nanofluid-based storage with the earlier published work is also performed and found in good agreement. Chapter 7 presents the results and discussion of the integrated solar thermal system.

Chapter - 7

Application of the Integrated Solar Thermal System for Biogas Production

7.1 Introduction

This Chapter reports the experimental procedure and results of the integrated solar thermal system to use as a heat source for biogas production. The experiments were performed under two conditions, namely controlled and uncontrolled conditions. The uncontrolled experiment was carried out for developing the relationship between shell tank and biogas digester in terms of temperature variations. A programing language was developed based on the relation obtained from uncontrolled conditions.

7.2 Uncontrolled Conditions

7.2.1 Experimental setup and procedures of uncontrolled conditions

The main aim of the uncontrolled experiment was to develop the relationship between the shell tank and biogas digester in terms of temperature variations. This relationship will help to develop a programing language for maintaining a constant temperature range in the biogas digester. The experimental procedure of the uncontrolled condition was similar to the cascaded collector presented in subsection 4.3.3.

Figure 7.1 shows the schematic diagram of uncontrolled experimental setup. Water from the reservoir tank is pumped to the solar collector which gets heated. The heated water circulates through the latent heat storage system to where the energy is absorbed and stored. The heat is further transferred to the shell tank through the heat exchanger to raise the temperature of the fluid in the shell tank. During unavailability of solar radiation, the stored heat from the LHS is transferred to the fluid in the shell tank.

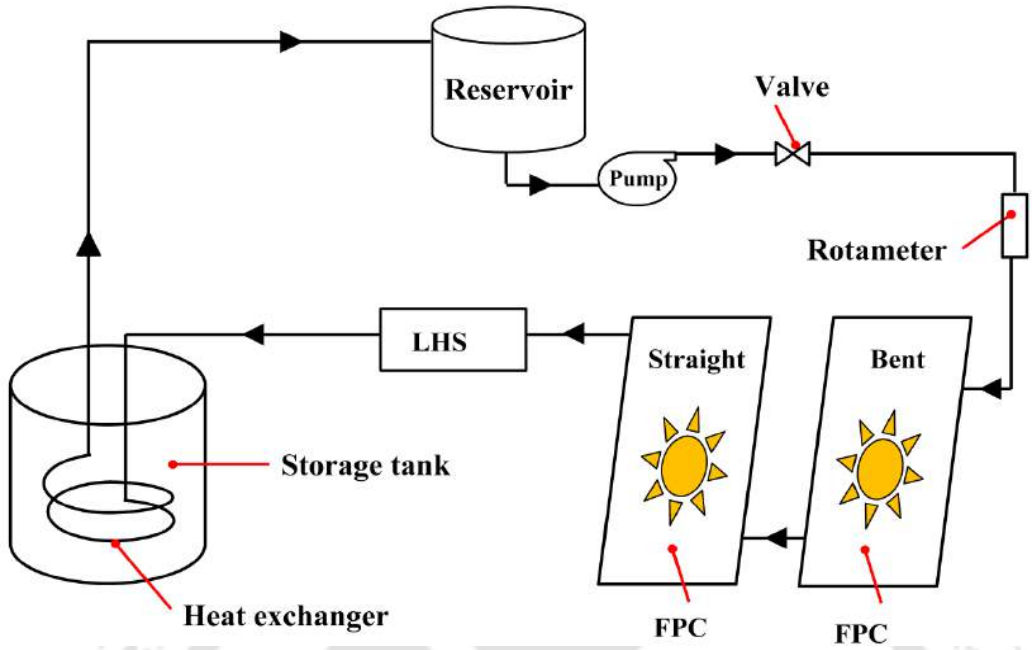

Fig.7.1 Schematic diagram of uncontrolled experimental setup

The main focus of this experiment was the storage tank. The storage tank carried two tanks, namely biogas digester and shell tank. The shell tank was filled with water whereas the biogas digester was filled with feed material. Further, to eliminate heat loss from the shell, the inverted tank was placed over the biogas digester. Figure 7.2 presents the schematic diagram of the shell, biogas digester, inverted tank and various locations of thermocouples.

There were four number of T-types thermocouples which were placed in the storage tank to measure the temperature of the shell and biogas digester. Two thermocouples were placed at the top (Ta_t) and bottom (Ta_b) of the shell tank. The biogas digester temperature was measured by the two thermocouples which were placed at the bottom (Bi_b) and top (Bi_t) region of the biogas digester. Temperature of the heat exchanger at the inlet and outlet was measured by using T-type thermocouples which were placed at the inlet (Hx_i) and outlet (Hx_e) of the heat exchanger. Experiment on the heat exchanger was carried out to study the temperature variation between the inlet and outlet side. For that, two T-type thermocouples with an accuracy of ± 0.5 ºC were placed at the inlet and outlet side of the heat exchanger.

The flow rate was measure by a rotameter. The photograph of the helical coil heat exchanger is depicted in Fig.7.3.

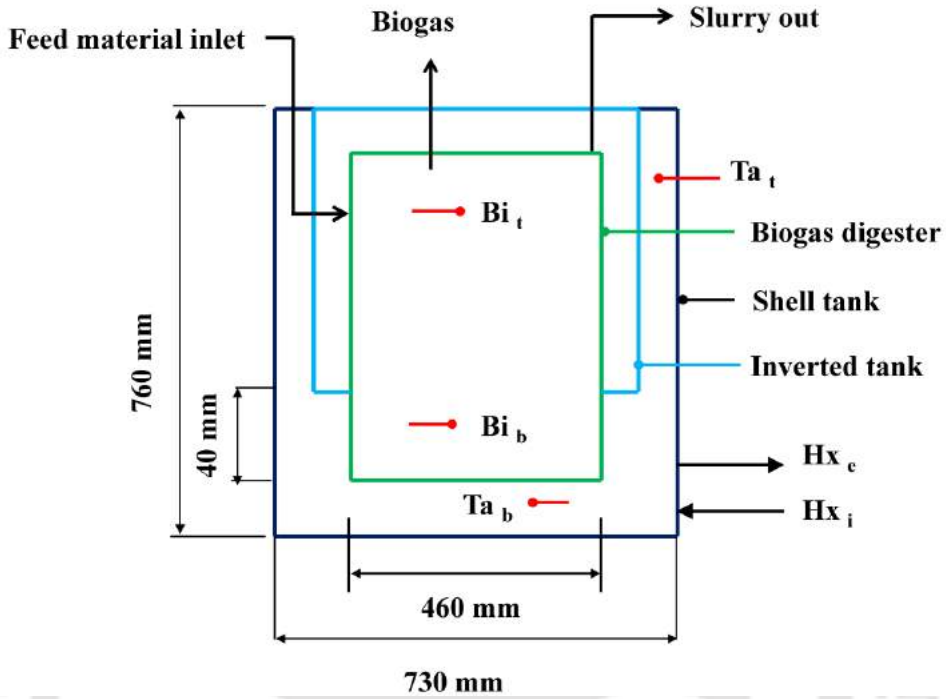

Fig.7.2 Schematic diagram of the various components in the storage tank

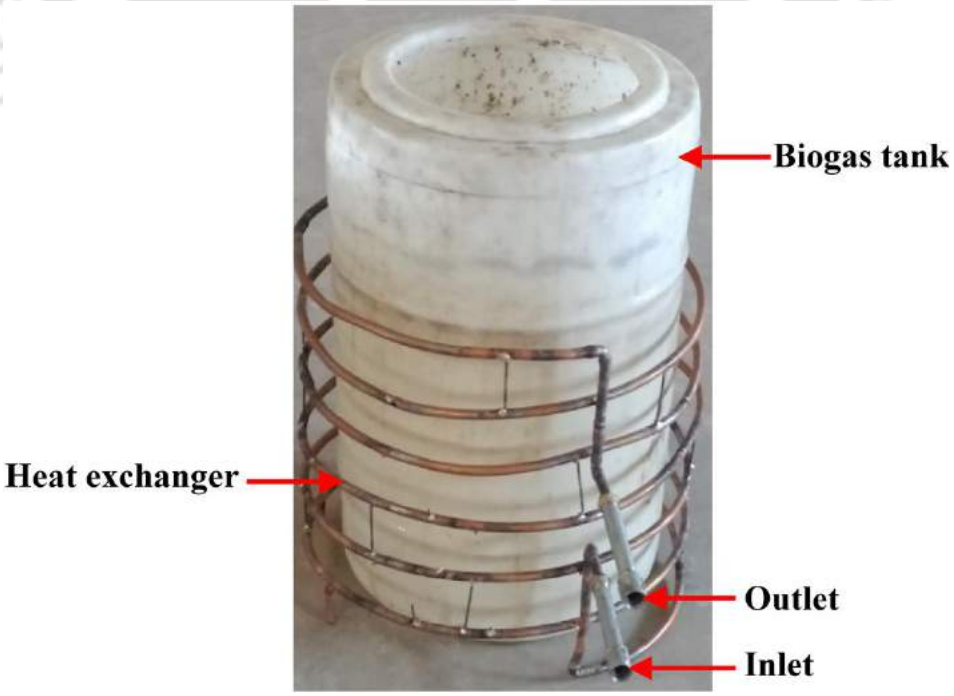

Fig.7.3Photograph of the helical coil heat exchanger

7.3 Results and Discussion

7.3.1 Temperature variation in biogas digester and shell tank without control system

Since the outlet temperature from collector-2 ($T_{o\,c2}$) is the inlet of the shell tank, it is important to plot the variation of the average solar insolation and outlet water temperature with time. The variation of solar insolation and outlet water temperature versus time at mass flow rate of 0.0083 kg.s^{-1} is presented in Fig.7.4. The variation in solar insolation during the test period varied from 280 W.m^{-2} to 860 W.m^{-2} with an average of 662 W.m^{-2}. The maximum solar insolation was recorded between 10:50 h and 12:30 h. The outlet water temperature from the collector-2 ($T_{o\,c2}$) varied from 309.8 K and reached the maximum temperature of 326.3 K at 13:30 h and then decreased. Similarly, the average ambient air temperature (T_a) was in the range of 299 K–308 K with an average value of 303.5 K.

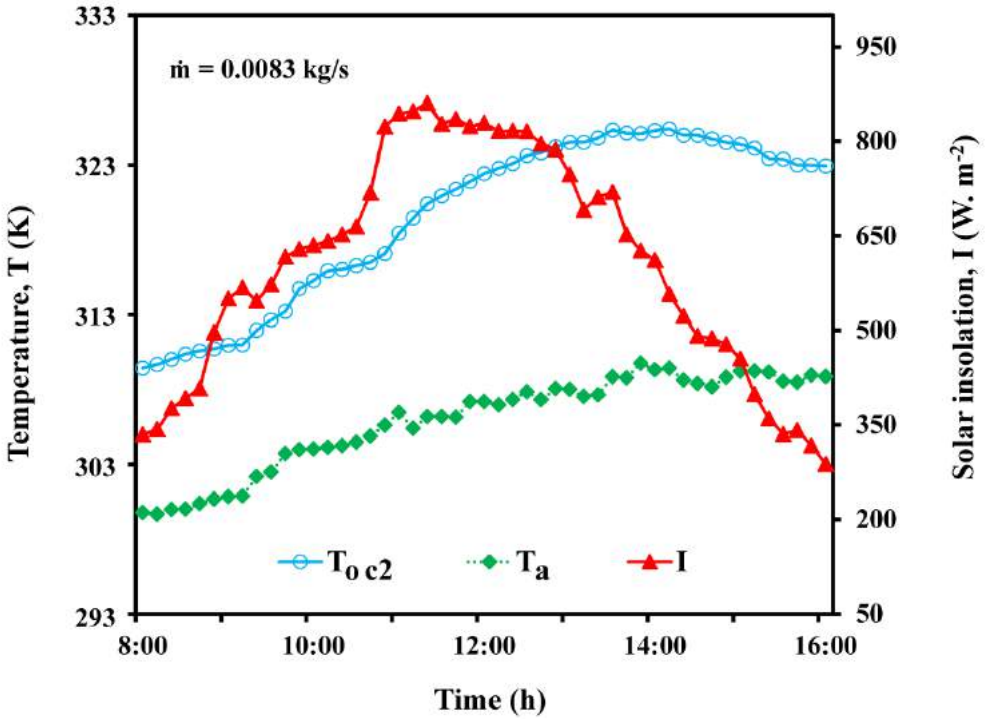

Fig.7.4 Variation of solar insolation and outlet water temperature versus time

The variation of temperature in the shell tank (top (Ta_t) and bottom (Ta_b)) and biogas digester temperature (top (Bi_t) and bottom (Bi_b)) versus time is shown in Fig.7.5.

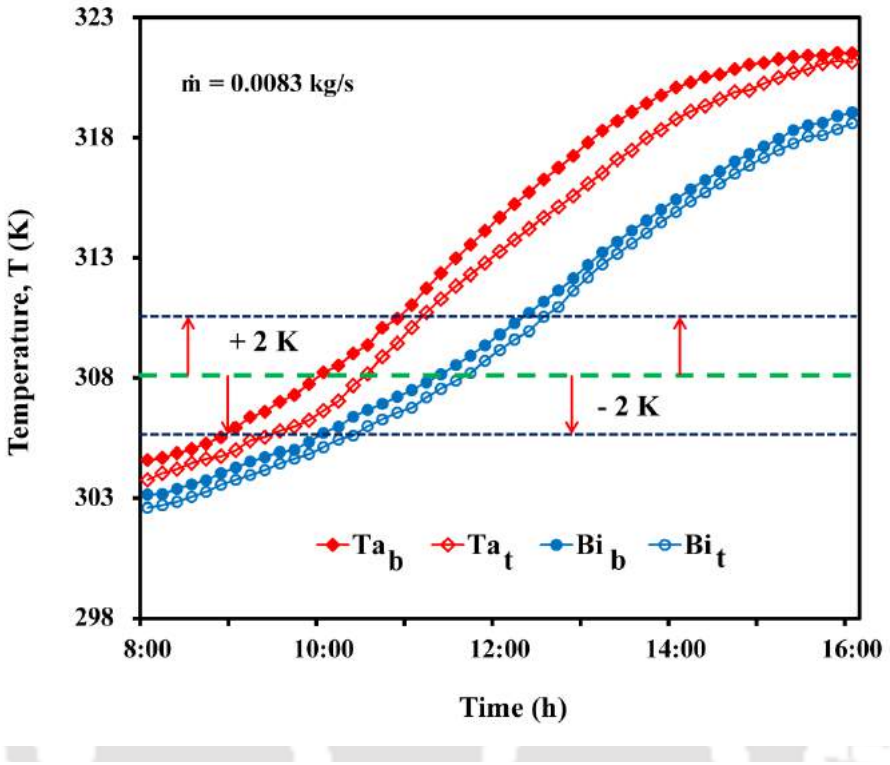

Fig.7.5 Variation of shell and biogas digester temperature versus time

It is observed from the figure that the shell tank temperature at the bottom and top varied from 304.5 K to 321.7 K and 303.7 K to320.9 K, respectively. Since the inlet of the heat exchanger is located at the bottom portion, the biogas digester temperature at the bottom portion was higher than the top. The temperature in biogas digester varied from 303.2 K to 319.1 K at the bottom whereas this variation at the top was from 302.7 K to 318.6 K. The average biogas digester temperature was about 311 K. Zinder *et al*. (1984) reported the optimum temperature range for growing methane forming bacteria in the range from 303 K to 313 K with an average of 308 K and deviation of ± 2 K. It is evident from Fig.7.5 that during the period 8:00 h – 10:20 h, the temperature inside the biogas digester was 5 K lower than the ideal value.

However, after 13:00 h, the temperature inside the biogas digester was 9 K higher than the ideal value. Similar experiments were also carried out at the same flow rate to check the repeatability and is reported in Fig.7.6.

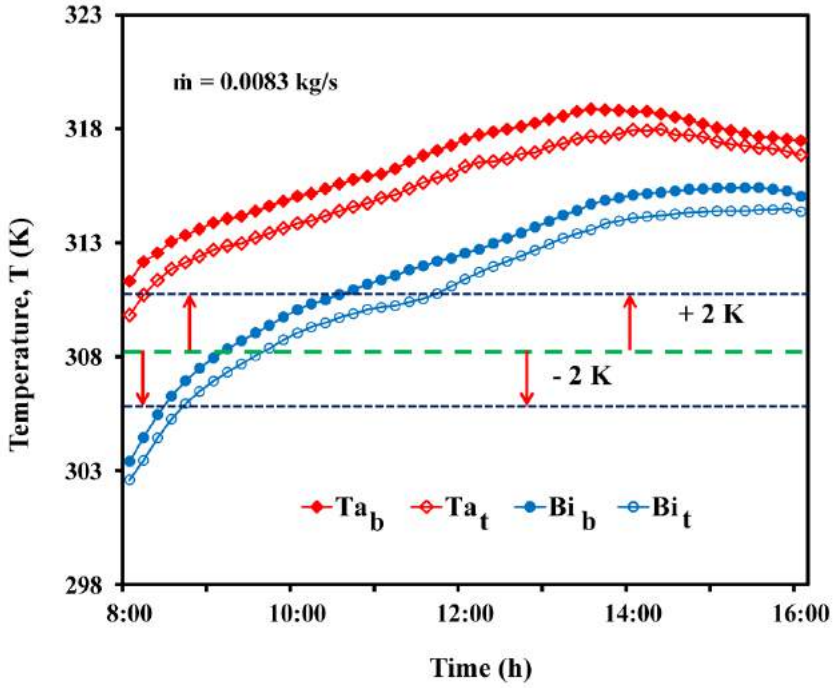

Fig.7.6 Variation of shell and biogas digester temperature versus time

The figure showed that the biogas digester temperature varied in the range from 303.1 K to 314 K whereas inside the shell tank, the variation was in the range 310 K – 318 .1 K. It is clear from Fig.7.6 that during the period 8:00 h – 10:20 h, the temperature inside the biogas digester was 5 K lower than the ideal value. However, after 13:00 h, the temperature inside the biogas digester was 9 K higher than the ideal value. It can be concluded from the two uncontrolled results that the biogas average temperature varied in the range from 307.5 K to 309 K when the shell tank temperature varied from 313 K to 315 K. Due to the observed temperature fluctuation inside the biogas digester, it was necessary to develop a control mechanism to ensure favourable temperature range for the growth of mesophilic microbes.

7.3.2 Heat exchanger temperature variations

The temperature variation at the inlet and outlet side of the heat exchanger versus time for the uncontrolled test is plotted in Fig.7.7. It is observed that the heat exchanger inlet temperature (Hx_i) increased from 314 K at 8:00 h and reached a peak value of 329 K during the mid-day. Similarly, the heat exchanger outlet temperature (Hx_e) was 303 K in the morning and 315.2 K during the mid-day. The maximum temperature drop at the inlet and outlet side of the heat exchanger was approximately 12.6 K which was recorded between 11:30 h to 12:00 h. Since the outlet of the collector was connected to the heat exchanger inlet, the inlet temperature of the heat exchanger was higher.

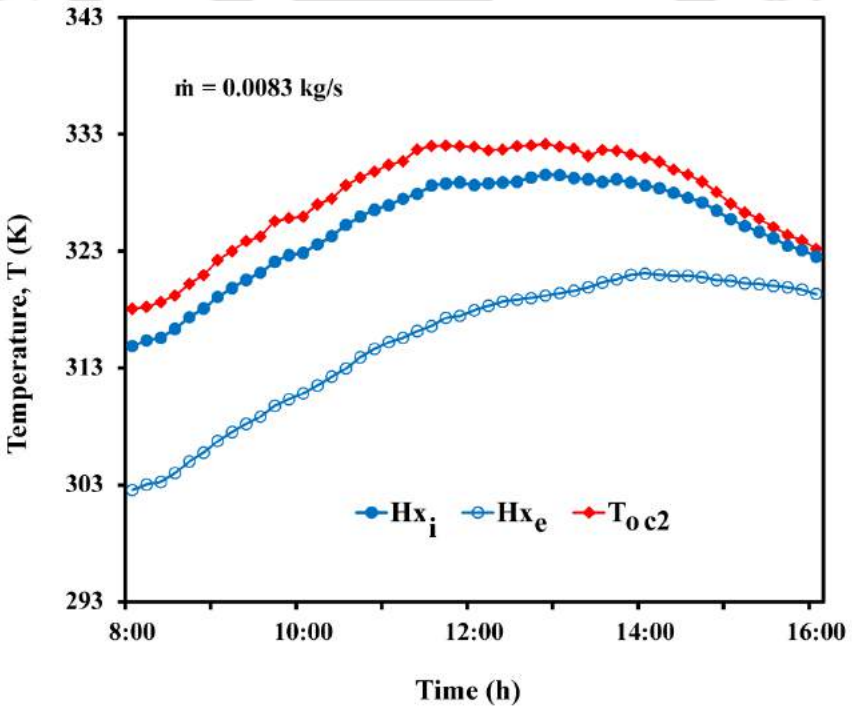

Fig.7.7 Heat exchange temperature variation versus time

Similar experiments were also carried out at the same flow rate to check the repeatability and reported in Fig.7.8. It is observed that the inlet temperature of the heat exchanger varied from 307.9 K in the morning to 321.7 K at 16:00 h. The peak heat exchanger inlet temperature was 324 K which was at 14:00 h. The maximum temperature drop between inlet and outlet side was found to be 6.9 K at 12:00 h.

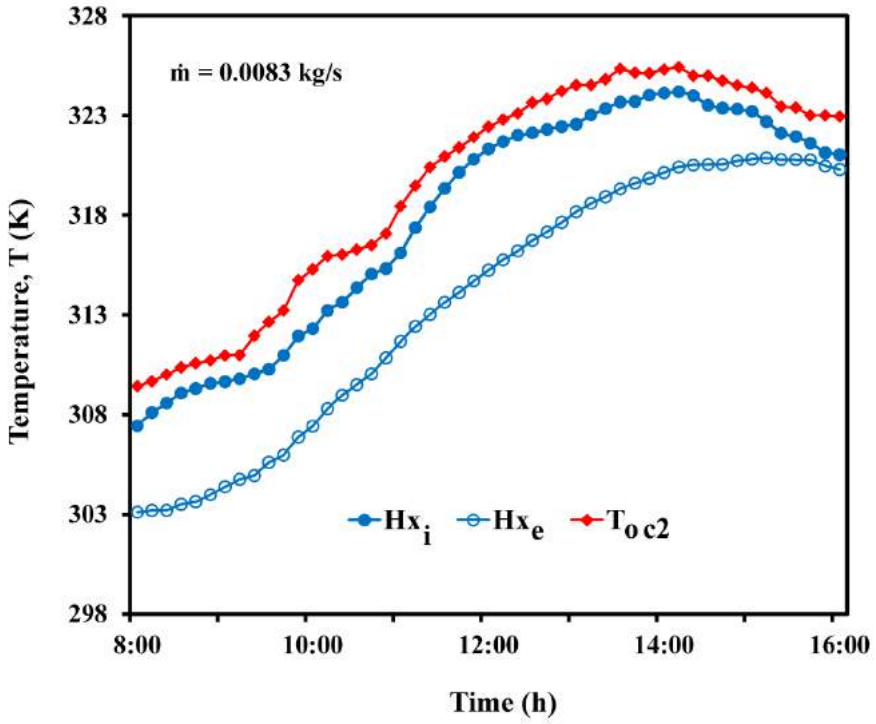

Fig.7.8 Heat exchanger temperature variation versus time

7.4 Controlled Conditions

7.4.1 Experimental setup and procedure

The aim of the controlled experiment is to maintain the temperature of the feed material inside the biogas digester at 308 ± 2 K for mesophilic digestion. In order to maintain the temperature inside the biogas digester under control condition, a feedback control system consist of two solenoid valves, Arduino microcontroller, motor driving modules, thermostat and DC voltage supply was used along with the cascade system. This is shown in Fig.7.9. The various instruments used and the computer code developed for the micro controller is presented in the **Appendix–E** and **Appendix–F**.

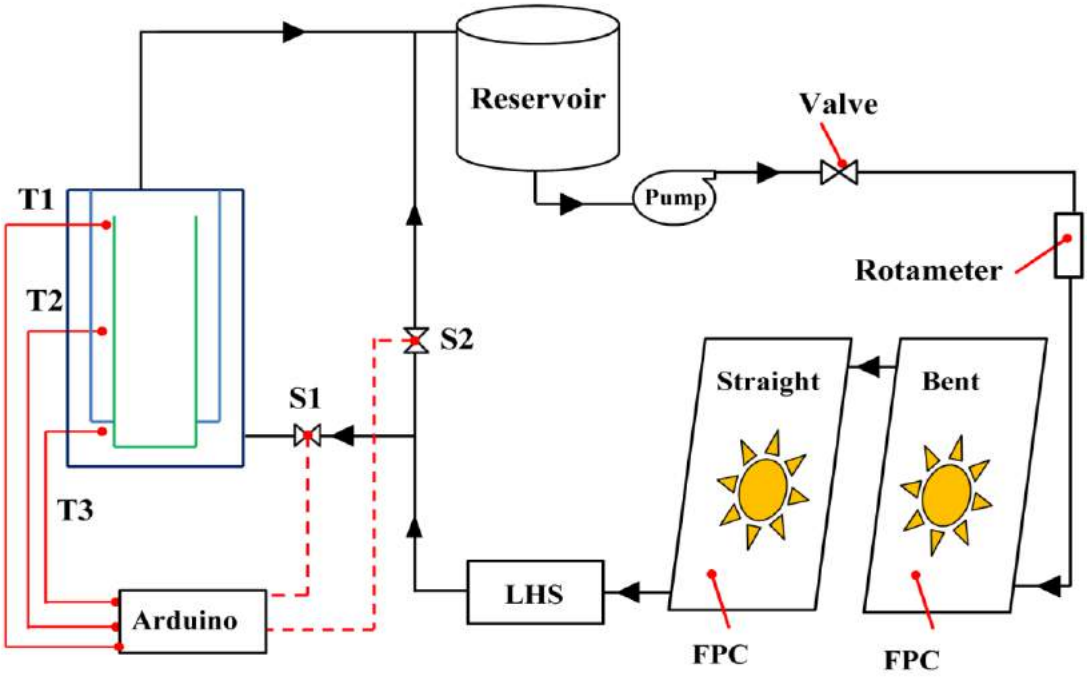

Fig.7.9 Schematic diagram of the controlled solar thermal plant experimental setup

Using the results obtained from the uncontrolled experiment, a relationship between the temperature of the digester and shell tank was developed which was incorporated in C language program with necessary algorithms. This algorithm was to divert the water flow away from the shell tank when the shell temperature exceeds 315 K. Alternatively when the shell temperature falls below 313 K, the solenoidal valves are actuated for providing the desired flow rate in the shell tank. At the end of the experiment (night period), when the temperature falls below the desired limit, the controlled electric heater placed in the shell tank heats the biogas digester.

The temperature reading from the shell tank was measured by three LM35 temperature sensors (T1, T2 and T3) which were placed at the top, middle and bottom of the shell tank. These sensors are capable of measuring temperature in the range from -50 ºC to150 ºC. The analog reading from the LM35 temperature sensors are detected by the Arduino microcontroller. Based on the signals sent from the microcontroller, the motor driving module controls the solenoidal valves thereby diverting the fluid flow. The program was written in such a way that when the temperature in the shell tank reaches 315 K, the solenoid valve (S1) is closed and

solenoid valve (S2) open. During this, the heat energy is stored in the latent heat storage system to use at night or cloudy time. Similarly, when the shell temperature drops below 313 K, the solenoid valve (S1) is open and solenoid valve (S2) closed.

7.5 Results and Discussion

Figure 7.10 shows the variation of outlet water temperature ($T_{o\ c2}$), ambient temperature (T_a) and solar insolation (I) versus time obtained during the experiment. The controlled experiment was carried out at a constant flow rate of 0.0083 kg.s^{-1} during the period from 6:00 h to 19:00 h.

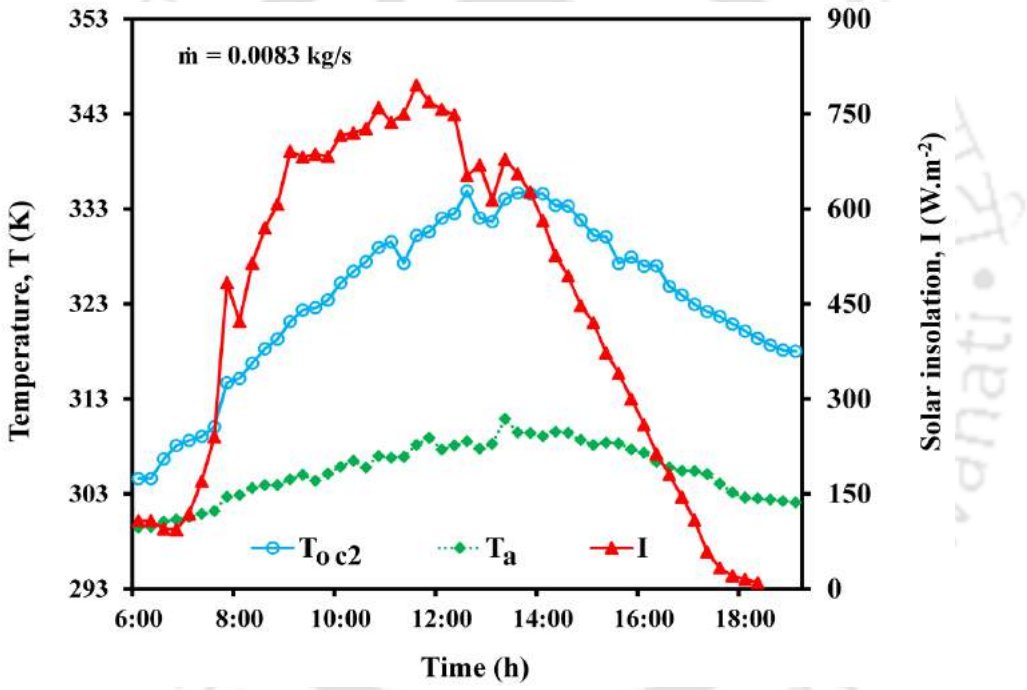

Fig.7.10 Variation of solar insolation and outlet water temperature versus time

It is clear from the figure that the solar insolation is negligible after 17:00 h. The solar insolation during the test period varied from 187 W.m^{-2} at early morning and reached peak value of 795 W.m^{-2} at the mid-day. The maximum solar intensity was recorded between 11:00 h and 12:20 h. The outlet water temperature during the experiment varied from 304 K and reached 335 K at the mid-day and then decreased to 319 K at 19:00 h. During this period, the ambient temperature was varying in the range of 300 K – 310 K with an average of 305 K.

The result of the control experiment, i.e., the variation of the biogas digester temperature and shell tank temperature at flow rate of 0.0083 kg.s^{-1} is plotted in Fig.7.11.

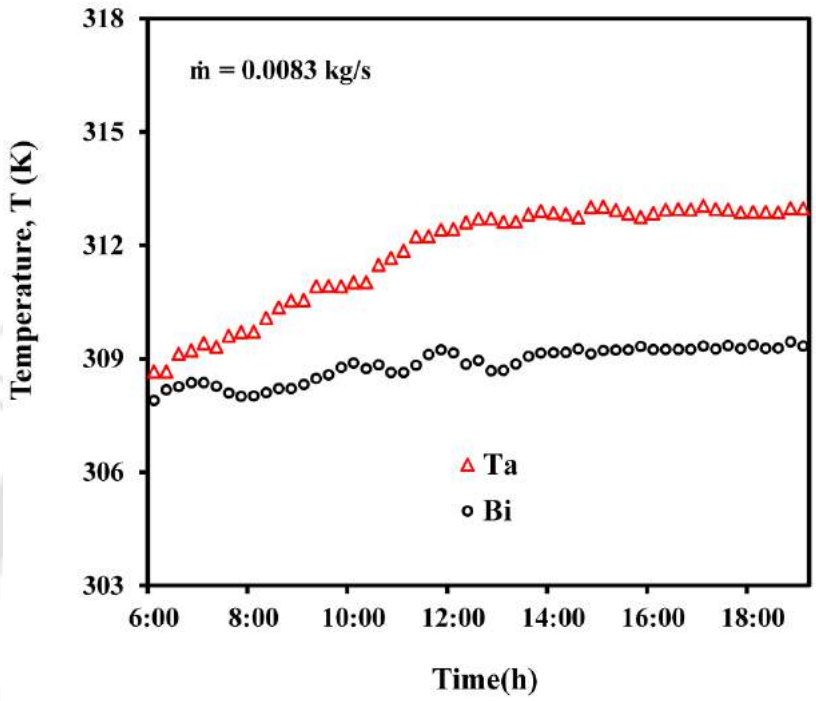

Fig.7.11 Variation storage tank and biogas digester temperature versus time

It is clear from the figure that the shell tank temperature varied from 308.9 K to 313 K for the period of experiments. This range is maintained with the help of controlling devices described in section 7.4.1. It is evident from the figure that the temperature in the biogas digester varied from 308.1 K to 309.2 K. Similar experiments were also carried out at the same flow rate to check the repeatability and are plotted in Fig.7.12. It was observed from the figure that the shell tank temperature varied from 309.2 K to 313.4 K for the period of investigation whereas this variation in biogas digester was found to be in the range from 308.3 K to 309.1 K. The maximum temperature fluctuations in the biogas digester for the two cases were found to be 1.1 K. The result of the controlled experiment reveals that the biogas digester temperature can be maintained at favourable range for the growth of mesophilic microbes. The solar thermal system integrated with controlled devices can be considered as a viable solution for improving biogas production.

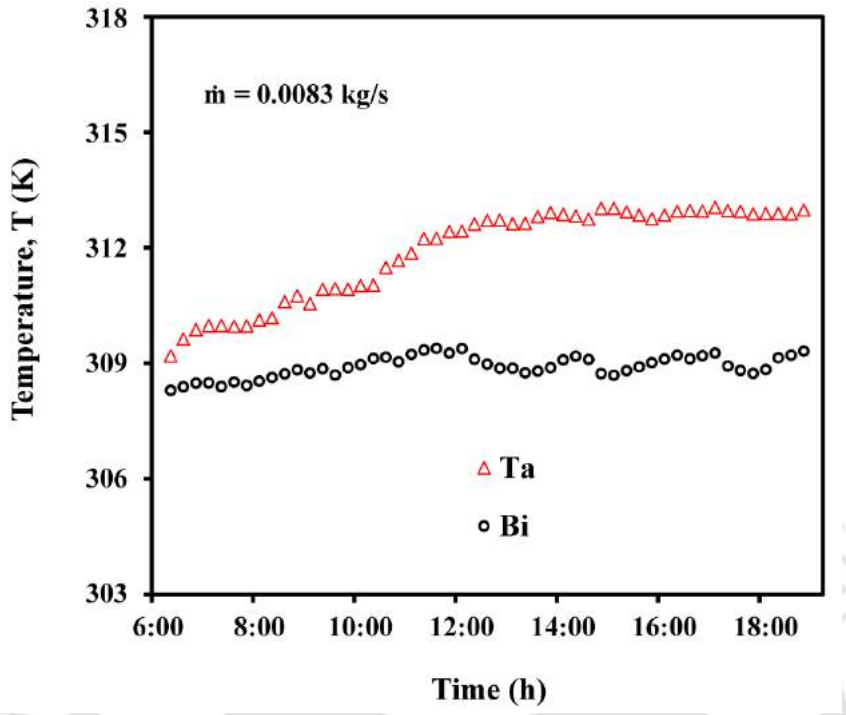

Fig.7.12 Variation storage tank and biogas digester temperature versus time

7.6 Summary

The experimental procedure and results of the controlled and uncontrolled experiment carried out for the integrated solar thermal system was presented in this Chapter. It was observed from the experimental study that the temperature in the biogas digester and shell tank was higher at the bottom compared to the top side. The results of uncontrolled experiment revealed that the average temperature inside biogas varied in the range from 307.4 K – 309.1 K when the temperature inside the shell reaches 313 K to 315 K. The controlled experiment using controlling device maintained the shell tank temperature in the range from 308.9 K – 313.4 K and the biogas digester temperature in the range 308.1 K – 309.2 K. The maximum temperature fluctuation inside the biogas digester was found to be 1.1 K for the period of experiments. Finally, the temperature variation of the heat exchanger at the inlet and outlet side was investigated and observed to be 12.6 K variation. Chapter 8 presents the conclusions arrived at from the present thesis work along with future work.

Chapter - 8

Conclusions and Scope for Future Work

8.1 Conclusions

The present thesis discusses the performance evaluation of a forced convection solar thermal system comprising of straight tube collector, bent tube collectors and a latent heat storage system. Subsequently, the performance of an uncontrolled system for heating biogas digester was investigated using the integrated thermal systems. Finally, a controlled heating system integrated with the latent heat energy storage system was developed. The components of the solar water heating system were designed based on the available solar radiation, mass flow rate of water and energy requirement. The straight and bent tube solar collectors have been evaluated experimentally as well as numerically based on energy and exergy analysis. Experiments were carried out at different mass flow rate of water with 0.0083 $kg.s^{-1}$, 0.0125$kg.s^{-1}$, 0.016 $kg.s^{-1}$, 0.021 $kg.s^{-1}$ and 0.025 $kg.s^{-1}$. The numerical model considered a single straight riser tube and bent riser tubes attached with an absorber plate at the bottom to predict outlet water and absorber plate temperature. Numerical results were in good agreement with the experimental results. The effects of various parameters on energy and exergy efficiencies were also investigated.

The paraffin wax based LHS was designed based on the available temperature from the solar collector and the required temperature for biogas production. Decision regarding number of tubes, cylinder orientation and tube arrangement was arrived at with the help of numerical model which ensured cost effectiveness and efficient latent heat storage system. The performance of the shell and tube type LHS during charging and discharging process were investigated experimentally as well as numerically. For the numerical model, Boussinesq approximation was employed to account for the buoyancy of the molten layer of the phase change material. Darcy law's source term was also used to include the velocity of the phase change material.

Effective heat capacity method was included in the model for combining the latent heat with the specific heat of the phase change material. Since the conductivity of paraffin wax is low, enhancement in thermal conductivity was found to be necessary. The dispersion of Al_2O_3 nanoparticle (nanofluid) in pure paraffin wax and comparison with pure paraffin wax was investigated numerically and validated with the earlier published work. Performance parameters such as melt fraction, charging/discharging time, energy storage/discharge rate were assessed for various operating conditions. Finally, the application of the integrated thermal system with controlled and uncontrolled experiments was investigated. The summary of the investigated flat plate solar collector, paraffin wax based latent heat storage and the integrated solar thermal system are given in the following subsections.

8.1.1 Result of flat plate solar collector

Experimental investigation on the performance of solar water heating collector using exergy and energy analysis for both straight and bent tube collectors under various weather conditions have been carried out and validated with numerical results. The significant conclusions of the present study are as follows:

- The maximum deviation error in prediction of outlet water temperature and absorber plate temperature using straight tube collector was 5% and 2%, respectively.
- The maximum deviation error in prediction of outlet water temperature and absorber plate temperature using bent tube collector was 4.8% and less than 4%, respectively.
- At higher solar insolation, the error between experimental and predicted result was higher. However, the error value was lower at lower solar insolation.
- The 3-D time-averaged numerical model simulation offers a new route for predicting the outlet water and absorber plate temperature which will be helpful for designing efficient solar water heating systems.

- For all investigated flow rate, the plate temperature obtained from the experiment was higher than numerical values, but the reverse was true for outlet water temperature.
- The average exergy efficiency at flow rate of 0.0125 kg/s for the straight tube collector was 3.68% whereas for the bent tube collector the corresponding value was 4.4%.
- The peak thermal efficiency of the bent tube collector was 20% higher than the straight tube collector for the investigated mass flow rate.
- The maximum outlet water temperature of the bent and straight tube was observed to be 334 K and 328 K at 0.0083 kg/s flow rate whereas the minimum was 313 K and 310 K at 0.025kg/s flow rate.
- Outlet water temperature in the range 303 K – 340 Kwas achieved for the investigated solar water heater. Hence, this system could be regarded as an alternate option for heating biogas digester for growing of methane forming bacteria.

8.1.2 Result of thermal energy storage system

In the present investigation, performance evaluation of paraffin wax filled latent heat storage has been carried out experimentally and numerically. Due to the poor thermal conductivity of paraffin wax, both charging and discharging process was time taking. Hence, enhancement technique was applied using Al_2O_3 nanoparticle (nanofluid) and comparison study was also carried out. Major conclusions are listed as follows:

- Charging is a convection-dominated process whereas discharging is a conduction-dominated process. As a result of this, charging is faster process than discharging process.
- For the selected 5 MJ capacity of LHS, the optimized number of tubes was 17 with horizontal cylinder orientation.
- Partial charging/discharging was effective compared to full charging/discharging.

- The validation results indicated a maximum deviation of 5 K between the numerical and experimental values during charging whereas it was 7 K during the discharging process.
- Paraffin wax filled LHS complete charging/discharging was achieved at 90 min/120 min whereas this value was found to be 40 min/ 68 min for Al_2O_3 nanoparticles dispersed paraffin based LHS.
- The time needed to achieve complete melt for the nanofluid based LHS was 55.5% lower than pure paraffin wax. Similarly, discharging time for pure paraffin wax was 1.8 times higher than nanofluid based LHS.
- The addition of nanoparticle decreased the specific heat and latent heat of the storage material. This resulted in decrease in the total energy stored/released for the system with nanofluid based storage compared to that with pure paraffin.
- The total heat stored was 3.57 MJ for the nanofluid at 40 minutes whereas 5.24 MJ for pure paraffin wax based LHS at 90 minutes during the charging process. Similarly, during the discharging process, the total heat discharged from the nanofluid based storage was 3.3 MJ at 68 minute and 4.8 MJ for pure paraffin based LHS at 120 minutes.

8.1.3 Result of the integrated thermal system

Experimental investigation of the integrated thermal system with and without control mechanism was carried out. The aim was to maintain the biogas digester temperature in favourable ranger using control mechanism. Uncontrolled experimental study at a flow rate of 0.0083 kg/s revealed that the shell tank temperature at the bottom and top varied from 304.5 K to 321.7 K and 303.7 K to 320.9 K whereas this variation in the biogas digester was from 303.2 K to 319.1 K and 302.7 K to 318.6 K, respectively. Similar experiment also indicated that the biogas digester temperature was in the range of 303.1 K to 314 K and was 310 K – 318 .1 K for the shell tank. In all cases of the uncontrolled experiment, the biogas average temperature varied in the range from 307.5 K to 309 K when the shell tank

temperature was in the range from 313 K to 315 K. The controlled experiment maintained the shell tank temperature in the range from 308 K to 313 K and the biogas digester temperature in the range 308.1 K – 309.2 K. The maximum temperature fluctuation in the biogas digester was 1.1 K for the period of experiments. In addition, the maximum temperature drop between the inlet and outlet side of the heat exchanger was observed to be 12.6 K.

8.2 Scope for Future Work

In the present investigation, the performance of a system was carried out at various operating conditions with solar collectors, thermal energy storage and integrated thermal system experimentally and numerically. The key results of the research have been underlined in section 8.1. However, there are lots of scopes for further research on the developed integrated thermal units. Some of the future scopes and suggestions for further studies are as follows:

- The flow in the system was considered to be laminar with a significantly low flow rate of water. However, the study may be performed under turbulent flow condition to enhance the heat transfer rate.
- In the controlled experiment of the present study, the average biogas digester temperature is observed to be in the range of 308 K to 310 K which was good for growing mesophilic methane forming-bacteria. Performance analysis can be done for thermophilic condition with turbulent flow of water in the system.
- Simulation of the entire system can be conducted for scale-up.

Reference

Agarwal, V. K., and D. C. Larson, Calculation of the top loss coefficient of a flat-plate collector. Solar Energy. 27 (1) (1981) 69-71.

Agyenim, Francis, Neil Hewitt, Philip Eames, and Mervyn Smyth, A review of materials, heat transfer and phase change problem formulation for latent heat thermal energy storage systems (LHTESS). Renewable and Sustainable Energy Reviews. 14 (2) (2010) 615-628.

Ai, Desheng, Lizan Su, Zhe Gao, Changsheng Deng, and Xiaming Dai, Study of ZrO_2nanopowders based stearic acid phase change materials. Particuology. 8 (4) (2010) 394-397.

Akgün, Mithat, Orhan Aydın, and Kamil Kaygusuz, Experimental study on melting/solidification characteristics of paraffin as PCM. Energy Conversion and Management. 48 (2) (2007) 669-678.

Akpinar, Ebru Kavak, and Fatih Koçyiğit, Energy and exergy analysis of a new flat-plate solar air heater having different obstacles on absorber plates. Applied Energy. 87 (11) (2010) 3438-3450.

Akhtar, N., and S. C. Mullick, Computation of glass-cover temperatures and top heat loss coefficient of flat-plate solar collectors with double glazing. Energy. 32 (7) (2007)1067-1074.

Al-Ansary, Hany, and O. Zeitoun, Numerical study of conduction and convection heat losses from a half-insulated air-filled annulus of the receiver of a parabolic trough collector. Solar Energy. 85 (11) (2011) 3036-3045.

Alta, Deniz, Emin Bilgili, C. Ertekin, and Osman Yaldiz, Experimental investigation of three different solar air heaters: Energy and exergy analyses. Applied Energy. 87 (10) (2010) 2953-2973.

Altfeld, K., W. Leiner, and M. Fiebig, Second law optimization of flat-plate solar air heaters Part I: The concept of net exergy flow and the modeling of solar air heaters. Solar Energy. 41 (2) (1988) 127-132 and 309-317.

Alshamaileh, Ehab, Testing of a new solar coating for solar water heating applications. Solar Energy. 84 (9) (2010) 1637-1643.

Aly, S. L., and A. I. El-Sharkawy, Effect of storage medium on thermal properties of packed beds. Heat Recovery Systems and CHP. 10 (5-6) (1990) 509-517.

Amer, E. H., J. K. Nayak, and G. K. Sharma, Transient method for testing flat-plate solar collectors. Energy Conversion and Management. 39 (7) (1998) 549-558.

Amrutkar, Sunil K., Satyshree Ghodke, and K. N. Patil, Solar flat plate collector analysis. IOSR Journal of Engineering. 2 (2) (2012) 207-213.

Attar, I., and A. Farhat, Efficiency evaluation of a solar water heating system applied to the greenhouse climate. Solar Energy. 119 (2015) 212-224.

Avci, Mete, and M. Yusuf Yazici, Experimental study of thermal energy storage characteristics of paraffin in a horizontal tube-in-shell storage unit. Energy Conversion and Management. 73 (2013) 271-277.

Babu, K., and TS Prasanna Kumar, Effect of CNT concentration and agitation on surface heat flux during quenching in CNT nanofluids. International Journal of Heat and Mass Transfer. 54 (1) (2011) 106-117.

Badache, Messaoud, Stéphane Hallé and Daniel Rousse, A full 3^4 factorial experimental design for efficiency optimization of an unglazed transpired solar collector prototype. SolarEnergy. 86 (9) (2012) 2802-2810.

Baetens, Ruben, Bjørn Petter Jelle, and Arild Gustavsen, Phase change materials for building applications: a state-of-the-art review. Energy and Buildings. 42 (9) (2010) 1361-1368.

Bakari, Ramadhani, Rwaichi JA Minja, and Karoli N. Njau, Effect of glass thickness on performance of flat plate solar collectors for fruits drying. Journal of Energy. 2014 (2014) 1-8.

Balaji, K., S. Iniyan, and V. Muthusamyswami, Experimental investigation on heat transfer and pumping power of forced circulation flat plate solar collector using heat transfer enhancerin absorber tube. Applied Thermal Engineering. 112 (2017) 237-247.

Banos, Raul, Francisco Manzano-Agugliaro, F. G. Montoya, Consolacion Gil, Alfredo Alcayde, and Julio Gómez, Optimization methods applied to renewable and sustainable energy: A review. Renewable and Sustainable Energy Reviews. 15 (4) (2011) 1753-1766.

Bansal, N. K., S. C. Bhand, Sant Ram, and K. K. Singh, A study of a greenhouse concept on conventional biogas systems for enhancing biogas yield in winter months. International Journal of Energy Research. 9 (2) (1985) 119-128.

Beba, Ali, Analysis of a solar-heated biogas fermenter. Solar Energy. 40 (3) (1988) 281-287.

Bejan, Adrian, Advanced engineering thermodynamics. 1st Edition, John Wiley and Sons, (1988).

Bejan, Adrian, Entropy generation minimization: The new thermodynamics of finite-size devices and finite-time processes. Journal of Applied Physics. 79 (3) (1996) 1191-1218.

Bejan, Adrian, Second-law analysis in heat transfer and thermal design. Advances in Heat Transfer. 15 (1982) 1-58.

Benli, Hüseyin, Experimentally derived efficiency and exergy analysis of a new solar air heater having different surface shapes. Renewable Energy. 50 (2013) 58-67.

Bhatt, M. K., S. N. Gaderia, and S. A. Channiwala, Distribution of heat losses in a single glazed flat plate collector at variable wind velocity: An experimental simulation. World Academy of Science, Engineering and Technology. 78 (2011) 453-457.

Bolaji, Bukola O., Flow design and collector performance of a natural circulation solar water heater. Journal of Engineering and Applied Sciences. 1 (1) (2006) 7-13.

Bonacina, C., Comini, G., Fasano, A. and Primicerio, M., Numerical solution of phase change problems. International Journal of Heat and Mass Transfer. 16 (1973) 1825–1832.

Bonmati, A., X. Flotats, Laia Mateu, and E. Campos, Study of thermal hydrolysis as a pretreatment to mesophilic anaerobic digestion of pig slurry. Water Science and Technology. 44 (4) (2001) 109-116.

Budihardjo, I., and G. L. Morrison, Performance of water-in-glass evacuated tube solar water heaters. Solar Energy. 83 (1) (2009) 49-56.

Buhr, H. O., and J. F. Andrews, The thermophilic anaerobic digestion process. Water Research. 11 (2) (1977) 129-143.

Cai, Y., Ke, H., Dong, J., Wei, Q., Lin, J., Zhao, Y., Song, L., Hu, Y., Huang, F., Gao, W. and Fong, H., Effects of nano-SiO_2 on morphology, thermal energy storage, thermal stability,and combustion properties of electrospun lauric acid/PET ultrafine composite fibers asform-stable phase change materials. Applied Energy. 88 (6) (2011) 2106-2112.

Cardinale, N., F. Piccininni, and P. Stefanizzi, Economic optimization of low-flow solar domestic hot water plants. Renewable Energy. 28 (12) (2003) 1899-1914.

Chen, Ye, Jay J. Cheng, and Kurt S. Creamer, Inhibition of anaerobic digestion process: A review. Bioresource Technology. 99 (10) (2008) 4044-4064.

Chen, Y. R., V. H. Varel, and A. G. Hashimoto,Effect of temperature on methane fermentation kinetics of beef-cattle manure.Biotechnology and Bioengineering Symposium. 10 (1980) 325-339.

Chiou, J. P., and M. M. El-Naggar, Optimum slope for solar insolation on a flat surface tilted toward the equator in heating season. Solar Energy. 36 (5) (1986) 471-478.

Coelho, Nuno Miguel Gabriel, Ronald L. Droste, and Kevin J. Kennedy, Evaluation of continuous mesophilic, thermophilic and temperature phased anaerobic digestion of microwaved activated sludge. Water Research. 45 (9) (2011) 2822-2834.

Courtney, B., and D. Dorman, Worldwide fossil fuels. Chemistry Department of Louisiana State University. (2003).

Cruickshank, Cynthia, Evaluation of a stratified multi-tank thermal storage for solar heating applications, PhD Dissertation, Queen's University Kingston, Ontario, Canada. (2009).

Dagdougui, Hanane, Ahmed Ouammi, Michela Robba, and Roberto Sacile, Thermal analysis and performance optimization of a solar water heater flat plate collector: Application to Tétouan. Renewable and Sustainable Energy Reviews. 15 (1) (2011) 630-638.

Darzi AAR, Jourabian M, Farhadi M., Melting and solidification of PCM enhanced by radial conductive fins and nanoparticles in cylindrical annulus. Energy Conversion Management. 118 (2016)253–63.

De Mes, T. Z. D., A. J. M. Stams, J. H. Reith, and G. Zeeman, Methane production by anaerobic digestion of wastewater and solid wastes. Bio-methane and Bio- hydrogen. (2003) 58-102.

Do Ango, AC Mintsa, M. Medale, and C. Abid, Optimization of the design of a polymer flat plate solar collector. Solar Energy. 87 (2013) 64-75.

Dow, Kirstin, and Thomas E. Downing, The atlas of climate change. Mapping the World's Greatest Challenge. London: Earthscan and Stockholm: Stockholm Environment Institute. (2006).

Dović, Damir, and Mladen Andrassy, Numerically assisted analysis of flat and corrugated plate solar collectors thermal performances. Solar Energy. 86 (9) (2012) 2416-2431.

Duffie, John A., and William A. Beckman, Solar engineering of thermal processes. New York, John Wiley and Sons. (1991).

Duffie, John A., and William A. Beckman, Solar engineering of thermal processes. New York, John Wiley and Sons. (2013).

Duran, M., and R. E. Speece,Temperature-staged anaerobic processes. Environmental Technology. 18 (7) (1997) 747-753.

Dutta Gupta, K. K., and Samir Kumar Saha, Energy analysis of solar thermal collectors. Renewable Energy and Environment. (1990) 283-287.

Ekramian, E., S. Gh Etemad, and M. Haghshenasfard, Numerical analysis of heat transfer performance of flat plate solar collectors. Journal of Fluid Flow, Heat and Mass Transfer. 1 (2014) 38-42.

Elsayed, Moustafa M., Optimum orientation of absorber plates. Solar Energy. 42 (2) (1989) 89 -102.

Esapour M, Hosseini MJ, Ranjbar AA, Pahamli Y, Bahrampoury R., Phase change in multi- tube heat exchangers. Renewable Energy. 85(2016)1017–1025.

Facão, Jorge, Optimization of flow distribution in flat plate solar thermal collectors with riser and header arrangements. Solar Energy. 120 (2015) 104-112.

Fang, Guiyin, Shuangmao Wu, and Xu Liu, Experimental study on cool storage air-conditioning system with spherical capsules packed bed. Energy and Buildings. 42 (7) (2010) 1056-1062.

Farahat, S., F. Sarhaddi, and H. Ajam, Exergetic optimization of flat plate solar collectors. Renewable Energy. 34 (4) (2009) 1169-1174.

Farid, Mohammed M., Amar M. Khudhair, Siddique Ali K. Razack, and Said Al-Hallaj, A review on phase change energy storage: Materials and Applications. Energy Conversion and Management. 45 (9) (2004) 1597-1615.

Fatigun, A. T., G. E. Adesakin, and M. Gwani, Experimental determination of the effect of tube spacing on the performance of a flat plate solar collector. International Journal of Environmental Sciences. 3 (1) (2012) 363-370.

Fischer, A. J., and R. A. Greene, Plant scale tests on thermophilic digestion. Sewage Works Journal. (1945) 718-729.

Gadi, Mohamed B., Design and simulation of a new energy-conscious system (CFD and solar simulation). Applied Energy. 65 (1) (2000) 251-256.

Garba, B., Effect of temperature and retention period on biogas production from lignocellulosic material. Renewable Energy. 9 (1-4) (1996) 938-941.

Garg, H. P., and R. K. Agarwal, Some aspects of a PV/T collector/forced circulation flat platesolar water heater with solar cells. Energy Conversion and Management. 36 (2) (1995) 87-99.

Garg, H.P. and Rani, U., Loss coefficients from solar flat-plate collectors. Applied Energy. 7 (1) (1980) 109-117.

Gertzos, K. P., S. E. Pnevmatikakis, and Y. G. Caouris, Experimental and numerical study of heat transfer phenomena inside a flat-plate integrated collector storage solar water heater (ICSSWH) with indirect heat withdrawal. Energy Conversion and Management. 49 (11) (2008) 3104-3115.

Ghamari, D. M., and R. A. Worth,The effect of tube spacing on the cost-effectiveness of a flat-plate solar collector. Renewable Energy. 2 (6) (1992) 603-606.

Gong, Zhen-Xiang, and Arun S. Mujumdar, Finite-element analysis of cyclic heat transfer in a shell-and-tube latent heat energy storage exchanger. Applied Thermal Engineering. 17 (6) (1997) 583-591.

Gorla, Rama Subba Reddy, Finite element analysis of a flat plate solar collector. Finite Elements in Analysis and Design. 24 (4) (1997) 283-290.

Gumus, M, Reducing cold-start emission from internal combustion engines by means of thermal energy storage system. Applied Thermal Engineering. 29 (4) (2009) 652-660.

Gunerhan, Huseyin, and Arif Hepbasli, Exergetic modeling and performance evaluation of solar water heating systems for building applications. Energy and Buildings. 39 (5) (2007) 509-516.

Gupta, M. K., and S. C. Kaushik, Exergetic performance evaluation and parametric studies of solar air heater. Energy. 33 (11) (2008) 1691-1702.

Gupta, R. A., S. N. Rai, and G. N. Tiwari, An improved solar assisted biogas plant (fixed dome type): A transient analysis. Energy Conversion and Management. 28 (1) (1988) 53-57.

Halawa, Edward, and W. Saman, Thermal performance analysis of a phase change thermal storage unit for space heating. Renewable Energy. 36 (1) (2011) 259-264.

Hazami, Majdi, Sami Kooli, Meriem Lazâar, Abdelhamid Farhat, and Ali Belghith,Energetic and exergetic performances of an economical and available integrated solar storage collector based on concrete matrix. Energy Conversion and Management. 51 (6) (2010) 1210-1218.

He, Bo, and Fredrik Setterwall, Technical grade paraffin waxes as phase change materials for cool thermal storage and cool storage systems capital cost estimation. Energy Conversion and Management. 43 (13) (2002) 1709-1723.

He, Wei, Xiaoqiang Hong, Bingqing Luo, Hongbing Chen, and Jie Ji, CFD and comparative study on the dual-function solar collectors with and without tile-shaped covers in waterheating mode. Renewable Energy. 86 (2016) 1205-1214.

Heukelekian, H., Further studies on thermophilic digestion of sewage solids. Sewage Works Journal. (1930) 219-227.

Hill, D. T., R. D. Holmberg, and J. P. Bolte,Operating and performance characteristics of scraped swine manure as a thermophilic anaerobic digestion substrate. Agricultural Wastes. 14 (1) (1985) 37-49.

Ho, Ching Jenq and J. Y. Gao, Preparation and thermophysical properties of nanoparticle-in-paraffin emulsion as phase change material. International Communications in Heat and Mass Transfer. 36 (5) (2009) 467-470.

Hobbi, Alireza and Kamran Siddiqui, Experimental study on the effect of heat transfer enhancement devices in flat-plate solar collectors. International Journal of Heat and Mass Transfer. 52 (19) (2009) 4650-4658.

Holman, Jack Philip, and Walter J. Gajda, Experimental methods for engineers. New York, McGraw-Hill. 7 (2001).

Ho-Ming Yeh, Chii-Den Ho and Chun-Hung Chen, The effect of collector aspect ratio on the collector efficiency of Sheet and tube solar fluid heaters. Tamkang Journal of Science and Engineering. 2 (2) (1999) 61-68.

Hottel, Hoyt, and B. Woertz, Performance of flat-plate solar-heat collectors. Trans. ASME, United States. 64 (1942) 91 - 95.

Ihaddadene, Nabila, Razika Ihaddadene, and Azzeddine Mahdi, Effect of distance between double glazing on the performance of a solar thermal collector. International Conference on Renewable Energies and Power Quality (ICREPQ14). 1 (12) (2014) 302-306.

Ioan Sarbu and Calin Sebarchievici, A comprehensive review of thermal energy storage. Journal of Sustainability.10 (1) (2018).

Iqbal, M., Optimum collector slope for residential heating in adverse climates. Solar Energy. 22 (1) (1979) 77-79.

Ismail N. R., The influence of the type of absorber plates and flow rate on the performance of simple solar heaters. Journal of Ilimiah Peurodeun (JIP), Widyagama University of Malang. (2005) 20 - 32.

Ismail N. R., Effect of absorbent plate type and flow rate on simple solar heater performance. Journal of Ilimiah Peurodeun (JIP), Widyagama University of Malang. 3 (2) (2007) 391- 410.

Jafarkazemi, Farzad, and Emad Ahmadifard, Energetic and exergetic evaluation of flat plate solar collectors. Renewable Energy. 56 (2013) 55-63.

Jamil Ahmad, M., and G. N Tiwari, Optimization of tilt angle for solar collector to receive maximum radiation. TheOpen Renewable Energy Journal. 2 (1) (2009) 19-24.

Janjai, S., A. Esper, and W. Mühlbauer, Modelling the performance of a large area plasticsolar collector. Renewable Energy. 21 (3) (2000) 363-376.

Jesumathy, S. P., M. Udayakumar, S. Suresh, and S. Jegadheeswaran, An experimental studyon heat transfer characteristics of paraffin wax in horizontal double pipe heat latent heatstorage unit. Journal of the Taiwan Institute of Chemical Engineers. 45 (4) (2014) 1298-1306.

Jesumathy, Stella P., M. Udayakumar, and S. Suresh, Heat transfer characteristics in latent heatstorage system using paraffin wax. Journal of Mechanical Science and Technology. 26 (3) (2012) 959-965.

Kahani, Mostafa, S. Zeinali Heris, and Seyed Mahmoud Mousavi, Effects of curvature ratio and coil pitch spacing on heat transfer performance of Al_2O_3/water nanofluid laminar flow through helical coils. Journal of Dispersion Science and Technology. 34 (12) (2013)1704-1712.

Kalbasi, Rasool, and Mohammad Reza Salimpour, Constructal design of horizontal finsto improve the performance of phase change material rectangular enclosures. Applied Thermal Engineering. 91 (2015) 234-244.

Kalogirou, Soteris A., Solar energy engineering: Processes and systems. Academic Press. (2013).

Kalogirou, Soteris A., Solar thermal collectors and applications. Progress in Energy and Combustion Science. 30 (3) (2004) 231-295.

Kalogirou, Soteris A, Thermal performance, economic and environmental life cycle analysis ofthermosiphon solar water heaters. Solar Energy. 83 (1) (2009) 39-48.

Kalogirou, Soteris A., and Christos Papamarcou, Modelling of a thermosyphon solar waterheating system and simple model validation. Renewable Energy. 21 (3) (2000) 471-493.

Kamkari B, Shokouhmand H., Experimental investigation of phase change material melting inrectangular enclosures with horizontal partial fins. International Journal of Heat and Mass Transfer 78 (2014) 839–851.

Kandasamy, Ravi, Xiang-Qi Wang, and Arun S. Mujumdar, Transient cooling of electronics using phase change material (PCM)-based heat sinks. Applied Thermal Engineering. 28 (8) (2008) 1047–1057.

Karanth, Vasudeva K., N. Madhwesh, and M. S. Manjunath, Numerical and experimental study of a solar water heater for enhancement in thermal performance. International Journal of Research in Engineering and Technology (IJRET). 4 (3) (2015) 548-553.

Karsli, Suleyman, Performance analysis of new-design solar air collectors for drying applications. Renewable Energy. 32 (10) (2007) 1645-1660.

Kashyap, D. R., K. S. Dadhich, and S. K. Sharma, Biomethanation under psychrophilicconditions: A review. Bioresource Technology. 87 (2) (2003) 147-153.

Katumba, G., L. Olumekor, A. Forbes, G. Makiwa, B. Mwakikunga, J. Lu, and EvaWäckelgård, Optical, thermal and structural characteristics of carbon nanoparticles embedded in ZnO and NiO as selective solar absorbers. Solar Energy Materials and Solar Cells. 92 (10) (2008) 1285-1292.

Kern, J., and I. Harris, On the optimum tilt of a solar collector. Solar Energy.17 (2) (1975)97-102.

Keyanpour-Rad, M., H. R. Haghgou, F. Bahar, and E. Afshari, Feasibility study of the application of solar heating systems in Iran. Renewable Energy. 20 (3) (2000) 333-345.

Kibria, M. A., M. R. Anisur, M. H. Mahfuz, R. Saidur, and I. H. S. C. Metselaar, Numericaland experimental investigation of heat transfer in a shell and tube thermal energy storagesystem. International Communications in Heat and Mass Transfer. 53 (2014) 71-78.

Khalifa, Abdul-Jabbar N., Thermal performance of locally made flat plate solar collectors usedas part of a domestic hot water system. Energy conversion and Management. 40 (17)(1999) 1825-1833.

Khalifa, Abdulmajed, Lippong Tan, Abhijit Date, and Aliakbar Akbarzadeh, A numericaland experimental study of solidification around axially finned heat pipes for hightemperature latent heat thermal energy storage units. Applied Thermal Engineering. 70(1) (2014) 609-619.

Khan, M. M. A., A. B. M. Abdul Malek, M. A. H. Mithu, and D. K. Das, Design, fabricationand performance evaluation of natural circulation rectangular box-type solar domesticwater heating system. International Journal of Sustainable Energy. 29 (3) (2010) 164-177.

Khodadadi, J. M., and S. F. Hosseinizadeh, Nanoparticle-enhanced phase change materials (NEPCM) with great potential for improved thermal energy storage. InternationalCommunications in Heat and Mass Transfer. 34 (5) (2007) 534-543.

Khodadadi, J. M., and Y. Zhang, Effects of buoyancy-driven convection on melting within spherical containers. International Journal of Heat and Mass Transfer. 44 (8) (2001) 1605-1618.

Kotas, Tadeusz Jozef, The exergy method of thermal plant analysis. Elsevier. (2013).

Kroeker, E. J., D. D. Schulte, A. B. Sparling, and H. M. Lapp, Anaerobic treatment process stability. Journal (Water Pollution Control Federation). (1979) 718-727.

Kumar, Sharad, and R. P. Saini, CFD based performance analysis of a solar air heater duct provided with artificial roughness. Renewable Energy. 34 (5) (2009) 1285-1291.

Kundu, Balaram, Performance analysis and optimization of absorber plates of different geometryfor a flat-plate solar collector: A comparative study. Applied Thermal Engineering. 22(9) (2002) 999-1012.

Kurtbas, Irfan, and Aydın Durmuş, Efficiency and exergy analysis of a new solar air heater. Renewable Energy. 29 (9) (2004) 1489-1501.

Lacroix M., Numerical simulation of a shell-and-tube latent heat thermal energy storage unit. Solar Energy. 50 (4) (1993) 357–67.

Lecoeuche, S., and S. Lalot, Prediction of the daily performance of solar collectors. InternationalCommunications in Heat and Mass Transfer. 32 (5) (2005) 603-611.

Lettinga, Gatze, Salih Rebac, and Grietje Zeeman, Challenge of psychrophilic anaerobic wastewater treatment. TRENDS in Biotechnology. 19 (9) (2001) 363-370.

Li, Min, A nano-graphite/paraffin phase change material with high thermal conductivity. Applied Energy. 106 (2013) 25-30.

Li, Wei, and Chengcheng Kong, Numerical study on the thermal performance of a shell and tubephase change heat storage unit during melting process. Advances in Mechanical Engineering. 6 (2014) 360283.

Liu, Hongim, and Hazim B. Awbi, Performance of phase change material boards under natural convection. Building and Environment. 44 (9) (2009) 1788-1793.

Liu, Geng, Y. A. Cengel, and R. H. Turner, Exergy analysis of a solar heating system. Journal of Solar Energy Engineering. 117 (3) (1995) 249-251.

Lo, K. V., P. H. Liao, and A. C. March, Thermophilic anaerobic digestion of screened dairymanure. Biomass. 6 (4) (1985) 301-315.

Luminosu, I., and L. Fara, Determination of the optimal operation mode of a flat solar collectorby exergetic analysis and numerical simulation. Energy. 30 (5) (2005) 731-747.

Luostarinen, Sari, Anaerobic on-site wastewater treatment at low temperatures. Jyväskylä studies in biological and environmental science. 158 (2005).

Maatouk, Khoukhi, Non-gray radiative and conductive heat transfer in single and double glazing solar collector glass covers. International Journal of Thermal Sciences. 45 (6) (2006) 579-585.

Mackie, R. I., and M. P. Bryant, Anaerobic digestion of cattle waste at mesophilic andthermophilic temperatures. Applied Microbiology and Biotechnology. 43 (2) (1995)346-350.

Madigan, Michael T., John M. Martinko, and Jack Parker, Brock biology of microorganisms. 11th Edition, Upper Saddle River, New Jersey, (1997).

Madhukeshwara, N., and E. S. Prakash, An investigation on the performance characteristics ofsolar flat plate collector with different selective surface coatings. International Journal of Energy and Environment. 3 (1) (2012) 99-108.

Madhusudan, M., G. N. Tiwari, D. S. Hrishikeshan, and H. K. Sehgal, Optimization of heat losses in normal and reverse flat-plate collector configurations: Analysis and performance. Energy Conversion and Management. 21 (3) (1981) 191-198.

Mahanta, P., U. K. Saha, A. Dewan, P. Kalita, and B. Buragohain, Biogas digester: Adiscussion on factors affecting biogas production and field investigation of a novel duplex digester. Journal of the Solar Energy Society of India. 15 (2) (2005).

Markvart, Tomas, Solar electricity. 6th Edition, John Wiley and Sons, (2000).

Martinopoulos, G., D. Missirlis, G. Tsilingiridis, K. Yakinthos, and N. Kyriakis, CFDmodeling of a polymer solar collector. Renewable Energy. 35 (7) (2010) 1499-1508.

Matuska, Tomas, Vladimir Zmrhal, and Juliane Metzger, Detailed modelling of solar flat-plate collectors with design tool kolektor 2.2. In 11th International IBPSA Conference, Scotland. (2009) 2289-2296.

Mazman, Muhsin, Luisa F. Cabeza, Harald Mehling, Miquel Nogues, Hunay Evliya, and Halime Ö. Paksoy, Utilization of phase change materials in solar domestic hot water systems. Renewable Energy. 34 (6) (2009) 1639-1643.

Medrano, M., M. O. Yilmaz, M. Nogués, I. Martorell, Joan Roca, and Luisa F. Cabeza, Experimental evaluation of commercial heat exchangers for use as PCM thermal storage systems. Applied Energy. 86 (10) (2009) 2047-2055.

Mehling, H. and L.F. Cabeza, Heat and Cold Storage with PCM. Springer, Berlin. (2002).

Mills, A., Farid, M., Selman, J.R. and Al-Hallaj, S., Thermal conductivity enhancement ofphase change materials using a graphite matrix. Applied Thermal Engineering. 26 (14) (2006) 1652-1661.

Mustafa, Unmer and Ismail. N. R., Collectors innovation to increase performance solar waterheater. International Journal of Research in Engineering and Technology. 2 (9) (2013) 464-470.

Meynell, P. J., Methane: Planning a Digester. 1st Edition, Prism Press (1976).

Ng, K. W., Z. X. Gong, and A. S. Mujumdar, Heat transfer in free convection-dominated melting of a phase change material in a horizontal annulus. International Communications in Heat and Mass Transfer. 25 (5) (1998) 631-640.

Nidal Y Abdalla Akl, Nano materials solar selective paint for flat plate collectors. International Conference on Solar Energy for MENA Region (INCOSOL). 37 (2012) 22-23.

Nijaguna, B. T, Biogas technology. New Age International. (2006).

Niyas, Hakeem, and P. Muthukumar, Performance analysis of latent heat storage systems. International Journal of Scientific and Engineering Research. 4 (2013) 2229-5518.

Niyas, H., Prasad, L. and Muthukumar, P., Performance investigation of high-temperaturesensible heat thermal energy storage system during charging and discharging cycles. Clean Technologies and Environmental Policy. 17(2) (2015) 501-513.

Niyas, Hakeem, Sunku Prasad, and P. Muthukumar, Performance investigation ofa lab–scalelatent heat storage prototype: Numerical results. Energy Conversion and Management. 135 (2017) 188-199.

Njomo, Donatien, and Michel Daguenet, Sensitivity analysis of thermal performances of flat plate solar air heaters. Heat and Mass Transfer. 42 (12) (2006) 1065-1081.

Park, S. R., A. K. Pandey, V. V. Tyagi, and S. K. Tyagi, Energy and exergy analysis of typicalrenewable energy systems. Renewable and Sustainable Energy Reviews. 30 (2014) 105-123.

Petela, R., Exergy of heat radiation. ASME Journal ofHeat Transfer. 86 (2) (1964) 187-192.

Potter, Nancy I., How Brazil achieved energy independence and the lessons the United Statesshould learn from Brazil's experience. Washington University Global Studies Law Review. 7 (2008) 331.

Prakash, B. Jaya, B. Vishnuprasad, and V. Venkata Ramana, Performance study on effect of nanocoatings on liquid flat plate collector: An experimental approach. Int. J. Mech. Eng. Rob. Res. 2 (4) (2013) 379-384.

Prasad, C. R., and S. R. C. Sathyanarayan, Studies in biogas technology. Part III. Thermalanalysis of biogas plants. In Proceedings of the Indian Academy of Sciences. 2 (3) 1979)377-386.

Quaschning, Volker, Understanding renewable energy systems. Routledge, 2nd Edition. (2016).

Rabha, D. K., P. Muthukumar, and C. Somayaji, Energy and exergy analyses of the solar drying processes of ghost chilli pepper and ginger. Renewable Energy. 105 (2017) 764-773.

Ramezanzadeh, B., M. M. Attar, and M. Farzam, Effect of ZnO nanoparticles on the thermal and mechanical properties of epoxy-based nanocomposite. Journal of Thermal Analysis and Calorimetry. 103 (2) (2010) 731-739.

Rathod, M. K., and Jyotirmay Banerjee, Experimental investigations on latent heat storage unitusing paraffin wax as phase change material. Experimental Heat Transfer. 27 (1) (2014) 40-55.

Rathod, Manish K., and Jyotirmay Banerjee, Thermal performance enhancement of shell and tube latent heat storage unit using longitudinal fins. Applied Thermal Engineering. 75 (2015) 1084-1092.

Reddy, Amulya Kumar N., C. R. Prasad, P. Rajabapaiah, and S. R. C. Sathyanarayan, Studies in biogas technology Part IV. A novel biogas plant incorporating a solar water- heater and solar still. In Proceedings of the Indian Academy of Sciences. 2 (3) (1979) 387-393.

Ren, Qinlong, and Cho Lik Chan., GPU accelerated numerical study of PCM melting process in an enclosure with internal fins using lattice Boltzmann method. International Journal ofHeat and Mass Transfer.100 (2016) 522-535.

Rise information portal technologies-hot water systems.(Website:http://www.see.murdoch.edu.au/resources/info/Tech/lowtemphotwatersys).

Şahan, Nurten, Magali Fois, and Halime Paksoy, Improving thermal conductivity phase changematerials: A study of paraffin nanomagnetite composites. Solar Energy Materials and Solar Cells. 137 (2015) 61-67.

Sambo, A. S., B. Garba, and B. G. Danshehu, Effect of some operating parameters on biogas production rate. Renewable Energy. 6 (3) (1995) 343-344.

Sarı, Ahmet, Form-stable paraffin/high density polyethylene composites as solid–liquid phasechange material for thermal energy storage: Preparation and thermal properties. Energy Conversion and Management. 45 (13) (2004) 2033-2042.

Sarma, Dhrupad, Parimal Bakul Barua, and Diganta Hatibaruah, Optimization of glazing cover parameters of a solar flat plate collector (FPC). International Journal of Engineering Trends and Technology (IJETT). 14 (2) (2014) 74-80.

Sasmito, Agus Pulung, Jundika Candra Kurnia, and Arun Sadashiv Mujumdar, Numerical evaluation of laminar heat transfer enhancement in nanofluid flow in coiled square tubes. Nanoscale Research Letters. 6 (1) (2011) 376.

Seddegh, S., Wang, X. and Henderson, A.D, A comparative study of thermal behaviour of a horizontal and vertical shell-and-tube energy storage using phase change materials. Applied Thermal Engineering. 93 (2016) 348-358.

Seddegh, Saeid, Xiaolin Wang, and Alan D. Henderson, Numerical investigation of heat transfer mechanism in a vertical shell and tube latent heat energy storage system. Applied Thermal Engineering. 87 (2015) 698-706.

Selmi, Mohamed, Mohammed J. Al-Khawaja, and Abdulhamid Marafia, Validation of CFDsimulation for flat plate solar energy collector. Renewable Energy. 33 (3) (2008) 383-387.

Sekhar, Y. Raja, K. V. Sharma, and M. Basaveswara Rao, Evaluation of heat loss coefficientsin solar flat plate collectors. ARPN Journal of Engineering and Applied Sciences. 4 (5)(2009) 15-19.

Singh, D., K. K. Singh, and N. K. Bansal, Heat loss reduction from the gas holder/fixed gas dome of a community-size biogas plant. International Journal of Energy Research. 9 (4) (1985) 417-430.

Shariah, Adnan, and Bassam Shalabi, Optimal design for a thermosyphon solar water heater. Renewable Energy. 11 (3) (1997) 351-361.

Sharma, A., V.V. Tyagi, C.R. Chen, and D. Buddhi, Review on thermal energy storage with phase change materials and applications. Renewable and Sustainable Energy Reviews. 13 (2009) 318-345.

Smith, Peter R, Planning and installing solar thermal systems. Earth Scan 14AST Cross Street, London, England. (2011) 86-87.

Soares, N., J. J. Costa, A. R. Gaspar, and P. Santos, Review of passive PCM latent heat thermal energy storage systems towards buildings' energy efficiency. Energy and Buildings. 59 (2013) 82-103.

Subramanyam, S., Use of solar heat to upgrade biogas plant performance. Energy Conversion and Management. 29 (1) (1989) 73-75.

Sukhatme, Suhas P., and J. K. Nayak, Solar energy: Principles of thermal collection and storage. Tata McGraw Hill Publishing Company, New Delhi, 3rd Edition. (2008).

Sultana, Tanzeen, Graham L. Morrison, and Gary Rosengarten,Thermal performance of anovel rooftop solar micro-concentrating collector. Solar Energy. 86 (7) (2012) 1992-2000.

Suzuki, Akio, A fundamental equation for exergy balance on solar collectors. Journal of Solar Energy Engineering. 110 (2) (1988) 102-106.

Suzuki, A., H. Okamura, and I. Oshida, Application of exergy concept to the analysis ofoptimum operating conditions of solar heat collectors. Journal of Solar Energy Engineering. 109 (4) (1987) 337-342.

Taherian, H., A. Rezania, S. Sadeghi, and D. D. Ganji, Experimental validation of dynamic simulation of the flat plate collector in a closed thermosyphon solar water heater. EnergyConversion and Management. 52 (1) (2011) 301-307.

Tanha, Kamyar, Alan S. Fung, and Rakesh Kumar, Performance of two domestic solar waterheaters with drain water heat recovery units: Simulation and experimental investigation. Applied Thermal Engineering. 90 (2015) 444-459.

Tchinda, Réné,N., A review of the mathematical models for predicting solar air heaters systems. Renewable and Sustainable Energy Reviews. 13 (8) (2009) 1734-1759.

Teng, Tun-Ping, and Chao-Chieh Yu, Characteristics of phase-change materials containingoxide nano-additives for thermal storage. Nanoscale Research Letters. 7 (1) (2012) 611.

Teyeb, A., L. Dehmani, C. Kerkeni, and L. Kaabi, Parametrical study of the influence of the climatic data and the construction properties on the efficiency of a collector/storage solar water heater. Revue Des Energies Renouvelable. 11(1) (2008) 87-94.

Tiari, Saeed, Songgang Qiu, and Mahboobe Mahdavi, Discharging process of a finned heat pipe–assisted thermal energy storage system with high temperature phase change material. Energy Conversion and Management. 118 (2016) 426-437.

Tiwari, G. N., and A. Chandra, A solar-assisted biogas system: A new approach. Energy Conversion and Management. 26 (2) (1986) 147-150.

Tiwari, G. N., D. K. Rawat, and A. Chandra, A simple analysis of conventional biogas plant. Energy Conversion and Management. 28 (1) (1988) 1-4.

Torres-Reyes, E., J. J. Navarrete-González, and J. G. Cervantes-de Gortari, Thermodynamic optimization as an effective tool to design solar heating systems. Energy. 29 (12) (2004) 2305-2315.

Trp, Anica, An experimental and numerical investigation of heat transfer during technical grade paraffin melting and solidification in a shell-and-tube latent thermal energy storage unit. Solar Energy 79 (6) (2005) 648-660.

Tyagi, S. K., Shengwei Wang, M. K. Singhal, S. C. Kaushik, and S. R. Park, Exergy analysis and parametric study of concentrating type solar collectors. International Journal of Thermal Sciences. 46 (12) (2007) 1304-1310.

Ucar, A., and M. Inalli, Exergoeconomic analysis and optimization of a solar-assisted heating system for residential buildings. Building and Environment. 41 (11) (2006) 1551-1556.

Usmani, J. A., G. N. Tiwari, and Avinash Chandra, Performance characteristic of a greenhouse integrated biogas system. Energy Conversion and Management. 37 (9) (1996) 1423-1433.

Vajjha, Ravikanth S., Debendra K. Das, and Praveen K. Namburu, Numerical study of fluid dynamic and heat transfer performance of Al_2O_3 and CuO nanofluids in the flat tubes of a radiator. International Journal of Heat and Fluid Flow. 31 (4) (2010) 613-621.

Valan, Arasu Amirtham, Agus P. Sasmito, and Arun S. Mujumdar, Numerical performance study of paraffin wax dispersed with alumina in a concentric pipe latent heat storage system. Thermal Science. 17 (2) (2013) 419-430.

Van Lier, Jules B, Thermophilic anaerobic waste water treatment, temperature aspects and process stability. Ph.D Thesis Dissertation, Wageningen Agricultural University, Wageningen, Netherland. (1995).

Varel, V. H., H. R. Isaacson, and M. P. Bryant, Thermophilic methane production from cattle waste. Applied and Environmental Microbiology. 33 (2) (1977) 298-307.

Varol, Yasin, and Hakan F. Oztop, Buoyancy induced heat transfer and fluid flow inside a tilted wavy solar collector. Building and Environment. 42 (5) (2007) 2062-2071.

Vejen, Niels Kristian, Simon Furbo, and Louise Jivan Shah, Development of 12.5 m^2 solar collector panel for solar heating plants. Solar Energy Materials and Solar Cells. 84 (1) (2004) 205-223.

Velraj, R. V. S. R., R. V. Seeniraj, B. Hafner, Christian Faber, and Klemens Schwarzer, Heat transfer enhancement in a latent heat storage system. Solar Energy. 65 (3) (1999) 171-180.

Vendan, S. P., L. P. A. Shunmuganathan, T. Manojkumar, and C. Shiva Thanu, Study on design of an evacuated tube solar collector for high temperature steam generation. 2 (12) (2012) 539-541.

Vindis, P., B. Mursec, M. Janzekovic, and F. Cus, The impact of mesophilic and thermophilicanaerobic digestion on biogas production. Journal of Achievement in Material and Manufacturing Engineering. 36 (2) (2009) 192-198.

Vishal R. Bhadane, Prasad P. Patil, R. Y. Patil, Experimental investigation and CFD analysis of flat plate collector of solar water heating system – A review, International Journal for Research in Applied Science and Engineering Technology. 5 (1), (2017) 234- 240.

Vyshak, N. R., and G. Jilani, Numerical analysis of latent heat thermal energy storage system. Energy Conversion and Management. 48 (7) (2007) 2161-2168.

Wang, Jifen, Huaqing Xie, Zhixiong Guo, Lihui Guan, and Yang Li, Improved thermal properties of paraffin wax by the addition of TiO_2 nanoparticles. Applied Thermal Engineering . 73 (2) (2014) 1541-1547.

Wang, Jifen, Huaqing Xie, and Zhong Xin, Thermal properties of paraffin based compositescontaining multi-walled carbon nanotubes. Thermo-chimica Acta. 488 (1) (2009) 39-42.

Wang, Shaoning, and Bo Hong, Optimum design of tilt angle and horizontal direction of solar collectors under obstacle's shadow for building applications. Journal of Building Construction and Planning Research. 3 (2) (2015) 60-67.

Watmuff, J. H., W. W. S. Charters, and D. Proctor. "Solar and wind induced external coefficients-solar collectors." *Cooperation Mediterraneenne pour l'Energie Solaire* (1977): 56.

Wang, Wei-Wei, Kun Zhang, Liang-Bi Wang, and Ya-Ling He, Numerical study of the heat charging and discharging characteristics of a shell-and-tube phase change heat storage unit. Applied Thermal Engineering. 58 (1) (2013) 542-553.

Weitbrecht, Volker, David Lehmann, and Andreas Richter, Flow distribution in solar collectors with laminar flow conditions. Solar Energy. 73 (6) (2002) 433-441.

Wiegant, W. M., M. Hennink, and G. Lettinga, Separation of the propionate degradation to improve the efficiency of thermophilic anaerobic treatment of acidified waste waters. Water Research. 20 (4) (1986) 517-524.

Wijeysundera, N. E., and M. Iqbal, Effect of plastic cover thickness on top loss coefficient offlat-plate collectors. Solar Energy. 46 (2) (1991) 83-87.

Wing, Han Kwong, and Lee Chung Chiang, A second law concept of an equivalent solar collector. Energy. 16 (5) (1991) 859-865.

Whillier, Austin, Plastic covers for solar collectors. Solar Energy. 7 (3) (1963) 148-151.

White, F., Fluid Mechanics. Elsevier Academic Press, Amsterdam, 5thEdition. (2003).

Wu, Shuying, Dongsheng Zhu, Xiurong Zhang, and Jin Huang, Preparation and melting/freezing characteristics of Cu/paraffin nanofluid as phase-change material (PCM). Energy and Fuels. 24 (3) (2010) 1894-1898.

Wu, Shuying, Dongsheng Zhu, Xinfang Li, Hua Li, and Junxi Lei, Thermal energy storagebehavior of Al $_2$O $_3$-H $_2$ O nanofluids. Thermochimica Acta. 483 (1) (2009) 73-77.

Xia, L., P. Zhang, and R. Z. Wang, Preparation and thermal characterization of expandedgraphite/paraffin composite phase change material. Carbon. 48 (9) (2010) 2538-2548.

Xiaowu, Wang, and Hua Ben, Exergy analysis of domestic-scale solar water heaters. Renewableand Sustainable Energy Reviews. 9 (6) (2005) 638-645.

Yadav, Y. P., G. N. Tiwari, and A. Chandra, An improved solar assisted biogas plant: Atransient analysis. Energy Conversion and Management. 27 (2) (1987) 153-157.

Yate Ding and S.B. Riffat, Thermochemical energy storage technologies for building applications: a state-of-the-art review. International Journal of Low-Carbon Technologies. 8 (2) (2013) 106 – 116.

Zeng, Ju-Lan, Fu-Rong Zhu, Sai-Bo Yu, Ling Zhu, Zhong Cao, Li-Xian Sun, Guang-Rong Deng, Wen-Pei Yan, and Ling Zhang, Effects of copper nanowires on the properties of an organic phase change material. Solar Energy Materials and Solar Cell. 105 (2012) 174- 178.

Zeng, Ju-lan, Zhong Cao, Dao-wu Yang, F. Xu, L. Sun, X. Zhang, and L. Zhang, Effects ofMWNTs on phase change enthalpy and thermal conductivity of a solid-liquid organic PCM. Journal of Thermal Analysis and Calorimetry.95 (2) (2009) 507-512.

Zeng, J. L., L. X. Sun, F. Xu, Z. C. Tan, Z. H. Zhang, J. Zhang, and T. Zhang, Study of a PCM based energy storage system containing Ag nanoparticles. Journal of Thermal Analysis and Calorimetry. 87 (2) (2007) 371-375.

Zinder, S. H., S. C. Cardwell, T. Anguish, M. Lee, and M. Koch, Methanogenesis in athermophilic (58 ºC) anaerobic digestor: Methanothrix sp as an important aceticlasticmethanogen. Applied and Environmental Microbiology. 47 (4) (1984) 796-807.

Zhao, Xudong, Zhangyuan Wang, and Qi Tang, Theoretical investigation of the performance of a novel loop heat pipe solar water heating system for use in Beijing, China. Applied Thermal Engineering. 30 (16) (2010) 2526-2536.

Zhong, Yajuan, Sizhong Li, Xinghai Wei, Zhanjun Liu, Quangui Guo, Jingli Shi, and Lang Liu, Heat transfer enhancement of paraffin wax using compressed expanded natural graphite for thermal energy storage. Carbon. 48 (1) (2010) 300-304.

Zhu, Li, Yiping Wang, Zhenlei Fang, Yong Sun, and Qunwu Huang, An effective heatdissipation method for densely packed solar cells under high concentrations. Solar EnergyMaterials and Solar Cells. 94 (2) (2010) 133-140.

Appendix

Appendix-A

Design Formula of Flat Plate Solar Collector

The design of the FPC system was carried out considering area of the collector, aperture width, spacing between two consecutive tubes and number of tubes.

(i) Collector area

The ratio of heat gain by the working fluid to heat absorbed by the collector is the optical efficiency of a solar collector. The optical efficiency ($\tau\alpha$) was obtained from the relationship (Vendan *et al.* 2012)

$$\tau\alpha = \frac{\dot{m}C_p\Delta T}{IA} \qquad \textit{Eq.}\ (A1)$$

Study on mass flow rate ($\dot{m}$) through the collector by Kalogirou (2004) reported 0.02 Kg/s as minimum flow rate for testing FPC. Majority studies on solar collector (He *et al*. 2016 and Zhao *et al*. 2010) using water as a working fluid reported the maximum temperature change between outlet and inlet (ΔT) side of the collector were in the range from 15 K to 25 K.

The area of the collector (A) is defined as

$$A = nWl \qquad \textit{Eq.}\ (A2)$$

(ii) Tube spacing

Collector efficiency factor (F') as a function of tube spacing (W) was determined by the expression (Duffie and Beckman 2013)

$$F' = \frac{1}{UW^{-1}}\left\{\frac{1}{U(D(W-D)F} + \frac{1}{C_b} + \frac{1}{\pi D_i h_{fi}}\right\} \qquad \textit{Eq.}\ (A3)$$

The fin efficiency factor (*F*) for negligible change in temperature gradient on the surface of absorber plate defined as

$$F = \frac{\tanh[\frac{M(W-D)}{2}]}{\frac{M(W-D)}{2}} \qquad Eq.\ (A4)$$

where *M* is dimensions number and is defined as

$$M = \sqrt{\frac{U}{\delta k_i}} \qquad Eq.\ (A5)$$

For laminar flow R_{ed} <2100, the Nusselt number is given as

$$N_{ud} = \frac{h_{fi} D_i}{K_f} = 3.656 \qquad Eq.\ (A6)$$

For turbulent flow R_{ed} >2100, the Nusselt number obtained from the relationship

$$N_{ud} = 0.023 \mathrm{R}_{ed}^{0.8} \mathrm{Pr}^{0.33} \qquad Eq.\ (A7)$$

(iii) Number of tubes

The number of tubes affects the width of the collector (*B*). The width of the collector was determined by the expression

$$B = nW \qquad Eq.\ (A8)$$

Appendix-B

Energy Analysis

Some important correlation used for deriving energy equation is given below.

The heat removal factor (F_R) was determined fromthe relationship **(**Duffie and Beckman 2013)

$$F_R = \frac{\dot{m}C_p}{AU}\left[1-\exp\left(\frac{-F'UA}{\dot{m}C_p}\right)\right] \qquad Eq.\ (B1)$$

The total heat loss coefficient (U) of an FPC comprises of three terms, *viz.*, top heat loss, bottom heat loss and side heat loss. Since the value of side loss is very small compared with other two losses, this term is neglected. The total heat loss coefficient (U) was obtained by the expression

$$U = U_t + U_b \qquad Eq.\ (B2)$$

The heat loss from the top of the absorber plate (U_t) for single glazing was determined from (Jafarkazemi and ahmadifard 2013)

$$U_t = \left[\frac{1}{h_w} + \frac{1}{\frac{C}{T_p}\left[\frac{T_p - T_a}{1+f}\right]^e}\right]^{-1} + \frac{\sigma\left(T_p + T_a\right)\left(T_p^{\,2} + T_a^{\,2}\right)}{\left(\varepsilon_p + 0.00591h_w\right)^{-1} + \frac{1+f+0.133\varepsilon_p}{\varepsilon_g} - 1} \qquad Eq.\ (B3)$$

where

$$f = 1 - 0.07866\left(1 + 0.089h_w - 0.1166h_w\varepsilon_g\right) \qquad Eq.\ (B4)$$

$$C = 520\left(1 - \frac{0.00005}{\beta_a^{\,2}}\right) \qquad Eq.\ (B5)$$

$$e = 0.43\left(1 - \frac{100}{T_p}\right) \qquad Eq.\ (B6)$$

Similarly, the top heat loss coefficient can be expressed as a function of sky temperature (T_{sky}) and glass cover temperature (T_g) and is expressed as (Jafarkazemi and ahmadifard 2013)

$$U_t = \frac{h_w(T_g - T_a) + \sigma\varepsilon_g\left(T_g^{\,4} - T_{sky}^{\,4}\right)}{T_p - T_a} \qquad Eq.\ (B7)$$

where

$$T_{sky} = T_a - 6 \qquad Eq.\ (B8)$$

The heat loss at the back of the absorber plate (U_b) was obtained from the expression

$$U_b = \frac{k_b}{\delta_b} \qquad Eq.\ (B9)$$

The convective heat loss from bottom and side wall ($h_b = h_w$) of the collector as a function of wind speed is expressed as (Watmuff *et al.*1977)

$$h_b = 2.8 + 3V_w \qquad Eq.\ (B10)$$

Appendix-C

Modified Thermo-Physical Properties of nanopcm (nanofluid)

The effective thermal conductivity of the nanofluid using Maxwell model and Brownian motion was obtained from (Vajjha *et al.* 2010)

$$K_{npcm} = \frac{K_{np} + 2K_{pcm} - 2\varphi\left(K_{pcm} - K_{np}\right)}{K_{np} + 2K_{pcm} + 2\varphi\left(K_{pcm} - K_{np}\right)} K_{pcm} + 5\times10^{4}\zeta\varphi\rho_{pcm}\beta_{1}\, C_{p\,pcm}\sqrt{\frac{\sigma T}{\rho_{np} d_{np}}}\, f(T,\varphi)$$

Eq. (*C*1)

where

$$f(T,\varphi) = (2.8217\ \times10^{2}\varphi + 3.917\times10^{-3})\frac{T}{T_{ref}} + (-3.0669\times10^{-2}\varphi - 3.91123\times10^{-3})$$

Eq. (*C*2)

$$\beta_{1} = 8.4407(100\varphi)^{-1.07304}$$

Eq. (*C*3)

The first part of Eq. (*C*1) was obtained from the Maxwell model while the second part accounts for Brownian motion which causes the temperature dependence of the effective thermal conductivity. The term ζ is correction factor comes from the Brownian motion term since there is no Brownian motion in the solid phase, this value is defined as the same as melt fraction (θ) given in Chapter 3.

Thermo-physical properties of the nanofluid are functions of concentration of nanoparticles, PCM and temperature. The density was determined (ρ_{pcm}) from the relationship (Kandasamy *et al.* 2008)

$$\rho_{pcm} = \frac{750}{0.001(\mathrm{T} - 317.15) + 1}$$

Eq. (*C*4)

The nanofluid suspension density (ρ_{npcm}) was obtained from (Sasmito *et al.* 2011)

$$\rho_{npcm} = \varphi\rho_{np} + (1-\varphi)\rho_{pcm}$$

Eq. (*C*5)

The specific heat of the nanofluid was assumed to be a weighted average of the PCM and nanoparticle. This was determined using relationship (Sasmito *et al.* 2011)

$$C_{p\ npcm} = \frac{\varphi(\rho C_p)_{np} + (1-\varphi)(\rho C_p)_{pcm}}{\rho_{npcm}} \qquad Eq.\ (C6)$$

The latent heat of nanofluid (L_{npcm}) was obtained using the expression (Sasmito *et al.* 2011)

$$L_{npcm} = \frac{(1-\varphi)(\rho \text{L})_{\text{pcm}}}{\rho_{npcm}} \qquad Eq.\ (C7)$$

The PCM viscosity (μ_{pcm}) was determined using the expression (Valan *et al.* 2013)

$$\mu_{pcm} = 0.001\exp\left(-4.25 + \frac{1790}{T}\right) \qquad Eq.\ (C8)$$

The viscosity of the nanofluid (μ_{npcm}) was determined using the relationship (Valan *et al.* 2013)

$$\mu_{npcm} = C_1 \exp(C_2\varphi)\mu_{pcm} \qquad Eq.\ (C9)$$

The mass fraction of the nanofluid (m_{np}) was obtained using the expression (Valan *et al.* 2013)

$$m_{np} = \frac{\varphi\rho_{npcm}}{(\rho_{\text{pcm}} + \varphi(\rho_{\text{npcm}} - \rho_{\text{pcm}})} \qquad Eq.\ (C10)$$

Appendix-D

Uncertainty analysis

Let w_R be the uncertainty in the result (R) and $w_1, w_2, \ldots\ldots w_n$ be the uncertainty in the independent variables. The result R is a given function of independent variables $x_1, x_2, \ldots\ldots x_n$. If the uncertainties in the independent variables are knows, then the uncertainty in the result (R) is obtained from (Rabha*et al.* 2017 and Holman 2001)

$$w_R = \left[\left(\frac{\partial R w_1}{\partial x_1} \right)^2 + \left(\frac{\partial R w_2}{\partial x_2} \right)^2 + \left(\frac{\partial R w_3}{\partial x_3} \right)^2 + \ldots. + \left(\frac{\partial R w_n}{\partial x_n} \right)^n \right]^{1/2} \qquad Eq.\ (D1)$$

Reynolds number of the heat absorbing fluid depends on mass flow rate, viscosity and the inner diameter of the absorber tube. The overall uncertainty was determined using relationship

$$w_{\mathrm{Re}} = \left[\left(\frac{\partial \mathrm{Re}}{\partial \dot{m}} w_{\dot{m}} \right)^2 + \left(\frac{\partial \mathrm{Re}}{\partial d} w_d \right)^2 \right]^{1/2} \qquad Eq.\ (D2)$$

The total uncertainty for the solar collector efficiency at constant values of (τ, α,$C_p$and A_c) was determined using the expression

$$w_\eta = \left[\left(\frac{\partial \eta}{\partial \dot{m}} w_{\dot{m}} \right)^2 + \left(\frac{\partial \eta}{\partial T_o} w_{T_o} \right)^2 + \left(\frac{\partial \eta}{\partial T_i} w_{T_i} \right)^2 + \left(\frac{\partial \eta}{\partial I} w_I \right)^2 \right]^{1/2} \qquad Eq.\ (D3)$$

Total uncertainty for the exergy efficiency of the solar collector (at constant values of (T_s,$C_p$and A) was determined from the expression

$$w_{\hat{\mathrm{E}}} = \left[\left(\frac{\partial \hat{\mathrm{E}}}{\partial \dot{m}} w_{\dot{m}} \right)^2 + \left(\frac{\partial \hat{\mathrm{E}}}{\partial T_o} w_{T_o} \right)^2 + \left(\frac{\partial \hat{\mathrm{E}}}{\partial T_i} w_{T_i} \right)^2 + \left(\frac{\partial \hat{\mathrm{E}}}{\partial I} w_I \right)^2 + \left(\frac{\partial \hat{\mathrm{E}}}{\partial T_a} w_{T_a} \right)^2 \right]^{1/2} \qquad Eq.\ (D4)$$

Appendix-E

Accessories Used in the Experimental Setup

Arduino microcontroller

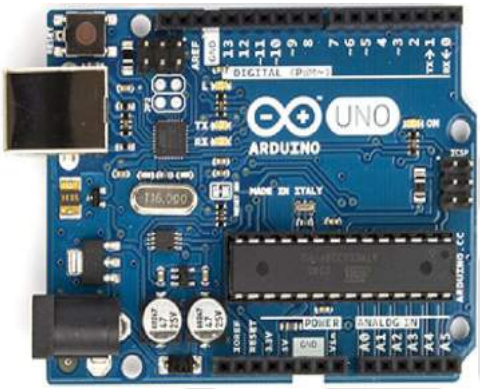

Motor driving modules

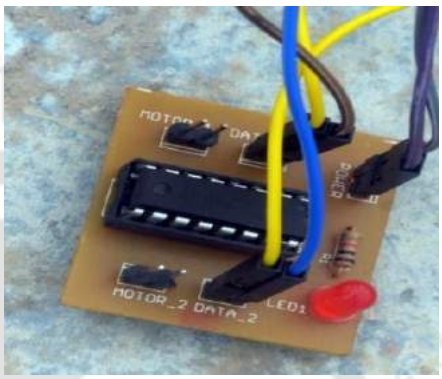

LM35 temperature sensor

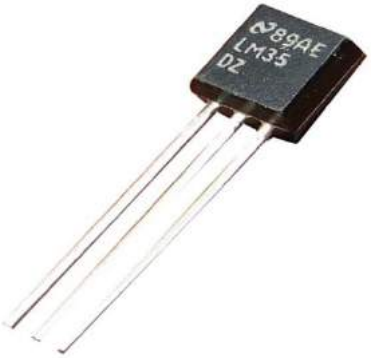

Selonoidal valve

Thermocouple

Data cable

Pyranometer

Flow meter (Rotameter)

Data acquisition system

JR-1 thermometer

Appendix-F

Programing Code Used for Controlled Experiments

```
const int sensor1=A1; // Assigning analog pin A1 to variable 'sensor'
const int sensor2=A2; // Assigning analog pin A1 to variable 'sensor'
const int sensor3=A3; // Assigning analog pin A1 to variable 'sensor'
const int sensor4=A4; // Assigning analog pin A1 to variable 'sensor'
int ValvePin1 = 4;
int ValvePin2 = 5;
int Relay_pin = 8;    // heating element connected to Relay or RC plug switches
float thermocouple1;  //variable to store temperature of sensor1
float thermocouple2;  //variable to store temperature of sensor2
float thermocouple3;  //variable to store temperature of sensor3
float thermocouple4;  //variable to store temperature of sensor4
float meanTemperature;
float vout;  //temporary variable to hold sensor reading


void setup()          // run once, when the sketch starts

{

  pinMode(sensor1,INPUT); // Configuring pin A1 as input
  pinMode(sensor2,INPUT); // Configuring pin A2 as input
  pinMode(sensor3,INPUT); // Configuring pin A3 as input
  pinMode(sensor4,INPUT); // Configuring pin A3 as input
  pinMode(ValvePin1,OUTPUT);      // sets the digital pin as output
  pinMode(ValvePin2,OUTPUT);      // sets the digital pin as output
  pinMode(Relay pin, OUTPUT);
  Serial.begin(9600);

}

//==========Functions====================//
//valve 1 is opening the flow to heat exchanger
void openValve1(){
   digitalWrite(ValvePin1, HIGH);
   Serial.println("Valve 1 Open");
}
//valve 2 is diverting the flow from heat exchanger
void openValve2(){
   digitalWrite(ValvePin2, HIGH);
   Serial.println("Valve 2 Open");
}
```

```
void closeValve1(){
  digitalWrite(ValvePin1, LOW);
  Serial.println("Valve 1 closed");
}

void closeValve2(){
  digitalWrite(ValvePin2, LOW);
  Serial.println("Valve 2 closed");
}

void loop()  // run over and over again
{
        //reading temperature of sensor1
        vout=analogRead(sensor1);
        vout=(vout*500)/1023;
        thermocouple1=vout;

        //reading temperature of sensor2
        vout=analogRead(sensor2);
        vout=(vout*500)/1023;
        thermocouple2=vout;

        //reading temperature of sensor3
        vout=analogRead(sensor3);
        vout=(vout*500)/1023;
        thermocouple3=vout;

        //reading temperature of sensor4
        vout=analogRead(sensor4);
        vout=(vout*500)/1023;
        thermocouple4=vout;

        //taking mean temperature of all the three therocouples
        meanTemperature=(thermocouple1+thermocouple2+thermocouple3)/3.0;

        //mean temperature printing
        Serial.print("in DegreeC=");
        Serial.print("\t");
        Serial.print(meanTemperature);

         if((meanTemperature > 40))
        {
          openValve2();
          closeValve1();
        }
```

```
        if((meanTemperature < 38))
        {
          openValve1();
          closeValve2();
        }

        if(thermocouple4  < 30)
        {                                   // if temperature is very low
                digitalWrite(Relay_pin, HIGH);                          // turn ON
Heater
        }
        else if(thermocouple4  > 35)
        {                                                   // else if temperature is moderate,
turn OFF Heater
                digitalWrite(Relay_pin, LOW);
         }
        else
        {
        }

        Delay (1000); //Delay of 1 second for ease of viewing
}
```

Publications from This Thesis

JournalPapers

1. **D. G. Gunjo,** P. Mahanta and P. S. Robi, CFD and experimental investigation of flat plate solar water heating system under steady state condition. Renewable Energy. 106 (2017) 24-36.(Doi: https://doi.org/10.1016/j.renene.2016.12.041).
2. **D. G. Gunjo,** P. Mahanta and P. S. Robi, Exergy and energy analysis of a novel type solar collector under steady state condition: Experimental and CFD analysis. Renewable Energy. 106 (2017) 655-669.

(Doi: https://doi.org/10.1016/j.renene.2017.07.072).

3. **D. G. Gunjo,** P. Mahanta and P. S. Robi, Melting enhancement of a latent heat storage with dispersed Cu, CuO and Al_2O_3 nanoparticles for solar thermal applications. Renewable Energy. 121C (2018) 652-665.
   (Doi: https://doi.org/10.1016/j.renene.2018.01.013).
4. **D. G. Gunjo**, P. Mahanta and P.S. Robi, Improving digestion of lignocellulosic biomass using solar water heating collector. Advanced in Waste Management Springer. (2018) (**Accepted**).

Conference Papers

1. **D. G. Gunjo**, S. R. Jena,P. Mahanta, P. S. Robi, Performance evaluation of latent heat storage filled with paraffin wax for solar thermal applications. 6th International Conference on Advances in Energy Research (ICAER 2017) on 12 –14th December 2017, at IIT Bombay.
2. **D. G. Gunjo**, P. Mahanta and P. S. Robi, Energetic and exergetic analysis of bent tube solar collector. National Conference on Sustainable Mechanical Engineering:Today and Beyond (SMETB'17), on 25 − 26th March 2017, at Tezpur University, Department of Mechanical Engineering.
3. **D. G. Gunjo**, P. Mahanta and P.S. Robi, Designing and utilizing of the solar water heater for digestion of lignocellulosic biomass.1stInternational Conference on Waste Management (RECYCLE 2016), on 1 – 2th April 2016, at IIT Guwahati.

4. **D. G. Gunjo,** P. Mahanta and P. S. Robi, Effect of pitch on heat transfer characteristics of helical coil to be used for biogas production. National Conference on Emerging Technologies' Contribution in Promoting Defence and Industry (NCETCPDIC), on July 2015, at Defence University, College of Engineering, Bishoftu, Ethiopia, 192−198.